TRANSMITTED WAVEFRONT TESTING OF COMPLEX OPTICS

by

Gregory Allen Williby

A Dissertation Submitted to the Faculty of the

COMMITTEE ON OPTICAL SCIENCES (GRADUATE)

In Partial Fulfillment of the Requirements
For the Degree of

DOCTOR OF PHILOSOPHY

In the Graduate College

THE UNIVERSITY OF ARIZONA

2003

UMI Number: 3108968

INFORMATION TO USERS

The quality of this reproduction is dependent upon the quality of the copy submitted. Broken or indistinct print, colored or poor quality illustrations and photographs, print bleed-through, substandard margins, and improper alignment can adversely affect reproduction.

In the unlikely event that the author did not send a complete manuscript and there are missing pages, these will be noted. Also, if unauthorized copyright material had to be removed, a note will indicate the deletion.

UMI®

UMI Microform 3108968

Copyright 2004 by ProQuest Information and Learning Company.

All rights reserved. This microform edition is protected against unauthorized copying under Title 17, United States Code.

ProQuest Information and Learning Company
300 North Zeeb Road
P.O. Box 1346
Ann Arbor, MI 48106-1346

THE UNIVERSITY OF ARIZONA ®
GRADUATE COLLEGE

As members of the Final Examination Committee, we certify that we have read the dissertation prepared by Gregory Allen Williby

entitled Transmitted Wavefront Testing of Complex Optics

and recommend that it be accepted as fulfilling the dissertation requirement for the Degree of Doctor of Philosophy

John E. Greivenkamp	12/2/03 Date
James C. Wyant	12/2/03 Date
James Schwiegerling	12/2/03 Date
	Date
	Date

Final approval and acceptance of this dissertation is contingent upon the candidate's submission of the final copy of the dissertation to the Graduate College.

I hereby certify that I have read this dissertation prepared under my direction and recommend that it be accepted as fulfilling the dissertation requirement.

Dissertation Director John E. Greivenkamp — 12/8/03 Date

STATEMENT BY AUTHOR

This dissertation has been submitted in partial fulfillment of requirements for an advanced degree at The University of Arizona and is deposited in the University Library to be made available to borrowers under rules of the Library.

Brief quotations from this dissertation are allowable without special permission, provided that accurate acknowledgment of source is made. Requests for permission for extended quotation from or reproduction of this manuscript in whole or in part may be granted by the head of the major department or the Dean of the Graduate College when in his or her judgment the proposed use of the material is in the interests of scholarship. In all other instances, however, permission must be obtained from the author.

SIGNED: 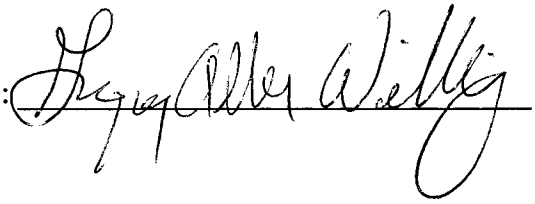

ACKNOWLEDGEMENTS

The author would like to thank everyone at the sponsor of this research who helped in providing funding and equipment and who served as a sounding board for discussing experimental setups and analysis algorithms.

For my family - past, present, and future

TABLE OF CONTENTS

LIST OF FIGURES 10

LIST OF TABLES 20

ABSTRACT 21

1 INTRODUCTION TO TRANSMITTED WAVEFRONT TESTING 23

1.1 Common Issues with Testing Optical Elements 27

1.1.1 Testable Parameters 27

1.1.2 Types of Output 28

1.1.3 Judging the Output 30

1.1.4 Null Optics – Pros and Cons 32

1.1.5 Qualifying Contact Lenses 34

1.2 Methods of Testing Transmitted Wavefronts 36

1.2.1 Star Testing 36

1.2.2 Shack-Hartmann Wavefront Sensor 38

1.2.3 Moiré Deflectometry 42

1.2.4 Lateral Shear Interferometry (LSI) 48

1.2.5 Phase Shifting Interferometry (PSI) 51

1.2.6 Sub-Nyquist Interferometry (SNI) 53

1.2.7 Other Techniques for Testing Ophthalmic Optics 55

1.3 Case Study for Testing Soft Contact Lenses 57

1.4 Scientific Questions Regarding the Testing of Immersed Optics 62

2 DESIGN OF AN EXTENDED DYNAMIC RANGE INTERFEROMETER 64

TABLE OF CONTENTS - *Continued*

2.1 Design Principles 66

2.2 Specifics of CLOVER Hardware 75

2.3 Theory of Wavefront Calibration 82

2.4 Specifics of CLOVER Software 92

3 VARIOUS ISSUES WITH TESTING SOFT CONTACT LENSES 97

3.1 Understanding the Material of Soft Contact Lenses 98

3.1.1 Making Soft Contact Lenses 101

3.1.2 The Need for Saline 102

3.2 Measuring the Index of Refraction 103

3.2.1 Measuring Saline 104

3.2.2 Measuring Hydrogels 105

3.3 Mounting Soft Contact Lenses 109

3.3.1 Initial Cuvette Design 111

3.3.2 Current Cuvette Design 113

3.4 Automated Lens Centering 115

4 TRANSMITTED WAVEFRONT TESTING OF SPHERICAL GLASS AND CONTACT LENSES 120

4.1 Detailed Explanation of Testing a Glass Calibration Lens 120

4.2 Study on Repeatability 146

4.3 Testing Other Spherical Glass and Contact Lenses 147

4.4 Testing Over the Complete Aperture of Contact Lenses 154

TABLE OF CONTENTS - *Continued*

5 TRANSMITTED WAVEFRONT TESTING OF TORIC, BIFOCAL, AND MULTIFOCAL CONTACT LENSES 159

5.1 Testing Toric Contact Lenses 160

5.2 Testing Bifocal Contact Lenses 167

5.2.1 Annular Zone Finding for Bifocal Lenses 170

5.2.2 Modal-Zonal Fitting for Bifocal Lenses 175

5.3 Multifocal Contact Lenses 180

5.3.1 Comparing Different Designs 181

5.3.2 Star Testing 182

6 TREATMENT ON RADIAL AXIAL POWER MAPS 185

6.1 Various Definitions of Power 186

6.2 Radial Axial Power Maps for Contact Lens Wavefronts 189

6.3 Representative Power Maps 195

6.3.1 Output from Synthetic Data 195

6.3.2 Output from Spherical Lenses 199

6.3.3 Output from Toric Lenses 205

6.3.4 Output from Bifocal Lenses 208

6.3.5 Output from Multifocal Lenses 211

7 TRADEOFF BETWEEN DYNAMIC RANGE AND SENSITIVITY 214

7.1 Dynamic Range Ratio (DRR) 214

7.2 Testing Over a Range of Solution Factors 219

7.3 Testing to the Nyquist Limit 229

TABLE OF CONTENTS - *Continued*

7.4 Discussion on Experiments Performed 231

8 TRANSMITTED WAVEFRONT TESTING OF OTHER COMPLEX OPTICS .. 235

8.1 Diffractive Lenses 235

8.2 Solgel Lenses 243

9 CONCLUDING REMARKS 249

9.1 Conclusions from Accomplished Tasks 251

9.2 Future Work 254

9.2.1 Immersion Testing 254

9.2.2 Reflection Testing 255

9.2.3 Reverse Raytracing 257

APPENDIX A: SAMPLE MODEL 259

REFERENCES 263

LIST OF FIGURES

FIGURE 1.1 – The 3 fields of development. All fields are of equal importance. 26

FIGURE 1.2 – Star testing. 37

FIGURE 1.3 – Basic operation of a Shack-Hartmann wavefront sensor. 39

FIGURE 1.4 – Shack-Hartmann spot pattern for a bifocal contact lens. The spot pattern does not show the presence of annular rings with different powers. 42

FIGURE 1.5 – Schematic for a moiré deflectometer. The deflected ray is due to the test optic (Kafri, 1985). 43

FIGURE 1.6 – Schematic for the OMS-101 moiré deflectometer. The distance traveled (Δz) between the top and bottom configurations is related to the focal lengths of the reference lens and test lens. Note that the test lens is at the rear focal point (F') of the reference lens. 46

FIGURE 1.7 – Basic LSI system. The imaging lens has as conjugates the test lens and detector. The interferogram is present only in the region of overlap between the two beams. 49

FIGURE 1.8 – SNI detector. The red box indicates the region corresponding to a single pixel. The only light sensitive portion is pinhole in the upper right quadrant of the pixel (Gappinger, 2002). 54

FIGURE 1.9 – Cartoons for (a) toric and (b) bifocal contact lenses. 59

FIGURE 1.10 – Zemax interferogram for a bifocal contact lens in double pass..... 60

LIST OF FIGURES - *Continued*

FIGURE 1.11 – Twymann-Green interferogram for same lens as Fig. 1.10..... 61

FIGURE 2.1 – Plot of typical aspheric wavefront and its derivative. The maximum of the derivative gives the maximum expected fringe frequency. 66

FIGURE 2.2 – Solution space of acceptable detectors. 68

FIGURE 2.3 – Magnification over the space of possible detectors..... 69

FIGURE 2.4 – Construction for determination of maximum fringe frequency supported by the imaging lens. 70

FIGURE 2.5 – CLOVER interferometer. 75

FIGURE 2.6 – Magnification target used to correlate test aperture diameter to number of pixels. Each ring increases by 1 mm in diameter..... 93

FIGURE 3.1 – Chemical structure for the monomer hydroxyethyl methacrylate (HEMA) (Mandell, 1974)..... 99

FIGURE 3.2 – Soft stabilized molding manufacturing process for hydrogel contact lenses..... 101

FIGURE 3.3 – Index of refraction of saline solution versus time (Brumfield, 2003). ... 104

FIGURE 3.4 – Simple cuvette with V-block holding a lens in a vertical orientation. The deviation from circular fringes in the vicinity to the V-block indicates deformation of the lens..... 110

LIST OF FIGURES - *Continued*

FIGURE 3.5 – Third iteration of initial cuvette design. Shown are the (a) cuvette, (b) lens barrel clamp and lens barrel. 112

FIGURE 3.6 – Current cuvette. Lenses are inserted on a middle window, and pushed on a dovetail stage between the two fixed windows of the cuvette. 114

FIGURE 3.7 – Pseudo-bright field image created by summing four interferograms. The dark ring is the edge of the lens where light is scattered out of the imaging lens' aperture. The outermost ring is the edge of the cuvette's window. 117

FIGURE 3.8 – Modulation map for soft contact lens. 118

FIGURE 4.1 – Outline of calibration process used to estimate the test wavefront at the test plane. 122

FIGURE 4.2 – Mach-Zehnder interferometer with labeled test and reference planes. .. 124

FIGURE 4.3 – Image of the reference wavefront (Img$\{W_R\}$). 125

FIGURE 4.4 – Portion of a Mach-Zehnder interferometer illustrating the relationship between the reference wavefront and its image. 126

FIGURE 4.5 – Bad pixel identification by eroding regions of poor modulation: (a) typical interferogram, (b) bad pixel mask due to modulation only, and (c) enhanced bad pixel mask. 128

FIGURE 4.6 – Image of the test wavefront produced by the calibration optic specified in Table 4.1. 129

LIST OF FIGURES - *Continued*

FIGURE 4.7 – Check on the generation of the wavefronts: (a) Img$\{W_T\}$ – Img$\{W_R\}$ and (b) OPD_T. 131

FIGURE 4.8 – Difference between Img$\{W_T\}$ – Img$\{W_R\}$ and OPD_T. The ideal result is a plane. 133

FIGURE 4.9 – Zernike fit to difference between Img$\{W_T\}$ – Img$\{W_R\}$ and OPD_T..... 134

FIGURE 4.10 – Zernike fit to difference with tilt removed. The PV of this surface is 0.00038 λ, while the RMS is 0.000031 λ, or about 17 picometers. 135

FIGURE 4.11 – Measured wavefront ($\tilde{W}_T$) for the calibration lens..... 136

FIGURE 4.12 – Positive and negative powered test beams (dashed) with respect to the planar reference beam (solid). The reference beam comes to focus at the rear focal point for the imaging lens (F'_I). 137

FIGURE 4.13 – Comparison of OPD surfaces for the purpose of determining the level of induced aberrations: (a) $OPD_{T\ @\ Detector}$ and (b) $OPD_{T\ @\ Test\ Plane}$. 139

FIGURE 4.14 – Complete analysis routine for comparing measured-to-modeled performance. 141

FIGURE 4.15 – Modeled wavefront (W_T^M) for calibration lens. 142

FIGURE 4.16 – Measured minus modeled ($\tilde{W}_T - W_T^M$) wavefront difference for calibration lens. 143

FIGURE 4.17 – Zernike fit to the measured minus modeled wavefront difference..... 144

LIST OF FIGURES - *Continued*

FIGURE 4.18 – Interferogram of -20 D glass lens in air over 3 mm. The departure for this interferogram is 41.36 λ. 148

FIGURE 4.19 – Zernike fit to wavefront difference for -20 D lens. 149

FIGURE 4.20 – Measured wavefront ($\tilde{W}_T$) minus tilt and focus. 150

FIGURE 4.21 – Measured OPD from Intelliwave minus tilt and focus. 151

FIGURE 4.22 – Interferogram of -10 D contact lens over 5 mm. 152

FIGURE 4.23 – Zernike fit to wavefront difference for -10 D contact lens over 5 mm. 153

FIGURE 4.24 – Measured wavefront for -10 D contact lens with tilt and focus removed 154

FIGURE 4.25 – Full lens interferogram for -10 D lens. 155

FIGURE 4.26 – Unwrapped wavefront for -10 D lens over a 14 mm aperture 156

FIGURE 4.27 – Unwrapped wavefront for -10 D lens. 157

FIGURE 5.1 – Identifying the orientation of a toric contact lens: (a) the pseudo-bright field image via interferograms, and (b) the image with the fiducial marks identified by placing three "O"s on each central mark. 161

FIGURE 5.2 – Interferogram of a toric contact lens over 5 mm. 162

FIGURE 5.3 – Zernike fit to wavefront difference over 5 mm. 163

FIGURE 5.4 – Full lens interferogram for analyzed toric lens 165

LIST OF FIGURES - *Continued*

FIGURE 5.5 – Full lens interferogram for a weaker toric lens. 166

FIGURE 5.6 – Measured wavefront at test plane for a toric contact lens over 13 mm.. 167

FIGURE 5.7 – Synthetic wavefronts for a bifocal contact lens (a) without piston and (b) with piston between the zones. Piston is necessary to provide a continuous surface on the lens. 169

FIGURE 5.8 – Interferogram of a bifocal contact lens over 5 mm. 171

FIGURE 5.9 – Measured wavefront at the test plane for a bifocal lens over 5 mm..... 172

FIGURE 5.10 – Measured wavefront minus best-fit sphere (BFS)..... 173

FIGURE 5.11 – Map of the sign for radial slope..... 174

FIGURE 5.12 – Processed map of radial slope used for zone identification. 175

FIGURE 5.13 – Residual map between a bifocal wavefront and the Zernike fit to the same wavefront. 176

FIGURE 5.14 – Polynomial fit to measured wavefront in Fig 5.9. 177

FIGURE 5.15 – Residual map between a bifocal wavefront and the polynomial fit to the same wavefront. 178

FIGURE 5.16 – Measured wavefront at the test plane for a multifocal lens over 5 mm. 181

FIGURE 5.17 – Measured wavefront for a multifocal lens of a different design. Note the larger depression. 182

LIST OF FIGURES - *Continued*

FIGURE 5.18 – Modified CLOVER arrangement for star testing. 183

FIGURE 5.19 – Modified star test to compare bifocal and multifocal lenses: (a) through-focus images for a bifocal and (b) through-focus images for a multifocal lens. 184

FIGURE 6.1 – Single refracting surface used in describing the various definitions of power. The subscripts on d refer to the three types of power: position, axial, and instantaneous. Note that the distances corresponding to axial and instantaneous power lie in the same plane but differ in length..... 187

FIGURE 6.2 – Determination of axial power for contact lens wavefronts. 189

FIGURE 6.3 – Power map for a synthetic parabolic wavefront (R = 1000 mm). 196

FIGURE 6.4 – Power map for a synthetic spherical wavefront (R = 1000 mm)..... 197

FIGURE 6.5 – Power map for a 200 D synthetic spherical wavefront (R = 5 mm). Note that the sage of this wavefront is outside the area of small angles, and thus the reported power for such a wavefront has no meaning. 198

FIGURE 6.6 – Power map for measured wavefront ($\tilde{W}_T$) for calibration lens. 199

FIGURE 6.7 – Same map as Fig. 6.6, but with central 2% eliminated. 200

FIGURE 6.8 – Power map for modeled wavefront (W_T^M) for calibration lens. 201

FIGURE 6.9 – Difference between measured and modeled power maps. 202

FIGURE 6.10 – Power map for the measured wavefront ($\tilde{W}_T$) for a -10 D contact lens. 203

LIST OF FIGURES - *Continued*

FIGURE 6.11 – Difference power map for a -10 D contact lens. 204

FIGURE 6.12 – Power map for a synthetic toric wavefront..... 205

FIGURE 6.13 – Power map for a synthetic toric wavefront with different conic constants in each principal meridian..... 206

FIGURE 6.14 – Power map for the measured wavefront from a toric contact lens..... 207

FIGURE 6.15 – Power map for the modeled wavefront. 208

FIGURE 6.16 – Power map for the measured wavefront from a bifocal contact lens.. 209

FIGURE 6.17 – Power map for the raw wavefront from a bifocal contact lens..... 210

FIGURE 6.18 – Power map for a multifocal contact lens from the wavefront shown in Fig. 5.16. 212

FIGURE 6.19 – Power map for a multifocal contact lens from the wavefront shown in Fig. 5.17. 213

FIGURE 7.1 – Interferogram for f/2 cylindrical lens immersed in water. The solution factor is 2.8079..... 221

FIGURE 7.2 – Interferogram over a 2.8 mm test aperture (SF = 2.8079)..... 222

FIGURE 7.3 – Zernike fit to measured wavefront ($\tilde{W}_T$) for f/2 cylindrical lens (SF = 2.8079). 222

FIGURE 7.4 –Measured wavefront minus best-fit cylinder (SF = 2.8079)..... 223

FIGURE 7.5 – Interferogram over a 2.8 mm test aperture (SF = 4.4728)..... 224

LIST OF FIGURES - *Continued*

FIGURE 7.6 –Measured wavefront minus best-fit cylinder (SF = 4.4728)..... 225

FIGURE 7.7 – Full lens interferogram for f/2 cylindrical lens (SF = 9.2246). 226

FIGURE 7.8 –Measured wavefront minus best-fit cylinder (SF = 9.2246)..... 227

FIGURE 8.1 – Bright field images of a diffractive lens formed via liquid crystal. The lens is off in (a) and on in (b)..... 236

FIGURE 8.2 – Interferograms for diffractive lens with (a) lens off and (b) lens on..... 237

FIGURE 8.3 – Close-up of the interferogram in Fig. 8.2 (b). 238

FIGURE 8.4 – Interferogram (a) and close-up (b) for a new diffractive lens without gaps. 239

FIGURE 8.5 – Unwrapped wavefront (a) and wavefront minus tilt and focus (b) for the diffractive lens. 240

FIGURE 8.6 – Images from compound diffractive-refractive imaging system: (a) diffractive lens off and (b) diffractive lens on. 241

FIGURE 8.7 – MTF plot for the diffractive lens. 242

FIGURE 8.8 – Initial solgel lenses examined over a diameter of 0.85 mm: (a) interferogram and (b) unwrapped wavefront. 244

FIGURE 8.9 – Solgel sample with three high quality lenses. From left-to-right are lenses R, C, and L. 245

LIST OF FIGURES - *Continued*

FIGURE 8.10 – Unwrapped wavefronts for solgel lenses: (a) lens R, (b) lens C, and (c) lens L. The PV numbers are 0.9870, 0.9439, and 0.8978 λ..... 246

LIST OF TABLES

TABLE 2.1 – Selected requirements for interferometer..... 64

TABLE 3.1 –Composition and characteristics of leading soft contact lenses..... 99

TABLE 3.2 – Full names for monomers used in soft contact lenses (Tighe, 1997)..... 100

TABLE 4.1 – Parameters for calibration optic..... 130

TABLE 4.2 – PV and RMS values for the two comparable OPD surfaces..... 139

TABLE 4.3 – Repeatability study on CLOVER using the calibration lens. Data was collected over ten trials..... 147

TABLE 5.1 – Polynomial terms used in fitting bifocal wavefronts..... 179

TABLE 5.2 – Relationships between bifocal and Zernike coefficients..... 179

TABLE 7.1 – Relevant data from the repeatability study on CLOVER using the calibration lens. Data was collected over ten trials..... 217

TABLE 7.2 – Derived DRR statistics for calibration lens. The wavelength for the interferometer is 543.5 nm..... 218

TABLE 7.3 – Results for an f/2 cylinder over a range of solution factors. The spherical radius is shown only as a means of verifying the validity of the conversion between ophthalmic power and radius..... 228

TABLE 7.4 – Results for an f/2 cylinder over a range of solution factors..... 228

TABLE 7.5 – Results for an f/2 cylinder over an increasing test aperture..... 230

TABLE 8.1 – Comparison in reported radius of curvature between CLOVER and WYKO profilometer for solgel lenses..... 246

ABSTRACT

The advancement of optical systems arises from furthering at least one of the three fields of optical development: design, fabrication, and testing. One example of such advancement is the growth in customization of contact lenses, which is occurring in part due to advances in testing. Due to the diverse quantities that can be derived from it, the transmitted wavefront is the tested parameter. There are a number of tests that can evaluate a transmitted wavefront, including moiré deflectometry, Shack-Hartmann wavefront sensing, and interferometry. Interferometry is preferred for its sensitivity and spatial resolution. The dynamic range issue is mitigated by the required immersion of the contact lenses in saline due to the complex nature of the lens material. The partial index-match between the lens and surrounding saline reduces the measured power of the lens and enables testing in an absolute, or non-null, configuration. Absolute testing allows for the generation of ophthalmic prescriptions and power maps from the transmitted wavefront.

Designing a non-null interferometer is based on three principles. The transmitted light must be collected, the resulting interference must be resolved, and the imaged wavefront must be calibrated. The first two principles are fulfilled by proper choices for the imaging lens and detector. Calibration comes from removing the wavefront-dependent induced aberrations via reverse raytracing. Reverse raytracing demands an accurate model of the interferometer. With such a model, theoretical wavefronts can be produced

and compared to measured wavefronts. The difference between measured and modeled wavefronts quantifies the answer to the fundamental question in transmitted wavefront testing: does the optic perform as desired?

Immersion in index-matching fluid provides an adjustable increase in the dynamic range of the interferometer. The increase comes at the expense of sensitivity. The tradeoff between dynamic range and sensitivity can be quantified by the dimensionless ratio between the two numbers. This ratio is interpreted as a degree of difficulty for a measurement. Combined with absolute testing, immersion provides the ability to measure fast cylindrical lenses, which are notoriously difficult to test. Understanding the parameters of the interferometer provides a simple condition for determining the gain from immersion.

1 INTRODUCTION TO TRANSMITTED WAVEFRONT TESTING

Optical science encompasses a vast spectrum of research areas. There is research being done in all parts of the world, on all scales, in all facets of life, from medicine to national defense, from fundamental science to applied engineering. Within the branch of optics known as optical engineering there exists a wide range of research opportunities. Optical engineering is the application of scientific principles to specific, practical problems using optical techniques. Often optical engineering efforts lead to the development of a new device or an improvement to an existing device. Whatever the opportunity, the solution to the problem includes some configuration of light sources, detectors, and other optical elements. The development of optical elements is a field of vast research, and covers the scope of this dissertation.

There are three main fields concerning the development of optical elements: design, fabrication, and testing. The fields are listed in this order not because of importance or relevance, but simply because this is the chronological order of development. Design defines the optical configuration. This is the time when the desired specifications are matched with surfaces, coatings, and materials to create the desired element. The process is the same regardless of the type of element or system developed; simple mirrors, lens assemblies, and more exotic elements, such as diffraction gratings or computer generated holograms (CGH), are all designed using the same principles. Fabrication takes the

designed model and turns it into a real element. Simply stated, though far from simple in practice, fabrication is the conversion from software to hardware. Finally, testing qualifies the manufactured optic. Often, the results of the test are compared to the expected results for the design, thereby closing the development loop.

The first field, optical design, has undergone a renaissance due to the widespread use and advances of the personal computer. Before the personal computer, the simple act of tracing rays required tedious interfacing with a mainframe via punch cards, or before that, long hours with a slide rule. Today, the computer found in any lab can trace millions of rays in a matter of seconds (Robb, 1990; Sinclair, 1991). The use of lens design code, such as Code V (Optical Research Associates, Pasadena, California), Oslo (Lambda Research Corp., Littleton, Massachusetts), or Zemax (Zemax Development Corp., San Diego, California), has freed the designer from the vast majority of the mathematics associated with lens design. The computer has also enabled radical ideas to be explored with little cost of time or money.

A particular area of growth due to the advances of lens design code is the number and variety of surface types available to the designer today. Later in this dissertation the testing of some highly aspheric optics is examined. These surfaces would not exist as parts of real elements if the means to design them and quickly evaluate their performance did not exist. One only needs to look at any of the user's guides for the design software to see the variety of surface types available today. The assortment of available surfaces is

due to not only the superior computing power available, but to advances in materials and manufacturing.

The second field of development is fabrication. As previously mentioned, there have been significant improvements in manufacturing techniques in recent decades. Again, the computer plays an integral role in these technologies. Techniques such as injection molding, single-point diamond turning (SPDT), computer-controlled polishing (CCP), and magnetorheological finishing (MRF) have all flourished due to in part the proliferation of computing power (Karow, 1993; Shorey, 2001).

The third field, testing, complements the other two fields by providing insight into how well the manufacturing process carried out the instructions of the design. Testing can take a number of forms, from a simple measurement with a ruler or other mechanical gauge, to elaborate, million dollar instruments with atomic resolution. Different tests provide different outputs. The desired output may be a single number, such as focal length or diffraction efficiency, or much more complex, such as a 3D model of the optic.

One may wonder which field is most important, or which field drives the others. Even though the typical development process is design, fabrication, and testing, this is not the order of importance. In fact, the answer is that all three fields are vital to a successful design and each field expands and limits the others. The three fields are of equal importance, and all fields influence the others, a notion supported by others (Lee, 2003).

The fields should be thought of as a cycle with no beginning or end, turning in whatever direction is necessary to produce the desired element. Figure 1.1 illustrates this idea.

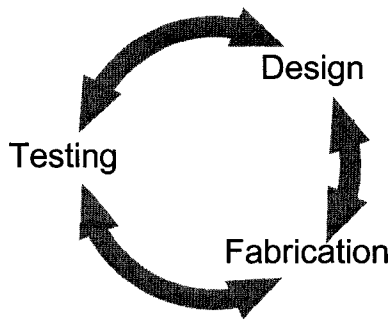

FIGURE 1.1 – The 3 fields of development. All fields are of equal importance.

Progress is made when one field is pushed to new levels of performance. This often comes about from the limitations or constraints of another field. For example, a successful design is useless if it cannot be fabricated. Yet if this is the only design that meets all system requirements, then efforts may be warranted in the fabrication field to push current technology to make the design possible. These three fields are not independent; they are an intertwined set of criteria, capabilities, and techniques that make developing optical elements possible.

The following discussions and presented research pertain to the field of testing. Advances in both design and fabrication have generated a need for new testing techniques. While one example is examined in detail, the metrology of soft contact lenses, the questions, both asked and answered, and the techniques developed are applicable to numerous instruments and testing scenarios.

1.1 Common Issues with Testing Optical Elements

Testing was introduced as the qualification of the fabricated optical element. While this is an accurate definition, it does not begin to indicate the magnitude of issues surrounding the task of testing an optic. Like any project, the paramount constraints of scope, cost, and time must be balanced in accordance with the development of the optical element as a whole. Different projects will place different weights on these constraints. For example, the testing of an 8 meter primary mirror for a multi-million dollar telescope will likely place accuracy and completeness (scope) ahead of cost and time. For mass-produced optics, speed and cost will certainly be pressed to maximize efficiency. The real question in this case is to what level the accuracy of the test will be compromised to accommodate speed and cost.

The issues regarding testing are summarized in a few, basic questions:

What are the testable parameters?

What results from the test are desired?

How will the results be judged?

1.1.1 Testable Parameters

Any element under test has multiple testable parameters. The task is to identify those parameters that are of interest. These may be the set of parameters used in designing the element or the set of parameters that influence the performance of the element. Often, these two sets have a great overlap, thereby indicating the parameters of true importance.

For a simple example, consider a first-surface mirror with power. While parameters such as thickness, weight, or thermal expansion could be measured, more likely candidates are curvature, surface figure, diameter, surface roughness, and reflectivity. As elements become more complex, or become systems with multiple elements, the determination of which parameters to test becomes more important. Not only will complex elements or systems be expected to perform over a variety of inputs (e.g. wavelengths, fields, or spatial frequencies), but the parameters that dictate performance will grow in number and complexity. This leads to the act of tolerancing, whereby a model of the element is analyzed to determine the parameters critical to performance (Shannon, 1997; Fischer, 2000). Tolerancing is beyond the scope of this dissertation, save for a brief discussion of the need to have an accurate model in calibrating instrumentation.

1.1.2 Types of Output

Along with the selection of the appropriate parameters to test comes the selection of what output should be reported. The two selection processes are coupled. For example, reporting MTF can only occur if some quantity related to MTF has been tested. Once again, the view that testing is not an isolated act is important. The choices made in testing must be in accordance with the other developmental fields of design and fabrication. The output from the test should be relevant to the criteria under which the element was designed and manufactured.

While by no means a complete list, below are listed some common outputs from a variety of optical tests. This list is geared towards refractive and reflective elements, i.e. lenses and mirrors (Malacara, 1992; Geary, 1993; Stover, 1995).

- Aberration Content
- Absorption
- Bidirectional Reflectance/Scatter/Transmittance Distribution Function (BRDF/BSDF/BTDF)
- Centration
- Coating Uniformity
- Departure from a Standard (or Master) Element
- Focal Length
- Index of Refraction
- Line Spread Function (LSF)
- Modulation Transfer Function (MTF)
- Optical Transfer Function (OTF)
- Point Spread Function (PSF)
- Polynomial Fit to Surface or Wavefront
- Radius of Curvature (R of C)
- Reflectivity
- Scratch/Dig
- Stokes Parameters
- Strehl Ratio (SR)

- Stress, Strain, and Stria
- Surface Peak-to-Valley (PV)
- Surface Root-Mean-Square (RMS)
- Surface Roughness
- Transmitted Wavefront
- Wavefront Curvature or Slope

1.1.3 Judging the Output

Once the type of output is selected, the criteria against which that output will be judged needs to be determined. In short, this is establishing the go/no-go line. Obviously, the criteria need to be at levels that guarantee the optic will perform its designed task. However, setting the criteria beyond the level at which the optic was designed is a disservice to the entire development process. Like so many aspects of optical development, the optimal solution may never be found, but a serviceable solution is almost always available.

One method for judging the output is to compare the output of the real optic against the theoretical output of its model. The benefit of this method is that it can quantify the answer to the question: "Does the optic perform as designed?" The downside to this method is that the instrumentation used to collect the output must either be accurately modeled or of much greater quality than the test optic so as not to be a source of error.

Imagine the scenario of MTF testing a lens by imaging bar targets. The modeled MTF, most likely formed using Fourier techniques (Goodman, 1996), will be free of errors such as fabrication tolerances on the bar target, alignment between the target and lens, and variations in illumination across the target. These errors, and many others, all must be considered when comparing measured versus modeled output.

Another method for evaluating performance is to simply compare the tested parameter against a known optical standard. The Strehl ratio (SR) is a perfect example. Optical metrologists know that an SR of 0.8 or higher indicates acceptable performance for near diffraction-limited systems, as this number is rooted in the Rayleigh or Marechal criterion for resolution (Wyant, 1992; Smith, 2000). A different example is the combination of PV and RMS. The PV of a surface gives the extremes for departure from the ideal, while RMS quantifies the surface as a whole. Optical surfaces are often specified with an RMS expressed as a fraction of a wave, such as $\lambda/10$.

Comparing PV to RMS gives a feel for the surface figure. If the PV is only slightly greater than the RMS, then the surface is fairly irregular at the PV/RMS level. If the PV is significantly greater (factor of ten or more) than the RMS, the PV is being skewed by an outlying point(s). The rule of thumb for PV to RMS is that the PV should be a factor of 2 to 8 for a quality optical surface (Miller, 1996).

1.1.4 Null Optics – Pros and Cons

At this point, a brief diversion to discuss the topic of null optics is in order. The type of output "Departure from a Standard (or Master) Element" implies that testing be done against a superior part. This superior part, or at least what is supposed to be a superior part, is often used in such a way that the output of the test is a null condition. Thus, the superior part is referred to as a null optic. Examples of null results include the absence of fringes in the case of interferometry, or the lack of spot movement in a Shack-Hartmann wavefront sensor. In any case, the null optic is a test part-specific optic employed to make the testing possible or easier.

Basically, there are two ways in which a null optic improves an optical test. Either the null optic behaves the same as or opposite of the test optic. If the null optic mimics the test optic, then the instrumentation should in some fashion subtract the outputs from the null and test optics. For example, a Mach-Zehnder interferometer with a test optic in one arm and a null optic in the other arm will produce no fringes if the two optics perform identically.

Null optics are most often used when the cost associated with the null optic is insignificant to the project as a whole. In this context, cost not only means dollars, but also man-hours with respect to design time and fabrication. An example of a project where the cost of a null optic is insignificant is the production of primary mirrors for telescopes. The University of Arizona manufactures the largest mirrors in the world,

over 8 m in diameter, to serve as primary mirrors in telescopes (West, 1992). The cost of the mirror alone, not including the total cost of building the telescope, overwhelms the cost of using a null optic. This is often the case with specific, one-of-a-kind optics. So much effort goes into the project as a whole that the added work associated with using a null optic is not noticed. A popular choice for a null optic today is a CGH. For more on the use of CGHs with telescopes, see Burge (1995).

The obstacles to using null optics are numerous. Going back to the idea that any project is constrained by scope, cost, and time, the use of null optics pushes on all three constraints. Scope is increased because all the issues associated with developing the test optic are also applicable to the null optic. Any cost or time used in developing the null optic takes resources away from the test optic. In addition, using null optics to ease the testing of some other optic brings up a very interesting question: How do you test the null optic? And if testing the null optic is straightforward, why not use that method to test the original optic under development? Plus, the null optic must be tested to levels greater than those desired for the test optic and aligned to such a level of precision that alignment errors are negligible. The problem of qualifying the null optic, to then qualify the test optic is analogous to a cat chasing its tail. It's a problem with no apparent beginning or end, and one that is usually best avoided by not using null optics.

Finally, there is the common case of a partial null optic: an optic that makes testing easier while not being identical in performance to the test optic. Usually the partial null optic

removes the majority of the power of the lens under test. For any test optic with power, power will be the dominant error, or difference from flat. Examples of partial nulls include the reference optics used with commercial laser Fizeau interferometers. Refractive partial nulls predominately contain spherical surfaces, and many single lens nulls have a plano surface. This is done to ease the manufacturing of these elements to tolerances greater than those desired for the test optic. Simple partial nulls are also easier to align.

1.1.5 Qualifying Contact Lenses

Contact lenses present several unique testing issues, which are covered throughout this dissertation. Initially, the question is how best to qualify these lenses. These are mass produced optics, so the process needs to be one that can be done quickly and cheaply. There are thousands of different prescriptions, so the instrumentation must be able to handle a wide range of test part powers. Not all of the designs are rotationally symmetric (i.e. toric lenses for correcting astigmatism), so the instrumentation needs to be robust, and probably needs to examine the entire test aperture of the lens. Bifocal contact lenses can have regions of power less than a millimeter in diameter, so the instrumentation must be able to make accurate measurements over sub-millimeter regions. What is ultimately desired is the performance of the lens measured against the labeled, or at least known, performance.

In order to measure the performance of a lens, the lens needs to be tested in such a way that only its own performance is measured. Testing against a null optic measures performance against the null, and does not measure performance in an absolute sense. Plus, with the potential for thousands of different lenses being tested, the use of null optics is not practical. The use of null optics is unnecessary for a different reason as well. The lenses must be tested in saline solution (more on this in Chpt. 3). The similarity in index of refraction between the saline and the contact lens effectively reduces the power to a point that testing in an absolute sense is feasible.

Of all possible testable parameters, the one that makes the most sense to measure in this case is the transmitted wavefront. The transmitted wavefront is the parameter most closely related to lens performance. By directly measuring the effect of the lens on an incident wavefront, a plethora of information can be obtained. In general, MTF, PSF, and aberration content can all be measured from the transmitted wavefront. Another advantage is that since the wavefront is being measured in an absolute sense, the power, and ultimately the prescription for the lens, can be measured. This would not be possible if null optics were being used. The use of null optics would also be cost prohibitive, as potentially thousands of different lens prescriptions will be tested. Each prescription would require its own null optic. Also, the transmitted wavefront is one of the easier lens parameters to measure. Since the lens is immersed in a fluid of nearly the same index, getting a reflection off a surface would take significantly more power from the light source. In addition, two surfaces would need to be measured to get an idea of the

performance of the lens, whereas only one transmitted wavefront is needed to measure performance. For these reasons, the desired fundamental quantity is the transmitted wavefront. The question now is how best to collect the transmitted wavefront over a range of lens powers and wavefront profiles.

1.2 Methods of Testing Transmitted Wavefronts

There are several ways to examine the transmitted wavefront of an optic in order to qualify the optic's performance. Discussed here are some of the more common techniques, or techniques that have been mentioned in the literature with regards to the specific testing of ophthalmic optics, including contact lenses. The first method discussed, star testing, is used mostly only in the qualitative sense. The next two methods, Shack-Hartmann (S-H) wavefront sensing and moiré deflectometry, are geometric tests. The following three methods, lateral shearing interferometry (LSI), phase shifting interferometry (PSI), and sub-Nyquist interferometry (SNI) are, of course, tests based on the interference of optical waves. For completeness, also mentioned are other tests discussed in the literature specific to measuring ophthalmic optics.

1.2.1 Star Testing

Star testing is essentially the examination of a point image. Often used in astronomy (hence the name), the star test is good at quickly and straightforwardly providing

qualitative information. However, the star test is not designed to easily provide quantitative information (Welford, 1992).

The star test is simple to set up; the only unique component to the test is a microscope objective, or some other type of magnifying optic. The objective images to infinity (in the case of use with the eye) and magnifies the test optic's focal plane, as shown in Fig. 1.2. The objective must have a greater numerical aperture (NA) than the test lens, ensuring that all the light of the point image is collected.

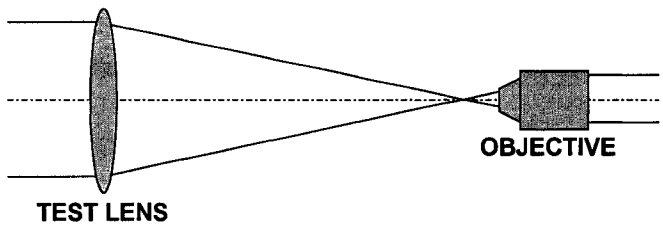

FIGURE 1.2 – Star testing.

The illumination for the star test can either be a point source truly at infinity or a collimated pinhole. In the case of a collimated pinhole, great care must be taken in alignment to avoid the introduction of additional aberrations.

With star testing, the aberrations are detected in the image plane of the test optic. This is typically done by scanning along the axis, looking at various out-of-focus images. The ideal image is the well known Airy disk pattern. With some training, deviations from the Airy disk pattern can provide some qualitative information about the aberrations present.

In general, aberrations move energy from the central core of the Airy disk to the outer rings (Welford, 1992). So by adding defocus, more light is present in the outer rings, which makes anomalies in the light distribution of the outer rings easier to detect. The presence of spherical aberration will cause a rotationally symmetric error in the distribution of the outer rings. Geary suggests the use of zonal masks at the test lens to map out the longitudinal spherical aberration (Geary, 1993). Astigmatism is the source of two-fold symmetry in the detected spot. This pattern is often referred to as the Maltese cross (Welford, 1992). Coma is present when the spot has only a single axis of symmetry. Assuming the pinhole is nominally aligned to the axis of the test optic, the presence of coma is then due to a slight tilt or misalignment in the optical setup.

Star testing was performed in a qualitative sense on some bifocal contact lenses. The results of the tests are presented in the chapter on testing bifocal lenses.

1.2.2 Shack-Hartmann Wavefront Sensor

A derivative of the Hartmann screen test, the Shack-Hartmann wavefront sensor (S-H) is a geometric test measuring wavefront slope (Shack, 1971; Ghozeil, 1992; Platt, 2001). The basic operation of a Shack-Hartmann is illustrated in Fig. 1.3.

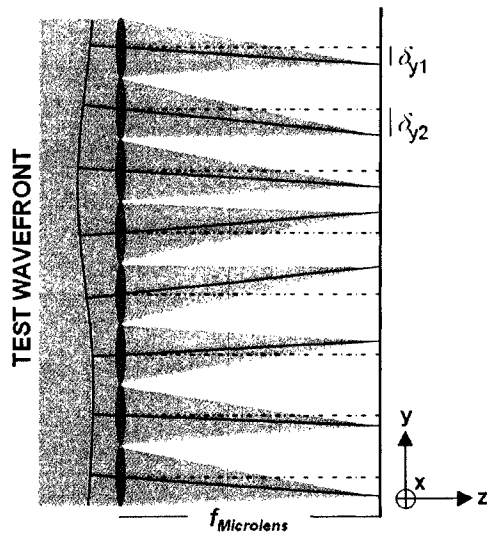

FIGURE 1.3 – Basic operation of a Shack-Hartmann wavefront sensor.

The test wavefront is incident on a lenslet array. The lenslet array consists of a regular grid of microlenses. Each lenslet samples the wavefront. A planar wavefront produces focus spots that lie on a regular grid. These positions are noted as the reference locations. With the non-planar test wavefront incident on the lenslet array, the spots move according to the average wavefront slope across the aperture of each lenslet. In effect, each microlens forms an imaging system, with the aperture stop at the microlens. The ray passing through the center of the lens becomes a chief ray, as shown in Fig. 1.3, and locates the center of the spot. It should be noted that the spot centroid predicted by geometrical optics is identical to the physical optics' centroid (Mahajan, 1985).

By noting the change in positions for the focus spots between the planar reference wavefront and the test wavefront, the wavefront slope across each lenslet can be determined via Eq. 1.1 (Groening, 2000).

$$\nabla_{(x,y)}W(x,y) = \frac{\delta_{(x,y)}}{\sqrt{\left(f^2 + \delta_x{}^2 + \delta_y{}^2\right)}} \qquad \text{Equation 1.1}$$

The shift of the spots in x and y are denoted as $\delta_{(x,y)}$. The focal length of the microlenses is f. Typically, the determined wavefront slopes are then integrated to form a measure of the test wavefront. This can be done in either a zonal or modal fashion (Southwell, 1980).

Clearly, the unique component in the Shack-Hartmann is the lenslet array. The design of the lenslet array is critical to getting the desired dynamic range, sensitivity, and spatial resolution. The focal length of the microlenses acts as a lever arm in this test; increasing the focal length increases the spot shift for a given wavefront slope, and therefore increases the sensitivity of the measurement. However, a longer focal length may cause dynamic range issues, as the spots may wander too far from the reference positions, or cross each other, both unacceptable conditions for most Shack-Hartmann algorithms (Smith, 2003).

Perhaps the biggest downside to the Shack-Hartmann test is the achievable spatial sampling. The spatial sampling is obviously dictated by the pitch of the lenslet array. Well-defined spots, free of diffraction effects near their center, are needed to accurately

determine the spot shifts. This requires that the diameter of the microlenses be significantly greater than the wavelength used. Typical lenslet diameters are hundreds of microns, so the sampling of a wavefront is on the order of only 1-10 samples/mm (Artzner, 1992; Groening, 2000).

In the field of ophthalmic testing, a modified Hartmann test has been used to test progressive spectacle lenses (Castellini, 1994). The modification was to scan a single beam across the lens, and note the deflected beam's position. The results obtained matched the predicted power to within 0.1 diopters. A traditional Hartmann test (screen instead of lenslet array) has been used to measure spectacle lenses (Statton, 1981). Specific tests of contact lenses using a Hartmann technique are not commonly seen in the literature, probably due to the poor spatial resolution. From Dr. Jim Schwiegerling at the University of Arizona comes Fig. 1.4, which shows a Shack-Hartmann pattern for a bifocal contact lens on the eye. The spacing between spots is nominally 400 μm, making the identification of sub-millimeter features, such as the annular zones of bifocal contact lenses, impossible.

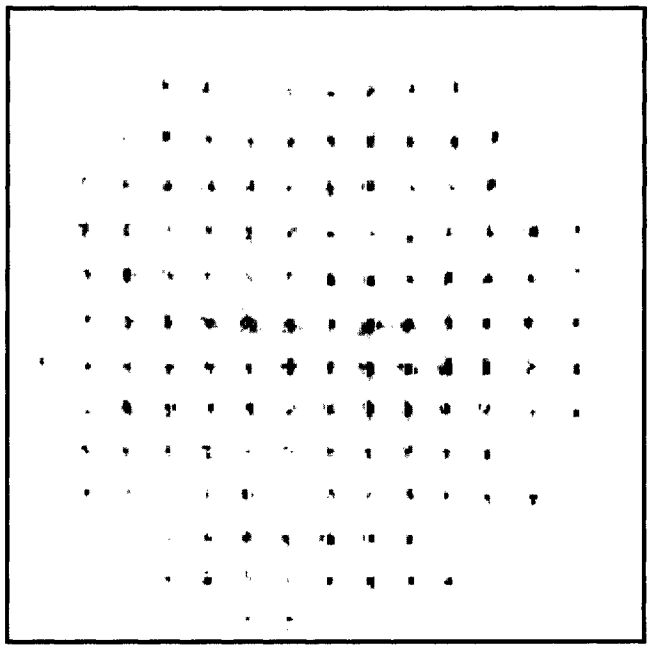

FIGURE 1.4 – Shack-Hartmann spot pattern for a bifocal contact lens. The spot pattern does not show the presence of annular rings with different powers.

1.2.3 Moiré Deflectometry

Moiré deflectometry is in many ways a combination of geometric and interferometric techniques. By using two binary gratings spaced some distance apart, a moiré fringe pattern can be produced which contains information about wavefront slope in the direction normal to the gratings. In *Optical Shop Testing,* Creath and Wyant discuss the relationship between moiré fringe patterns and interferometry (Creath, "Moire and ...", 1992). If the two gratings are considered snapshots of plane waves, then the moiré fringes produced are in the same location as the interference fringes produced by two plane waves traveling in the direction of the gratings. However, the moiré pattern only predicts the location of the fringes, and does not give the sinusoidal pattern that plane

wave fringes would have. Since wavefront slope is measured only in one direction, moiré deflectometry is most similar to the interferometric technique of lateral shearing interferometry (LSI). In fact, since the position and spacing of the fringes determines the wavefront slope, the results of moiré deflectometry are identical to those of LSI. Moiré deflectometry can be thought of as a geometric method for constructing the fringe pattern of LSI. The schematic for a moiré deflectometer is shown in Fig. 1.5.

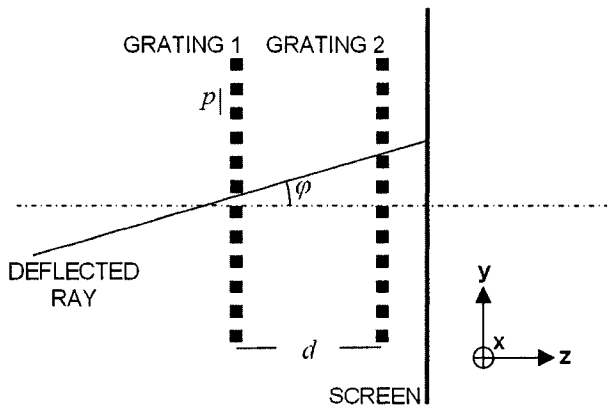

FIGURE 1.5 – Schematic for a moiré deflectometer. The deflected ray is due to the test optic (Kafri, 1985).

Each binary grating can be described by the general relationship given in Eq. 1.2, where p is the grating period or pitch and k is an integer.

$$y = kp \qquad \text{Equation 1.2}$$

The gratings are usually inclined by an angle θ with respect to each other ($\theta/2$ with respect to the x-axis), so that the direction of deflection is unambiguous. For an undeviated ray ($\varphi = 0$), the grating equations are given in Eq. 1.3 with k and m both integers.

$$y\cos\left(\frac{\theta}{2}\right) = x\sin\left(\frac{\theta}{2}\right) + kp$$
$$y\cos\left(\frac{\theta}{2}\right) = -x\sin\left(\frac{\theta}{2}\right) + mp \qquad \text{Equation 1.3}$$

Solving for the ray deflection in the region of small angles gives ($l = m - k$).

$$x = \frac{lp}{\theta}. \qquad \text{Equation 1.4}$$

The fact that θ is small leads to a moiré fringe spacing much greater than the spacing of either grating (p). This magnification, sometimes called the "moiré shift amplification", is at the heart of the usefulness of the moiré technique (Kafri, 1985). Defects in either grating, too small to be seen when viewed individually, become magnified by the factor p/θ and are thus quite visible. Back in the nineteenth century, this technique was used by Lord Rayleigh to determine the quality of gratings (Creath, "Moire and ...", 1992).

For a deviated ray, a perturbation of φd is added in the y direction, and the ray deflection is now x'.

$$x' = \frac{\varphi d}{\theta} - \frac{lp}{\theta} \qquad \text{Equation 1.5}$$

Finally the desired quantity for the ray deviation (φ) is determined by the ray deviation δx.

$$\delta x = x' - x = \frac{\varphi d}{\theta},$$
$$\therefore \quad \varphi = \frac{\delta x \cdot \theta}{d} \qquad \text{Equation 1.6}$$

The final equation is noted as being the fundamental equation for moiré deflectometry (Kafri, 1985). Since the ray deviation goes as $1/d$, the sensitivity of the measurement can be increased by increasing d. Not surprisingly, this increase in sensitivity carries with it a loss of spatial resolution (Kafri, 1985; Kreske, 1988).

Moiré deflectometry has been used to test lenses, including soft contact lenses in saline solution (Keren, 1992; Kreske, 1992; Kreske, 1988; Kafri, 1985). In their 1992 papers, Keren, et. al. and Kreske, et. al. describe a deflectometer named the OMS-101 as an instrument specifically designed to measure soft contact lenses in saline solution. Ignoring the specific packaging of the OMS-101, the basic layout (Fig. 1.6) uses two reference optics and a mirror to produce the test wavefront presented to the deflectometer.

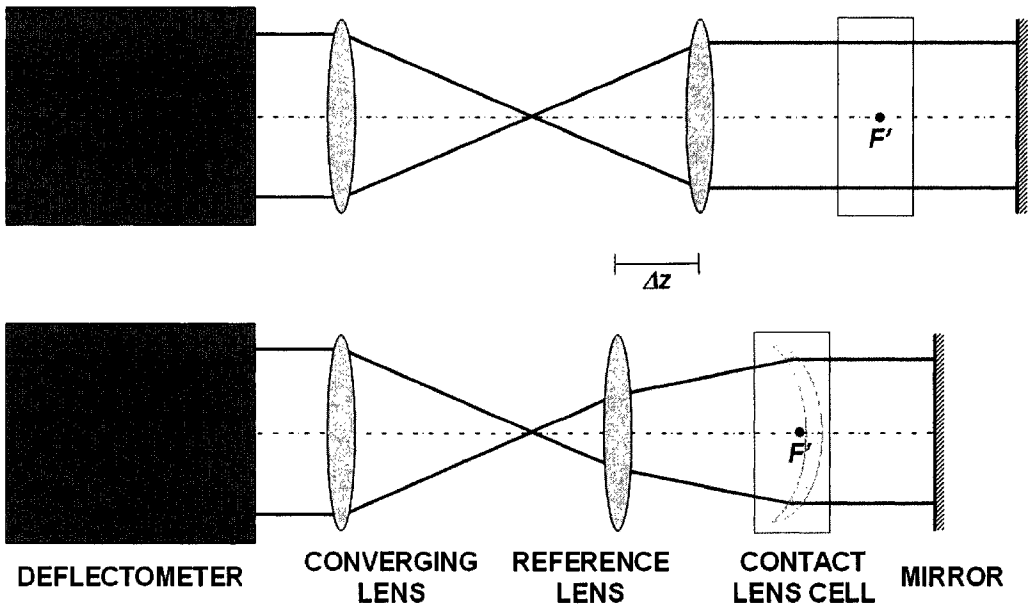

FIGURE 1.6 – Schematic for the OMS-101 moiré deflectometer. The distance traveled (Δz) between the top and bottom configurations is related to the focal lengths of the reference lens and test lens. Note that the test lens is at the rear focal point (F') of the reference lens.

The setup is such that the test lens is at the rear focal point (F') of the reference lens. The reference lens, contact lens cell, and mirror are all on a stage that can be scanned along the optical axis. Initially, the stage is positioned so that the reference and converging lenses are confocal. The rear focal point for the converging lens is coincident with the front focal point for the reference lens, thereby producing a collimated beam leaving the reference lens when a collimated beam is incident on the converging lens. When a test lens is added, the stage is moved the necessary distance to restore collimation (Δz). This is determined by monitoring the moiré fringe pattern, watching the fringes rotate as the stage is scanned until the fringes return to their reference location.

Kreske suggests that the conversion from stage travel to focal length of the test lens be viewed as a Newtonian imaging problem (1992). However, a more intuitive analysis comes from Gaussian reduction. Gaussian reduction gives the system power for the reference lens/test lens combination separated in air by a distance t as:

$$\begin{aligned} &\phi_{System} = \phi_{Reference} + \phi_{Test} - \phi_{Reference}\phi_{Test}t, \\ &t = \frac{1}{\phi_{Reference}}, \\ &\therefore \quad \phi_{System} = \phi_{Reference}. \end{aligned} \qquad \text{Equation 1.7}$$

The test lens has no influence over the system power. However, the test lens does shift the principal planes for the system. This shift in the front principle plane can be considered the cause for needing to shift the entire system to restore collimation. With no test lens, the principle planes are at the reference lens. The shift Δz must therefore be equal to the shift of the front principle plane from the reference lens. This leads to a relationship between Δz and the power of the test lens, as shown in Eq. 1.8.

$$\begin{aligned} \Delta z = VP &= \frac{\phi_{Test}}{\phi_{System}}\left(\frac{1}{\phi_{Reference}}\right), \\ \phi_{System} &= \phi_{Reference}, \\ \therefore \quad \Delta z &= \frac{\phi_{Test}}{\phi_{Reference}^{\,2}} = \frac{f_{Reference}^{\,2}}{f_{Test}} \end{aligned} \qquad \text{Equation 1.8}$$

This is the same result as Kreske's (1) (1992). Worth noting is that this result is identical to the focimeter principle described by Smith and Atchison (Smith, 1997). The obvious concern, which is not addressed in any of the cited papers, is how the shift Δz is measured. The method used to measure Δz may introduce significantly more error than that associated with checking for collimation via the moiré fringe pattern's orientation.

Also worth noting is that the conversion between stage travel and test lens power goes with the square of the assumed power for the reference lens. The tolerance on this value must be considerably less than the desired accuracy for the measurement.

The work lead by Burnabeu appears to have made advances to this technique (Quiroga, 1999; Canabal, 1998). Improvements include the use of square or two-dimensional gratings to measure deflections in perpendicular directions and incorporating phase shifting algorithms for non-sinusoidal waveforms (Canabal, 1998). The phase shift is provided by a lateral translation of one grating with respect to the other (Quiroga, 1999). Quiroga also mentions that the distance d between the two gratings should be such that the second grating is located at a Talbot image of the first grating. This condition provides maximum fringe contrast. As Talbot images are periodic phenomena, sensitivity can still be manipulated by selecting a different Talbot image location. Also discussed are Fourier transform methods for better measuring the ray deflections in x and y by examination of the transform of the moiré fringe pattern. The technique is used to map out the spherical and cylindrical power maps for a progressive spectacle lens. The agreement between this technique and data from a focimeter is well under 0.1 diopters.

1.2.4 Lateral Shear Interferometry (LSI)

LSI is the physical optics equivalent to the geometrical test of moiré deflectometry. With LSI, interference is used to produce a fringe pattern which measures wavefront slope.

Both tests measure the wavefront deviations in one direction only, and therefore require two measurements to characterize toric lenses.

A straightforward LSI system is shown in Fig. 1.7 (Wyant, 1975; Mantravadi, "Lateral ...", 1992).

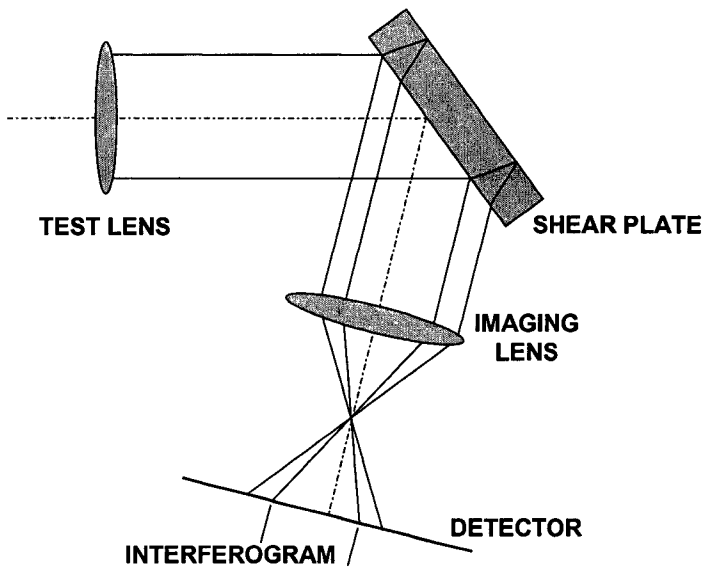

FIGURE 1.7 – Basic LSI system. The imaging lens has as conjugates the test lens and detector. The interferogram is present only in the region of overlap between the two beams.

The refraction of the wavefront reflected off the back of the parallel plate (shear plate) provides the lateral shear between the two reflected wavefronts. LSI is an example of both division of amplitude and division of wavefront, as the wavefronts interfered are identical to the incident wavefront, except for the reduction in amplitude.

Briefly, the fringe pattern produced by LSI gives the wavefront slope in the direction of the shear (S) for a given wavefront $W(x,y)$. Following Mantravadi, the fringes produced, differences in optical path, can be expressed as

$$W(x+S,y)-W(x,y)=m\lambda, \qquad \text{Equation 1.9}$$

for a shear in the x-direction where m is an integer. Viewing the difference as the numerator to the classical definition of a derivative, the wavefront slope can be determined from the following (Spiegel, 1999):

$$\frac{dW}{dx}=\frac{W(x+S,y)-W(x,y)}{(x+S)-x}, \qquad \therefore \left(\frac{dW}{dx}\right)S=m\lambda \qquad \text{Equation 1.10}$$

The above relationship is only true in the limit that $S \rightarrow 0$, but is quite useful over small S. In fact, if S were to go to zero, then there would be no difference in path, and the resulting fringe pattern would contain no useful information (Mantravadi, "Lateral ...", 1992). From this argument, and from Eq. 1.10 comes the realization that an increase in shear increases the sensitivity. Yet increasing S causes confusion as to the meaning of the measured interference, and reduces the area over which the wavefront is tested.

Wyant and Smith wrote about the testing of ophthalmic lenses using LSI (Wyant, 1975). In the paper, the claim is made that relative local power can be measured directly from the fringe spacing. Since the fringe locations are dictated by wavefront slope, the fringe spacing maps out the local wavefront curvature.

Kasana and Rosenbruch have studied the use of LSI for measuring various lens properties (1983). Discussed in their work is the difficulty of LSI to accurately provide very small defocus errors where only a fraction of a fringe is present. To better identify the focal length of the test lens, they implement a scanning mirror along the optical axis and average the readings from both sides of focus. They also discuss the idea of using LSI to first measure the focal length of a lens, then immersing the lens in an unknown liquid, and measuring the focal length again to arrive at the index of refraction for the unknown liquid (Kasana, 1983).

1.2.5 Phase Shifting Interferometry (PSI)

Phase shifting interferometry (PSI) is the enhancement of classical interferometric techniques via electronic detectors, precise motion control, and computing power (Greivenkamp, 1992). PSI improves upon the classical interferometric techniques by recording a series of interferograms with a known temporal phase shift ($\delta(t)$) between each interferogram. From the addition of amplitudes for the two interfering beams comes the fundamental equation for PSI:

$$I(x,y,t) = I'(x,y) + I''(x,y)\cos\left(\phi(x,y) + \delta(t)\right). \qquad \text{Equation 1.11}$$

The unknowns are the average intensity (I'), the intensity modulation (I''), and the phase difference (ϕ). The recorded intensity at each pixel is I. Therefore, a minimum of three interferograms are needed to produce the unwrapped phase.

There are several advantages to PSI. First, the problem of identifying fringe maxima or minima is avoided. The reconstruction process computes the local phase pixel-by-pixel via an algorithm that only depends on the recorded irradiance value for each pixel (I) and the assumed (or possibly measured) phase shift between each interferogram (δ). The ambiguity between convex and concave wavefronts is eliminated. As Greivenkamp points out, the addition of phase is analogous to pushing on one side of test optic in a Newton interferometer, and watching which way the fringes move (Mantravadi, "Newton...", 1992). It can be shown that the phase difference is insensitive to fixed noise (Greivenkamp, 1992). Since the recovery of phase is done on a pixel-by-pixel basis, variations in source intensity do not matter (as long as the light level is well above the noise level of the detector). Finally, since several interferograms are recorded, the technique of PSI benefits from averaging. The different algorithms used to collect and unwrap the phase can be designed to exploit not only averaging, but other factors such as a decrease is sensitivity to phase shifter error or second-order detector nonlinearity (Creath, 1986; Greivenkamp, 1992; Strand, 1999; Schwider, 1983; Brophy, 1990; Ghiglia, 1998; Schmit, 1995; Joenathan, 1994).

PSI has been used to evaluate ophthalmic optics. In *Contact Lenses*, Loran references the work of El-Nasher and Larke, who used interferometric techniques to measure radii of lenses to within 2% of the manufacture results (Loran, 1997). El-Nasher and Larke used an interference microscope to measure radii on the front and back surfaces. No phase shifting was used, and no discussion was given regarding the role of index in testing

through the lens (El-Nasher, 1980). The work of Mohr is perhaps the best example thus far of transmitted wavefront testing of ophthalmic optics (Mohr, 1989). Mohr discusses the difficulties of testing in reflection such aspheric optics as those commonly found in ophthalmics, and concludes that transmission testing is superior. The reported results include the mapping of surface astigmatism to an uncertainty of 0.005 diopters. However, this level of accuracy was achieved through the use of null optics, thereby making this level of accuracy a measure of comparison and not absolute power. PSI is the technique developed in this dissertation, and more on the design, calibration, and results of using PSI to measure contact lenses follows.

1.2.6 Sub-Nyquist Interferometry (SNI)

Sub-Nyquist interferometry (SNI) is not a unique form of interferometry due to a specific geometry, but rather how the produced interferograms are collected and analyzed (Gappinger, 2002). SNI can be used in all of the well-known interferometric configurations, and is most often used as an enhancement to phase shifting interferometry (PSI) (Greivenkamp, 1992). The unique aspect of SNI begins at the detector. Instead of trying to collect as much light as possible, as most detectors do, SNI uses a sparse array detector that allows only a fraction of the light to fall on each pixel. Shown in Fig. 1.8, the sparse array detector is typically a standard detector with an opaque pinhole mask superimposed.

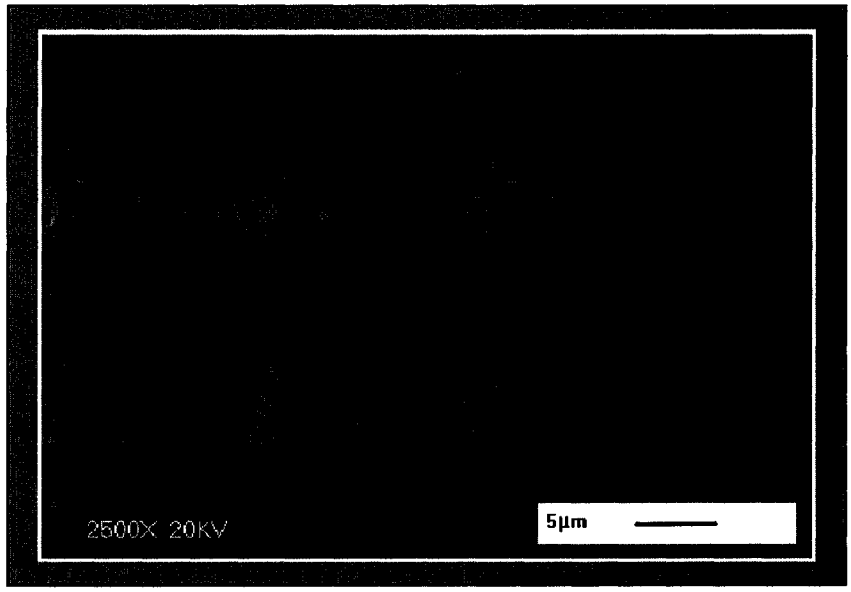

FIGURE 1.8 – SNI detector. The red box indicates the region corresponding to a single pixel. The only light sensitive portion is pinhole in the upper right quadrant of the pixel (Gappinger, 2002).

The pinhole mask allows for high frequency fringes to be detected, like those produced by highly aspheric wavefronts. This is accomplished by allowing the fringes to alias. Typically aliasing is avoided, as it confuses the correct high frequency with a lower frequency (Greivenkamp, 1992). Since aliasing is a local phenomenon, the correct frequency can be recovered using some very general, unrestrictive assumptions (Greivenkamp, 1987; Lowman, 1993). The significant assumption is that the slope or, in some cases, a higher derivative of the wavefront is continuous. This will be the case for all optics with smooth surfaces. The other assumption is that in order for the recovery of the high frequency fringes to be unique, there must be a region where aliasing is known not to exist. This region can be as small as a 2 x 2 grouping of pixels in the case of slope continuity.

The benefit of SNI comes from the fact that since high frequency fringes can be resolved, no null optics or other compensators are needed to measure highly aspheric parts. Due to the way in which the phase is collected and recovered, the dynamic range of SNI over traditional PSI is twice the ratio of the original pixel size to the pinhole size (assuming contiguous pixels). For the detector shown in Fig. 1.8, the pinholes are 2.35 μm spaced 15 μm apart (Gappinger, "High modulation...", 2003). The gain in dynamic range is therefore about 12.7 times that for PSI. The factor of two comes from the fact that the phase retrieval process in PSI is limited to the Nyquist frequency of the detector, while the technique used with SNI allows for phase unwrapping out to the sampling frequency of the pinhole array (Greivenkamp, 1987; Greivenkamp, 1992; Gaskill, 1978; Gappinger, "High modulation...", 2003; Lowman, 1993).

SNI has been used to measure progressive spectacle lenses (Gappinger, "Non-null ...", 2003). The particular sub-Nyquist interferometer used was able to measure over 240 λ of departure from a progressive spectacle lens over a diameter of about 41 mm. The collected wavefront was also used to produce spherical and cylindrical power maps of the progressive lens.

1.2.7 Other Techniques for Testing Ophthalmic Optics

At this point, a brief listing of other techniques used in the qualification of ophthalmic optics is in order. Most of these techniques test a surface, not a wavefront, and are based

on common ophthalmic instrumentation. Worth mentioning is the fact that any measure of power from a single lens parameter must include assumptions of several other lens parameters. The errors associated with these assumptions must be considered when reporting the measured power.

Certainly the most direct method for testing power is the focimeter. The focimeter works much like the described operation of the moiré deflectometer, in that a collimating lens is used in conjunction with the test lens. The combination is translated until collimation is restored, and the distance traveled is the back vertex focal length of the test lens (Loran, 1997; Smith, 1997; Fowler, 1989).

The radiuscope is an autostigmatic microscope (Steel, 1977; Smith, 1997). The radiuscope is just the measuring of the distance between two positions: the center of curvature and the cat's eye position. In ophthalmics, the technique of noting the distance between the two locations where light will be reflected back at the same angle is known as Drysdale's method (Mandell, 1974). Steel suggests overcoming the poor reflection of an immersed contact lens by using crossed polarizers and a retarder to get better visibility (Steel, 1977).

The keratometer has been used to measure the radius of curvature of lenses (Loran, 1997). However, there are several issues with this technique. First, the necessity of testing contact lenses in solution and therefore in some sort of cell results in added

refraction between the cell/air interface. This can be compensated for if the index of the saline solution is known. Since the keratometer is calibrated for convex surfaces only, the testing of concave surfaces will give erroneous results. While not stated in the reference, the source of this error must be due to the sign difference for spherical aberration between convex and concave surfaces. Reflections off both the front and back surfaces may produce unwanted ghost images. Finally, Loran mentions that in an effort to get a brighter image by increasing the amount of light produced, the heat given off by the lamp may raise the temperature of the saline to a point where the reading is no longer valid.

Spiers and Hull suggest a Fourier filtering technique for measuring progressive lenses. By placing different gratings in the transform plane, the deflection of the grating can be used to map out local power. This is really no different than the moiré deflectometry techniques already mentioned (Spiers, 2000).

1.3 Case Study for Testing Soft Contact Lenses

When initially presented with a problem, the good scientist or engineer tries to gather as much information as possible about the problem before generating and analyzing possible solutions. The story of how the problem of testing soft contact lenses was initially analyzed, and how the hardware and software produced came to be is worth mentioning. This case study is an excellent example of both the art and science of optical engineering. In many ways, the following story is the blueprint by which the bulk of the work in this

dissertation was carried out. All topics mentioned here are covered in greater detail throughout the dissertation.

The sponsor initially presented the problem as needing robust metrology to test a wide variety of soft contact lenses. Current technology did an adequate job of testing spherical lenses, but was incapable of testing more complex designs. Developed instrumentation was to be as flexible as possible, allowing for the potential of testing future products with unknown asphericities.

Three specific types of lenses were initially discussed: spheres, torics, and bifocals. The complications of testing spherical contacts are those of testing contact lenses in general, which due to their number and complexity are given their own chapter (Chpt. 3). Toric contact lenses present the challenge of testing a non-rotationally symmetric optic. While the astigmatism of the lenses is mitigated by the index match between the lens and surrounding saline to the point that the aspheric wavefront can be treated no differently than a spherical wavefront, the ability to compare measured data to modeled data requires that the fiducial marks (see Fig. 1.9) at the periphery of the lens be visible in the recorded interferograms. Bifocal contact lenses present problems from having annular zones of varying diameters and powers. This leads to the requirements that the instrumentation not only detects the zones, but has the resolution to properly measure the zones. So the problem now becomes one where the whole lens must be examined (for toric angle

identification) and yet be tested at a high spatial resolution (for the annular zones of bifocals).

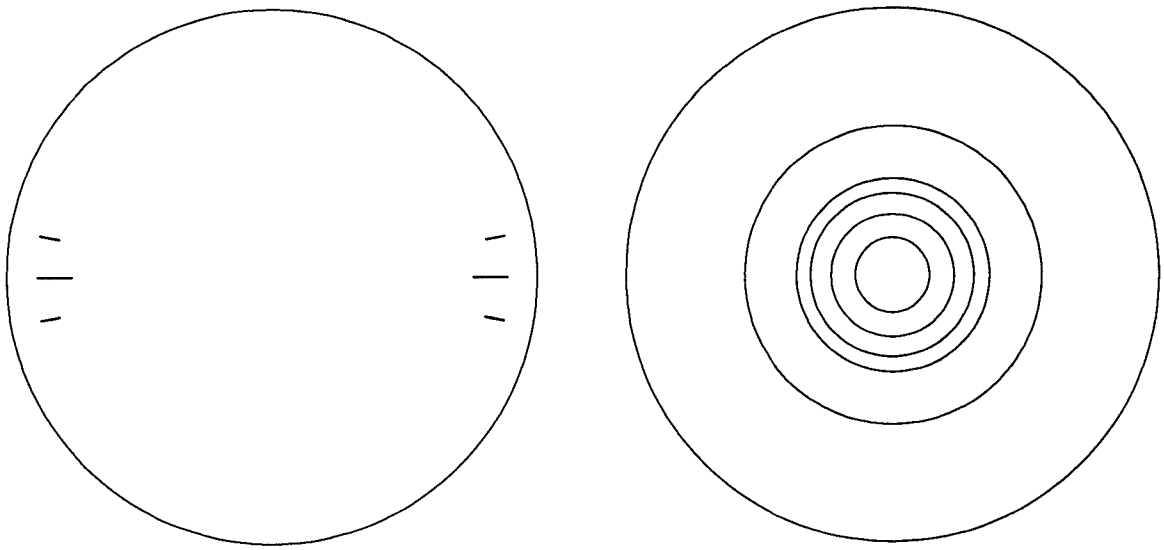

(a) (b)

FIGURE 1.9 – Cartoons for (a) toric and (b) bifocal contact lenses.

Given the requirements on testing a wide variety of lenses, with potentially unusual asphericities, over a range of powers and with a high spatial resolution, the natural first choice for the instrumentation was phase shifting interferometry (PSI). PSI is the standard method for modern optical testing, and therefore a natural first choice. No other method has the combination of ease-of-use and accuracy as PSI. However, it was unclear whether or not interferometry would be able to handle the unusual bifocal lenses. The biggest unknown with bifocals was whether or not the transitions between zones would cause problems. While interferometry is a very robust tool, in general it lacks the capability to test optics where the resulting fringe pattern is not continuous. That is to

say, part discontinuities are often a downfall for an interferometer. The other common downfall is that the optic under test simply produces too high a fringe frequency. This issue is taken up in Chpt. 2.

To check the effect of the zone junctions, a supplied model for a bifocal lens immersed in saline was put into Zemax, and theoretical fringes produced (see Fig. 1.10).

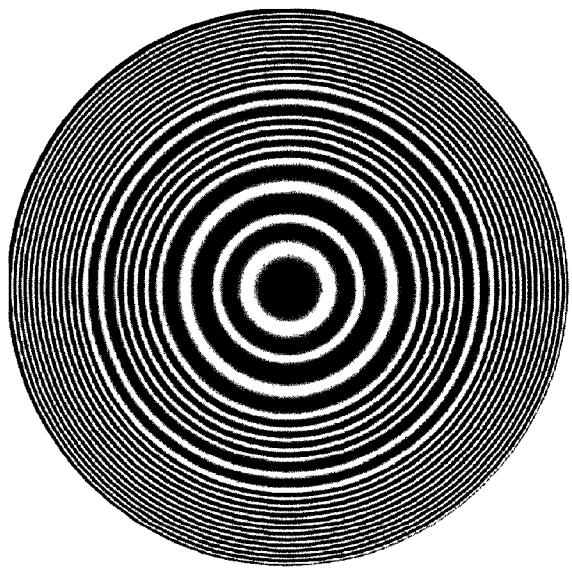

FIGURE 1.10 – Zemax interferogram for a bifocal contact lens in double pass.

The model showed no serious problems; the fringes looked testable. Yet there was still some doubt due to the fact that the model itself did not contain discontinuities, but rather represented the annular zone surface as a spline surface in Zemax. To definitively prove if interferometry would work, a lens was placed in an existing Twymann-Green

interferometer. The resulting fringe pattern for the lens, with the same prescription as the lens that was modeled in Zemax, is shown in Fig. 1.11.

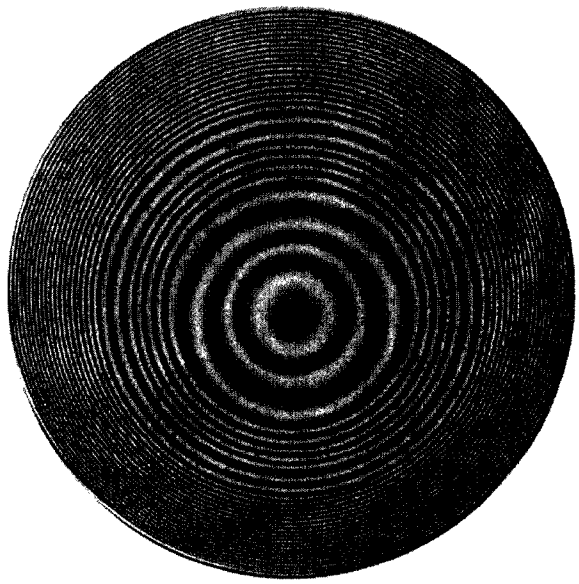

FIGURE 1.11 – Twymann-Green interferogram for same lens as Fig. 1.10.

Not only were the fringes testable well beyond the required test aperture, the visual agreement between the measured and modeled interferograms was proof that PSI would work on contact lenses.

One can go back over the criteria for testing and see why other methods are inferior to PSI. The Shack-Hartmann simply doesn't have the spatial resolution for testing bifocals. A look back at Fig. 1.4 shows that the annular zones of a bifocal contact lens would not be resolved with most Shack-Hartmann instruments. Star testing, while useful in a qualitative sense, is very hard to quantify. Measuring power via a star test is not practical

at all. Moiré deflectometry, as discussed earlier, is the principle behind the current metrology in the sponsor's lab. While adequate on spherical lenses, the necessary tradeoff between spatial resolution and sensitivity make it a poor candidate for testing bifocals. The same can be said for lateral shear interferometry. Plus, both the shearing tests of moiré deflectometry and LSI only measure power in one direction. Two tests would have to be run to measure toric lenses. This leaves interferometry as the best choice for an initial test bed. Sub-Nyquist interferometry (SNI) was determined to be unnecessary. SNI is typically only used when the dynamic range of a part is so great that testing by other means is not possible. With the lenses tested in solution, the reduction in effective power is enough to allow a conventional sensor to resolve the interference pattern. The conclusion was that PSI would be the most viable method of testing. A custom interferometer would be needed, one that could accommodate a range of powers, track part rotation, and provide high spatial resolution.

1.4 Scientific Questions Regarding the Testing of Immersed Optics

The testing of contact lenses while immersed in saline solution raises some interesting, more general questions regarding the pros and cons of such a technique. While contact lenses must be tested in some sort of liquid to preserve the optical properties of the lens' material, the vast majority of optics can be tested in air. Yet there is a benefit to this immersion technique, namely the effective power of the optic is reduced. Thus the dynamic range of the interferometer is increased. The range of powers (really wavefront slopes) that can be resolved is increased by the ratio of differences in index between the

lens and its surrounding medium. This factor, here called the solution factor (SF) since it comes from the index of the solution surrounding the test optic (Ford, 1997), is given by Eq. 1.12. For this definition, the dynamic range of the interferometer is increased by SF.

$$SF = \frac{n_{Lens} - n_{Air}}{n_{Lens} - n_{Solution}} \qquad \text{Equation 1.12}$$

An added benefit to the increase in dynamic range is that the errors associated with transmitted wavefront testing are reduced with a reduction in the power of the test optic. Not surprising, a flat test wavefront, nominally identical to the reference wavefront, can be tested at the resolution of the interferometer.

Of course, there is a downside to immersion testing. While the dynamic range of the interferometer is increased by the ratio of the differences in index, the sensitivity of the interferometer should be reduced by that same ratio. An easy way to think of this is to imagine a divot on the test optic. As the index of the surrounding solution approaches the index of the test optic, the divot becomes harder to resolve. The first question is then at what point is resolution lost. This should define an upper bound on the gain in dynamic range possible due to immersion. Second, what is the resolution near this limit? What is the general trend as the index match is increased? These are the more fundamental, scientific questions taken in up in a later chapter (Chpt. 7).

2 DESIGN OF AN EXTENDED DYNAMIC RANGE INTERFEROMETER

In Chpt. 1 the argument was made that the best way to test contact lenses is by using an interferometer in a single-pass configuration, thereby measuring the transmitted wavefront. With the testing method established, the next task is to design an interferometer that meets the necessary requirements. These requirements stem from the variety of optics to be tested, the desired output from the test, and achieving the best precision and accuracy possible. Table 2.1 lists some of the general requirements handed down from the sponsor for the testing of contact lenses. Note that optical power is expressed in the ophthalmic units of diopters (D), which are equivalent to inverse meters.

Range of Base Powers (D)	-20.00 to +14.00
Range of Added Cylinder Powers (D)	0.00 to -5.00
Range of Added Bifocal Powers (D)	0.00 to +5.00
Wavelength (nm)	~ 550 (peak photopic)
Max. Diam. Optical Zone (mm)	9
Max. Diam. Contact Lens (mm)	15

TABLE 2.1 – Selected requirements for interferometer.

Given the above requirements, one must select the appropriate interferometer components, from source to detector, which will make testing the full range of contact lenses possible. Since a single-pass configuration is desired, the obvious choice for a layout is one based on a Mach-Zehnder interferometer (Malacara, "Twymann-Green...",

1992). For the specific instrument built, a codename was given by the sponsor: CLOVER (Contact Lens Optical VERification).

Testing in a non-null configuration brings into play three crucial considerations for the design of the interferometer. First, the wavefront must be collected and captured by the imaging optics. This requires matching the parameters of the test wavefront, imaging lens, and detector. Second, the interference incident on the detector must be resolved. The standard solution, and the solution used in CLOVER, is not to let the interference fringes change in phase by more than π/pixel, thereby demanding that the fringe frequency is less than the Nyquist frequency for the detector (Gappinger, 2002; Gaskill, 1978). If this condition cannot be met, then a technique like SNI would be needed. Finally, the wavefront reconstructed at the detector must be calibrated to account for the induced aberrations by the interferometer's imaging optics. The lack of a common path between the reference and test arm wavefronts results in different aberrations in each wavefront. The specific calibration process used to remove the induced aberrations is discussed in the third section of this chapter.

It should be mentioned for clarity that the term wavefront is being used to describe the distribution of phase, or optical path length, at a given plane in the interferometer or its model. This is different from the classical definition of a wavefront: a surface of constant phase (Hecht, 1987). Yet the definition used here is widely used in the testing community, and should not be the source of confusion.

2.1 Design Principles

The starting point for the selection of the imaging optics (imaging lens and detector) is determining the necessary dynamic range of the interferometer. Dynamic range is measured in fringe frequency, which comes directly from wavefront slope. So a relationship is needed is between the given test optics' power and subsequent fringe frequency. A convenient unit for this conversion is waves/radius. Waves/radius is a measure of the wavefront derivative and describes, at any point along the wavefront, the amount of departure across a length equal to the radius due to the local wavefront slope (Wyant, 1992). Figure 2.1 shows a typical wavefront across its normalized radius ($W(\rho,\theta)$) and the subsequent derivative in waves/radius.

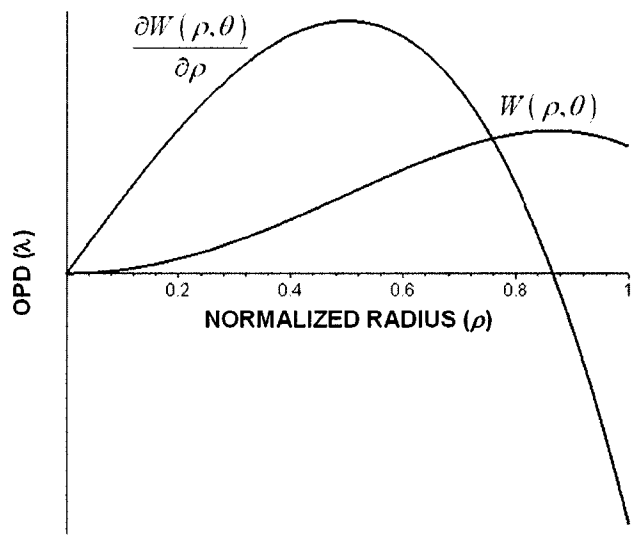

FIGURE 2.1 – Plot of typical aspheric wavefront and its derivative. The maximum of the derivative gives the maximum expected fringe frequency.

If the test optic is modeled in lens design code, such as Zemax, then the maximum waves per radius can be determined from the maximum absolute value for the ray fan. Assuming rotational symmetry, the relationship between wave and ray fans (assuming that the wave fan is in waves and the ray fan is in units of length) is:

$$\max\left(\frac{\partial W(\rho)}{\partial \rho}\right) = \frac{\max\left(\left|\varepsilon_{\rho}\right|\right)}{-2\lambda(f\#)} \qquad \text{Equation 2.1}$$

The benefit of using waves/radius is that this quantity is invariant on magnification. This parameter is not tied to any specific set of conjugates or detector size.

Once the maximum fringe frequency is established, the minimum number of pixels/radius falls out directly from the sampling requirement of at least two pixels/wave of OPD to satisfy the Nyquist condition (Gaskill, 1978; Greivenkamp, 1992). This minimum number of pixels/radius may be superseded by a required spatial resolution. If the required sampling frequency associated with this spatial resolution is greater than the sampling frequency derived from the Nyquist requirement, then this becomes the necessary sampling frequency of the detector.

With the necessary number of pixels across the imaged wavefront established, the next step is to evaluate the candidates for the detector. A detector is decided on before the imaging optics because, on the whole, the choices for detectors will be more limited than those for the imaging optics. The only condition imposed thus far is that the number of pixels must be greater than the maximum waves per radius by a factor of four; one factor

of two for the Nyquist condition, and another factor of two for the conversion between radius and diameter. A convenient means to start the selection process is to plot the detector's two major sampling parameters: number of pixels and pixel spacing, expressed as a frequency, as shown in Fig. 2.2. The requirement on the number of pixels across the diameter can be added to this plot, eliminating a certain portion of the solution space. In the limit towards a 100% fill factor, the reciprocal of pixel frequency becomes the pixel size. Note that square, contiguous pixels are being assumed, so that pixel size is the reciprocal of pixel frequency.

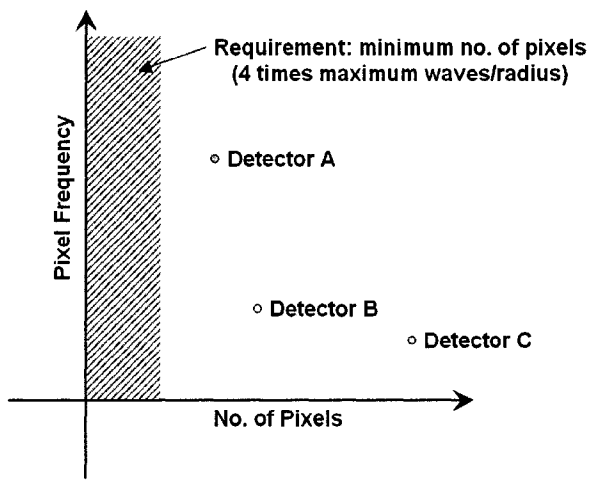

FIGURE 2.2 – Solution space of acceptable detectors.

By assuming that the test part will be imaged to fill the detector, the same graph can be used to show the different magnifications (m) associated with each detector. The graph (Fig. 2.3) spans the range of all possible magnifications, from 0 to infinity (ignoring any sort of sign convention).

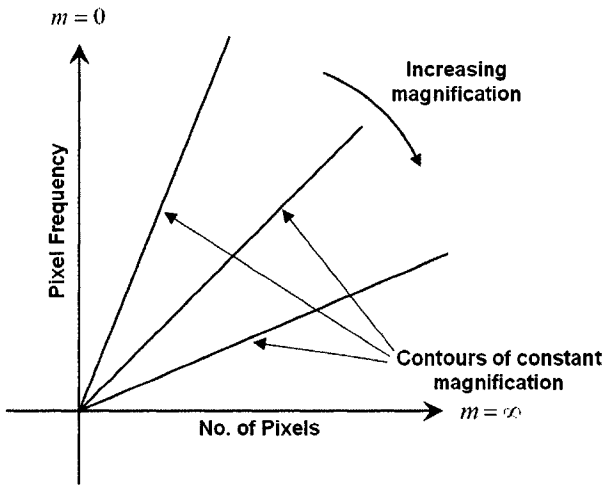

FIGURE 2.3 – Magnification over the space of possible detectors.

The vertical axis represents zero magnification (no pixels), while the horizontal axis represents an infinite magnification (the pixels are infinitely big). Lines extending from the origin are contours of equal magnification. The magnification for a specific detector comes from the following formula:

$$m = \frac{\text{No. of Pixels/Pixel Frequency}}{\text{Diameter of Test Part}}. \qquad \text{Equation 2.2}$$

At this point, the selection of which detector to use can be made using a variety of factors such as the number of frames/second, SNR, and cost. These are in addition to the already mentioned parameters regarding sampling and magnification. The choice of an acceptable detector not only fixes the magnification, but helps constrain the imaging lens as well.

To understand how the imaging lens' parameters fit with the test optics and detector, a good starting point is to determine the maximum fringe frequency supported by the imaging lens. The imaging lens has a maximum supported frequency coming from two conditions. The first condition is that the interfering rays must pass through the imaging lens. The second condition is that the two rays meet at the detector. The maximum possible fringe frequency allowed by the imaging lens comes from the construction of Fig. 2.4. Note that this is independent of the test part.

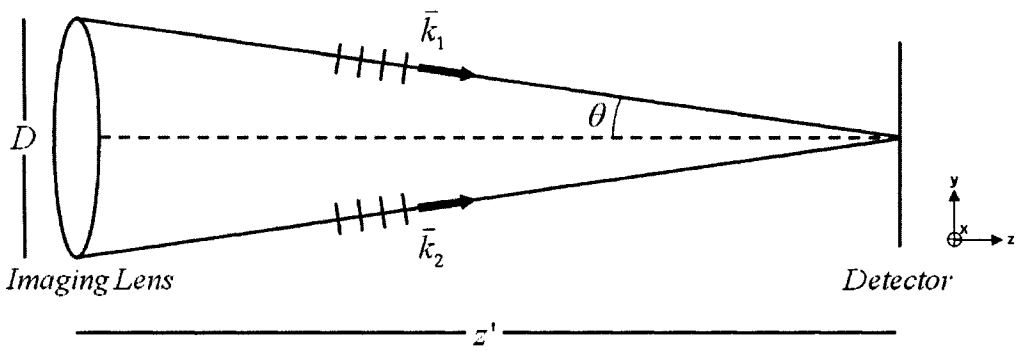

FIGURE 2.4 – Construction for determination of maximum fringe frequency supported by the imaging lens.

Intuitively, the maximum fringe frequency will occur when the two rays interfering span the maximum angle possible. This condition is satisfied by two rays, one from the top of the imaging lens, the other from the bottom, meeting on axis. Describing the two rays in common optical terms, the difference in phase ($\Delta\phi$) is:

$$E_{1,2} = A_{1,2}\exp\left[i\left(\vec{k}_{1,2}\cdot\vec{r}-\omega_{1,2}t\right)\right],$$
$$\therefore \Delta\phi = \left(\vec{k}_1\cdot\vec{r}-\omega_1 t\right)-\left(\vec{k}_2\cdot\vec{r}-\omega_2 t\right). \qquad \text{Equation 2.3}$$

Taking the position vector **r** and the propagation vectors **k** to be

$$\vec{r} = x\hat{\mathrm{i}} + y\hat{\mathrm{j}} + z\hat{\mathrm{k}},$$
$$\vec{k}_{1,2} = k_{1,2}\left(L_{1,2}\hat{\mathrm{i}} + M_{1,2}\hat{\mathrm{j}} + N_{1,2}\hat{\mathrm{k}}\right), \qquad \text{Equation 2.4}$$

and using the facts that $k_1 = k_2 = 2\pi/\lambda$ and $\omega_1 = \omega_2$ since the rays are coming from the same source, the difference in OPD in the yz-plane at the detector ($z = 0$) is:

$$\mathrm{OPD} = \frac{\Delta\phi}{2\pi}\lambda = \left(M_1 - M_2\right)y = 2\sin\theta\, y. \qquad \text{Equation 2.5}$$

In the region of small angles, this OPD becomes

$$\mathrm{OPD} = 2\left(\frac{D/2}{z'}\right)y = \frac{y}{(f\#)_w}. \qquad \text{Equation 2.6}$$

The distance between fringes (Δy) is given by the following:

$$m\lambda = \frac{y_1}{(f\#)_w},$$
$$(m+1)\lambda = \frac{y_2}{(f\#)_w}, \qquad \text{Equation 2.7}$$
$$\therefore \Delta y = y_2 - y_1 = (f\#)_w\lambda.$$

Finally, the maximum fringe frequency supported by the imaging lens is the reciprocal of Δy:

$$f_{\text{Imaging Lens}} = \frac{1}{\Delta y} = \frac{1}{(f\#)_w\lambda}. \qquad \text{Equation 2.8}$$

Note that this is identical to the cutoff frequency for a lens under the conditions of incoherent illumination (Goodman, 1996). The reason for this is that the optical transfer function (OTF) for a lens in the case of incoherent illumination is related to the

autocorrelation of the lens' pupil function, which is just the circular aperture of the lens. The displacement associated with the cutoff frequency for the autocorrelation leads to the same geometry as that of Fig. 2.4. Given this maximum frequency supported by the imaging lens, this must be greater than the maximum fringe frequency at the detector, as stated in Eq. 2.9.

$$f_{\text{Imaging Lens}} = \frac{1}{(f\#)_w \lambda} > f_{\text{Max. @ Detector}} \qquad \text{Equation 2.9}$$

Another condition needs to be brought in at this point, one that relates the pixel frequency (or pixel size) to the imaging lens. This condition is the desired matching of the resolutions of the imaging lens and detector. By doing this, neither system is limiting the performance of the other. For the imaging lens, the resolution is given by the Airy disk diameter. The detector's resolution is the reciprocal of the plotted pixel frequency, which approaches the pixel size as the fill factor is increased. Setting these equal gives:

$$\frac{1}{f_{\text{Pixel}}} = 2.44(f\#)_w \lambda,$$

$$\text{OR} \qquad \text{Equation 2.10}$$

$$\frac{1}{(f\#)_w \lambda} = 2.44 f_{\text{Pixel}}.$$

So now there exists an equation between pixel frequency and working *f*-number, and an inequality between working *f*-number and the maximum fringe frequency at the detector. But by having satisfied the sampling condition of at least two pixels/fringe, an inequality between pixel frequency and maximum fringe frequency already exists:

$$f_{\text{Pixel}} > 2 f_{\text{Max. @ Detector}}. \qquad \text{Equation 2.11}$$

Building off this relationship using the equations above leads to:

$$\begin{aligned} 2.44 f_{\text{Pixel}} &> 4.88 f_{\text{Max. @ Detector}}, \\ \frac{1}{(f\#)_w \lambda} &> 4.88 f_{\text{Max. @ Detector}}, \\ \therefore f_{\text{Imaging Lens}} &> 4.88 f_{\text{Max. @ Detector}}. \end{aligned} \qquad \text{Equation 2.12}$$

The conclusion is that by demanding that the resolution of the imaging lens match the resolution of the detector, the maximum frequency supported by the imaging lens is guaranteed to be greater than the maximum frequency at the detector by almost a factor of five. So the condition of matching resolutions is a good one to impose, for it ensures that the imaging lens will have no trouble supporting the interference pattern produced by the test part.

The criterion of matching resolutions fixes the working *f*-number for the imaging lens. Since magnification is also known, the independent *f*-number for the lens is set from

$$f\# = \frac{(f\#)_w}{(1-m)}. \qquad \text{Equation 2.13}$$

At this point, the first-order parameters not yet established are the focal length of the imaging lens (f), the diameter of the lens (D), and the object (z) and image (z') distances. There exist only three constraints for these four parameters:

$$\begin{aligned} f\# &= \frac{f}{D}, \\ \frac{1}{z'} - \frac{1}{z} &= \frac{1}{f}, \\ m &= \frac{z'}{z}. \end{aligned} \qquad \text{Equation 2.14}$$

Therefore, the problem is under-constrained and one of the remaining parameters may be freely set.

Considerations on setting the free parameter should start with the fact that the imaging lens must collect all of the light coming from the test arm. If the test optic has negative power, then the initially collimated light will be diverging, and the yet-unknown distance from the test optic to the imaging lens will determine an acceptable diameter. Another consideration is the overall packaging of the interferometer. The desired object-to-image distance can be used as a fourth constraint. If using off-the-shelf optics is important, then the available combinations of diameters and focal lengths may help determine the parameters for the imaging lens.

To summarize, the design of a non-null interferometer must account for the expected frequency of interference fringes produced by the class of optics to be tested. This drives the necessary sampling across the imaged wavefront, which aids in the selection of an appropriate detector. With the detector selected, the resolution of the imaging lens can be matched to the detector's resolution, thereby guaranteeing that the imaging lens will support the maximum fringe frequency. The remaining imaging parameters fall out of the standard imaging equations once an assumption is made regarding any one of the remaining free parameters. Following this design philosophy meets the first two conditions regarding testing in a non-null configuration.

2.2 Specifics of CLOVER Hardware

The design principles outlined above were used as they were discovered in the development of CLOVER. This resulted in an implementation not nearly as efficient, but just as effective, as outlined in the prior explanation. At this time, going over the specifics of the interferometer developed for the testing of contact lenses is in order. Figure 2.5 shows the hardware configuration for CLOVER.

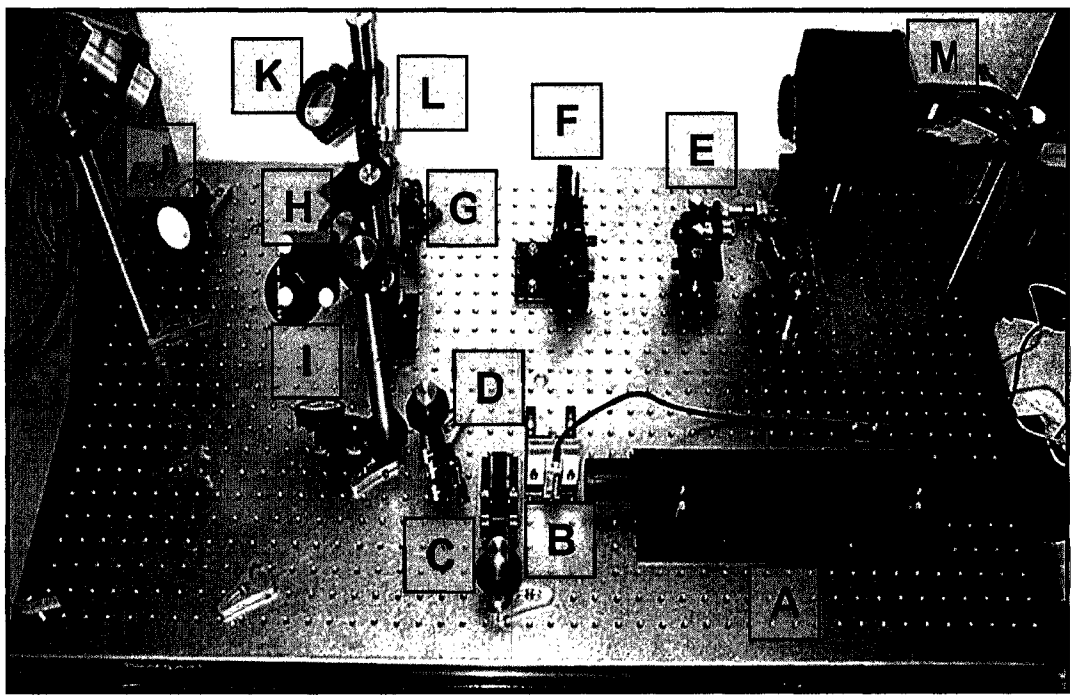

FIGURE 2.5 – CLOVER interferometer.

The beam path starts with the HeNe laser (A). The laser has a 2 mW maximum output at a wavelength of 543.5 nm. The coherence length is about 16 cm, from the manufacturer, due to the presence of six longitudinal modes in an effort to get more power out of the laser. This coherence length is significantly greater than those available from known

solid state lasers at the time of selection. This source was selected due to the wavelength's close proximity to the peak of the photopic curve, around 550 nm. The relatively low power coming from the laser is still many times more than what is needed to saturate the detector over a typical integration time.

Following the laser is the acoustic-optic, or AO, modulator (B). The AO modulator is used to provide vibration-free shuttering. This is accomplished by using the AO modulator to deflect the beam out of or into alignment with the spatial filter system (E). When the modulator is on, the first-order diffracted beam is in alignment with the spatial filter. The modulator is aligned with the laser so that when it is on, the efficiency of the first-order is as high as possible. When the modulator is off, all of the light is in the zero-order beam, and is blocked by the pinhole in the spatial filter. By aligning the interferometer to the first order beam, a nearly infinite extinction ratio is achieved for the shuttering operation. The need for this shuttering is due to the camera, and will be explained further in the discussion on the camera.

After the AO modulator comes the neutral density filters (C). The neutral density filters provide a convenient means for adjusting the light level presented to the interferometer. The AO modulator could be adjusted to attenuate the beam, but this adjustment would be very fine and would risk misaligning the entire interferometer.

The next component is two beam steering mirrors (D). Not only do the beam steering mirrors help keep the footprint of the interferometer to a minimum size, but they are crucial to alignment. Two mirrors provide all of the degrees of freedom needed to position a beam. A beam at any point can be described by six parameters: three positional parameters (x, y, z) and three angular parameters (L, M, N). With a two mirror beam steerer, the first mirror dictates the desired positional parameters at the second mirror, and the second mirror dictates the angle at which the beam leaves. So by using two mirrors, the beam can be presented to the interferometer with all six parameters coincident with the interferometer's axis.

Next the beam passes through the spatial filter system (E), which consists of an infinitely-corrected microscope objective and 5 μm pinhole. The original thinking was to use an infinitely-corrected objective since the beam was collimated entering the objective. However, the beam does not fill the objective, and the spatial filtering achieved is not optimal. Either an afocal beam expander should be added to fill the objective, or a negative lens and finite objective used to optimize the spatial filtering. While not optimal, the system in place provides a clean beam, so no changes are planned.

The beam coming out of the spatial filter is diverging, and so is collimated by the collimating lens (F). The collimating lens, along with the pinhole, defines the axis for the interferometer. For diffraction considerations, the collimating lens is nearly overfilled by the diverging beam. The collimating lens is an off-the-shelf achromatic doublet. Even

though this is a monochromatic instrument, the doublet is used for its correction of spherical aberration and coma, which can be introduced by misaligning the lens to the beam.

After the collimating lens, an iris is placed to allow for beam diameter adjustment (G). This is not possible in some interferometers, as diffraction from this aperture creeps further and further into the beam. However, the size of the desired beam combined with the short beam paths prevents diffraction effects from being an issue.

The collimated beam is then presented to the first of two beamsplitters (H). The test arm (I) and the reference arm (J) are laid out to provide a vertical beam to a horizontal test part. The two beams are recombined at the second beamsplitter (K). The test arm is the arm reflected off the beamsplitters so that the aspheric wavefronts coming from the test lens are not transmitted through, but more simply reflected off, the beamsplitter.

Immediately following the second beamsplitter is the imaging lens (L). The imaging lens is placed as close as possible to the test plane (plane of the test lens) to maximize magnification. The role of the imaging lens is to enable testing of the wavefront immediately following the test lens by imaging that wavefront onto the detector. Like the collimating lens, the imaging lens is an off-the-shelf achromatic doublet.

The final component is the detector (M). The detector is a Dalsa 4M15, with 2048 x 2048 square pixels, 14 μm in size. The camera has a 100% fill factor, meaning that no opaque regions exist on the CCD to shift the collected charge to during readout. This is known as a full frame sensor (Polderdijk, 2002). The other type of 100% fill factor sensor is a frame transfer sensor, which shifts the collected charge from the sensor to an identical, shielded sensor. Due to the size of the 4M15 collection area, over one square inch, having a second sensor is cost prohibitive. The solution is to shutter the light, blocking the light during readout. This explains the need for the AO modulator.

Going back to the design principles, the pixel frequency should be greater than twice the expected maximum fringe frequency. Also, if the resolution of the imaging lens matches that of the detector, then the imaging lens will support the expected maximum fringe frequency. So, how does CLOVER stack up to these constraints?

Given a maximum power of 25 diopters, the highest toric power possible, the expected maximum fringe frequency can be found. First, the power is reduced by the solution factor due to the immersion in saline during testing:

$$\phi_{\text{Aqueous}} = \frac{\phi_{\text{Air}}}{SF}$$

$$\therefore \phi_{\text{Aqueous}} = \frac{25}{\frac{(1.4012-1.336)}{(1.4012-1)}} = 4.063 \text{ D.} \qquad \text{Equation 2.15}$$

For all spherical and toric lenses, the wavefront slope monotonically increases along a radius. This fact can be used to make a tidy formula for the maximum fringe frequency.

The parabolic approximation works well for contact lenses, as their focal lengths are significantly greater than their optical zone diameters. So starting with the parabolic approximation relating OPD to the wavefront's curvature (R), which is the reciprocal of power,

$$\mathrm{OPD} = \frac{r^2}{2R}, \qquad \text{Equation 2.16}$$

where r is the radius of the optical zone (4.5 mm). Assuming the maximum fringe frequency is at the edge, the distance between fringes (δ) is found from:

$$\begin{aligned} \Delta\mathrm{OPD} = \lambda &= \frac{r^2}{2R} - \frac{(r-\delta)^2}{2R}, \\ 2R\lambda &= r^2 - \left(r^2 - 2\delta r + \delta^2\right). \end{aligned} \qquad \text{Equation 2.17}$$

Since r is much greater than δ, the δ^2 term can be dropped, leaving a simplified relationship:

$$\delta = \frac{R\lambda}{r}. \qquad \text{Equation 2.18}$$

Finally, the maximum fringe frequency can be computed at the detector by using the magnification,

$$f_{\text{Max. @ Detector}} = \frac{1}{m\delta} = \frac{r}{m\lambda R.} \qquad \text{Equation 2.19}$$

The necessary magnification is one that allows for the highest possible spatial resolution while imaging enough of the lens to identify the locations of the alignment fiducial marks for a toric lens (see Fig. 1.9 (a)). For the typical diameters of the lenses in question, a magnification of 2.044 meets these requirements. The detector is 2048 pixels across, and

each pixel is 14 μm in width. This leads to a testable diameter just over 14 mm. Using this magnification and the values already stated gives a maximum fringe frequency of:

$$f_{\text{Max. @ Detector}} = \frac{4.5}{2.044 \cdot 0.5435 \cdot 10^{-3} \cdot 246.13} = 16.5 \text{ mm}^{-1}. \quad \text{Equation 2.20}$$

Note that if the term δ^2 had been included, the maximum fringe frequency would be 16.4 mm^{-1}. How does this frequency compare to the pixel frequency? Given 14 μm pixels, the pixel frequency is:

$$f_{\text{Pixel}} = \frac{1}{0.014} = 71.4 \text{ mm}^{-1}. \quad \text{Equation 2.21}$$

The pixel frequency (71.4 mm^{-1}) is greater than twice the expected maximum fringe frequency (16.5 mm^{-1}), so the detector choice was a good one.

As for the imaging lens, the magnification (2.044) and pixel size (14 μm) leads to a desired working *f*-number of:

$$(f\#)_{w\ \text{DESIRED}} = \frac{1}{f_{\text{Pixel}} 2.44\lambda} = 10.6. \quad \text{Equation 2.22}$$

The selected imaging lens has a 200 mm focal length. Combined with the magnification, this leads to an image distance of 608.8 mm. The imaging lens is 50.8 mm in diameter, and the mount provides a 95% clear aperture. The actual working *f*-number is therefore:

$$(f\#)_{w\ \text{ACTUAL}} = \frac{608.8}{0.95 \cdot 50.8} = 12.6. \quad \text{Equation 2.23}$$

The actual *f*-number is slower than the desired by about 20%. The loss in resolution is insignificant; all fiducial marks are still clearly imaged, as later figures will show. The maximum fringe frequency supported by the imaging lens is:

$$f_{\text{Imaging Lens}} = \frac{1}{(f\#)_w \lambda} = \frac{1}{12.6 \cdot 0.5453 \cdot 10^{-3}} = 145.9 \text{ mm}^{-1}. \quad \text{Equation 2.24}$$

Even with the higher-than-desired working *f*-number, the imaging lens can support frequencies well beyond the expected maximum fringe frequency of 16.5 mm^{-1}. This is positive not only from a first-order point of view, but from a Fourier optics point of view as well. Considering the MTF imposed by the lens, even the maximum fringe frequency will have a high modulation.

The CLOVER interferometer is capable of imaging and resolving the fringes over the complete range of desired test optics. Thus, the first two conditions for non-null interferometry, collecting the wavefront and resolving the fringes, have been met. The third condition, wavefront calibration, is taken up next.

2.3 Theory of Wavefront Calibration

The third criterion mentioned in using an interferometer in a non-null setup is the calibration of the wavefront. While the first two criteria dealt with the hardware of the interferometer, calibration is a software issue. The use of raytracing code is critical to any non-null interferometer for a variety of reasons. First, the raytracing code enables calibration. Second, raytracing code allows for theoretical wavefronts to be generated,

providing a prescription for the test part. This allows a measured-to-modeled comparison to be made at the transmitted wavefront level.

Understanding the calibration process starts with examining what exactly is detected by the interferometer: the interference produced by two wavefronts in the plane of the detector. Given the well-known algorithms of PSI, the interference reveals the relative OPD between the two wavefronts (Creath, 1986; Greivenkamp, 1992). A known reference wavefront can then be used in conjunction with the OPD to infer the unknown test wavefront at the detector. The issue is that the desired wavefront is the test wavefront at the test part, and not at the detector. As the test wavefront propagates through the interferometer's optics, aberrations are induced. A calibration process is needed to convert this inferred test wavefront at the detector into a best estimate of the test wavefront at the contact lens.

To appreciate the need for calibration, consider a Mach-Zehnder interferometer in a null configuration, with a perfect null optic providing the reference wavefront. In the Mach-Zehnder configuration, two wavefronts are imaged simultaneously: the test and reference wavefronts. These wavefronts are nominally identical. Consequently, the aberrations added to each wavefront in imaging the wavefronts are also identical. The resulting OPD is zero. In this case, the aberrations have no effect on the OPD. The induced aberrations are effectively cancelled. Now consider the non-null case with an absolute, or planar, reference wavefront. The planar wavefront receives one set of aberrations (primarily

spherical aberration, since this wavefront is the result of an on-axis point source) while the test wavefront, spherical or aspheric, receives a different set of aberrations. No longer do the aberrations cancel when the OPD is produced, and thus the resulting test wavefront is affected by these aberrations.

The issue of induced aberrations has been addressed before. The errors caused by induced aberrations in a transmission test are analogous to retrace errors in a reflection test (Lowman, 1996; Greivenkamp, 1992; Gappinger, "Non-null...", 2003). Several authors have taken on the task of computing analytic expressions for interferometric setups (Jozwicki, 1991; Huang, 1993). Murphy, Brown, and Moore discuss the notion that the influence of the induced aberrations can be divided into two groups: errors on phase and errors on mapping, or the location of the fringes (Murphy, 2000). In almost all cases, the derived equations for the imaging errors are shown to vanish in the absence of fringes at the detector. In the case of a Mach-Zehnder interferometer, the lack of fringes indicates that the reference and test wavefronts are identical, and there are no errors due to the imaging optics, regardless of the shape of the wavefronts. More recently, the process of removing the induced aberrations via a model of the interferometer has been discussed (Gappinger, "Non-null...", 2003). Gappinger and Greivenkamp have developed an iterative reverse optimization procedure to improve the estimate of the model over given lens prescriptions and measured distances. Examined here is the technique at the heart of the reverse optimization procedure: reverse raytracing.

The problem of wavefront calibration is rooted in the fact that the induced aberrations depend on the incident wavefront. However, the magnitude of the added aberrations is typically a small fraction of the wavefront's magnitude. This allows for the aberrations to be treated as a perturbation to the wavefront. Mathematically, the operation of imaging the wavefront is defined in this context as

$$\mathrm{Img}\{W\} = W + A(W), \qquad \text{Equation 2.25}$$

where W is the original wavefront, and $A(W)$ are the induced aberrations. The notation $A(W)$ is used to indicate that the induced aberrations are a function of the wavefront. The imaging lens is the source of the induced aberrations. An intuitive way to see why different wavefronts receive different aberrations is to view the different wavefronts as shifts in conjugates.

The detected interference patterns represent the difference between the images of two wavefronts, and not the wavefronts themselves. Therefore, the $\mathrm{OPD_T}$ (OPD of the test beam) between the images of the test wavefront (W_T) and reference wavefront (W_R) at the detector plane is:

$$\begin{aligned} \mathrm{OPD_T} &= \mathrm{Img}\{W_T\} - \mathrm{Img}\{W_R\} \\ &= \left(W_T + A(W_T)\right) - \left(W_R + A(W_R)\right). \end{aligned} \qquad \text{Equation 2.26}$$

An inverse operation to the imaging process is needed. When the prescription of the interferometer is known, the system that generated the aberrations is not a black box, but rather a collection of optics that can be modeled. The model is the tool that enables an inverse operation to imaging, namely reverse raytracing. With reverse raytracing, the

wavefront at the test plane, typically the plane immediately following the test optic, is produced from the OPD and reference wavefront at the detector by tracing rays backwards through the system. The rays are said to be traced backwards because, in the interferometer, light travels from test plane to detector and now rays are traced from detector to test plane. This inverse operation, using Eq. 2.25 and Eq. 2.26, is defined as:

$$\begin{aligned}\tilde{W}_T &= \mathrm{Img}^{-1}\{W_T + A(W_T)\} \\ &= \mathrm{Img}^{-1}\{\mathrm{OPD_T} + \mathrm{Img}\{W_R\}\}.\end{aligned} \qquad \text{Equation 2.27}$$

Equation 2.27 illustrates how the process of reverse raytracing is implemented. Given the model of the interferometer, rays are traced along the reference arm, through the imaging optics and onto the detector. This is the image of W_R ($\mathrm{Img}\{W_R\}$). $\mathrm{OPD_T}$ is then added to the rays, changing both their position and angle. At this point, the image of W_T can be obtained. The rays are then traced back to the test plane. At the test plane the rays are converted to a wavefront, which is $\tilde{W}_T$, the estimate of the original test wavefront W_T.

The above explanation as to how best estimate the original test wavefront W_T ignores a key piece of available information, namely the wavefront detected when no test optic is in place. A common technique used in interferometry is to measure nothing, and then subtract this baseline measurement from subsequent measurements. Going back to equation 2.26, subtracting off a baseline measurement's OPD ($\mathrm{OPD_O}$) would give:

$$\begin{aligned}\mathrm{OPD_T} - \mathrm{OPD_O} &= \left(\mathrm{Img}\{W_T\} - \mathrm{Img}\{W_R\}\right) - \left(\mathrm{Img}\{W_O\} - \mathrm{Img}\{W_R\}\right) \\ &= \left(W_T + A(W_T)\right) - \left(W_O + A(W_O)\right).\end{aligned} \qquad \text{Equation 2.28}$$

By subtracting off a baseline measurement, the reference wavefront is completely eliminated, and the resulting OPD is the difference between the test arm with and without the test lens. In the common use of this technique, this result is taken as the best estimate for the original test wavefront. This is true in the limit that W_O goes to zero, a reasonable assumption, and in the limit where the difference between the induced aberrations $(A(W_T) - A(W_O))$ goes to zero. The assumption on the second limit is the dominant source of error in this technique, for this limit does not go to zero when W_O goes to zero. The limit on the difference of the induced aberrations goes to zero when the two wavefronts (W_T and W_O) become identical. That would only happen if the test lens was nonexistent or being tested in a perfect null condition.

The technique of subtracting a baseline measurement does not provide a benefit to reverse raytracing. This can be shown by reverse raytracing the difference in OPDs in Eq. 2.28. Applying reverse raytracing would give:

$$\begin{aligned}\tilde{W}_T &= \mathrm{Img}^{-1}\{W_T + A(W_T)\} \\ &= \mathrm{Img}^{-1}\{\mathrm{OPD_T} - \mathrm{OPD_O} + \mathrm{Img}\{W_O\}\}.\end{aligned} \qquad \text{Equation 2.29}$$

However, the image of the baseline wavefront is

$$\mathrm{Img}\{W_O\} = \mathrm{OPD_O} + \mathrm{Img}\{W_R\}, \qquad \text{Equation 2.30}$$

and so the estimate for the test wavefront would be (substituting Eq. 2.30 into Eq. 2.29)

$$\begin{aligned}\tilde{W}_T &= \mathrm{Img}^{-1}\{\mathrm{OPD_T} - \mathrm{OPD_O} + \mathrm{OPD_O} + \mathrm{Img}\{W_R\}\} \\ &= \mathrm{Img}^{-1}\{\mathrm{OPD_T} + \mathrm{Img}\{W_R\}\}.\end{aligned} \qquad \text{Equation 2.31}$$

This is identical to the result of Eq. 2.27. The benefit of including the baseline measurement has been eliminated.

The choice of calibration technique is between correcting for the induced aberrations via reverse raytracing and correcting for the errors in the interferometer via subtraction of a baseline measurement. The errors in CLOVER are quite small. Over a 12 mm aperture, typical numbers for the PV for a baseline measurement is 0.36 λ, while the RMS is 0.038 λ. Over a 5 mm aperture, the diameter of the test aperture under normal testing conditions, the numbers drop to 0.090 λ PV and 0.010 λ RMS. The magnitudes of these numbers are far less than what will be shown for the induced aberrations in Chpt. 4. Therefore, the calibration technique used with CLOVER is reverse raytracing. Baseline measurements are not used in conjunction with the data contained in this dissertation.

So, what's really going on here? Clearly the baseline wavefront contains useful information, and yet there seems to be no way of incorporating that information into the reverse raytracing calibration process. The problem is that the baseline measurement says something about the difference between the empty test arm and reference arm, but says nothing to the origin of the measured errors. Suppose the baseline measurement gives an RMS of $\lambda/20$, in the shape of astigmatism. To which arm should the astigmatism be attributed? Or what fraction of the astigmatism should be attributed to each arm? This is the problem – only the magnitude, and not the origin, of the wavefront error is known. If the error could be divided between the two interfering wavefronts,

then a reversed raytraced baseline wavefront could be saved, waiting at the test plane to be subtracted off from reversed raytraced test wavefronts. Furthermore, the assumption of a perfect plane wave in the reference arm could be improved by reverse raytracing the error not associated with the test arm. This under-constrained problem – two wavefronts, but only one OPD map – needs to be solved to take full advantage of the baseline measurement and reverse raytracing.

A brief explanation of the algorithm used in converting rays associated with W_R into rays describing W_T is in order. The amplitude of W_R, E_R, where $|E_R|^2 = W_R$, can be described in general, optical vernacular terms as

$$E_R = A_R \exp\left[i\left(\vec{k}_R \cdot \vec{r} - \omega_R t\right)\right]. \qquad \text{Equation 2.32}$$

Using the same definition for W_T, the difference in phase is then

$$\Delta\phi = \left(\vec{k}_T \cdot \vec{r} - \omega_T t\right) - \left(\vec{k}_R \cdot \vec{r} - \omega_R t\right). \qquad \text{Equation 2.33}$$

The two beams are from the same source, and therefore the following is true:

$$\begin{aligned} \omega_T &= \omega_R, \\ k_T &= k_R = k = \frac{2\pi}{\lambda}. \end{aligned} \qquad \text{Equation 2.34}$$

Taking the positive z-axis as the direction of light propagation, the position vector **r** is

$$\vec{r} = x\hat{\mathrm{i}} + y\hat{\mathrm{j}} + z\hat{\mathrm{k}}, \qquad \text{Equation 2.35}$$

the propagation **k**-vector (using direction cosines) is

$$\vec{k} = k\left(L\hat{\mathrm{i}} + M\hat{\mathrm{j}} + N\hat{\mathrm{k}}\right), \qquad \text{Equation 2.36}$$

and the OPD_T between the rays of the test and reference wavefronts can be expressed as

$$\begin{aligned} \mathrm{OPD_T} &= \frac{\Delta\phi}{2\pi}\lambda \\ &= (L_T - L_R)x + (M_T - M_R)y + (N_T - N_R)z. \end{aligned} \qquad \text{Equation 2.37}$$

$\mathrm{OPD_T}$ is described in the plane of the detector. Setting this plane to $z = 0$ gives the final form relating $\mathrm{OPD_T}$ to the rays,

$$\mathrm{OPD_T} = (L_T - L_R)x + (M_T - M_R)y. \qquad \text{Equation 2.38}$$

At any location in the model, each ray traced is described by seven parameters. The first six are the positional coordinates (x, y, and z) and the direction cosines (L, M, and N) which completely describe the trajectory of the ray. The seventh parameter is *OPL*, the optical path length of the ray from its origin. The conversion of rays from the reference arm to the test arm takes place in the plane of the detector, on a ray-by-ray basis. The formulas for converting the seven ray parameters are:

$$\begin{aligned} &x_T = x_R, \\ &y_T = y_R, \\ &z_T = z_R = 0, \\ &L_T = L_R + \left.\frac{\partial \mathrm{OPD_T}}{\partial x}\right|_{(x_T, y_T)}, \\ &M_T = M_R + \left.\frac{\partial \mathrm{OPD_T}}{\partial y}\right|_{(x_T, y_T)}, \\ &N_T = \sqrt{1 - L_T^{\,2} - M_T^{\,2}}, \\ &OPL_T = OPL_R + \mathrm{OPD_T}. \end{aligned} \qquad \text{Equation 2.39}$$

The first three equations are the result of the two rays meeting at the plane of the detector. The equations for L_T and M_T come directly from differentiating Eq. 2.38. The equation for N_T comes from the normalization of the direction cosines, and the last equation is the definition of OPD. In practice, the derivatives are evaluated by least-squares fitting a

second-order polynomial to a grouping of pixels centered at (x_T, y_T), and computing the coefficients on the linear terms. The conversion between rays and wavefronts can be done at any time by simply interpolating the positional coordinates and *OPL* values, thereby producing a wavefront on a regular grid.

Back to the general discussion on reverse raytracing, the reason that the result of the inverse operation is labeled an estimate is that a model of the interferometer is used to provide the correction. The model and the actual interferometer differ to some level. This difference is what is minimized by the iterative reverse optimization procedure outlined by Gappinger ("Non-null...", 2003). This technique is not used with CLOVER because, on the whole, this level of correction is not necessary to produce output at acceptable levels of accuracy.

The model of the interferometer is verified by measuring the magnification between the imaging lens' conjugates. Only two distances are not known from a prescription: the distance from the top of the cuvette (the cell containing the contact lens and saline solution) to the imaging lens and the distance from the imaging lens to the detector. In effect, these two distances are the object and image distances for the imaging lens. Since the imaging lens is known, knowledge of the magnification between the conjugate planes provides enough information to uniquely determine the two distances in question. A paraxial raytrace is used to update the model given the most recent magnification measurement.

2.4 Specifics of CLOVER Software

The software associated with CLOVER is critical not only from the standpoint of collecting the data, but analyzing the data as well. Since the reverse raytracing technique is used to calibrate wavefronts, a raytracing capability is needed. This capability also enables measured-to-model comparisons at the transmitted wavefront level. The software suite needs to be robust. The capabilities to model test optics and the interferometer, raytrace through such models, collect interferograms, and analyze calibrated wavefronts must be present.

There are three main, commercially available application used with CLOVER. The first is XCAP (EPIX, Inc., Buffalo Grove, Illinois). XCAP is used primarily to provide diagnostics and real-time control of the camera. The XCAP interface provides control over integration time, gain, and binning. Binning is the process of combining pixels at readout to form theoretical pixels of a larger size. XCAP provides real-time readout of the digital number (DN) at each pixel, a handy feature in adjusting the neutral density filters. XCAP is also used to determine the magnification. The magnification target (Edmund Industrial Optics, Barrington, New Jersey) is shown in Fig. 2.6.

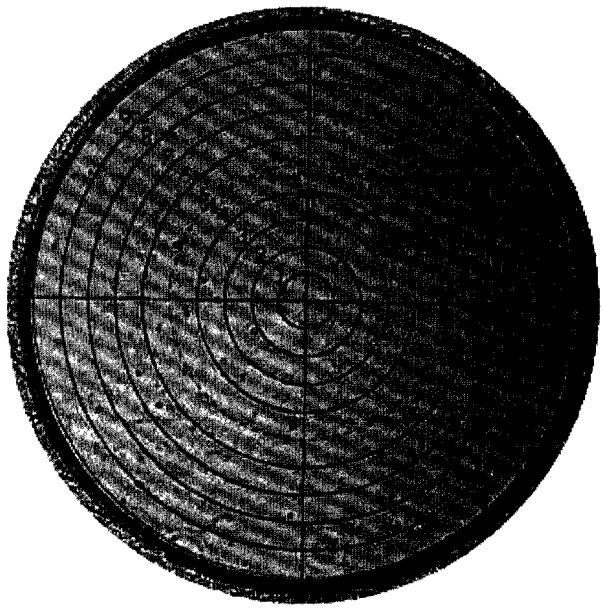

FIGURE 2.6 – Magnification target used to correlate test aperture diameter to number of pixels. Each ring increases by 1 mm in diameter.

The rings at 4, 6, and 8 mm are measured by overlaying a circle of known radius (in pixels) using the XCAP software and the average is taken. The depth of focus and resolution of the imaging system is such that variations in magnification when the cuvette is removed and replaced are on the order of 0.002.

The second piece of software is Intelliwave (Engineering Synthesis Design, Tucson, Arizona). Intelliwave is used for interferometer control, data acquisition, and phase unwrapping. Intelliwave provides the controls and timing signals necessary to make the phase shifter, detector, and AO modulator work in harmony.

The collection of interferograms is done in Intelliwave using the Bucket 5B algorithm (Engineering Synthesis Design, 2002; Schmit, 1995). This algorithm is similar to the widely-used Hariharan algorithm, in that both algorithms use five interferograms with a $\pi/2$ phase shift between each interferogram. However, the 5B algorithm comes about from averaging the numerator and denominators for two sets of four-frame algorithms. This averaging technique, first developed by Schwider, reduces the sensitivity to phase-shifter calibration error, as demonstrated by Schmit and Creath (Schwider, 1983; Schmit, 1995). By using this particular algorithm, the benefit of averaging is gained by taking a single extra frame. Taking two data sets and averaging the results would require twice as many frames. With each frame taking a significant amount of memory and time to collect, the fewer the frames the better. The 5B equation for the wrapped phase is:

$$\tan(\phi) = \frac{-I_1 + 4I_2 - 4I_4 + I_5}{I_1 + 2I_2 - 6I_3 + 2I_4 + I_5}. \qquad \text{Equation 2.40}$$

The phase is then unwrapped using a tiled modulation method. In short, the modulation for the wrapped phase is computed over a contiguous set of tiles, each tile containing several pixels. The tiles are unwrapped individually. Starting with the tiles of highest modulation, piston is added to eliminate the discontinuities in phase. This algorithm is designed to minimize the propagation of unwrapping errors and has proven to be more robust than the faster path following, or branch cut, algorithms (Ghiglia, 1998). The tiled algorithm in Intelliwave is the Tiled Modulation Guided (TMG) algorithm (Engineering Synthesis Design, 2002).

The final piece of software is IDL (Research Systems, Inc., Boulder, Colorado). IDL (Interactive Data Language) is used to model, raytrace, and analyze the collected OPD coming from Intelliwave. The real benefit to using IDL comes from its ability to treat arrays of data as single entities. Operations that need to be made on a pixel-by-pixel basis can be done using code that does not loop over the entire array. This greatly speeds up the raytracing and analysis process. The raytracing engine and overall modeling syntax used in IDL was developed by Dan Smith of the University of Arizona. The code was qualified against Zemax.

The two main programs, Intelliwave and IDL, can "talk" to each other on some levels. While simple IDL routines can be run within Intelliwave, the complete analysis process is too large to run under Intelliwave. However, data can be saved from Intelliwave in a native IDL format. This eliminates any "by-hand" data transfers.

To make a measurement, the following data is needed:

- Diameter of test aperture
- System magnification
- Model of interferometer (updated using given system magnification)
- Surface in model corresponding to the test plane

To compare the output to modeled output, the following additional data is needed:

- Prescription for test lens / cuvette
- Index of surrounding saline

- Type of lens (contact lenses only, choice of: sphere, toric, bifocal)

All other information is determined from the data present in Intelliwave. Efforts are ongoing to make providing the above information as smooth as possible.

3 VARIOUS ISSUES WITH TESTING SOFT CONTACT LENSES

Alluded to throughout the first two chapters is that this research is in support of the advancement of the development of soft contact lenses. There are a number of reasons why this is a worthwhile endeavor. First and foremost, advancing the capabilities of human vision and being able to better correct the natural defects of the eye benefits all. Improving vision will have trickle-down effect across all aspects of life, especially as life spans lengthen. Second, the ophthalmic industry is rapidly growing. This is due to the emerging ability of manufacturers to provide contact lenses for an increasing percentage of patients by developing the capability to customize lenses. Third, the industry is ripe for advancement in all three fields of development. Work is being done to improve the design process of contact lenses. This task is complicated by the fact that the combination of the human eye and brain is by far the most complex detector/image processor combination known to man. Efforts are ongoing in the fabrication field as well. Providing customized lenses requires tooling that can be customized at a reasonable cost. And, thanks in some small way to the work described in this dissertation; the field of testing is being advanced. The metrology of both contact lenses and the eye is being expanded and refined. Current techniques for measuring lenses, such as the aforementioned moiré deflectometry or use of optical sphereometers simply aren't the right tools for the expanding complexity of soft contact lenses (Mandell, 1974). New

metrology is being developed both to improve the measurements possible and to accommodate the unique issues that contact lenses as test optics pose.

3.1 Understanding the Material of Soft Contact Lenses

The name "soft contact lenses" gives a clue toward discovering the issues associated with testing this class of optics: they're "soft". This is to say that the lenses are not rigid but pliant. In general, the lenses conform to the eye, obviously a desired feature with respect to fit and comfort for the wearer. On the other hand, this flexibility does not make for an ideal optic to test. In fact, the nature of the material used in the lenses, along with other lens parameters, makes them quite difficult to test.

Briefly, soft contact lenses are made from a material chemically known as a hydrogel. Hydrogels are hydrophilic polymers, whose water content when fully hydrated can be anywhere from 30% to over 70% (Larsen, 1985; Tighe, 1997). The tradeoff in water content is between the ability to control the optical properties of the lens, mechanical strength, and comfort on the eye. Lenses with low water content are both more optically and mechanically stable, yet lenses with high water content are more gelatinous and therefore more comfortable to wear (Larsen, 1985).

Making hydrogel material, or simply a hydrogel, is a complex chemical process. The hydrogels specific to contact lenses start out as a combination of monomers, carbon chains of only a few atoms (Pimentel, 1963). Almost all combinations of monomers used

to manufacture soft contact lenses contain hydroxyethyl methacrylate (HEMA). HEMA is used because of its ability to use water to provide the hydrogel's unique flexibility (Tighe, 1997). Figure 3.1 shows the chemical structure of HEMA. Note that polymerization occurs at the left side of the molecule, and not with the functional group at the right side.

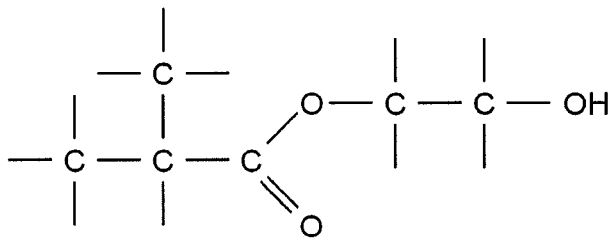

FIGURE 3.1 – Chemical structure for the monomer hydroxyethyl methacrylate (HEMA) (Mandell, 1974).

Table 3.1 shows the monomer combinations for several manufactured brands of soft contact lenses (Tighe, 1997; Proctor, 1997; CooperVision, 2003). Disputed values are listed as given by Proctor/Tighe. The full monomer names are given in Table 3.2.

Lens Brand Name	Manufacturer	Monomer Combination	Water Content	Material Trade Name
Acuvue	Vistakon	HEMA, MA	58%	Etafilcon-A
CSI	Wesley Jessen	MMA, G, M	38/41%	Crofilcon-A
Durasoft	Wesley Jessen	HEMA, EEMA, MA	30/38%	Phemefilcon-A
Focus	Ciba	HEMA, PVP, MA	55%	Vifilcon-A
Frequency 38	CooperVision	HEMA	38%	Polymacon
Optima	Bausch & Lomb	HEMA	38%	Polymacon

TABLE 3.1 – Composition and characteristics of leading soft contact lenses.

Monomer Abbreviation	Full Name
EEMA	ethoxyethyl methacrylate
G	glyceryl
HEMA	hydroxyethyl methacrylate
M	methacrylate
MA	mathacrylic acid
MMA	methyl methacrylate
PVP	polyvinyl pyrrolidone

TABLE 3.2 – Full names for monomers used in soft contact lenses (Tighe, 1997).

Added to the monomers is a combination of esters. Esters are acid derivatives, and make good solvents, as well as provide the strong odor of model airplane glue or fingernail polish remover (Pimentel, 1963). The role of the ester is to better facilitate the conversion of the monomers into polymers of the desired molecular weight. That is to say, the ester enables the gelling of the hydrogel. The most common ester used is one derived from boric acid. This ester is preferred because it is easily replaced with water after the lens is formed. Possible additions to the mixture are a cross-linking agent and a photoinitiator or UV catalyst. Once the liquid cocktail of monomers, esters, and catalysts is complete, the mixture is exposed to UV light. UV light is the mechanism by which polymerization occurs. The polymers are then cross-linked. Cross-linking is the process of placing the long polymer chains in the proper orientation to achieve the desired chemical and material properties. The new material is then washed, replacing the boric acid ester and other chemicals with water. This completes the process of making a hydrogel material. For more details on the various chemical compositions used, see U. S. Patents 4,495,313 and 4,680,336.

3.1.1 Making Soft Contact Lenses

An overview of one specific contact lens manufacturing process, soft stabilized molding, is shown in Fig. 3.2 (Loran, 1997).

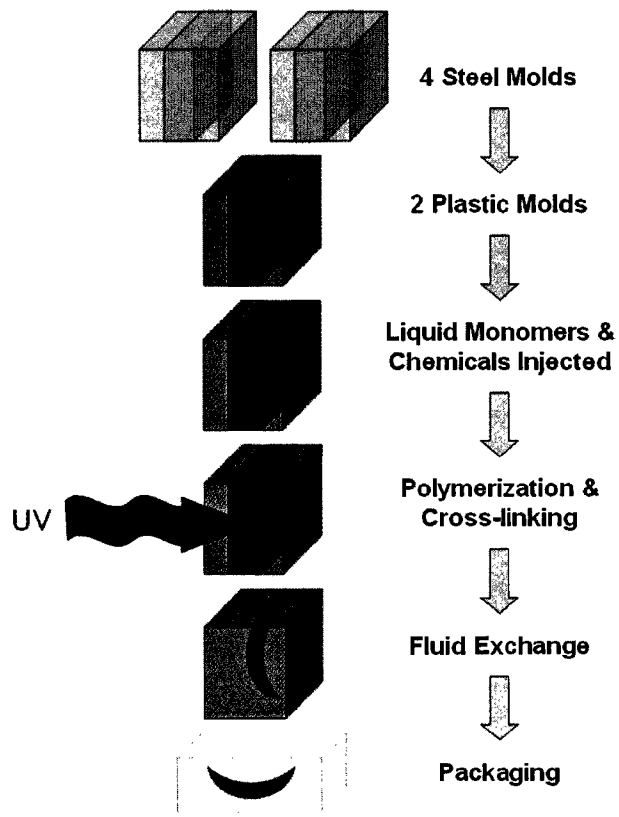

FIGURE 3.2 – Soft stabilized molding manufacturing process for hydrogel contact lenses.

Four steel molds are used to make two plastic molds, one for each surface of the contact lens. The plastic molds are at a minimum UV transparent. The two plastic molds are brought together, and the liquid cocktail of monomers and other chemicals is injected. UV light is then shined on the cavity, and polymerization and cross-linking occur. Then

the lenses are washed free of the boric acid ester and other chemicals, and replaced with saline solution. The final step is packaging in more saline solution. The introduction of saline solution, while vital to performance, is also the point where the ability to work with this material dramatically increases in difficulty.

In addition to stabilized molding, other manufacturing techniques exist. Spin casting is used by Bausch & Lomb on certain products (Loran, 1997). The parameters of mold diameter, amount of monomer, and spin speed can be manipulated to produce different curvatures and refractive powers. A cast molding process exists where a lens blank is molded and then polished before hydration. Lathe cut lenses have also been tried, both in the solid and hydrated states. Larsen writes in U. S. Patent 4,680,336 that the success of turning hydrated lenses is low, and "the method has not been adopted commercially".

3.1.2 The Need for Saline

Taking a step back, the definition of a hydrogel given above, while chemically accurate, does not satisfactorily describe the material. A good analogy is to consider hydrogel like a sponge. Analogous to a sponge, the material has some solid-like shape and volume, and yet that volume will change given the availability of a solution. While the material has no long-term memory, the relaxation time is significant. People who wear these lenses talk about having to let them soak in saline solution overnight if exposed to air for a significant amount of time. When hydrogels dry out, they become very brittle, and since they are so thin, they easily break. Again, imagine a very thin sponge, and how

brittle it would be if allowed to dry. Another useful analogy is to consider hydrogel materials like a net. The process of cross-linking can be thought of as making a net out of the strings of polymers. Like a net, hydrogels capture particles that are bigger than the net spacing, and allow smaller particles to pass through. This helps explain how oxygen and water can be passed through to the cornea, and how proteins and pollens can be caught in the lens, leading to allergic reactions and/or eye disease (Larsen, 1985).

Only when immersed in solution is the material consistent with its performance on the eye. On the eye, the tear film provides the necessary hydration (Mandell, 1974). Since this is wholly the area of interest, the lenses must be tested in saline solution. So now the test optic grows. Instead of testing just a lens, the test is done on the lens, some amount of saline solution, and the cuvette which holds the lens and saline solution. Needless to say, this presents some issues.

3.2 Measuring the Index of Refraction

From an optics standpoint, one of the critical parameters of any material is its index of refraction. In the case of testing lenses in solution, this is doubly important, for the index of both the lens material and the surrounding solution dictate the power of the lens. Furthermore, the measured power is the power of the lens in the solution. If there is any hope in inferring power in air, then the value for the index of the saline must be known to such a level as not to be the dominant source of error. As shown in both this chapter and the next, this is not an easy level to achieve.

3.2.1 Measuring Saline

For saline solution, the determination of index at any given time is straightforward. Since saline is a liquid, an Abbe refractometer does the job. The Abbe refractometer measures index by determining the critical angle between a known reference (a high-index prism) and the unknown sample. The challenge with the saline solution is that the refractive index varies over time due to evaporation. Figure 3.3 shows the change in index over time for an exposed sample of solution (Brumfield, 2003).

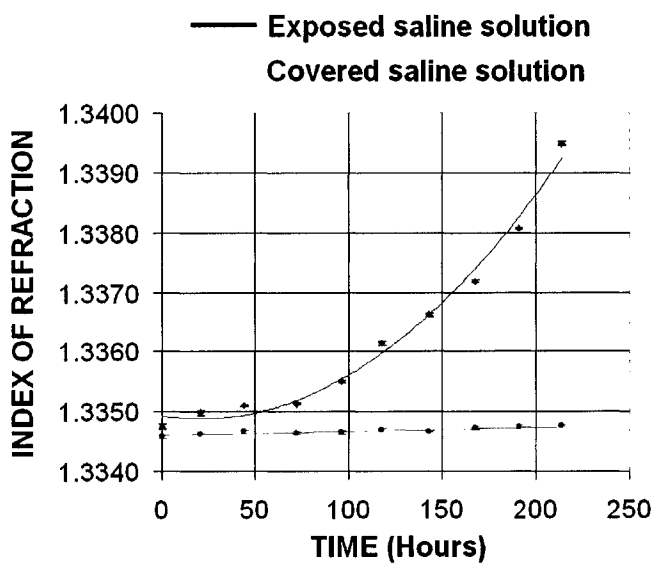

FIGURE 3.3 – Index of refraction of saline solution versus time (Brumfield, 2003).

Consequently, a design challenge for the lens holding system, or cuvette, is that the index of the saline must either be monitored or the system designed to minimize evaporation.

3.2.2 Measuring Hydrogels

Measuring the index of refraction of hydrogels is an even more daunting task than measuring a liquid whose index changes over time. This is largely due to the now apparent fact that the index of the hydrogel has to be measured while in solution.

Before diving into testing the index of a sponge-like material, now is a good time to discuss just how well these measurements need to be made. After all, if the value for index is only needed to about 0.1 or so, the argument based on the logic that the hydrogel is mostly saline, and saline is mostly water, and the index of water is 1.33, so the index of the hydrogel is mostly 1.33 would work. Since the lenses really are thin lenses, the thin lens approximation for power works quite well. The error in using the thin lens approximation for a 10 diopter lens is less than 1%. The basic equation relating power, index, and curvature is then

$$\begin{aligned}\phi &= (n_{\text{Lens}} - n_{\text{Saline}})(C_1 - C_2) \\ &= \Delta n \Delta C,\end{aligned} \qquad \text{Equation 3.1}$$

where Δn is the difference in index between the lens and surrounding medium, and ΔC is the difference in curvature between the two surfaces. Computing the differential of Eq. 3.1 leads to

$$\frac{\delta\phi}{\phi} = \frac{\delta\Delta n}{\Delta n} + \frac{\delta\Delta C}{\Delta C}. \qquad \text{Equation 3.2}$$

Assuming that the curvature is fixed - a questionable assumption given the nature of the lenses, but one that seems to hold up against the collected experimental data - the uncertainty in power given as an uncertainty in index is

$$\frac{\delta\phi}{\phi} = \frac{\delta\Delta n}{\Delta n}. \qquad \text{Equation 3.3}$$

The nominal values for index are $n_{\text{Lens}} = 1.4012$ and $n_{\text{Saline}} = 1.3358$, putting Δn at 0.0654. As a result, a 1% error in power comes from an uncertainty in Δn of 0.000654. The difference in index comes from two different index values. Even though those two index values are not necessarily independent, given the nature of the hydrogels, this is at best an upper bound on the uncertainty in measuring index. The challenge now is determining how to measure the index of hydrogels to this level of accuracy or better.

Armed with at least a layman's understanding of hydrogel materials, one quickly realizes that conventional techniques for measuring index of refraction simply will not work. There are a variety of reasons why this is. For example, the conventional method for determining index of refraction in the large-scale production of glass optics is to cast a prism at the same time the lenses are casted. The prism is then polished, and a prism spectrometer used to identify the index of refraction to an accuracy on the order of 1 part in 10^6 (Twyman, 1998). Unfortunately, hydrogels can not be made into prisms with highly-polished surfaces. Going back to the analogy of hydrogels as nets, consider cutting a net. Where exactly is the edge? This reasoning also precludes making a thin disc or prism out of the hydrogel, and measuring the index via focal length or angle of minimum deviation.

Stated earlier was the fact that the saline solution can be measured using an Abbe refractometer. Since the majority of the hydrogel is saline, perhaps this is a possibility. Unfortunately, the assumed index for the hydrogel is higher than that for the saline. The hydrogel is more solid-like than the saline, so it only makes sense that it should have a slightly higher index. Since the lowest index belongs to the saline, it is at this index that the shadow line of the Abbe refractometer will be formed.

Apparently, a more elegant technique is needed. Efforts have been ongoing here at the University of Arizona to develop instrumentation for measuring the index of hydrogels. The problem is complex for a variety of reasons. No assumptions can be made regarding the shape or surfaces of the sample. The sample must be tested in saline solution. Not only is the refractive index different between the saline and the hydrogel, but the dispersion is likely different as well.

Scanning techniques have been proposed, such as the use of an interference microscope or confocal microscopy (El-Nasher, 1980; Brumfield, 2003). The problem is that the test beam must pass through different materials: saline and hydrogel. This prevents dispersion compensation in the reference arm, complicating any interferometric technique. Another complication is that the reflection off each surface is quite small, and the surfaces are close together (about 100 μm).

Perhaps the biggest challenge is ensuring that the phase index is measured, and not the group index. Any probing technique is likely to measure the group index, and not the phase index, as most probing techniques use a source with a finite bandwidth for coherence considerations. The phase index is required to correlate data taken with an interferometer, as the OPD measured by an interferometer is generated by differences in phase index. The group index (n_G) is the ratio of the speed of light (c) to the group velocity (v_G). Group velocity is

$$v_G = \frac{d\omega}{dk} = \frac{c}{n_P - \lambda\left(\frac{dn_P}{d\lambda}\right)}, \qquad \text{Equation 3.4}$$

so that the group index becomes

$$n_G = \frac{c}{v_G} = n_P - \lambda\left(\frac{dn_P}{d\lambda}\right). \qquad \text{Equation 3.5}$$

Equation 3.5 shows that the group index depends on both the phase index (n_P) and the dispersion of the material ($dn_P/d\lambda$) (Saleh, 1991; Steel, 1967). If both quantities are unknown, then the group index does not provide enough information to produce the phase index.

Since the phase index gives rise to the OPD measured by an interferometer, one would think that an interferometric solution would be trivial. The problem with this is that no assumption can be made regarding the physical parameters of the hydrogel sample.

Therefore, the OPD measured cannot be separated into the index and path length, for both are unknown quantities. Again, there are two unknowns equaling only one piece of known information. The ultimate answer must be a technique were the physical characteristics are determined independent of the optical characteristics, and then the known dimensions of the sample used in conjunction with an interferometer to measure the phase index.

3.3 Mounting Soft Contact Lenses

Already established is the need to test the lenses in saline. The question here is how best to mount the lenses in a saline bath, providing maximum visibility and minimum stress or distortion to the lens, all while making the loading/unloading process as fast and simple as possible. A very simple cuvette, really just a box with polished windows is used with the current instrumentation in the sponsor's lab. This cuvette uses a V-block and gravity to position and hold the lens. With the resolution of an interferometer, one can quickly see that this type of cuvette distorts the lens, as shown in Fig. 3.4.

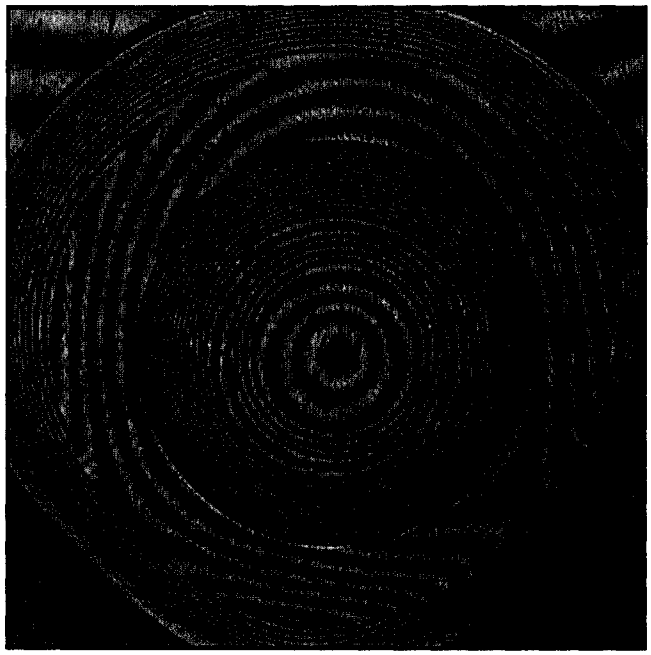

FIGURE 3.4 – Simple cuvette with V-block holding a lens in a vertical orientation. The deviation from circular fringes in the vicinity to the V-block indicates deformation of the lens.

The deviation from circular fringes apparent where the contact lens is touched by the V-block is proof that the lens is bending abnormally in these areas. So what's needed is a new cuvette, one that is optimized to the above criteria.

The design of the following cuvettes was a collaborative effort, between the team here at the University of Arizona and the sponsor. All cuvettes shown were provided by the sponsor.

3.3.1 Initial Cuvette Design

The initial philosophy was to keep the lenses hydrated and stabilized with regards to temperature before and during testing. To that end, the overall testing system consisted of an external holding tank with temperature stability and a pump to allow for circulation of stabilized saline solution between the holding tank and cuvette. Pumping the saline not only provides temperature stability but allows for passive filtering of the saline. This is a key benefit, for any debris in the saline could potentially get in between the two windows of the cuvette and ruin a measurement. Lenses are transported between the holding tank and cuvette in a barrel, thereby remaining in saline solution at all times. The third cuvette based off this design philosophy is shown in Fig. 3.5 along with the lens barrel carrier and sample lens barrel.

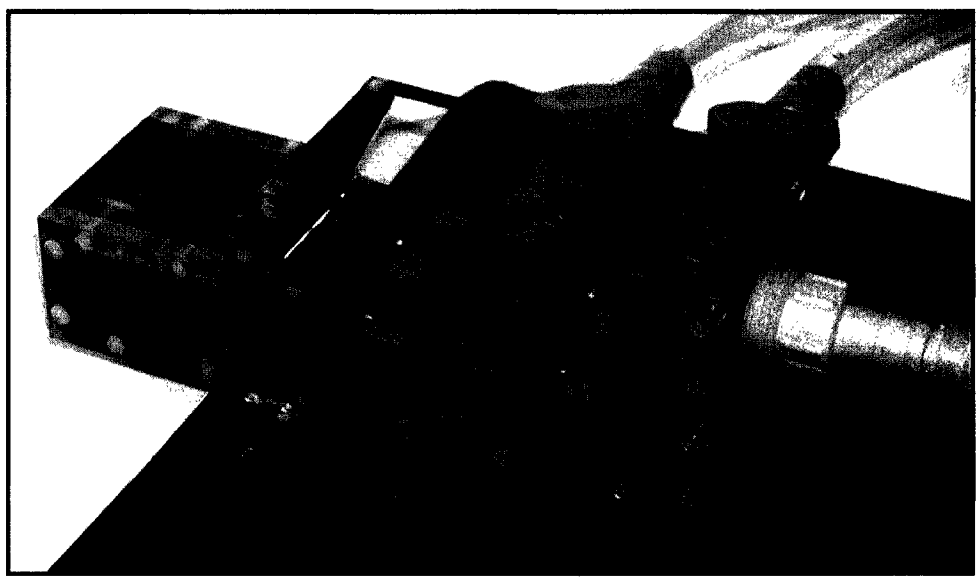

(a)

(b)

FIGURE 3.5 – Third iteration of initial cuvette design. Shown are the (a) cuvette, (b) lens barrel clamp and lens barrel.

The reason why the above cuvette was the third iteration was that the first two cuvettes were not made from plastic, but rather from stainless steel. The corrosive nature of saline was not appreciated, as corrosion occurred wherever the bare stainless came in contact with saline. Another lesson learned.

Lens barrels with different interfaces with the contacts were tried. Some provided a beveled surface, others a simple ring contact. This necessarily assumed that the surface at the point of contact would be rotationally symmetric. This assumption is not true for all types of lenses analyzed.

There were other problems with this design, most notably the time involved in getting a lens in place. First the lens was loaded into the barrel, and then the barrel loaded into the cuvette. Neither step was guaranteed to be a success. Sometimes the lens barrel clamp would bump the barrel while grabbing it, sending the lens outside the barrel where the clamp would shear the lens. This arrangement maximized the likelihood of dripping saline on or near the interferometer. Given the now respected corrosive nature of saline, this was not a preferred condition of operation.

3.3.2 Current Cuvette Design

The current design does not rely on any surface of the lens being rotationally symmetric, only that the edge of the lens be circular. The current design is also an improvement in terms of loading time, minimizing the possibility of dripping saline on the interferometer, and overall streamlining of the loading process. Lenses are now held by simply placing the lens concave-side down on a third window, which is then slid on a dovetail stage between the two fixed windows of the cuvette, as shown in Fig. 3.6. This does mean that the lenses are exposed to air, but the exposure time can be under one second with a little practice. Comparing this time to the time it takes to put a lens on an eye, the exposure time of less than one second is negligible with regards to the integrity of the measurement.

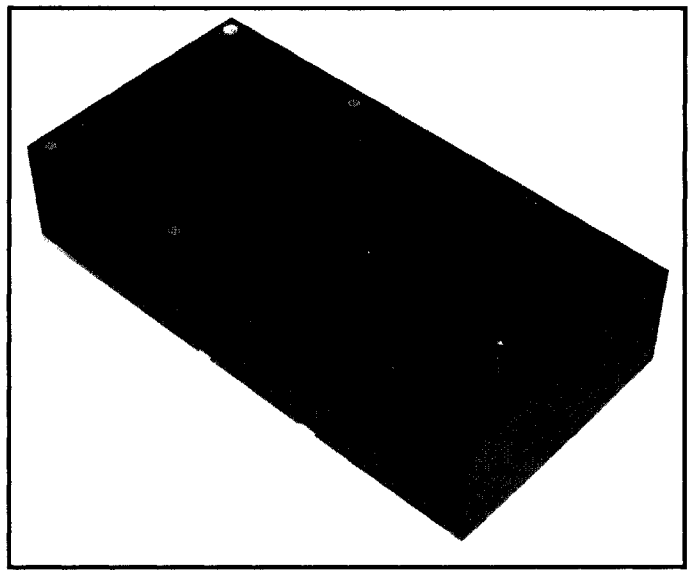

FIGURE 3.6 – Current cuvette. Lenses are inserted on a middle window, and pushed on a dovetail stage between the two fixed windows of the cuvette.

The concern with this mounting scheme is whether or not the lenses can support themselves. There is nothing preventing the lens from sagging in the middle. Yet the lenses do not sag, as verified by the normal transmitted wavefronts produced. Apparently the lenses can support themselves. This is not surprising, given that the majority of the lens is saline. The lenses are in enough of an equilibrium state with the surrounding saline that apparently supporting them is not a problem. A rigorous finite element analysis would have to be performed to unquestionably verify this claim.

The lenses are now reversed in their orientation with respect to the optical axis from the initial cuvette design. Light travels through the test lens opposite how it would on the eye. This means that the measured aberrations of the lens will be different, as this difference in orientation is really just a difference in lens bending, or shape factor. The

power of the lens remains the same. Since the lenses are compared to their respective model's performance, this difference in measured aberrations does not prohibit making measured-to-modeled performance evaluations.

Figure 3.8 shows no means for pumping saline between the cuvette and external holding tank. There is no inherent reason for its absence, and will most likely be added in the future for as much the filtering aspects as for the temperature stability. Also note that the amount of saline exposed to air is greater in this design than in the initial design. A cap is placed over the opening when lenses are not being tested to slow evaporation.

3.4 Automated Lens Centering

With the nonrestrictive mounting scheme used in the current cuvette, centering the lens is important. This does not necessarily mean moving the lens; the test aperture can be moved in software. As long as the center of the lens corresponds to the center of the test aperture, and the entire test aperture is in the field of view of the camera, a successful measurement can be made. The problem is that getting the test aperture and contact lens aligned is a tedious and subjective process. This is especially true for toric lenses, where there are no circular features (i.e. fringes) in the central region of the lens. Also at issue is that the quality of the alignment is subject to operator variation. Wherever possible, the instrumentation and testing algorithms should be independent of the operator. For these reasons, an automated process for centering is desired.

Assuming that the center of the optical zone is concentric with the lens, the problem becomes one of finding the edge of the lens. Luckily, the edge of the lens provides two possibilities for easy identification. First, since the test lens is conjugate with the detector, the test lens is like a field lens in some ways. Only at scattering points on the test lens will there be a noticeable change in the local irradiance at the detector. If the scattering point is slight, that is the ray deviation isn't enough for rays to miss the imaging lens, then a bright spot will appear. If the scattering is more severe, then the scattered light will miss the imaging lens, and that spot on the detector will be dark. If the edge of the lens is a source of strong scattering, then the edge of the lens will appear dark, as it does in Fig. 3.7. This image can then be processed to determine the center of the lens. While Fig. 3.7 looks like a bright field image, it is in fact the summation of four interferograms, with a $\pi/2$ phase step between each interferogram.

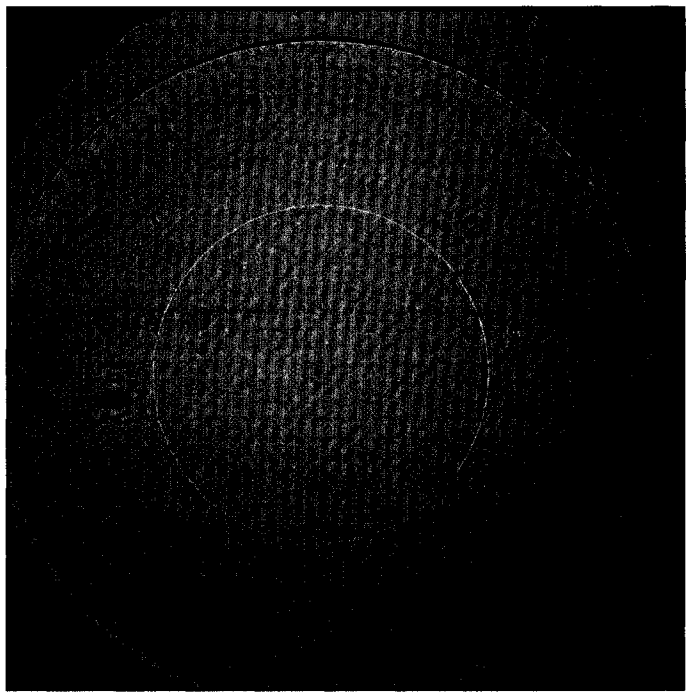

FIGURE 3.7 – Pseudo-bright field image created by summing four interferograms. The dark ring is the edge of the lens where light is scattered out of the imaging lens' aperture. The outermost ring is the edge of the cuvette's window.

The four interferograms are two pairs of interferograms π out of phase. In each pair a pixel with high modulation will sum to the peak of the intensity scale. However, bright spots in both interferograms will sum to twice the peak intensity. Consequently, the majority of the lens, the regions of high modulation, will appear in the middle of the black-to-white intensity scale of the bright field image. Two pairs are used simply for averaging. The central bright ring is the junction between the optical zone and the periphery of the lens. The optical zone is the central portion of the lens where the desired prescription is located. In this case, the scattered light is captured by the imaging lens, so the junction appears bright.

The other possibility, also rooted in the fact that the edge of the lens is a source of scattering, is to unwrap the phase of the entire camera and generate the subsequent modulation map. The edge – dark in all of the interferograms – has very poor modulation. So this map can be processed in a similar fashion to the bright field image to determine the lens center. Using the modulation map shown in Fig. 3.8 may be more robust than using the bright field image due to the better contrast visible in the modulation map. However, this is an extra piece of data that must be computed and stored. The tradeoff is between speed and contrast.

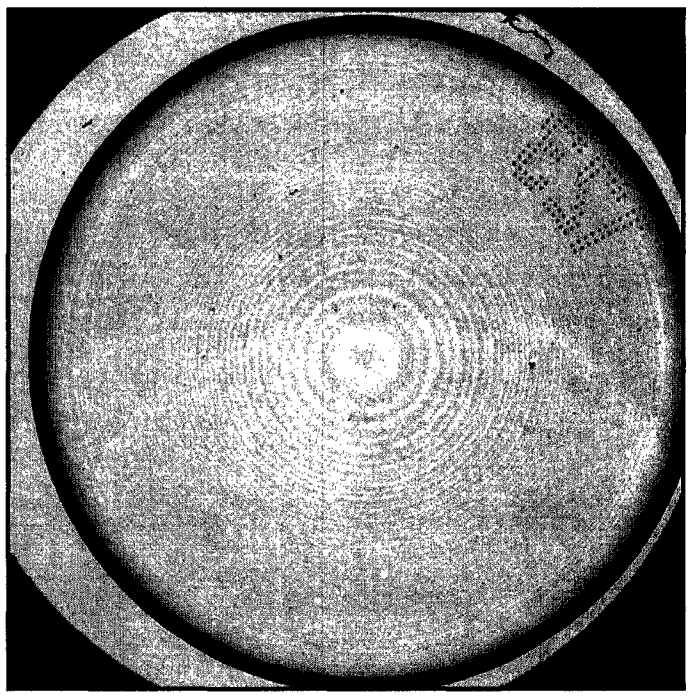

FIGURE 3.8 – Modulation map for soft contact lens.

At this time, neither method is used with CLOVER to provide automated lens centering. Centering is done by hand, using whatever rotationally symmetric features are available. This is part of the future work planned for this instrument.

4 TRANSMITTED WAVEFRONT TESTING OF SPHERICAL GLASS AND CONTACT LENSES

The issues regarding the design and implementation of an interferometer to test contact lenses in transmission have been addressed in the preceding chapters. The following is the treatment, both in general and specific terms, of the output from such an interferometer, with an emphasis on the output from contact lenses. The need for the reverse raytracing calibration process is established first. Once the output is calibrated, the transmitted wavefront can be analyzed in any way desired, including comparisons to modeled wavefronts. Since the emphasis is on ophthalmic optics, the paramount output is the prescription. For spherical lenses, this is simply the power of the lens. Toric and bifocal lenses are more complicated and will be discussed in the next chapter. The majority of the discussion on the induced aberrations and overall performance of CLOVER will be made in units of diopters (D), so that the impact on the ophthalmic prescription is known immediately.

4.1 Detailed Explanation of Testing a Glass Calibration Lens

The explanation starts with the calibration process itself, and what it says about the magnitude of the induced aberrations. A study of the induced aberrations needs to be done to see if they are in fact significantly greater than the errors of the interferometer.

Remembering that there are two possible calibration techniques, reverse raytracing or subtracting a baseline measurement, the need for reverse raytracing must be established.

Going back to the theory of wavefront calibration discussed in Chpt. 2, the operation of reverse raytracing is

$$\begin{aligned}\tilde{W}_T &= \mathrm{Img}^{-1}\left\{W_T + A\left(W_T\right)\right\} \\ &= \mathrm{Img}^{-1}\left\{\mathrm{OPD_T} + \mathrm{Img}\left\{W_R\right\}\right\}.\end{aligned} \qquad \text{Equation 4.1}$$

The idea is to generate an estimate of the transmitted wavefront at the test part ($\tilde{W}_T$) by tracing rays from the sum of the measured OPD ($\mathrm{OPD_T}$) and the image of the reference wavefront ($\mathrm{Img}\{W_R\}$). The process of generating $\tilde{W}_T$ is shown in Fig. 4.1. Alongside each step is a corresponding mathematical expression or equation.

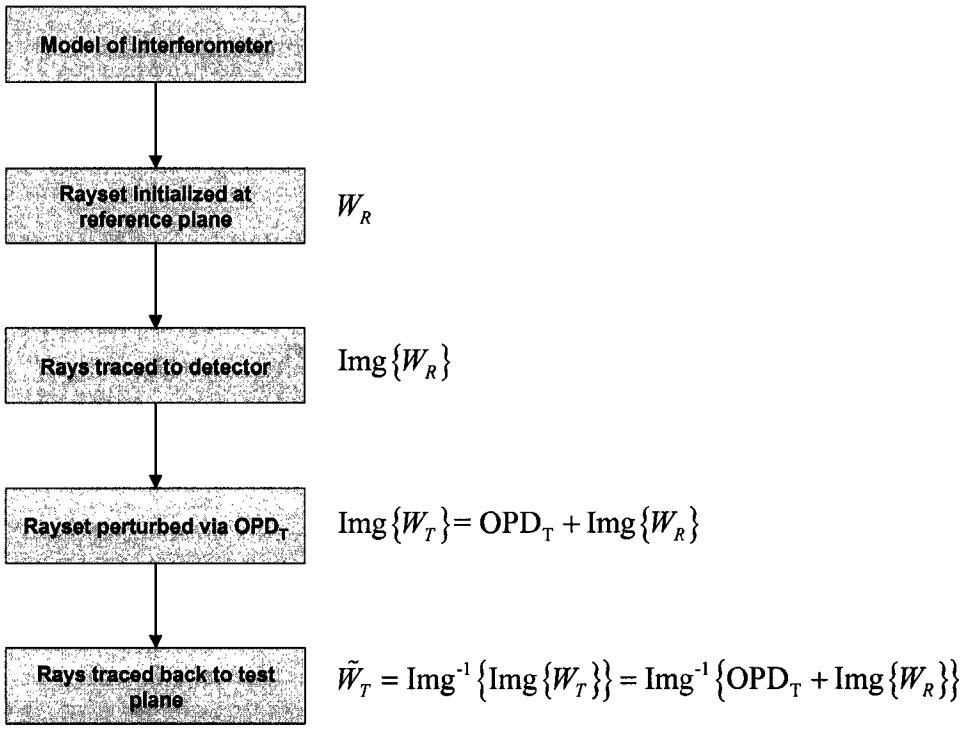

FIGURE 4.1 – Outline of calibration process used to estimate the test wavefront at the test plane.

Figure 4.1 outlines both ray and wavefront descriptions of the calibration process. The transition between the rayset and a wavefront can be done at any location. The wavefronts described here are really the distribution of optical path length across a plane in the interferometer, as mentioned in the introduction to Chpt. 2. To compute a wavefront at any plane, the *OPL* values for the rayset are used. A 2D interpolation is used to put the *OPL* values on a regular grid. This is done in IDL by using the functions **TRIANGULATE** and **TRIGRID**. The *OPL* values on a regular grid are then the discrete representation of the wavefront at the specified plane.

The calibration process starts with a model of the interferometer. The key to this model, and really to the instrument as a whole, is simplicity. The interferometer is designed in such a way that the two arms are identical except for the test optic. The design also has the test wavefront reflecting off the second beamsplitter, minimizing the influence of the beamsplitter on the wavefront. In keeping the model simple, catalog values for elements are used. Along with the design of the interferometer, this allows for the exclusion of all the nominally planar surfaces from mirrors and beamsplitters. The second beamsplitter would have to be included if the test wavefront passed through it. The benefits of eliminating the planar surfaces include the lack of needing coordinate breaks and faster raytracing speeds. The resulting model contains only the test optic and imaging lens.

The specific implementation of the model in IDL can be seen in Appendix A. The model is twofold in that it describes the reference and test arms at the same time, surface-by-surface. Each surface is listed twice; the first listing is the reference arm, the second listing is the test arm. In keeping with the design of the interferometer, all distances are identical between the two arms.

The next step in the calibration process is initializing a rayset in the reference plane. The reference plane is the plane in the reference arm that is conjugate with the detector, as shown in Fig. 4.2 on a simple Mach-Zehnder interferometer.

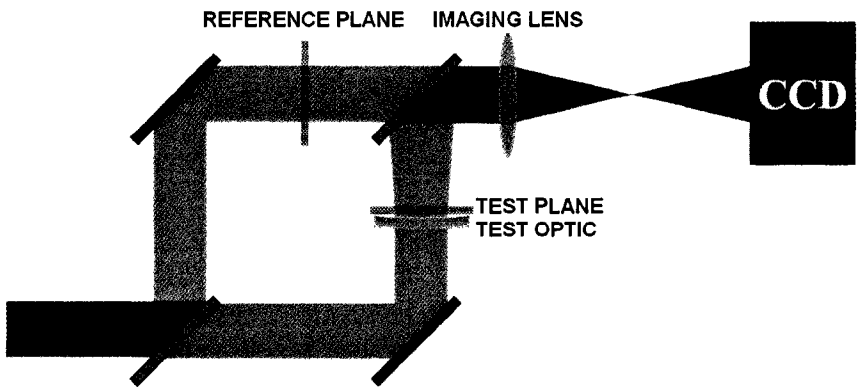

FIGURE 4.2 – Mach-Zehnder interferometer with labeled test and reference planes.

The test plane, being the more important plane to place, dictates the location of the reference plane. The most common location for the test plane in a transmission test is immediately behind the test optic. This is the case with CLOVER. The sample model shows that the test plane is 1 μm beyond the test optic.

The reference plane is the origin for the rays that will be traced to the detector, then back to the test plane. At the reference plane, the ray direction cosines and *OPL* values are all set to 0. A square pattern is used to position the rays. This is done simply out of convenience.

The next step is tracing the rays to the detector. This is done in a straightforward manner, and the resulting wavefront, $\mathrm{Img}\{W_R\}$, is shown in Fig. 4.3. The number of rays traced is specified by 201 rays across the diameter.

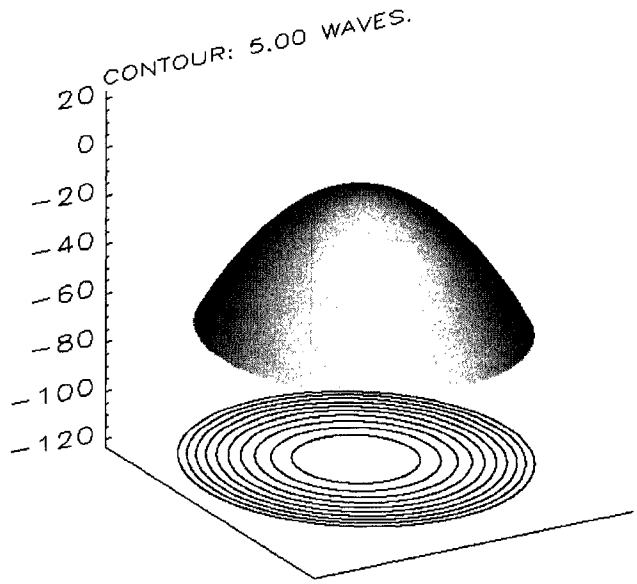

FIGURE 4.3 – Image of the reference wavefront (Img$\{W_R\}$).

A common misconception is to assume that the reference wavefront at the detector is flat since it is the image of a planar wavefront. This misconception comes from treating the wavefront in the reference plane as a traditional object. The term traditional object refers to an object that is the summation of point sources. With normal, or collinear imaging, each point source emits a wavefront that fills the aperture stop, and is imaged to a point in the image plane (Born, 1980). The source of the wavefront is in the object plane. This is not the case for the interferometer.

In the interferometer, the reference plane contains a planar wavefront. This wavefront is converging to an image point that is infinitely far away, as the source for this wavefront is the illuminated pinhole that is coincident with the front focal point of the collimating lens. The imaging lens, seeing a collimated beam, focuses the light at its rear focal point.

This bright spot at the rear focal point is the image of the illuminated pinhole. The detector is well beyond the focal point of the imaging lens, and so the reference wavefront in the plane of the detector is necessarily diverging. The curvature of the wavefront corresponds to the distance from the focal point of the imaging lens to the detector. This situation of imaging a planar wavefront is illustrated in Fig. 4.4.

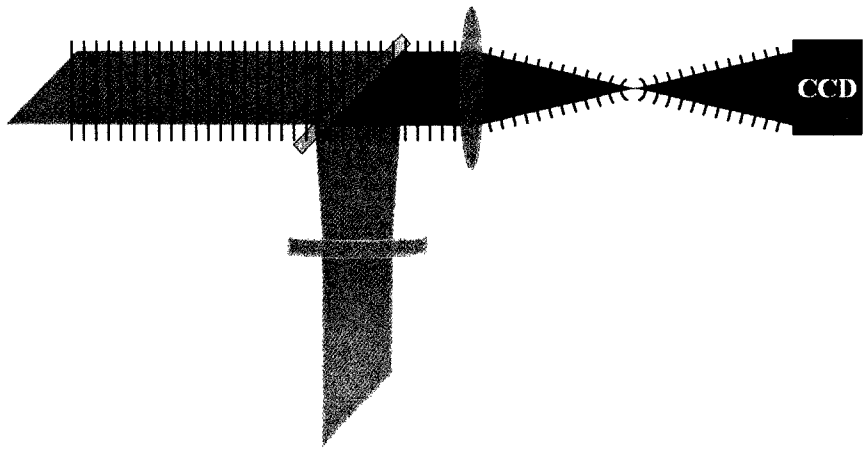

FIGURE 4.4 – Portion of a Mach-Zehnder interferometer illustrating the relationship between the reference wavefront and its image.

The next step, as outlined in Fig. 4.1, is to perturb the rayset using the measured OPD. In simple terms, the measured OPD is the difference in optical path between the two wavefronts interfering at the detector. As a reminder, the relationship between the two wavefronts and the OPD is

$$\mathrm{OPD_T} = \mathrm{Img}\{W_T\} - \mathrm{Img}\{W_R\}. \qquad \text{Equation 4.2}$$

Note that this convention – test minus reference – is consistent with general aberration theory (Shannon, 1997). Data transfer between Intelliwave and IDL is done by saving the data in Intelliwave in a native IDL format. Before the OPD data is used to perturb the

rays, a mask of bad pixels is created. An uncommon approach is taken to identifying bad pixels. Experiments showed that most bad pixels were due to debris in the saline solution. The debris is usually over several pixels, all of which should ultimately be deemed bad pixels. One would expect the pixels containing debris to have a low modulation and to be removed in a simple algorithm that thresholds the modulation map. This was shown not to be the case, for the pixels only partially blocked by the debris would have a fairly high modulation. Raising the threshold on the modulation map causes more pixels in good regions of the interferogram to be labeled as bad pixels. The speckled or spotty nature of the mask is not improved by raising the modulation threshold. The ideal algorithm is one that allows the modulation threshold to remain low, and then enlarges the bad pixel regions to encompass nearby pixels. This is the algorithm used with CLOVER, and is accomplished by using the **ERODE** function in IDL. Figure 4.5 shows (a) an interferogram along with (b) the bad pixel mask due to modulation alone and (c) the enhanced bad pixel mask. The fringes of the interferogram make the debris stand out more then they do in the modulation map or unwrapped wavefront.

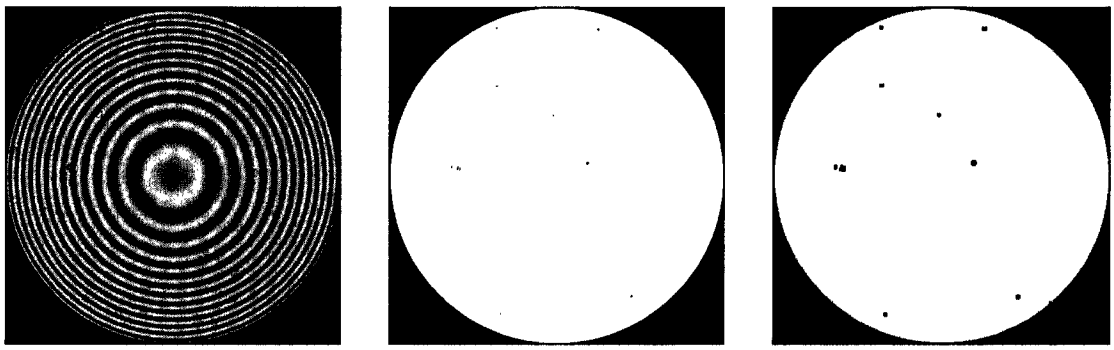

(a) (b) (c)

FIGURE 4.5 – Bad pixel identification by eroding regions of poor modulation: (a) typical interferogram, (b) bad pixel mask due to modulation only, and (c) enhanced bad pixel mask.

The bad pixel mask is used in the ray perturbation. The perturbation is done by fitting over a window of pixels (typically 9 x 9), as outlined in Chpt. 2. If not enough good pixels exist in the window, then the perturbation is not performed and the corresponding rays are dropped from the rayset. In this way, the bad pixels associated with the surface can be used to drop rays from the rayset. Remember that the final quantity sought is the test wavefront at the test plane, which will come from the rayset at the test plane. The OPD is really just part of the tool used in determining the rayset at the test plane. Whenever the rayset is converted to a wavefront, the interpolation produces a wavefront with no missing data. In the big picture, the notion of bad pixels in the OPD is inconsequential.

Once the test rays have been perturbed, but before they are propagated, a wavefront can be made from the rays. Generating this wavefront serves as a check on the consistency of the calibration process. This generated wavefront is the image of the test wavefront

(Img$\{W_T\}$), and should be consistent with the modeled reference wavefront and measured OPD. The image of the test wavefront produced by a glass calibration optic is shown in Fig. 4.6. Table 4.1 gives the prescription for the calibration optic, showing that this is about a +6.5 D lens in air. Testing is done over the central 5 mm of the calibration optic immersed in saline in a cuvette. Testing is done over a 5 mm aperture because this is the ANSI standard for contact lenses (White, 1998), and is the size aperture over which the sponsor wishes to evaluate lenses. This is the same optic responsible for the interferogram and pixel masks in Fig. 4.5.

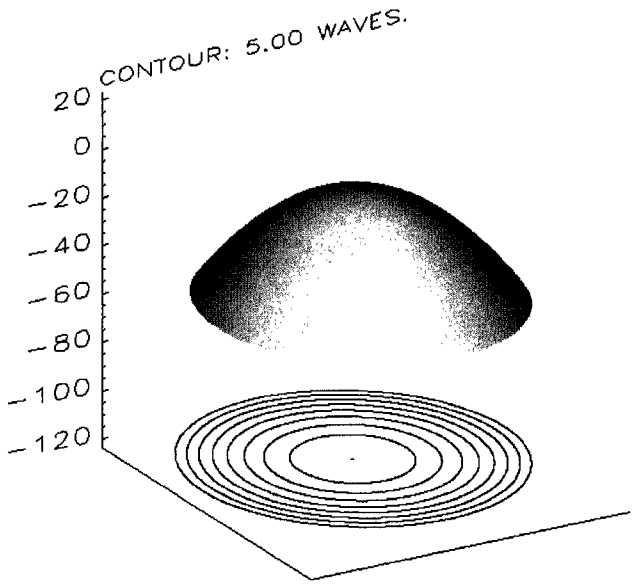

FIGURE 4.6 – Image of the test wavefront produced by the calibration optic specified in Table 4.1.

First Surface Curvature (mm^{-1})	0
Second Surface Curvature (mm^{-1})	-0.012815
Thickness (mm)	2.750
Index of Refraction	1.5128
Gaussian Power (D)	6.57

TABLE 4.1 – Parameters for calibration optic.

To check the consistency of the calibration process, the two images of the interfering test and reference wavefronts can be subtracted, giving back what should be OPD_T. This is simply carrying out the math of Eq. 4.2. Figure 4.7 shows (a) the difference between the two imaged wavefronts and (b) OPD_T for the calibration lens.

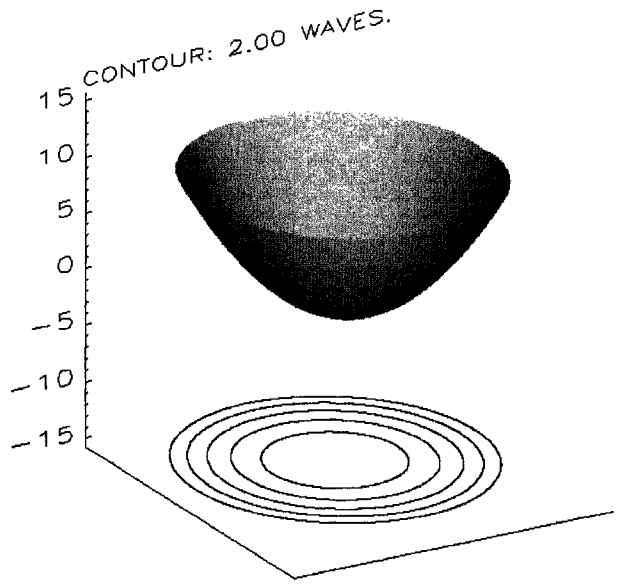

(a)

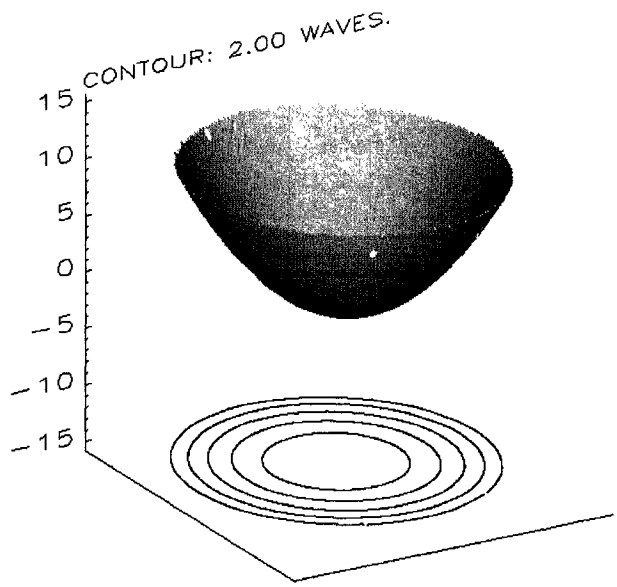

(b)

FIGURE 4.7 – Check on the generation of the wavefronts:
(a) Img$\{W_T\}$ – Img$\{W_R\}$ and (b) OPD_T.

The most noticeable difference between the two wavefronts is that OPD_T shows missing pixels while Img$\{W_T\}$ – Img$\{W_R\}$ is not missing data. This is because each imaged

wavefront, formed by interpolating a rayset, contains no regions of missing data. A far more subtle difference, one that may not even be ascertainable with the above images, is that the difference of the imaged wavefronts is smoother than OPD_T. The two surfaces have different spatial resolutions. OPD_T is sampled pixel-by-pixel, while the wavefronts are sampled ray-by-ray. For measurements made with CLOVER, imaged wavefronts of this size will cover over 700 pixels, while the rayset samples at 201 rays across the diameter.

The obvious final step in checking the calibration process is to subtract the two surfaces shown in Fig. 4.7. The ideal result is a plane. However, the plane will not necessarily be at zero waves along the vertical axis because the two surfaces may have different amounts of piston. Figure 4.8 shows the difference between the two surfaces, where the vertical axis is in waves.

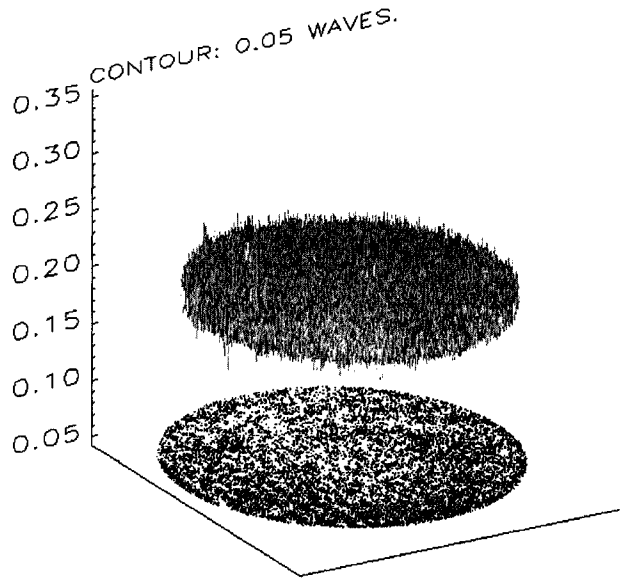

FIGURE 4.8 – Difference between Img$\{W_T\}$ – Img$\{W_R\}$ and OPD_T.
The ideal result is a plane.

The difference certainly appears to be planar, but the general shape is obscured by high frequency noise. This noise comes from a variety of factors, including the difference in spatial sampling between the two surfaces, all detector noises, and the inhomogeneity in index of the saline surrounding the test optic (this is a test of the calibration lens in the cuvette). Plots of single rows or columns show that the amplitude of the noise is about $\lambda/50$. A variety of techniques could be used to alleviate this problem; Zernike fitting provides a nice solution. Not only does Zernike fitting remove the high spatial frequency noise, but the Zernike coefficients can be used to compute aberration information about the wavefront (Wyant, 1992). The 36-term Zernike fit, using the Fringe or University of Arizona ordering, is shown in Fig. 4.9 (Focus Software, 2000). Note that the resolution on the vertical axis scale has been increased.

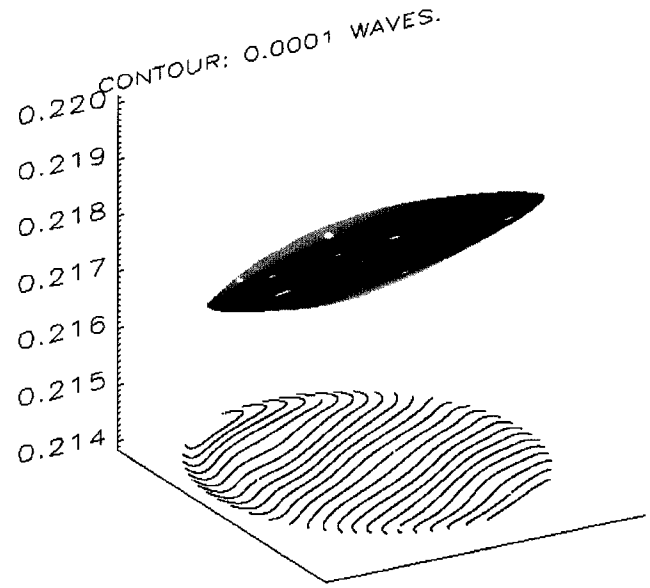

FIGURE 4.9 – Zernike fit to difference between Img$\{W_T\}$ – Img$\{W_R\}$ and OPD_T.

The Zernike fit reveals that the dominant aberration is tilt. This tilt is assumed to be artificial due to a lack of centering between the two surfaces. Small displacements between two spherical surfaces that are subtracted result in a linear term. As the displacement grows a cubic term will appear. The centering between the surfaces in CLOVER is done by computing the centroid for the surfaces and then shifting one surface until the centroids match. This method gives about tenth-pixel accuracy. Removing the erroneous tilt gives a better feel for the magnitude of the difference between the two surfaces in question, as shown in Fig. 4.10. Again note the increase in the vertical resolution.

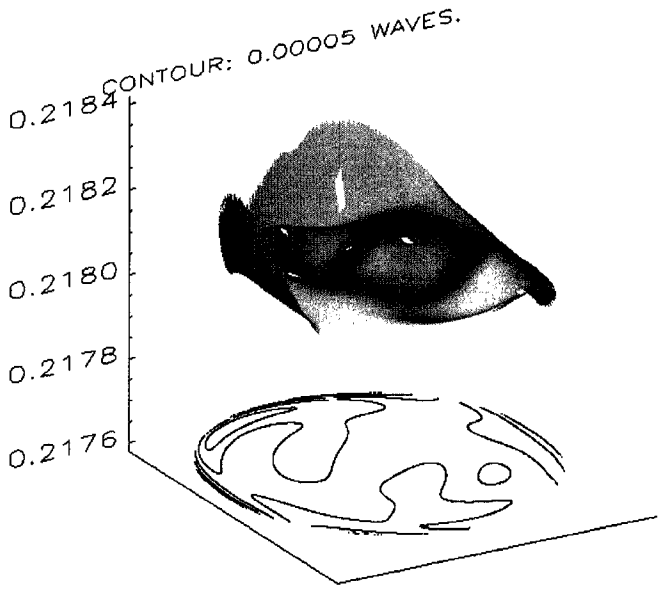

FIGURE 4.10 – Zernike fit to difference with tilt removed. The PV of this surface is 0.00038 λ, while the RMS is 0.000031 λ, or about 17 picometers.

This level of accuracy is well beyond other sources of error, and so the conclusion is that the inferred image of the test wavefront is in agreement with the modeled image of the reference wavefront and the measured OPD.

The final step is to estimate the test wavefront at the test plane via reverse raytracing. In theory, this removes the induced aberrations due to imaging the wavefront. For the given test optic, the calibrated test wavefront is in Fig. 4.11.

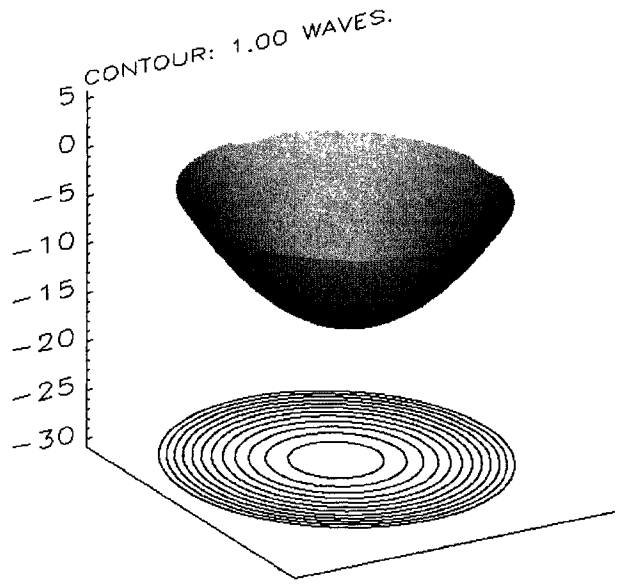

FIGURE 4.11 – Measured wavefront ($\tilde{W}_T$) for the calibration lens.

Note that this wavefront looks more like the wavefronts of Fig. 4.7, the measured OPD, than the image of the test wavefront shown in Fig. 4.6. In fact, the wavefront and its image have different concavities. This occurs for the same reason why the image of the planar reference wavefront is not planar. Figure 4.12 shows a representative imaging lens and detector for an interferometer operating in a non-null condition. The solid line represents the reference wavefront while the dashed lines are two possible test wavefronts.

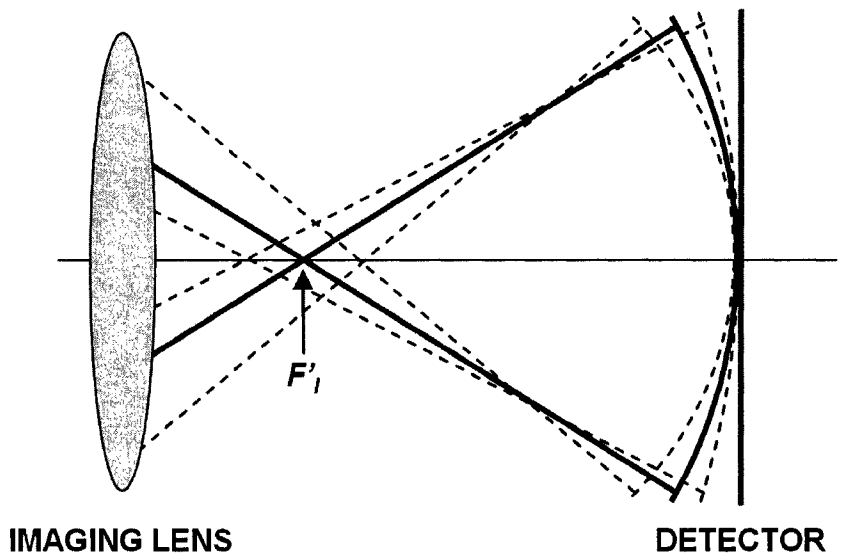

FIGURE 4.12 – Positive and negative powered test beams (dashed) with respect to the planar reference beam (solid). The reference beam comes to focus at the rear focal point for the imaging lens (F'_I).

A converging test beam, produced by an optic with positive power, will come to focus before the reference beam. At the detector, this beam will have less sag across the same diameter as the reference beam. A diverging test beam will come to focus after the reference beam and have more sag than the reference beam at the detector. But for both converging and diverging test beams leaving the test optic, the beam at the detector will be diverging.

At this point, the impact of reverse raytracing can be quantified. The goal is to compare the levels of the induced aberrations and baseline measurement. The best surfaces to use to judge the magnitude of the induced aberrations are the surfaces from the difference

between the two imaged wavefronts and the calibrated test wavefront. The difference between the imaged surfaces gives

$$\begin{aligned}\mathrm{Img}\{W_T\} - \mathrm{Img}\{W_R\} &= W_T + A(W_T) - (W_R + A(W_R)) \\ &= W_T - W_R + (A(W_T) - A(W_R)).\end{aligned} \qquad \text{Equation 4.3}$$

This difference is $\mathrm{OPD_T}$ to the level of accuracy demonstrated in the preceding check on the formation of the imaged wavefronts. So this difference represents the OPD at the detector. The OPD in the test plane is the difference between the estimated $\tilde{W}_T$ and the assumed $\tilde{W}_R$. Since $\tilde{W}_R$ is assumed to be zero, the OPD in the test plane is just the calibrated test wavefront. The compassion is therefore made between the OPD at the detector and the OPD at the test plane. To summarize:

$$\begin{aligned}\mathrm{OPD}_{\mathrm{T\ @\ Detector}} &= W_T - W_R + (A(W_T) - A(W_R)), \\ \mathrm{OPD}_{\mathrm{T\ @\ Test\ Plane}} &= \tilde{W}_T.\end{aligned} \qquad \text{Equation 4.4}$$

Figure 4.13 shows the two OPD surfaces, and Table 4.2 gives the PV, RMS, and measured power numbers (in-air equivalent) for the two surfaces. The measured power is determined from the Zernike coefficients corresponding to a 36-term fit to the surface.

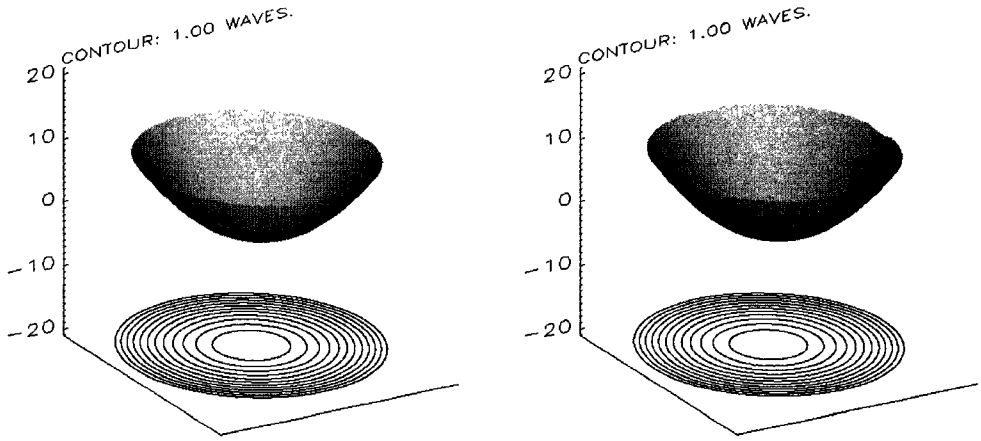

(a) (b)

FIGURE 4.13 – Comparison of OPD surfaces for the purpose of determining the level of induced aberrations: (a) $OPD_{T\ @\ Detector}$ and (b) $OPD_{T\ @\ Test\ Plane}$.

OPD SURFACE	PV (λ)	RMS (λ)	POWER (D)
$OPD_{T\ @\ Detector}$	12.364	3.548	6.646
$OPD_{T\ @\ Test\ Plane}$	12.981	3.734	6.515
DIFFERENCE	0.617	0.186	0.131

TABLE 4.2 – PV and RMS values for the two comparable OPD surfaces.

Over the same sized aperture, the baseline measurement gives a PV of 0.090 λ and an RMS of only 0.010 λ, as stated earlier in Chpt. 2. The need for reverse raytracing over simply removing a baseline measurement is now evident. The difference RMS from the calibration optic, whose power is in the lower half of the desired measurement range for CLOVER, is a factor of 18 greater than the RMS for a baseline measurement. The difference in the computed power represents 2% of the power of the calibration lens.

A subtle, but important, point to make is that the above numbers regarding the induced aberrations for the calibration lens are not the magnitude of the aberrations, but rather the magnitude of the difference of the aberrations. Taking a closer look at Eq. 4.4, the substitution of W_R equaling zero can be made in the top equation, giving:

$$\begin{aligned} \mathrm{OPD}_{\mathrm{T\,@\,Detector}} &= W_T + \left(A(W_T) - A(W_R)\right), \\ \mathrm{OPD}_{\mathrm{T\,@\,Test\,Plane}} &= \tilde{W}_T. \end{aligned} \qquad \text{Equation 4.5}$$

The term present in the top equation that is not present in the bottom equation is the difference in induced aberrations between the test and reference wavefronts. The magnitude of either aberration is not known. While W_R is assumed to be zero, $A(W_R)$ cannot be assumed to be zero as well. A planar wavefront is not excused from picking up aberrations while passing through the imaging lens. Modeling could be done to determine the level of the aberration, but that misses the main point: the difference in the induced aberrations is all that matters with regards to calibrating the test wavefront.

With the calibration process complete and justified, the next point to take up is the comparison of the measured wavefront to a modeled wavefront. This moves the analysis towards answering the ultimate question: does the test optic perform as modeled? Figure 4.14 shows the complete analysis routine, generating both measured and modeled wavefronts. Note that the entire calibration process of reverse raytracing is but one step in the complete analysis algorithm.

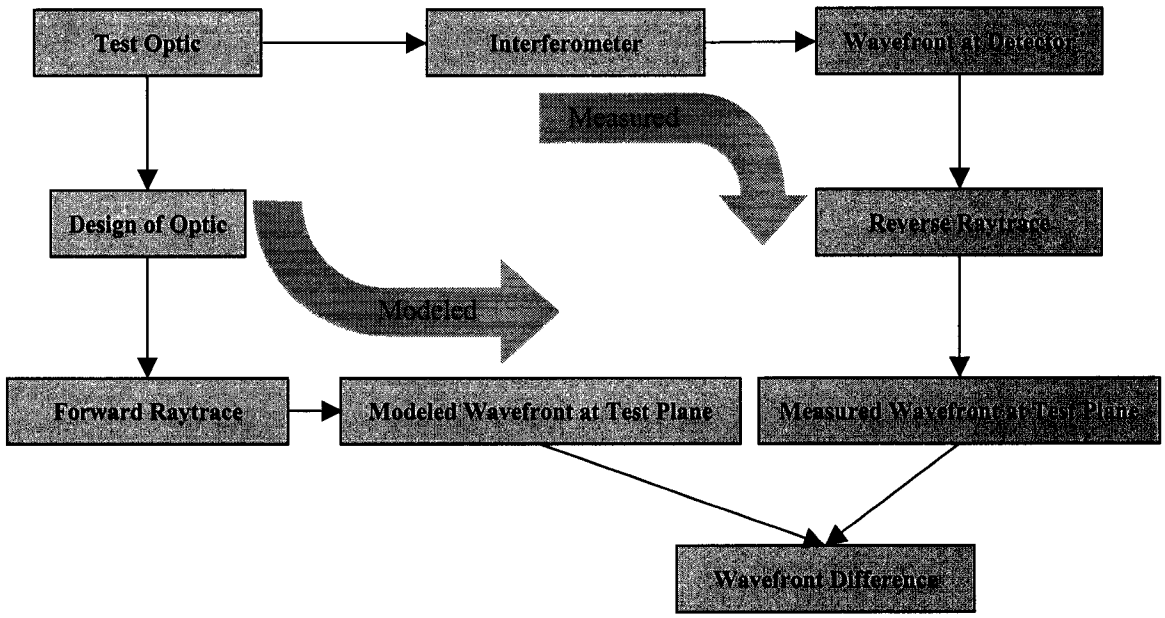

FIGURE 4.14 – Complete analysis routine for comparing measured-to-modeled performance.

There are two paths for the analysis routine: measured and modeled. The measured path had already been analyzed. This is the collecting of OPD data to produce the test wavefront at the detector, then calibrating that wavefront via reverse raytracing to estimate the wavefront at the test plane. The modeled path takes the design of the optic and performs a forward raytrace through the design of the test optic inserted into the design for the interferometer, stopping at the test plane. This produces the modeled wavefront at the test plane. The final step is to compare the measured and modeled wavefronts by subtracting the two surfaces, forming a wavefront difference. This difference is then analyzed and used to quantify the answer to the question of whether or not the optic performs as modeled.

The model of the interferometer is used in both paths. This illustrates the importance that the model plays in the overall analysis. Because the model is used both to calibrate measured data and to compute modeled data, the model must be accurate. As mentioned earlier, the key to the model is simplicity. By limiting the number of surfaces and parameters in the model, a high level of accuracy is achieved. The role of simplicity in hardware design and instrument calibration should not be overlooked.

Using the complete analysis routine on the calibration optic, the prescription for the lens (Table 4.1) is inserted into the model of the interferometer (see Appendix A) and the modeled wavefront at the test plane produced. The modeled wavefront ($W_T{}^M$) is in Fig. 4.15.

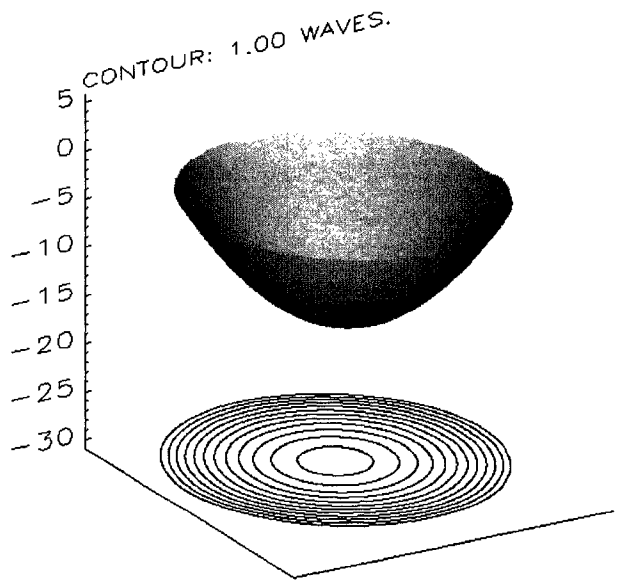

FIGURE 4.15 – Modeled wavefront ($W_T{}^M$) for calibration lens.

The final step in the complete analysis routine is the subtraction of the measured and modeled wavefronts, forming a wavefront difference surface. The operation of subtraction is not as straightforward as it seems. The two wavefronts are contained in rectangular 2D arrays in IDL. These arrays must be made the same size for pixel-by-pixel subtraction to work. Furthermore, the wavefronts are circular, and so their size and location within the 2D array must be made the same as well. Due to the pixilated edges of the circular data, the wavefront difference surface is reduced by 1% in diameter to avoid edge effects. While these are just software issues, performing these operations in such a way as to not jeopardize the integrity of the data is important. The wavefront difference for the measured and modeled wavefronts is in Fig. 4.16.

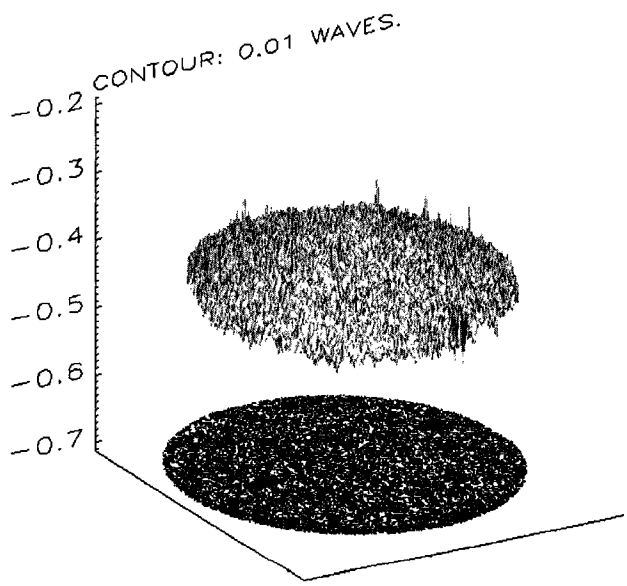

FIGURE 4.16 – Measured minus modeled ($\tilde{W}_T - W_T^M$) wavefront difference for calibration lens.

The wavefront difference suffers from the same problem that the check on the formation of the imaged wavefronts does: high frequency noise. This will be true for all wavefront differences, and so the Zernike fit to the difference is the quantity of interest. The Zernike fit to the above wavefront difference surface is in Fig. 4.17.

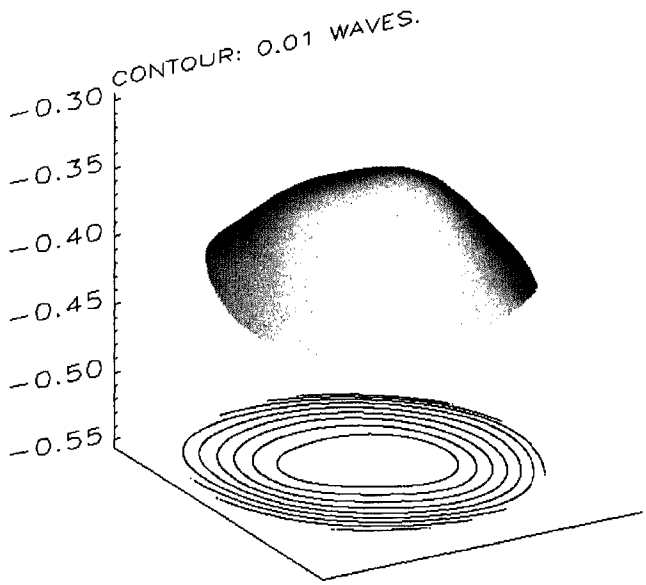

FIGURE 4.17 – Zernike fit to the measured minus modeled wavefront difference.

The wavefront difference is primarily power, or defocus. A difference in power like this is most likely due to a discrepancy in the difference in index for the immersed test optic and saline solution versus the values used in the model. For the data presented, the difference in index is 0.1772. Any error in this number will result in erroneous power in the wavefront difference.

How much of an error in index would it take to produce the power measured in the wavefront difference? This question goes back to the discussion in Chpt. 3, where this same question was asked with regards to determining the index for hydrogels. The answer can be determined by using the Zernike coefficients to produce the power of the wavefront difference. For the given wavefront difference, the power is -0.004 D. This is the power in saline; in air, the power becomes -0.011 D. Using this value and the power of the lens (+6.529), the percent error is 0.17%. So the error in the index difference is only 0.17% of 0.1772, or 0.0003. The divisions of the Abbe refractometer used are at 0.0005, giving a resolution of about 0.0003. Since this matches the error in index needed to account for the power of the wavefront difference, the claim that the power error can be attributed to a discrepancy in index is credible. Also note that the difference in power of 0.17% is a factor of six better than the 1% condition that describes normal conditions (Shannon, 1997). Even with the likely index discrepancy, a pass/fail condition of 1% would pass this lens.

The results from this one measurement lead to important conclusions. First, there is a need for reverse raytracing. The wavefront RMS removed via reverse raytracing is 18 times the wavefront RMS for a baseline measurement. So for any lens of consequential power, reverse raytracing will provide a better estimate of the test wavefront than subtracting a baseline measurement. Furthermore, the calibration technique works well enough that the difference between measured and modeled data can be explained single-handedly by the uncertainty in index. Finally, the discrepancy in index is probably not

large enough to alter the results of comparing lenses against a 1% criterion on power between measured and modeled data.

4.2 Study on Repeatability

The repeatability of CLOVER is an important parameter to the sponsor. Repeatability addresses the random errors associated with testing the same lens, on the same instrument, by the same operator, over a short time interval (White, 1998). A common measure of repeatability is the ratio between the random errors and the tolerance of the quantity measured. Since repeatability is a measure of the instrument's precision, this ratio is called the precision-to-tolerance (P/T) ratio. The sponsor desires a P/T ratio of 30%, where the precision is taken to be the 3σ point of the measured data. The quantity measured is the power of the lens, calculated from Zernike coefficients, at the test plane. The ANSI standard for the tolerance on power is ±0.25 D for all lenses up to ±10.00 D. Combining these criteria gives:

$$\begin{aligned} \frac{P}{T} &= \frac{3\sigma}{T}, \\ 30\% &= \frac{3\sigma}{0.25}, \\ \therefore \sigma &= 0.025 \text{ D} \end{aligned} \qquad \text{Equation 4.5}$$

A study was done where the calibration lens was tested ten times, both in air and in the cuvette surrounded by saline. The hypothesis was that the measurements made with the cuvette would have a higher variance because they are multiplied by the solution factor to get the equivalent in-air power. Plus, the saline inhomogeneity and possible cuvette

errors combine to increase the random errors of the measurement. Table 4.3 lists the measured standard deviation (in-air equivalent) and the corresponding P/T ratio.

Testing Condition	σ (D)	P/T (%)
Lens in Air	0.0041	4.9
Lens in Cuvette	0.0095	11.4

TABLE 4.3 – Repeatability study on CLOVER using the calibration lens. Data was collected over ten trials.

As predicted, the variance for testing the lens immersed is higher than testing in air. The P/T ratio in air is only half that for immersion testing. Yet in both cases, the P/T ratio meets the needs of the sponsor by at least a factor of two.

4.3 Testing Other Spherical Glass and Contact Lenses

To push the limits of the interferometer, a -20 D glass lens was tested in air. A contact lens of over -100 D would be needed to produce the same OPD. Testing was done over a 3 mm aperture to avoid aliasing. The interferogram over the test aperture is in Fig. 4.18.

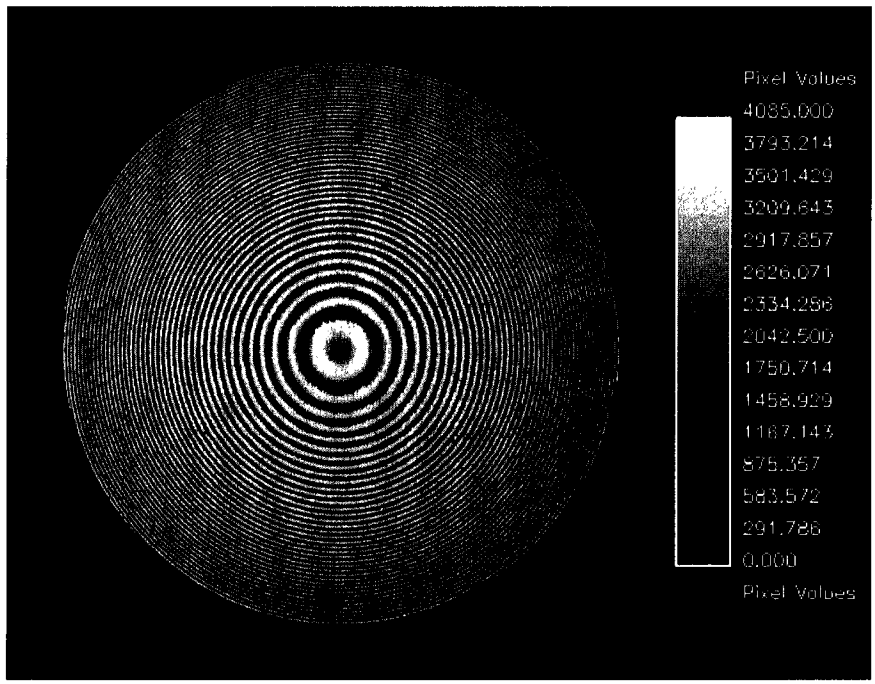

FIGURE 4.18 – Interferogram of -20 D glass lens in air over 3 mm.
The departure for this interferogram is 41.36 λ.

The Zernike fit to the wavefront difference is in Fig. 4.19. The power of this surface is -0.269 D. The measured power is -20.115 D, while the modeled power is -19.855 D. The difference between these two powers is -0.260 D, showing that the powers are in agreement with the wavefront difference. The wavefront difference power represents 1.3% of the modeled power, a much higher error than the 0.17% for the calibration lens. An investigation into this discrepancy follows.

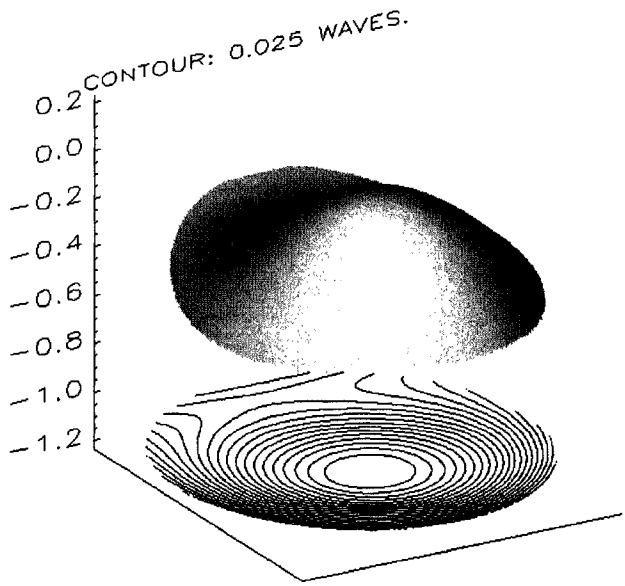

FIGURE 4.19 – Zernike fit to wavefront difference for -20 D lens.

The accuracy of the model is checked first. Satisfied that the model is okay, the next item to consider is the wavefront difference surface. The surface shows that the difference is primarily power, but there is a strong upslope to the surface at one edge. This is indicative of coma. However, there are a couple of reasons why coma may be present, one of which is a misalignment between the measured and modeled surfaces when subtracted. To show that the coma is in fact due to the measured data, the measured wavefront is shown in Fig. 4.20 with tilt and focus removed.

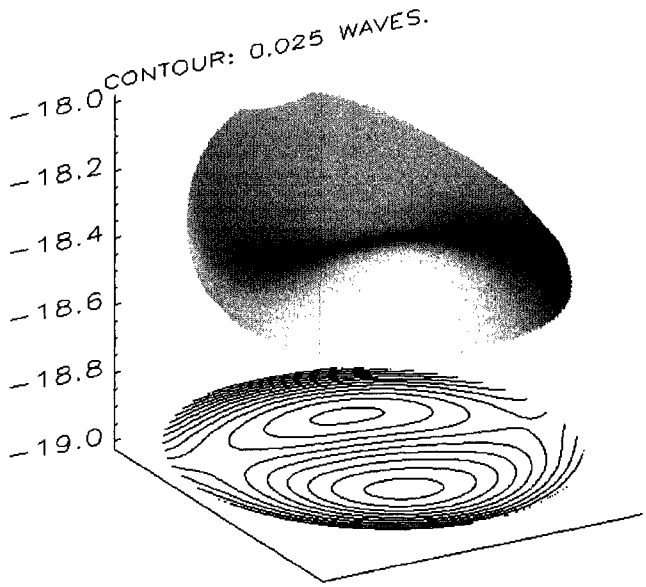

FIGURE 4.20 – Measured wavefront ($\tilde{W}_T$) minus tilt and focus.

Clearly there is coma in the measured wavefront. The erroneous coma will change the determined average curvature for the measured data. Since the modeled wavefront has no coma, the presence of coma accounts for the difference between the measured and modeled powers. To be sure that coma was not introduced during the calibration process, the OPD from Intelliwave can be analyzed for the presence of coma. Figure 4.21 shows the OPD from Intelliwave with tilt and focus removed.

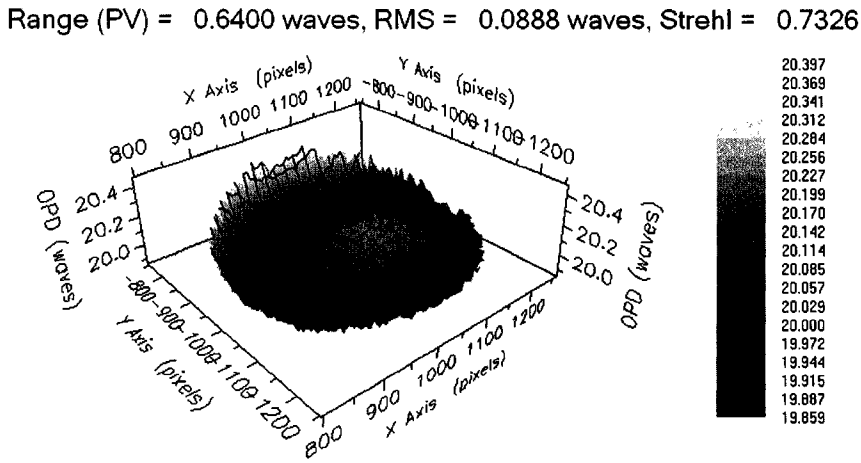

FIGURE 4.21 – Measured OPD from Intelliwave minus tilt and focus.

The similarities in shape and PV indicate that the coma originated with the measured data, and exists due to the hardware. This leads to questioning the alignment of the test part with the interferometer.

Modeling is necessary to determine the amount of tilt necessary to produce the given wavefront difference error. In Zemax, modeling was done by using two configurations, with the difference being field angle. The PV output from Zemax's **INTERFEROGRAM** was monitored until it matched the PV of the wavefront difference. Since the wavefront difference is void of any noise, comparing PV numbers is not as dangerous as it would be with noisy data. The result of the modeling is that a tilt of 3.99° would give the same PV. While not a complete analysis, this answer does indicate that the tilt necessary could have been present in the setup. In mounting the lens, the mount is checked for parallelism using a bubble level on an exterior surface. The lens

sits on a different surface buried in the mount, and the possibility for such a tilt is possible. The overriding conclusion is that the coma is probably not a defect in the lens, but rather comes from how the lens was mounted.

Moving on to contact lenses, the interferogram over the central 5 mm for a lens with a labeled power of -10.0 D is in Fig. 4.22. Figure 4.23 shows the Zernike fit to the wavefront difference.

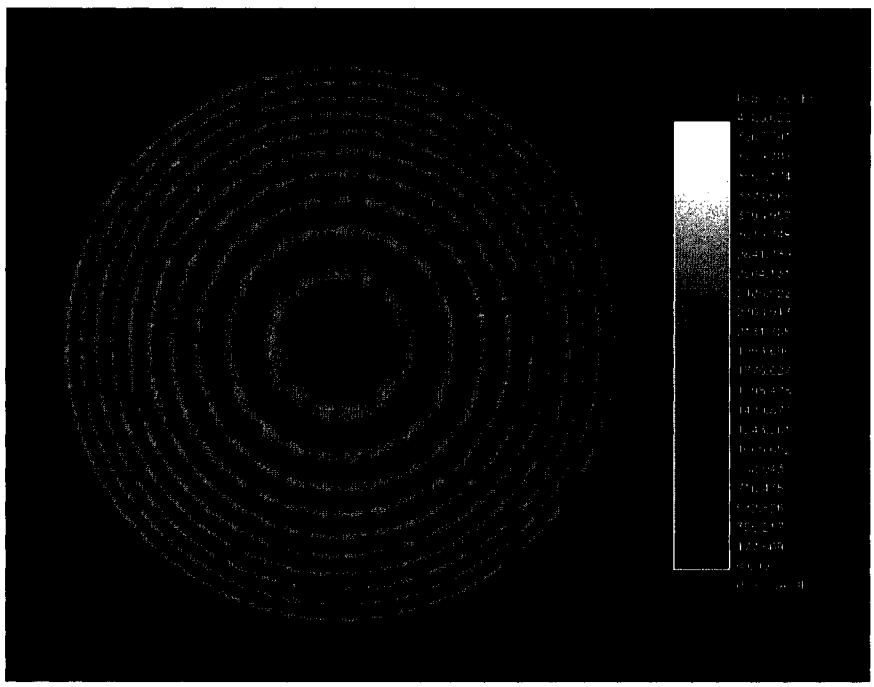

FIGURE 4.22 – Interferogram of -10 D contact lens over 5 mm.

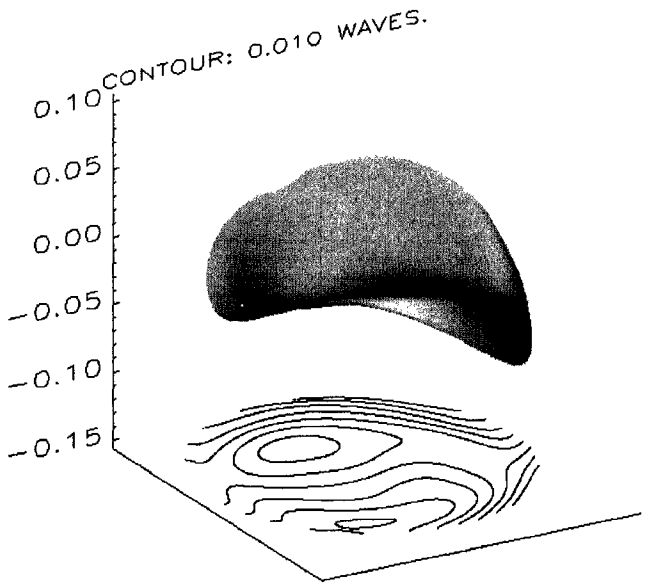

FIGURE 4.23 – Zernike fit to wavefront difference for -10 D contact lens over 5 mm.

The power of the wavefront difference is 0.005 D. The measured power is -10.005 D, while the model gives -9.999 D. This gives the remarkably low percent error of 0.06%. The success of this measurement is due solely to the agreement between the stated measured and modeled powers, and not the agreement between these powers and the labeled power of -10 D. Comparisons are always made between the measured and modeled powers derived from Zernike fits to the respective wavefronts.

One of the many interesting aspects to contact lenses is that they have a lot of spherical aberration. The lens bending or shape factor of these lenses, necessary to fit on the eye, puts them far from the shape for minimizing spherical aberration. Figure 4.24 shows the measured wavefront with tilt and focus removed. The residual surface is dominated by

negative spherical aberration. Summing the Zernike terms that contain ρ^4 terms places the spherical aberration at -1.65 λ.

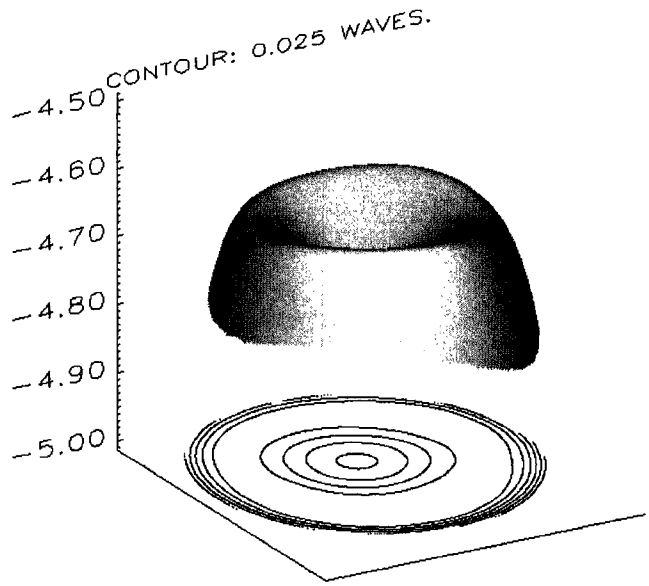

FIGURE 4.24 – Measured wavefront for -10 D contact lens with tilt and focus removed.

4.4 Testing Over the Complete Aperture of Contact Lenses

The current cuvette design allows for complete lens testing. As long as the fringe spacing does not exceed the Nyquist limit, there is no reason why the wavefront cannot be determined outside the optical zone. The only possible complication could be the junction at the optical zone, where the modulation is low (see Fig. 3.9). Figure 4.25 contains one of the captured full interferograms for the -10D lens analyzed in the last section.

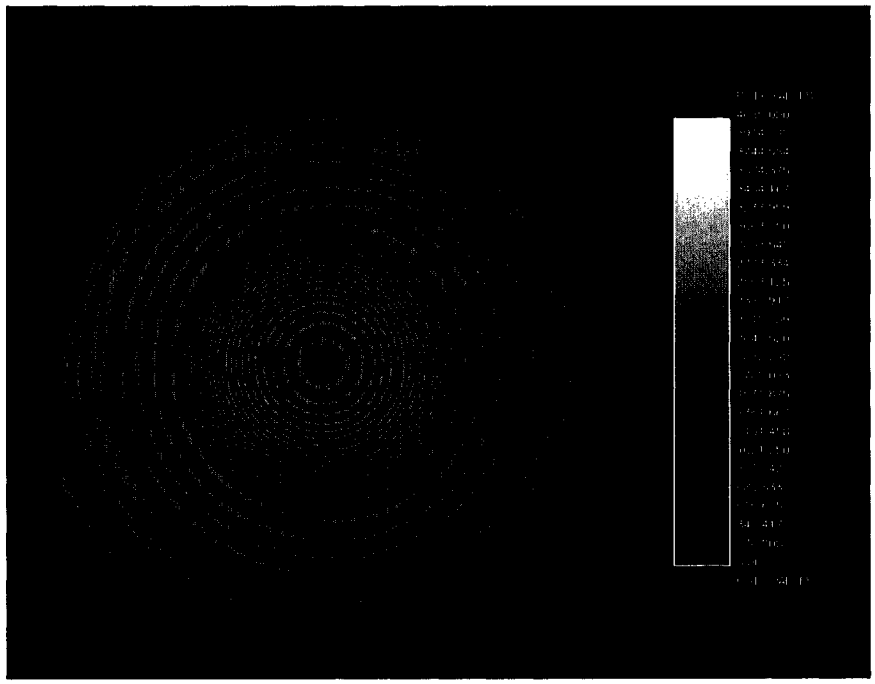

FIGURE 4.25 – Full lens interferogram for -10 D lens.

The central portion of the interferogram is the optical zone. The fringes over this portion of the lens are dictated by the desired optical prescription. The remainder of the lens is designed not for refractive correction but for other considerations. These considerations may include fit, rotational stability on the eye (critical for toric lenses), or stability off the eye in order to improve lens insertion. For this particular lens, the periphery has two distinct regions. The region surrounding the optical zone has very little power. Perhaps this is a result of simplifying the design or to accommodate a smooth surface over the front of the lens. The zone at the edge of the lens has a rapidly changing thickness, indicative of an edge bevel. The "123" mark at the top of the lens is imprinted on the lens to help wearers determine if the lens is inverted or not (JJVCI, 2003). Outside the contact lens, especially on the right side of the lens as shown in Fig. 4.25, is the near-null

fringe between light through the cuvette and the reference beam. The four corners of the complete interferogram show only the reference beam, as the test beam is blocked by the cuvette at this point. The Fresnel zones of the reference beam can be seen in the corners of the full interferogram. Figure 4.26 is the full unwrapped wavefront as shown in Intelliwave.

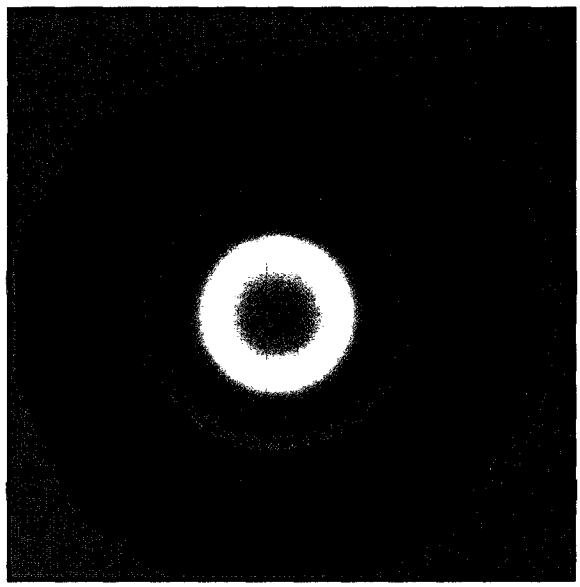

FIGURE 4.26 – Unwrapped wavefront for -10 D lens over a 14 mm aperture.

The blue circle is the 14 mm analysis aperture. Gray spots inside the aperture are bad pixels as determined by a modulation threshold of 0.7. Not only was the wavefront unwrapped over the optical zone junction, but even the wavefront between and around the "123" mark was unwrapped using the TMG unwrapping algorithm in Intelliwave. The color scale of the unwrapped wavefront indicates that the concavity of the wavefront switches near the edge. This is corroborated by viewing the surface of the OPD as seen

in Fig 4.27. The OPD surface also illustrates the change in power between the optical zone and the periphery.

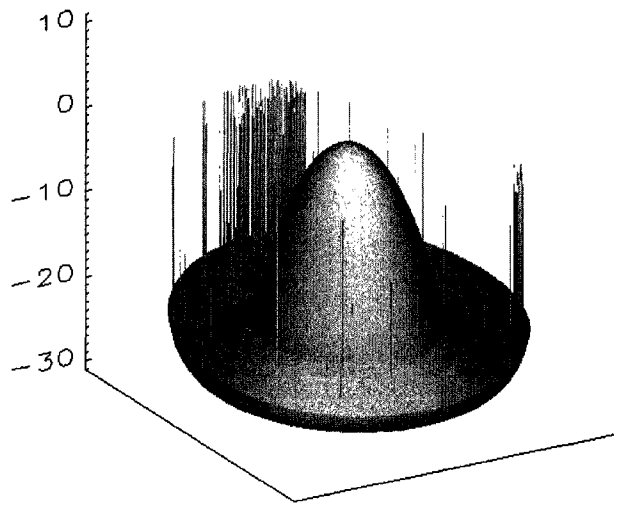

FIGURE 4.27 – Unwrapped wavefront for -10 D lens.

The OPD has been passed through a 5x5 median filter. The remaining bad pixels account for the spikes in the OPD surface. The concentration of spikes at the top is due to the "123" mark.

The ability to test the full lens is a welcome benefit to the sponsor. Just from a quality control standpoint, the ability to collect data over the full lens is valuable. Different zone junctions can be analyzed to determine if the wavefront is continuous over the junction.

The design of the periphery can be verified. The benefit of this capability will be made all the more impressive when toric lenses are tested.

5 TRANSMITTED WAVEFRONT TESTING OF TORIC, BIFOCAL, AND MULTIFOCAL CONTACT LENSES

The treatment in the preceding chapter dealt with the testing of spherical glass and contact lenses. The next step is to look at more complicated designs and understand the issues with testing such lenses. These are lenses that may lack rotational symmetry, a constant power across the optical zone, or both. Combining the design of these lenses with their physical makeup, one sees that these are truly complex optics.

There are three main classes of soft contact lenses: spheres, torics, and bifocals. Spherical lenses have already been analyzed, and once the difficulties of the lens material are understood, testing these lenses is straightforward. The other two classes, torics and bifocals, were introduced in Chpt. 1. For toric lenses, the challenge comes from the lack of rotational stability and, therefore, the need to rotationally orientate the measured and modeled data. Bifocal contact lenses have annular zones of differing power. These zones must be identified for accurate generation of the prescription by the analysis software. In addition, the annular zone structure of bifocals precludes the use of standard Zernike polynomials as a set of basis functions for fitting to the produced wavefronts.

While complicated, spheres, torics, and bifocals are established products that have proven themselves in the marketplace. Beyond these lenses are new classes of lenses. These are

lenses that exploit the advances in the fields of design, fabrication, and testing to provide a suitable correction to a greater number of eye conditions, such as presbyopia. This is a significant growth area in the ophthalmic industry; the need to swiftly prove the validity of designs and fabricated lenses is critical.

5.1 Testing Toric Contact Lenses

Toric lenses are spherocylinder lenses designed to correct astigmatism in the eye. The major challenge is not the asphericity of the wavefront, but rather the orientation of the test optic relative to the modeled data. Determining the orientation is necessary to accurately report the cylinder axis in the prescription of the lens. Perhaps, a way to solve this problem would simply be to put the lens in at a given orientation. This is a textbook example of "easier said than done". In the current cuvette, lenses are dropped into the saline, and then float down until they hit the window on the dovetail stage. Maintaining a given orientation to within the desired tolerance would be impossible. Rotating the lenses once seated would have to be done outside the cuvette, for controlled spinning of the lenses would also be incredibly difficult. Furthermore, rotating the entire cuvette causes further complications, such as ensuring parallelism between the axis of rotation and the test beam, rotating about the lens center, and increasing the time needed for a measurement.

The superior solution is to identify the orientation of the test lens and then rotate either the measured or modeled data. The cylinder axis of the lens is referenced from the

fiducial marks at the periphery of the lens. Using the trick of adding pairs of interferograms that are 180° out-of-phase to make a pseudo-bright field image makes the fiducial marks easily identifiable, as shown in Fig. 5.1.

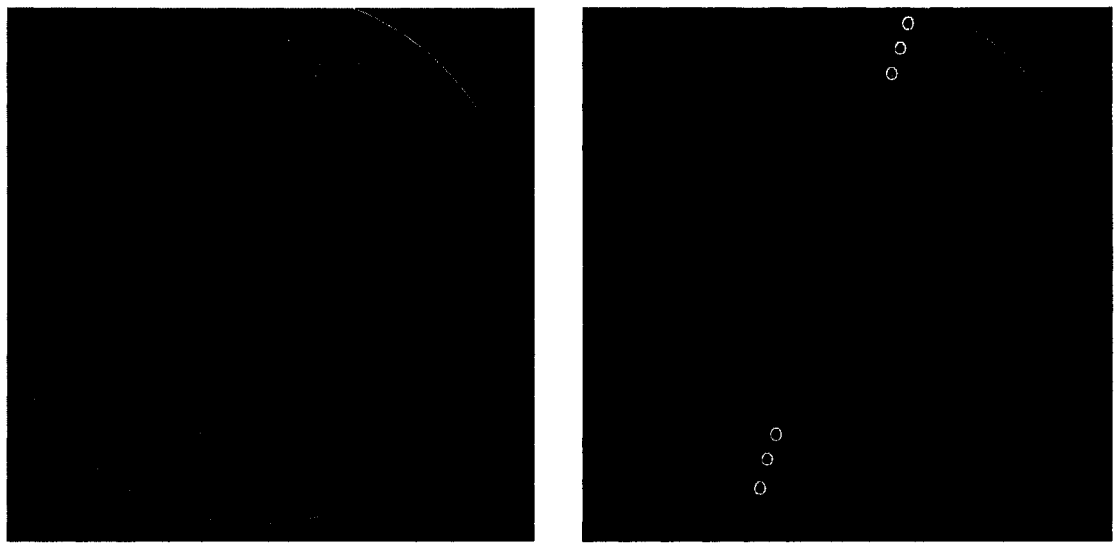

(a) (b)

FIGURE 5.1 – Identifying the orientation of a toric contact lens: (a) the pseudo-bright field image via interferograms, and (b) the image with the fiducial marks identified by placing three "O"s on each central mark.

Determination of the angle of the line passing through the central mark of each fiducial set is made by identifying three points on each central mark, and then fitting a line to the points using a least-squares fit. The identification of the points on the image is done by hand. The operator selects the points by placing an "O" at each location, as shown in Fig. 5.1. While this process could be automated with some additional work, the error with the by-hand method is quite low. For the above orientation, over ten trials, the angle of the fiducial marks is found to be 71.94° with an error (standard deviation of the mean) of

only 0.028°. The spread in the data is 0.31°. The 3σ point for the data is 0.25°, from which the claim is made that this method is good to a quarter-degree. For compassions, the ANSI tolerance on finding the cylinder axis is 8°, and the angle between the central fiducial mark and the secondary marks on either side is 10°.

With the orientation angle set, the lens is analyzed using the same procedure outlined for spherical lenses. Figure 5.2 shows the interferogram over 5 mm. Note the orientation of the elliptical fringes as compared to the orientation of the fiducial marks. The labeled angle for this lens is 180°, so the major axis of the ellipse should be aligned with the fiducial marks.

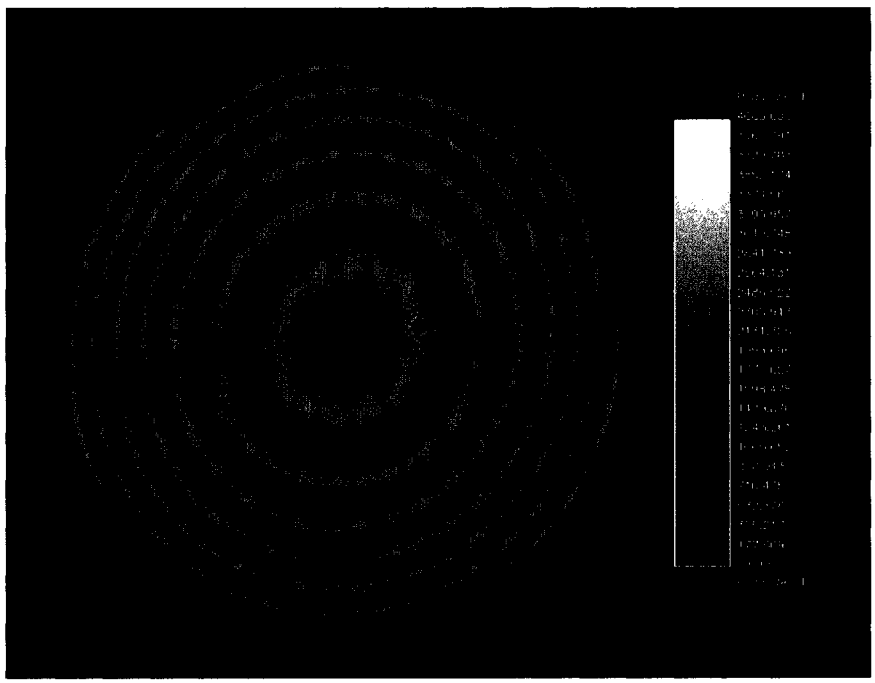

FIGURE 5.2 – Interferogram of a toric contact lens over 5 mm.

Figure 5.3 shows the Zernike fit to the difference between the measured and modeled wavefronts. To achieve this surface, the modeled data is rotated to match the given orientation angle of the measured data.

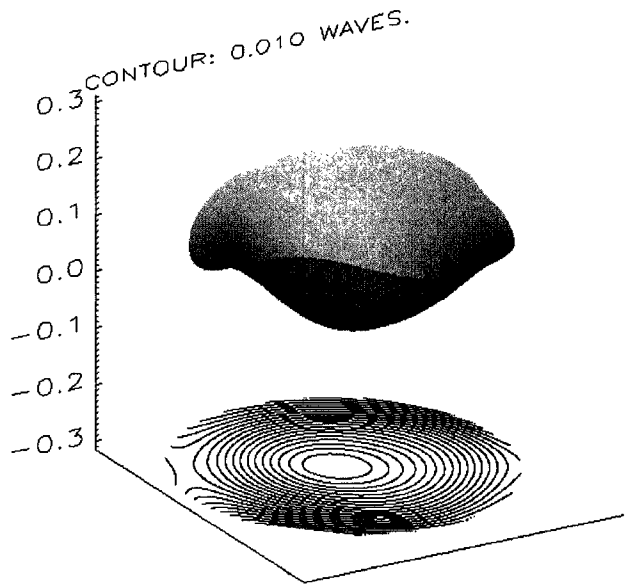

FIGURE 5.3 – Zernike fit to wavefront difference over 5 mm.

A discrepancy between the indices of refraction in the model and those present in the hardware can again be pointed to as a possible source for the power seen in the wavefront difference. In addition, centering the analysis aperture used to collect data seems to be more critical with these lenses than with spherical lenses. To first order, an error in centering the analysis aperture will have no effect on the data for both types of lenses, as tilt is removed from the unwrapped phase. However, displacements lead to higher-order odd terms as well, which may be contributing to the wavefront difference. A third possibility is that a decentration of the imaging lens could be introducing additional

astigmatism. The lack of rotational symmetry may leave these lenses more susceptible to errors when compared to perfectly-centered modeled data. The wavefront difference does not exhibit much astigmatism. This is a sign that the rotation of the modeled data has matched the measured data. If the two datasets were clocked differently, erroneous astigmatism would result. A fourth possibility is that the lens does not match the design due to fabrication errors. The measured prescription (in-air equivalent, in diopters) is -5.373 / -1.233 x 177.8°. The modeled prescription is -5.720 / -1.190 x 180.0°. The differences between the measured and modeled sphere and cylinder powers (in-air equivalents) lead to a percent error of 6.0% for the sphere and 3.6% for the cylinder power. The measured axis of 177.8° differs from the labeled axis of 180° by 2.2°, or 1.2%.

The full lens interferograms for toric lenses are fascinating. Figure 5.4 shows the full interferogram for the above analyzed lens.

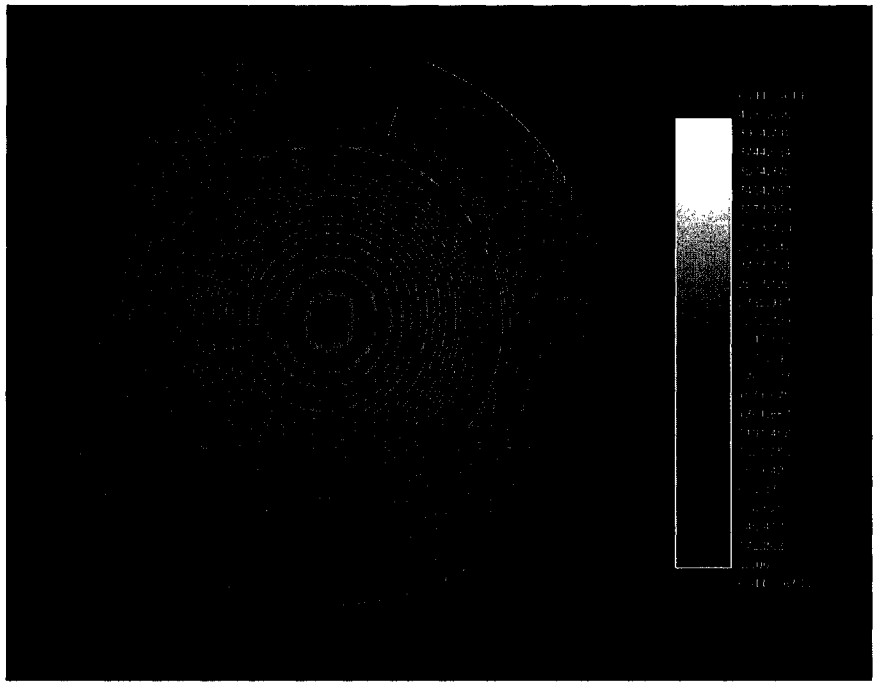

FIGURE 5.4 – Full lens interferogram for analyzed toric lens.

The optical zone is the central portion of the lens containing the elliptical fringes. Outside the optical zone, the fringes take on unusual shapes. This is due to the need for rotational stability on the eye. The interferogram reveals two crescent-shaped regions on either side of the lens. The OPD in these regions is such that it increases towards the lens. In effect, these two regions are wedges. The design of this lens must be relying on a blink of the eye to keep the lens in proper alignment. When the eye blinks, the eyelids would pass over these two wedges and presumably spin the lens into place. The full lens interferogram for a weaker toric lens is in Fig. 5.5.

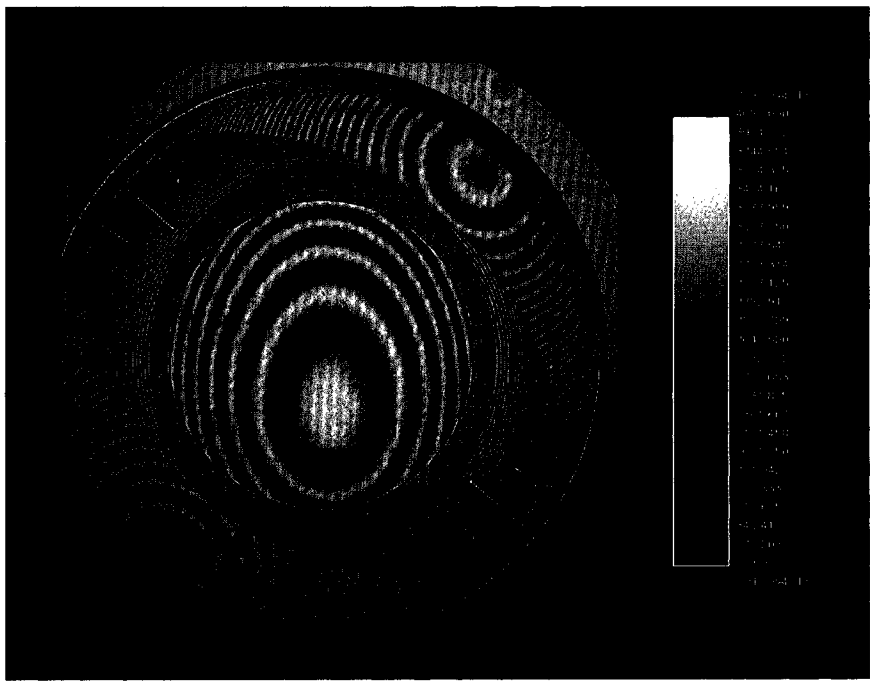

FIGURE 5.5 – Full lens interferogram for a weaker toric lens.

For some unknown reason the center of the fringe pattern is not coincident with the geometric center of the lens, as has been the case with prior lenses. The absence of fringes outside the lens suggests that the displacement of the central fringe in the optical zone is not due to a global tilt. In any event, this lens is included to show that the wavefront can be unwrapped outside the optical zone. Figure 5.6 shows the unwrapped wavefront. The wedged-shaped regions are sloped up, heading towards zero OPD near the edge. The spikes on either side of the lens are the fiducial marks which have been interpolated over during reverse raytracing.

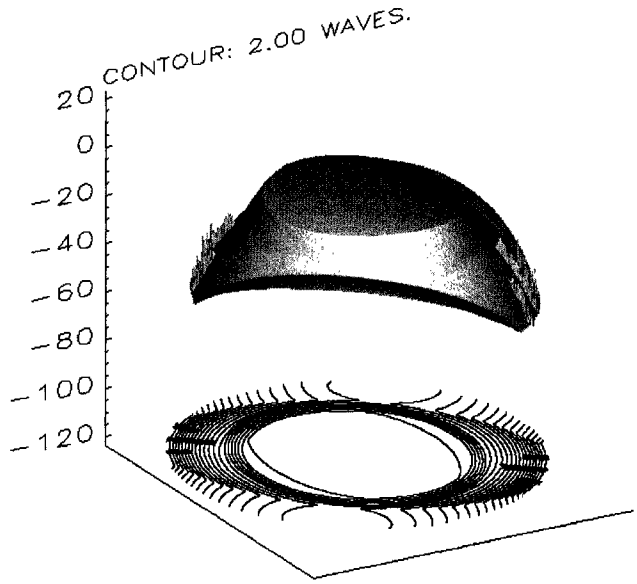

FIGURE 5.6 – Measured wavefront at test plane for a toric contact lens over 13 mm.

5.2 Testing Bifocal Contact Lenses

The final established class of contact lenses is bifocal lenses. Bifocal lenses are the most complex lenses of the three classes examined. One reason for this is that the surfaces for spherical and toric lenses can be described as biconics. This is not the case for bifocals. This particular design operates on the principle of simultaneous vision, or bivision (Mandell, 1974). As mentioned in Chpt. 1, within the optical zone of these lenses are annular zones with different powers. Each zone contains either the prescription for near or distance correction, thereby creating a bifocal. The zones are arranged so that in all but the brightest light levels both types of zones are illuminated. The eye receives two images, one that is in-focus and another that is out-of-focus. For the bifocals in this

study, the zones are five concentric annular rings, alternating distance/near correction, starting with distance correction in the central zone. Placing distance correction in the central zone must come from the fact that typically the eye's pupil is smallest under bright conditions, such as being outside, where the need for distance correction dominates.

Not surprisingly, bifocals are the hardest of the three types of lenses to model. A major reason for this is that the annular ring structure is not completely described by the given lens prescription. The labeled lens prescription gives all the information necessary to model spherical and toroidal contact lens. This is not the case with bifocal lenses for two reasons. First, the zones must have piston added to them to eliminate discontinuities in the wavefront. Assuming the surfaces of the contact are continuous, a good assumption given the discomfort associated with wearing a contact lens with edges and given a lack of discontinuity of the interferogram, the wavefront produced by a bifocal should be continuous. The only way for this to happen with multiple zones is to piston the zones. Figure 5.7 shows synthetic data (data not made from a prescription for a real lens but rather data made from the sag equation) for a -2.00 / +1.00 D bifocal (a) without and (b) with piston between the zones.

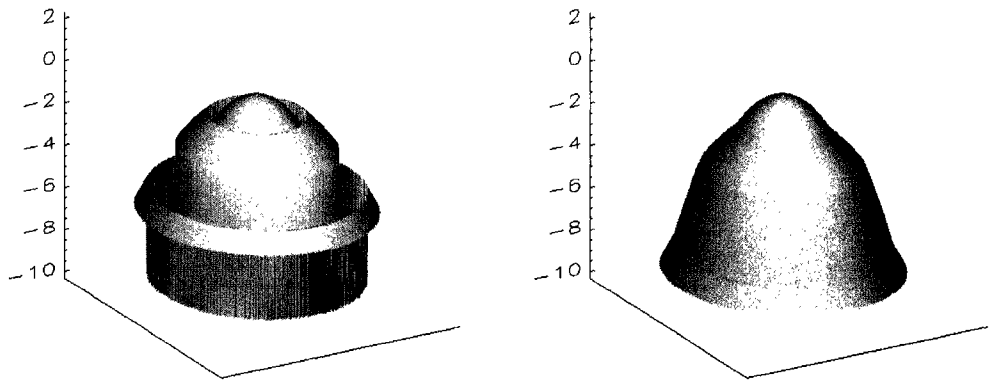

(a) (b)

FIGURE 5.7 – Synthetic wavefronts for a bifocal contact lens (a) without piston and (b) with piston between the zones. Piston is necessary to provide a continuous surface on the lens.

The surface without piston is not continuous, but does have the axial vertex for all zones coincident. The surface with piston is continuous, but does not have the zones' axial vertices coincident. Therefore, the zones with the same radius of curvature will no longer come to focus at the same position, but rather their foci will be separated by the amount of added piston. However, comparing the amount of shift to the radius of curvature for each zone reveals that the necessary shift is several orders of magnitude less than the radius and the difference in focal position is therefore negligible.

The other unknown piece of information regarding the modeling of bifocals is the blend between zones. Again using the argument that the surfaces of these lenses must be smooth enough to be comfortable on the eye, there can be no edges between the zones. Adding piston removes discontinuities, but could still leave peaks or troughs in the lens

surface. So some sort of blend must be designed between the zones to eliminate the peaks/troughs. For these reasons, modeled data is not provided for comparison. The lack of modeled data has no bearing on showing that the technology is capable of measuring these lenses.

There are two major analysis issues unique to bifocals. The first is the identification of the annular zones. This is necessary to produce a consistent prescription for the lens. The second issue is polynomial fitting to the wavefronts. The Standard Zernikes do not fit well to these surfaces, so a different technique is necessary.

5.2.1 Annular Zone Finding for Bifocal Lenses

Figure 5.8 contains the interferogram for a bifocal contact lens over the standard analysis aperture of 5 mm. The fringe spacing does not follow the familiar spacing of a spherical lens, indicating that some asphericity exists. Yet the fringes are continuous, and do not reveal the location of the annular zones.

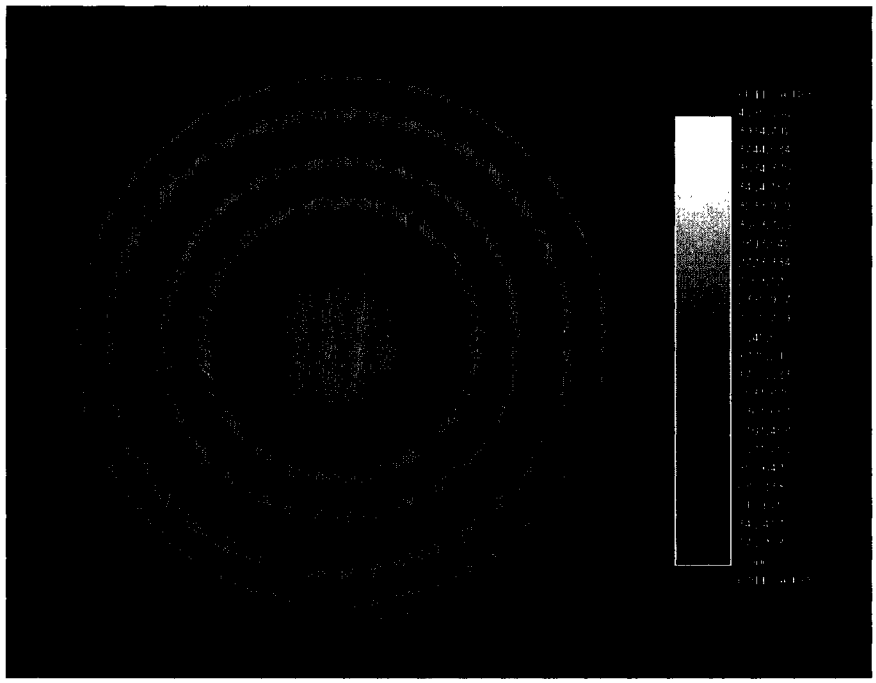

FIGURE 5.8 – Interferogram of a bifocal contact lens over 5 mm.

The measured wavefront over the same aperture is shown in Fig. 5.9. Now the presence of annular zones is obvious, both from the wavefront and the below contours. With an analysis aperture of 5 mm, three zones are fully captured, and a fourth zone is partially captured.

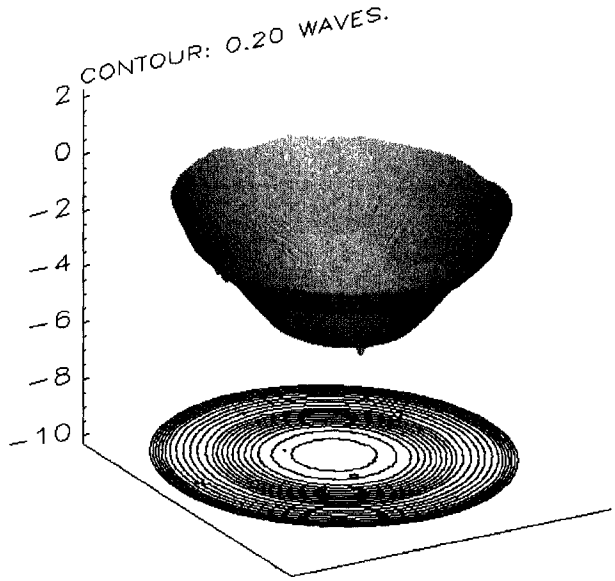

FIGURE 5.9 – Measured wavefront at the test plane for a bifocal lens over 5 mm.

The question is how best to identify theses zones. What makes a zone unique, and how can it be identified with no assumptions or as few assumptions as possible?

The algorithm developed to identify zones starts with subtracting off a best-fit sphere (BFS) from the wavefront. Since the annular zones of bifocals are all one of two powers, the BFS's power is ideally the average of these two powers, or is at least between the two powers. Spherical aberration is present in differing amounts in each zone, a fact that will be repeated during the discussion of radial power maps for bifocal lens. Figure 5.10 shows the measured wavefront minus the BFS.

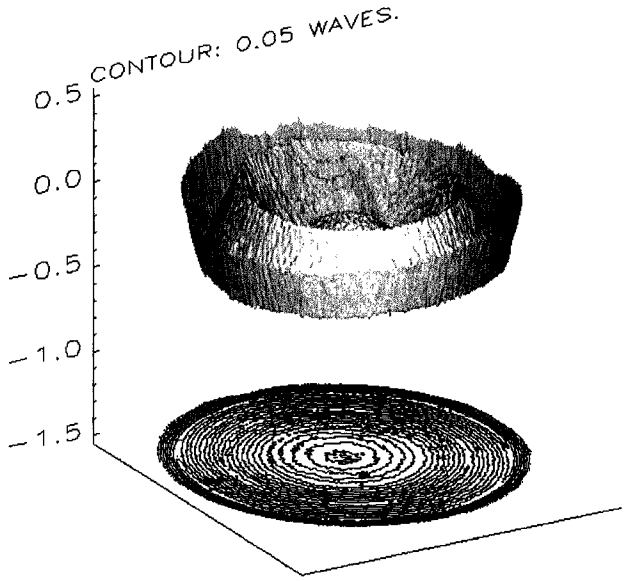

FIGURE 5.10 – Measured wavefront minus best-fit sphere (BFS).

Removing the BFS has left the near and distant zones with nearly equal-but-opposite powers, as can be seen in the more uniform spacing of the contours in Fig. 5.10 as opposed to Fig. 5.9. More importantly, the zones now alternate in slope. The central and third zones are now concave-down, while the second and forth zones are concave-up. This condition of alternating signs for curvature is the key to finding zones. The condition is exploited by once again using the technique of fitting a low-order polynomial to a small grouping of pixels. In this case, only the constant and linear terms are fit. Using a coordinate transformation allows for the slope along the radius of the wavefront to be determined. For the above wavefront, the concave-down zones have a negative radial slope, while the other zones have a positive radial slope. Keeping track of only the sign of the radial slope produces the map shown in Fig. 5.11.

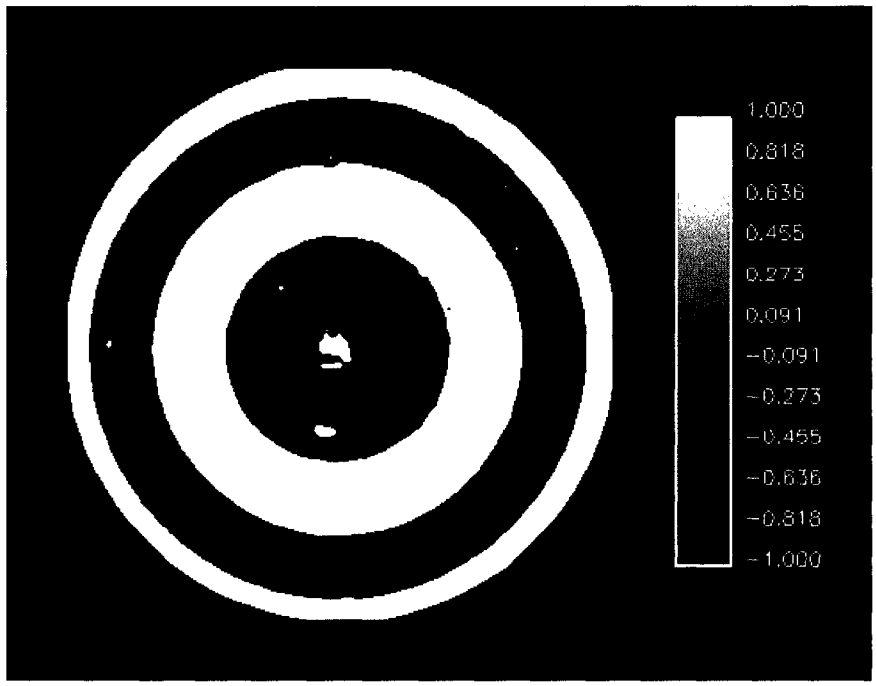

FIGURE 5.11 – Map of the sign for radial slope.

Once produced, the map is processed to eliminate small, erroneous zones. Use of IDL's **LABEL_REGION** simplifies this task. The final map used for zone identification is in Fig. 5.12, with each zone now a unique color.

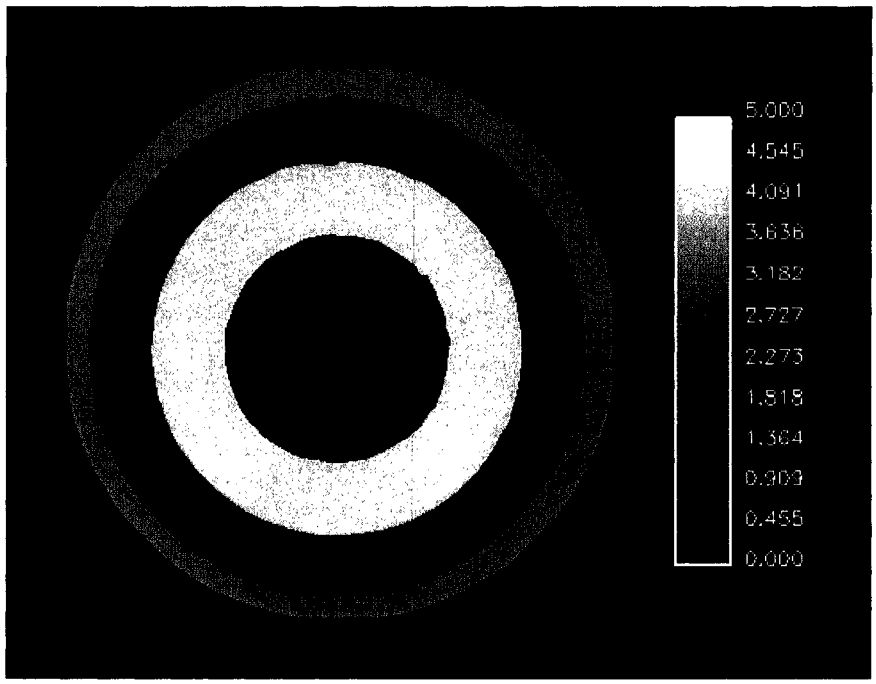

FIGURE 5.12 – Processed map of radial slope used for zone identification.

An important fact is the zones have been identified without assuming rotational symmetry. This gives a truer pixel-by-pixel identification for the zones than if a radial averaging technique was used. This technique ensures that zones contained in the analysis aperture will not suffer from centering issues when a polynomial fit is performed. The impact of this will be seen in the radial axial power maps discussed in the next chapter.

5.2.2 Modal-Zonal Fitting for Bifocal Lenses

The surfaces and wavefronts produced by spherical and toric lenses can be described quite nicely using Zernike polynomials. Unfortunately, this can not be said for bifocal lenses. These lenses produce wavefronts with specific, localized changes in curvature.

An infinite number of terms are needed to allow the Zernikes to match the changes in curvature at the specific locations. Figure 5.13 shows the residual map between a bifocal wavefront and the Zernike fit to the surface. The zone structure is still evident.

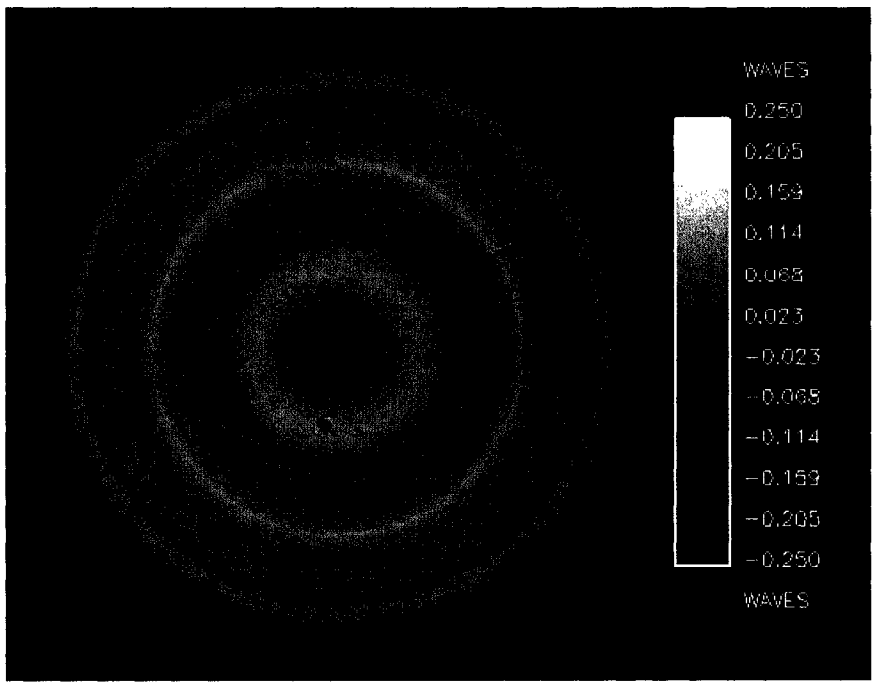

FIGURE 5.13 – Residual map between a bifocal wavefront and the Zernike fit to the same wavefront.

The apparent solution is a modal-zonal fit where a modal fit is performed over each zone of the bifocal wavefront. Annular Zernikes were studied as a possible set of basis functions for such a fit (Mahajan, 1981; Mahajan, 1994). Since each zone after the central zone is an annular region, Annular Zernikes could be used to provide the necessary fit. The other possibility is to simply fit a high-order polynomial to each zone (Schwiegerling, 1995). Polynomial fitting is used primarily as a means to suppress high-spatial frequency noise and to provide coefficients that can be used to generate a

prescription for the lens or annular portion of the lens. The benefit of Annular Zernikes over a simple polynomial set is the orthogonal nature of the Annular Zernikes. The downside is that the higher-order terms are quite long, and estimates for the annular and unit radii would be needed for each zone. Since a simple fit of a high-order (5^{th} order) polynomial over each zone provides a nice representation of a bifocal wavefront, this method is used in the analysis software. The polynomial fit to the measured bifocal wavefront (see Fig. 5.9) is shown in Fig. 5.14.

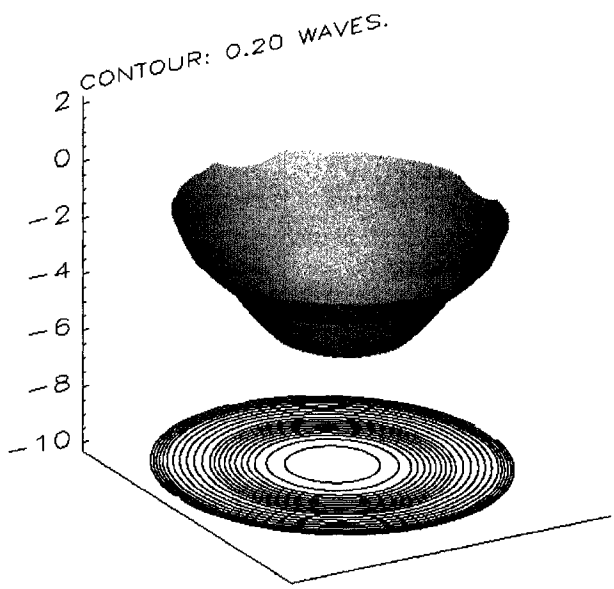

FIGURE 5.14 – Polynomial fit to measured wavefront in Fig 5.9.

Figure 5.15 contains the residual map between the measured wavefront and the polynomial fit to the wavefront. The zone structure is now eliminated from the residual map.

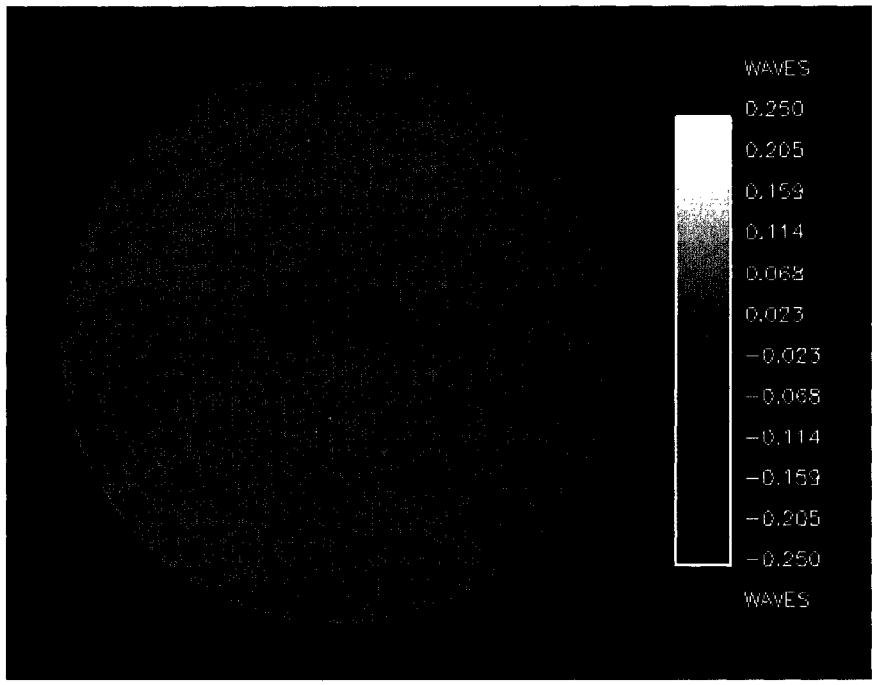

FIGURE 5.15 – Residual map between a bifocal wavefront and the polynomial fit to the same wavefront.

In order for the prescription generation routine to be run with bifocals, a conversion between the coefficients of the polynomial terms and the Zernike terms is needed. Table 5.1 lists the polynomial terms, nicknamed bifocal terms, while Table 5.2 lists the equations between bifocal terms and Zernike terms.

Bifocal Term	Expression	Bifocal Term	Expression
B_0	1	B_{10}	x^4
B_1	x	B_{11}	x^3y
B_2	y	B_{12}	x^2y^2
B_3	x^2	B_{13}	xy^3
B_4	xy	B_{14}	y^4
B_5	y^2	B_{15}	x^5
B_6	x^3	B_{16}	x^4y
B_7	x^2y	B_{17}	x^3y^2
B_8	xy^2	B_{18}	x^2y^3
B_9	y^3	B_{19}	xy^4
		B_{20}	y^5

TABLE 5.1 – Polynomial terms used in fitting bifocal wavefronts.

Bifocal Term	Zernike Equivalent
B_0	$Z_0-Z_3+Z_8$
B_1	Z_1-2Z_6
B_2	Z_2-2Z_7
B_3	$2Z_3+Z_4-6Z_8$
B_4	$2Z_5$
B_5	$2Z_3-Z_4-6Z_8$
B_6	$3Z_6$
B_7	$3Z_7$
B_8	$3Z_6$
B_9	$3Z_7$
B_{10}	$6Z_8$
B_{12}	$12Z_8$
B_{14}	$6Z_8$

TABLE 5.2 – Relationships between bifocal and Zernike coefficients.

Table 5.2 shows that the mapping from bifocal to Zernike coefficients is overconstrained. The analytic solution to the least-squares matrix method is used to provide a

transformation matrix between the two sets of coefficients. This enables bifocal coefficients to be used instead of Zernike coefficients in the code that generates the lens prescription.

For the bifocal lens analyzed, the coefficients put the power of the first zone at 3.155 D, the second zone at 6.486 D, and the third zone at 3.234 D. The fourth zone is not reported since a portion of the zone is outside the analysis aperture. Since no modeled data is available for comparison, the validity of these numbers is supported by the overall performance of the interferometer.

5.3 Multifocal Contact Lenses

Multifocal lenses are the next emerging class of contact lenses. These are aspheric lenses that are designed to provide an acceptable level of vision correction over a wide range of object distances. Judging by the wavefronts produced from these lenses, the mechanism being used to achieve such a long depth of focus is spherical aberration. Spherical aberration can be used to stretch the caustic to a point where the range of acceptable spot sizes in image space spans the complete range of object distances. The price that is paid for this extended depth of focus is that the spot size at all conjugates is greater than if the lens was designed for a single conjugate. For example, instead of having outstanding distance vision and poor near vision, these lenses can be used to provide good vision at both distance and near vision.

5.3.1 Comparing Different Designs

Due to the aspheric nature of these lenses, traditional metrology used to evaluate contact lenses does not provide easy-to-use information. Current metrology techniques, such as focimetry, work best with single-powered lenses. With CLOVER, the type of shape of the lens does not matter. As long as fringes can be resolved, the wavefront can be collected. This flexibility and robustness in the instrumentation is a real asset in developing new types of lenses.

Figure 5.16 shows the measured wavefront for a multifocal lens over 5 mm. The wavefront is dominated by two powers, near and distance correction, with a gradual transition between the two powers.

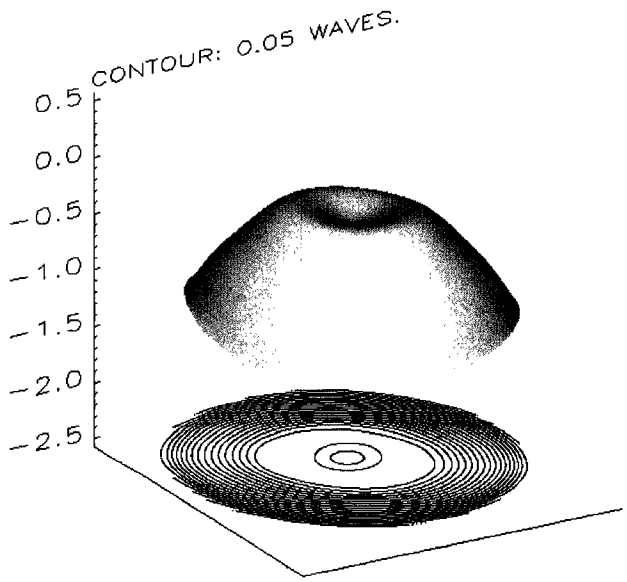

FIGURE 5.16 – Measured wavefront at the test plane for a multifocal lens over 5 mm.

The transition between powers is appreciably larger than the transitions between annular rings in bifocals. Figure 5.17 shows the measured wavefront for a multifocal lens of a different design. The overall shape of the wavefront is the same, but the depression in the center of the wavefront in noticeably bigger. The difference between the two designs will be expanded when the radial axial power maps for the two designs are compared in the next chapter.

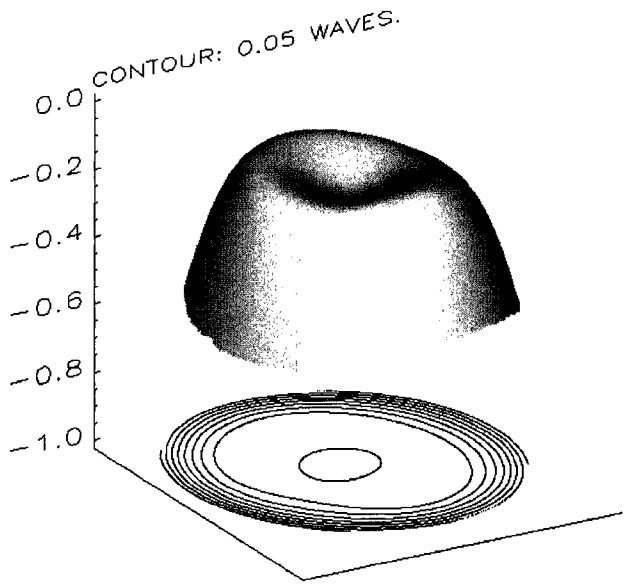

FIGURE 5.17 – Measured wavefront for a multifocal lens of a different design. Note the larger depression.

5.3.2 Star Testing

At the request of the sponsor, a modified star test was performed on bifocal and multifocal lenses. CLOVER was used to perform the test. The reference arm was

blocked, and the camera moved to point where the focus spot of the combined test lens/imaging lens fell on the detector. Figure 5.18 shows the modified CLOVER arrangement for star testing.

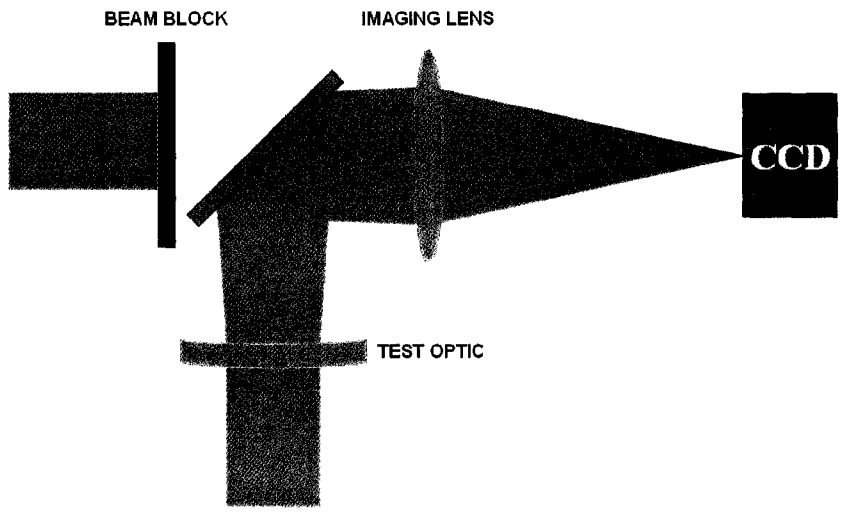

FIGURE 5.18 – Modified CLOVER arrangement for star testing.

The goal was to qualitatively uncover the difference in the focus spot between an annular-ring bifocal and a multifocal lens. To see the difference in the focus spots, a series of images were taken through focus for each lens. Conditions such as magnification and irradiance were held constant between the two lenses. The in-focus spot saturated the CCD, causing the vertical stretching or vertical lines seen in the focus spots. Figure 5.19 shows the series of images for (a) an annular-ring bifocal and (b) a multifocal lens. The two lenses have a nominal base power of -1.00 D.

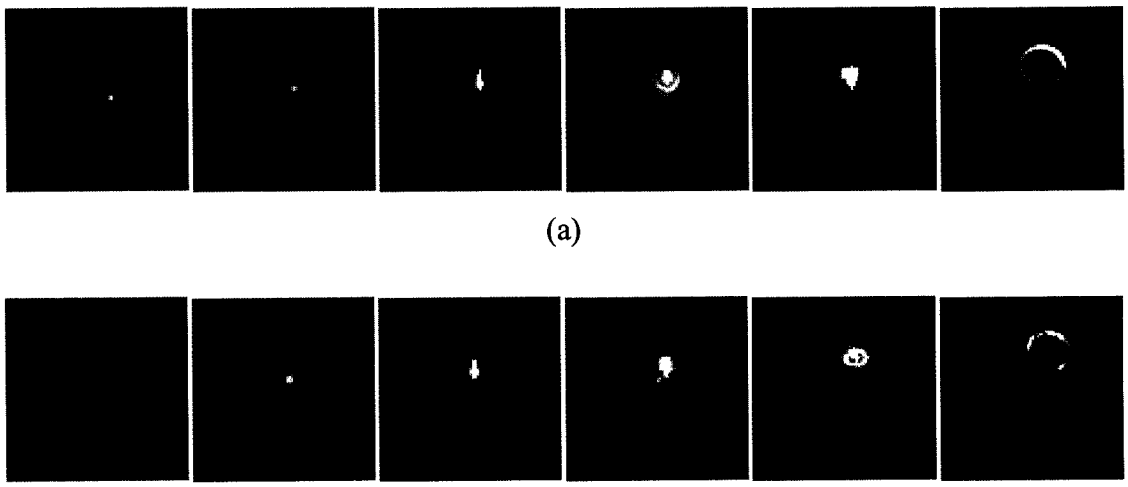

(a)

(b)

FIGURE 5.19 – Modified star test to compare bifocal and multifocal lenses: (a) through-focus images for a bifocal and (b) through-focus images for a multifocal lens.

The size and intensity of the focus spots make it hard to identify significant differences between the two focus spots. One obvious difference is the star-like shape to the Fresnel rings for the multifocal lens. The impact of this difference on the vision correction provided by the lens is not known. Also, more experiments would be needed to verify that the artifact is due to the lens and not due to some misalignment or vignetting in the modified interferometer configuration.

6 TREATMENT ON RADIAL AXIAL POWER MAPS

The ability to measure contact lenses and compare the results to modeled outputs has been demonstrated in the last two chapters. Comparing the measured performance to the modeled performance quantifies how well the lens operates compared to its design. There are a number of ways to make this comparison; in the preceding chapters the comparison was made by subtracting the measured and modeled wavefronts and computing a power for the wavefront difference. Power is used as the metric for the wavefront difference because power is the desired parameter for the lens. However, a single number does not capture the complexity of these lenses, nor does it provide much insight as to why the lens is or is not performing as expected.

To make better use of power, its localized nature can be utilized to make maps of power on a pixel-by-pixel basis. The formation of such a power map is a common technique in ophthalmics and can be used to quantify lens surfaces, transmitted wavefronts, and even the eye itself (Alonso, 1997; Sullivan, 1991; Roberts, 1994; Roberts, "Characterization of the...", 1994; Roberts, "The Accuracy of...", 1994; Klein, "Shape and Refractive...", 1995; Klein, "Axial and Instantaneous...", 1995). In ophthalmics, a common use of power maps is in describing the output from keratometers (Mandell, 1974; Loran, 1997; Schwiegerling, 2000). However, the power typically described in association with

keratometers is not the standard optical definition of power, i.e. the reciprocal of the effective focal length (Smith, 2000).

6.1 Various Definitions of Power

The term "power" has been expanded in the ophthalmic community to include any parameter that can be expressed in units of diopters. The standard optical definition, based on the difference in index and curvature for a refracting surface, is called "refractive", "focal", or "corneal refractive" power in ophthalmic literature (Klein, "Shape and Refractive...", 1995; Roberts, "The Accuracy of...", 1994). Other types of powers are also mentioned, and they arise from expressing different distances in diopters. These varying definitions of power are designated as shape-based powers by Klein and Mandell ("Shape and Refractive...", 1995). There are three identified shape-based powers: position, axial, and instantaneous powers. Figure 6.1 shows a refracting surface with labeled distances pertaining to the three shape-based powers.

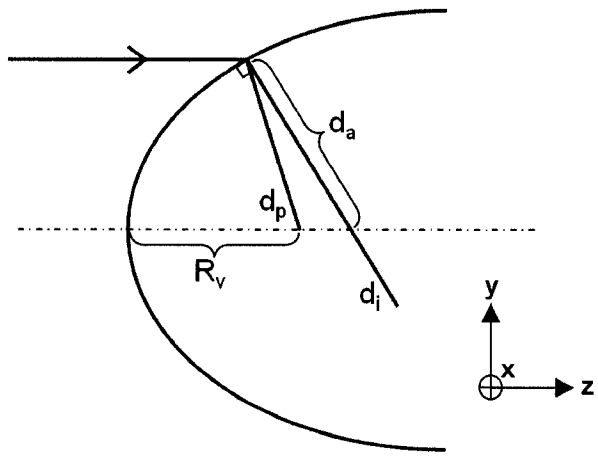

FIGURE 6.1 – Single refracting surface used in describing the various definitions of power. The subscripts on d refer to the three types of power: position, axial, and instantaneous. Note that the distances corresponding to axial and instantaneous power lie in the same plane but differ in length.

The three shape-based powers are specified using different distances. The distances are converted into a power-like quantity using

$$P_{p,a,i} = \frac{\Delta n}{d_{p,a,i}}, \qquad \text{Equation 6.1}$$

where Δn is the difference in refractive index at the refracting surface. The distances are defined using two points, one of which is always the point where the incoming ray intersects the refracting surface. For positional power, the other point is defined by the radius of curvature for the vertex (noted as R_v in Fig. 6.1). This point is independent of the incoming ray's position, so positional power is only a function of the ray's intersection with the refracting surface. Axial power defines the second point as the intersection of the vertex normal with the normal to the surface at the point of the ray's intersection. This second point depends not only on the position of the ray, but also on

the slope of the surface at the ray's intersection. For instantaneous power, the second point is the center of curvature for the surface at the point of the ray's intersection. The position of the center of curvature is computed using the standard definition from calculus: the center of a circle whose radius is the reciprocal of the curvature at the given point and whose center lies on the normal to the surface at the given point (Leithold, 1990; Schwiegerling, 2000). Instantaneous power depends on the position, slope and curvature of the surface at the ray's intersection. The different dependencies on shape for the three powers explain the name shape-based powers. Positional power is based on position alone, while axial power includes a slope-based component and instantaneous power is based on position, slope, and curvature (Klein, "Axial and Instantaneous...", 1995). For a spherical refracting surface, all three powers give the same result, which is identical to the standard answer for optical power.

As mentioned in the introduction, the use of power maps is common in describing the output of a keratometer or other videokeratographic device (Roberts, "The Accuracy of...", 1994; Klein, "Axial and Instantaneous...", 1995; Schwiegerling, 1995). The devices operate on technology based on Placido disks and, according to Klein and Mandell, measure axial power. This claim is also supported by Schwiegerling, who states that the ring spacing in the image and *a priori* knowledge of the device can produce the radial slope of the cornea (1995). A quantity based on axial power is what is desired by the sponsor, and the derivation of this power is the next topic of discussion.

6.2 Radial Axial Power Maps for Contact Lens Wavefronts

In the realm of contact lenses, the sag of the wavefront produced is small over the diameter of the lens being examined. A more accurate construction for axial power in the region of wavefronts produced by contact lenses is shown in Fig. 6.2.

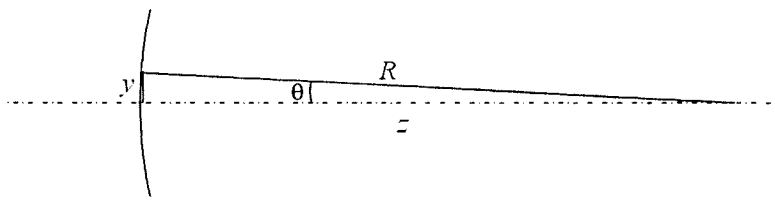

FIGURE 6.2 – Determination of axial power for contact lens wavefronts.

Figure 6.2 represents a meridian of a contact lens wavefront. While the derived quantity for radial axial power is not limited to surfaces of revolution, the derivation of axial power is carried out in a plane. Since axial power is a based on slope, the goal is to express the distance R as it relates to the slope of the surface. Since this is the treatment of wavefronts, and not refracting surfaces, there is no index of refraction dependence for the power. The quantity $1/R$ is the desired power.

The starting point for deriving radial axial power for contact lens wavefronts is the triangle whose sides are y, z, and R, giving:

$$y^2 + z^2 = R^2. \qquad \text{Equation 6.2}$$

Differentiation of Eq. 6.2 leads to the following:

$$\frac{y}{z} = \frac{dz}{dy}. \qquad \text{Equation 6.3}$$

The angle θ is related to y, z, and R by

$$\sin\theta = \frac{y}{R}, \qquad \tan\theta = \frac{y}{z}. \qquad \text{Equation 6.4}$$

In the region of small angles, sin θ and tan θ are equal, which combined with Eq. 6.3 and Eq. 6.4 leads to

$$\frac{y}{R} = \frac{y}{z} = \frac{dz}{dy}, \qquad \therefore \frac{1}{R} = \frac{1}{y}\frac{dz}{dy}. \qquad \text{Equation 6.5}$$

Equation 6.5 is the basic relationship between the slope of the surface and the reported axial power used in the following power maps for wavefronts produced by contact lenses. When applied to the cornea, where the small angle approximation no longer applies, axial power is related to (Schwiegerling, 2000)

$$\frac{1}{R} = \frac{1}{y}\frac{dz/dy}{\sqrt{1+(dz/dy)^2}}. \qquad \text{Equation 6.6}$$

In the limit of small angles, the quantity y/z is less than 1, which says $(dz/dy)^2$ is much less than 1. This allows the denominator of Eq. 6.6 to be expressed simply as y, which gives Eq. 6.5. One difference between the above two equations for axial power is the surface that produces constant power. For the small-angle-approximation form used with contact lenses, a paraboloid gives constant power as this surface has a linear first

derivative in the radial direction. For the equations used when analyzing corneas, a spherical surface gives constant power.

To apply Eq. 6.5 to a wavefront in polar coordinates of the form $W(r,\theta)$, the equation would be

$$\frac{1}{R} = \frac{1}{r}\frac{\partial W(r,\theta)}{\partial r}. \qquad \text{Equation 6.7}$$

Along a radius, the dependence on θ is fixed, leaving

$$\frac{1}{R} = \frac{1}{r}\frac{dW(r)}{dr}. \qquad \text{Equation 6.8}$$

The question now is how best to perform the radial derivative. There are a couple of issues in carrying out Eq. 6.8 on real data. The first issue is that real data is noisy. The derivative of noisy data is noisier than the original data, and is often too fluctuating to be useful. The second problem is that the data exists on a regular grid. While the array containing the wavefront could be rotated in IDL, this leads to interpolation errors and jeopardizes the validity of the results.

The solution to the first issue is simply to use the Zernike surface already formed for the wavefront. The Zernike surface is free of high-frequency spatial noise, and therefore the derivatives produced by the surface are also free of noise. In the case of bifocals, the modal-zonal polynomial fit is used in lieu of Zernikes. The answer to the second issue is to once again perform a least-squares polynomial fit over a small grouping of pixels. In the past, this technique has been used to determine the necessary angular perturbation in

converting rays from the reference wavefront to the test wavefront and in finding annular zones in bifocal lenses. Here the technique is used to provide coefficients for an analytic radial derivative.

For a given pixel, the polynomial $P(x,y)$ is fit over the pixel and its neighbors to form an estimate of $W(x,y)$. The fit is done in Cartesian coordinates using a least-squares technique.

$$W(x,y) \cong P(x,y) = A + Bx + Cy + Dx^2 + Exy + Fy^2 \qquad \text{Equation 6.9}$$

If a pixel is missing, or has been deemed a bad pixel by other criteria, then the pixel is not used in the fit. If too many pixels are missing from the neighborhood surrounding the central pixel, then the fit is not performed and no power is reported for the central pixel. Consequently, pixels at the wavefront's edge are usually missing from the resulting power map. The fit is done over x and y because this is the space over which the data exists. By using a second-order polynomial, the assumption is that the wavefront over such a small grouping of pixels is not more complex than a conic (Leithold, 1990).

The next step is a coordinate transformation. The transformation takes the fit from $P(x,y)$ into $P(r,t)$ where the coordinates (r,t) are Cartesian coordinates that have been rotated an angle θ so that the r-axis is aligned with the radius of the wavefront. This simplifies computing the radial derivative. The translation is nothing more than the standard transformation of coordinates for pure rotation (Spiegel, 1999). For a rotation of angle θ between the coordinates (x,y) and (r,t), the formulas are

$$\begin{aligned} x &= r\cos\theta - t\sin\theta, \\ y &= r\sin\theta + t\cos\theta. \end{aligned} \qquad \text{Equation 6.10}$$

Performing the transformation gives

$$\begin{aligned} P(r,t) = A & \\ &+B(r\cos\theta + t\sin\theta) \\ &+C(r\sin\theta + t\cos\theta) \\ &+D(r^2\cos^2\theta - rt\sin 2\theta + t^2\sin^2\theta) \\ &+E(r^2\cos\theta\sin\theta + rt\cos 2\theta - t^2\cos\theta\sin\theta) \\ &+F(r^2\sin^2\theta + rt\sin 2\theta + t^2\cos^2\theta). \end{aligned} \qquad \text{Equation 6.11}$$

Along the r-axis t equals 0, and so the analytic radial derivative simplifies to

$$\begin{aligned} \left.\frac{\partial P(r,t)}{\partial r}\right|_{t=0} &= B\cos\theta + C\sin\theta \\ &+2(D\cos^2\theta + E\cos\theta\sin\theta + F\sin^2\theta)r. \end{aligned} \qquad \text{Equation 6.12}$$

Dividing by r leads to the final form for computing the power $1/R$ from the local fit to the wavefront $P(r,t)$:

$$\begin{aligned} \frac{1}{R} &= \frac{1}{r}\left.\frac{\partial P(r,t)}{\partial r}\right|_{t=0} \\ &= 2(D\cos^2\theta + E\cos\theta\sin\theta + F\sin^2\theta) \\ &+\frac{B\cos\theta + C\sin\theta}{r}. \end{aligned} \qquad \text{Equation 6.13}$$

The above expression gives the radial derivative of the wavefront from a polynomial fit to the wavefront over Cartesian coordinates. One of the advantages to this algorithm is that the fit is done in the native (x,y) coordinates, and an analytic expression is used to compute the radial derivative from the Cartesian coefficients. An important note is that the fit in Cartesian coordinates must be done in global, and not local, coordinates. That is

to say, the values used for x and y must be the global values for x and y describing the point about which the fit is being performed. Care must also be taken to ensure that the fit is done with x, y, and P all in the same units. Also, the coefficients used have different units associated with them, as can be seen in Eq. 6.9. $P(x,y)$ has units of $W(x,y)$, which is the wavefront sag, in units of length, or m. Consequently, since x and y are lengths, the units on B and C are unity while the units on D, E, and F are m^{-1}. Note that these units agree with Eq. 6.13.

This algorithm is but one of many possibilities for computing the desired quantity $1/R$. All of the effort going into the polynomial fit and coordinate transformation is done to provide the best estimate possible for the radial derivative. The polynomial fit is not inherently necessary to computing radial axial power, but is simply the method chosen to provide the needed radial derivative.

This method of computing radial axial power is similar to what is presented by Klein and Mandell ("Axial and Instantaneous...", 1995). Both algorithms start with an analytic expression for a general surface and use the analytic expression to compute the derivative. Klein and Mandell then determine the location where the normal to the surface at the point in question intersects the arbitrarily-placed vertex normal. Here, thanks to the small-angle approximation, the determined radial derivative leads directly to the desired power.

6.3 Representative Power Maps

The following is a treatment on the radial axial power maps produced by the different types of lenses analyzed in prior chapters. Each class of lenses produces a distinctive power map. As this is an additional output to the testing, new features of these lenses appear that are hard, if not impossible, to ascertain from the wavefronts.

6.3.1 Output from Synthetic Data

To start, the algorithm for radial axial power is verified against synthetic data. The term 'synthetic data' refers to data representing a wavefront that is made from the general sag equation, as shown in Eq. 6.14 (Focus Software, 2000; Shannon, 1997).

$$z = \frac{x^2 / R_x + y^2 / R_y}{1 + \sqrt{\left(1 - \left(1 + k_x\right) x^2 / R_x^{\,2} - \left(1 + k_y\right) y^2 / R_y^{\,2}\right)}} \qquad \text{Equation 6.14}$$

Verification of the algorithm for radial axial power is done by forming a parabolic wavefront using the above sag equation ($k_x = k_y = -1$, $R_x = R_y = R$). For a value of R = 1000 mm, the resulting power should be 1.000 D. Figure 6.3 shows the power map for such a wavefront. The diameter of the wavefront corresponds to a 5 mm test aperture.

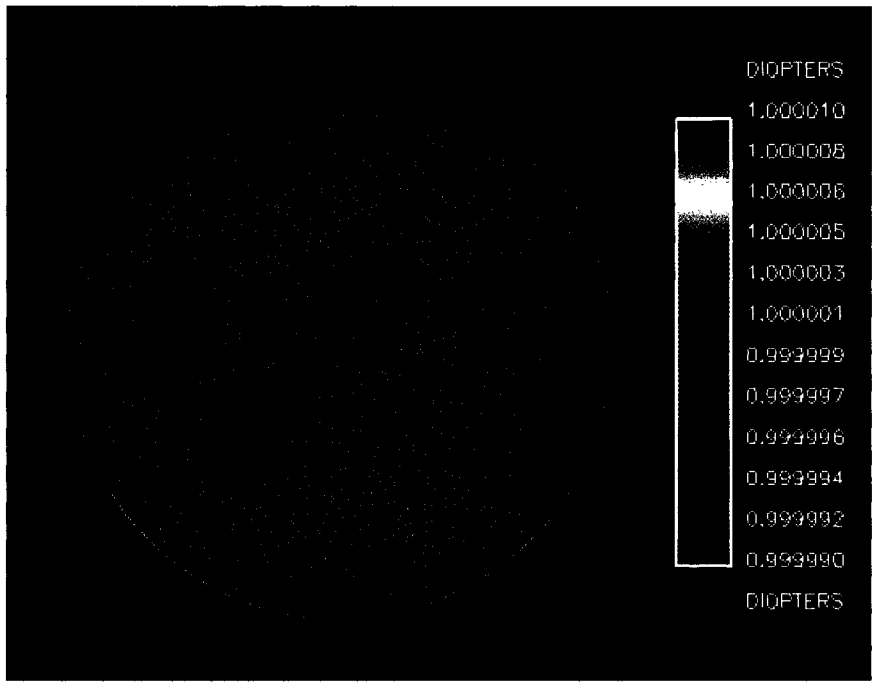

FIGURE 6.3 – Power map for a synthetic parabolic wavefront (R = 1000 mm).

Indeed, the reported power is a constant 1.000 D. The reported RMS for the map is 0.000000 D. Perhaps the only unexpected feature of this map is the missing data point at the center. This is common for axial power maps, as the second term (slope/radius) in Eq. 6.13 approaches the unstable condition of 0/0 near the axis. This is handled in the software by eliminating all IDL values of **NAN** or **INF** (two possible outputs for the undefined ratio 0/0). Here the error is confined to a single pixel. For real wavefronts, this error is but one of two factors that cause pixels near the center to give erroneous results; more on this to come.

The next wavefront is a synthetic spherical wavefront. Keeping R at 1000 mm gives the map shown in Fig. 6.4.

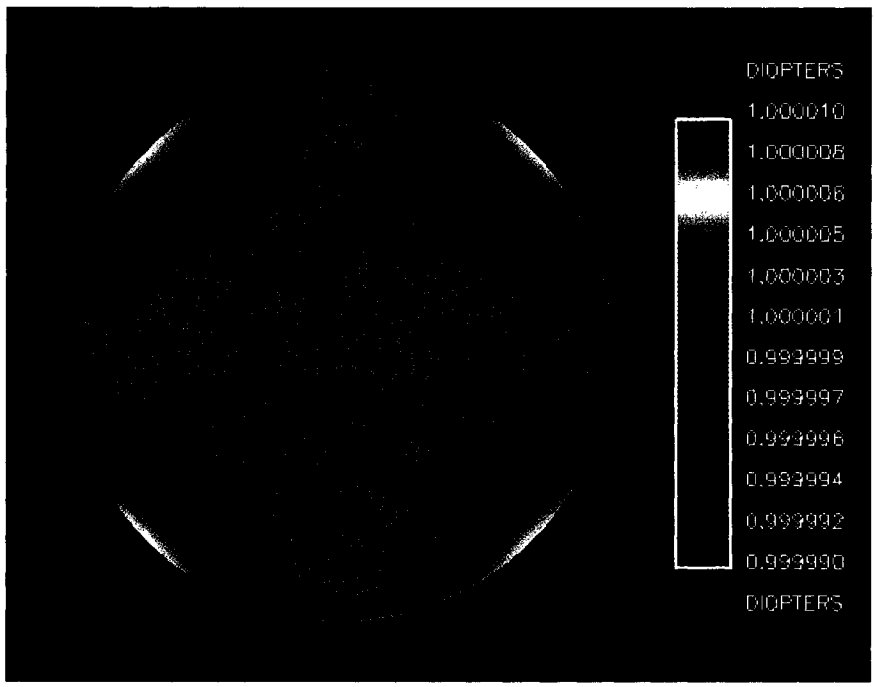

FIGURE 6.4 – Power map for a synthetic spherical wavefront (R = 1000 mm).

The spherical wavefront is nearly constant, but does show an increase in power in the diagonal directions. The colorbar resolutions for this map and the power map for the parabolic wavefront are the same. There are a couple of reasons for the difference between the two maps. First, a spherical wavefront is not supposed to give a constant; this is the consequence of the small angle approximation used to generate Eq. 6.5. Had Eq. 6.6 been used, the spherical wavefront would give a constant radial axial power. The reason this spherical wavefront is so much like the parabolic is that the sag of the wavefront is much smaller than the diameter of the wavefront. Figure 6.5 shows the map for a 200 D (R = 5 mm) spherical wavefront over the same 5 mm test aperture.

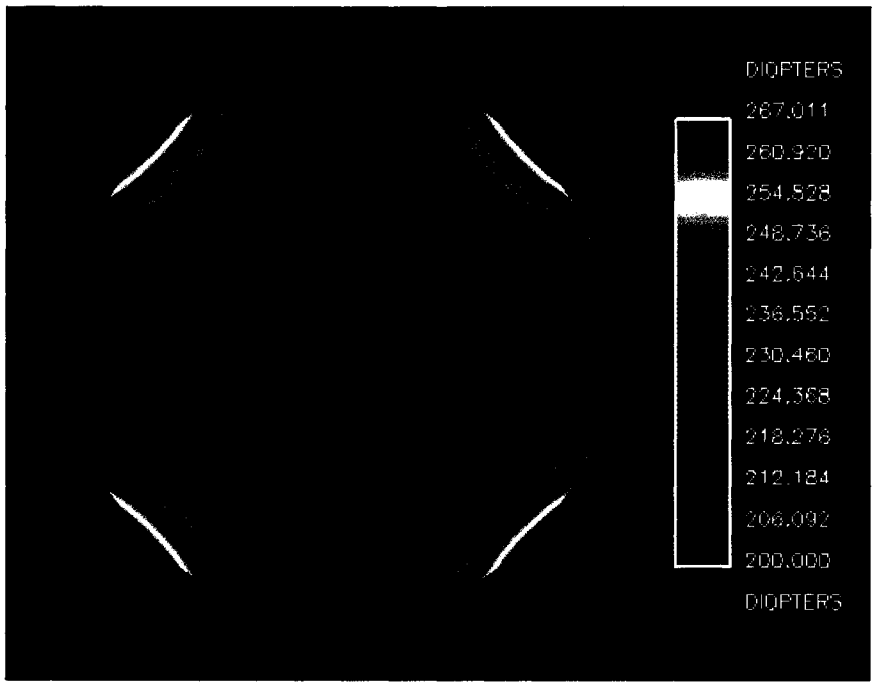

FIGURE 6.5 – Power map for a 200 D synthetic spherical wavefront (R = 5 mm). Note that the sage of this wavefront is outside the area of small angles, and thus the reported power for such a wavefront has no meaning.

Now the deviation is quite noticeable. This is of little concern, however, for a wavefront with as much sag as this is clearly outside the range of small angles over which the radial axial power was defined. The output for such a wavefront has no physical meaning.

The other point to make in comparing the parabolic and spherical maps is the parabolic wavefront can be fit exactly using a second-order polynomial. This is not true for a spherical wavefront, which would take a polynomial of infinite order to describe exactly.

6.3.2 Output from Spherical Lenses

Moving on to real measured and modeled data, the power map for the Zernike fit to the wavefront produced by the calibration lens appears in Fig. 6.6 (see Fig. 4.11 for the associated wavefront).

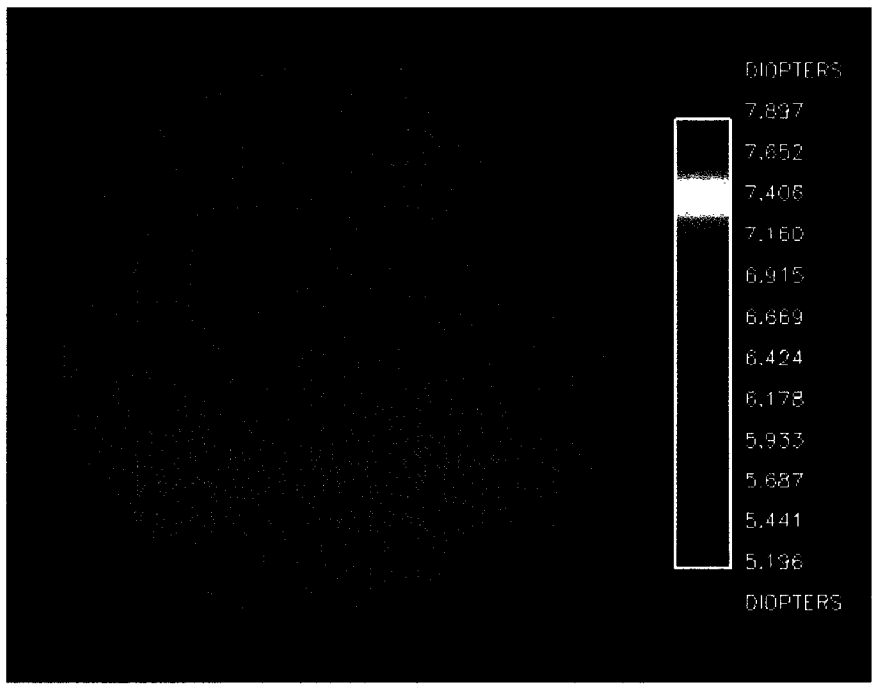

FIGURE 6.6 – Power map for measured wavefront ($\tilde{W}_T$) for calibration lens.

Now the full effect of the instability near the vertex for axial power is seen. The instability is greater than the central pixel because with real data there will be an offset of some fraction of a pixel between the vertex of the wavefront and the global origin used for the polynomial fit. This offset gives rise to a linear term, as was discussed in Chpt. 4. Consequently, the error near the vertex looks like tilt. The extent of the instability depends on the size of this offset. Also, the extent depends on the size of the

neighborhood of pixels used in performing the polynomial fit for the radial derivative. For this particular map, the PV is 2.701 D. Clearly this is artificially high due to the central pixels. Eliminating the central 2% of the map increases the colorbar resolution, giving a more informative map. The value of 2% is an arbitrary, but reasonable, choice.

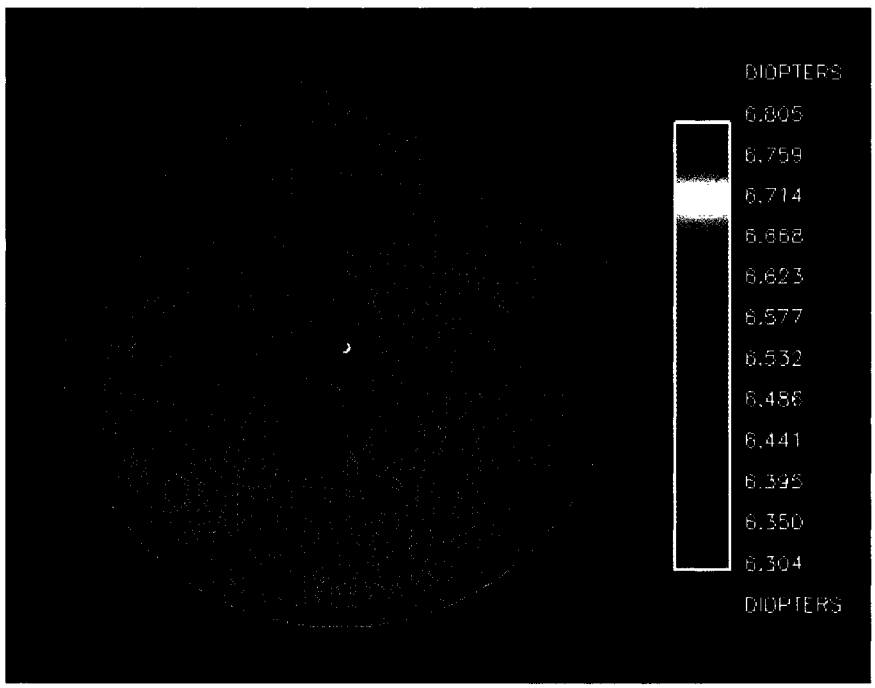

FIGURE 6.7 – Same map as Fig. 6.6, but with central 2% eliminated.

With the central 2% removed, more reasonable numbers can be derived from the power map. The average power over the map is 6.525 D. This is within 0.01 D of the power derived from the Zernike fit (6.515 D), as reported in Table 4.2. Since the two powers are fundamentally different, the two values are not expected to be in agreement. However, the fact that these two numbers are "in the same ballpark" does provide some validity to the radial axial power measurement as an accurate descriptor of the wavefront.

Given that the measured and modeled wavefronts have been shown to be in good agreement, their power maps should be similar as well. The power map for the modeled wavefront is in Fig. 6.8. Again the central 2% has been eliminated.

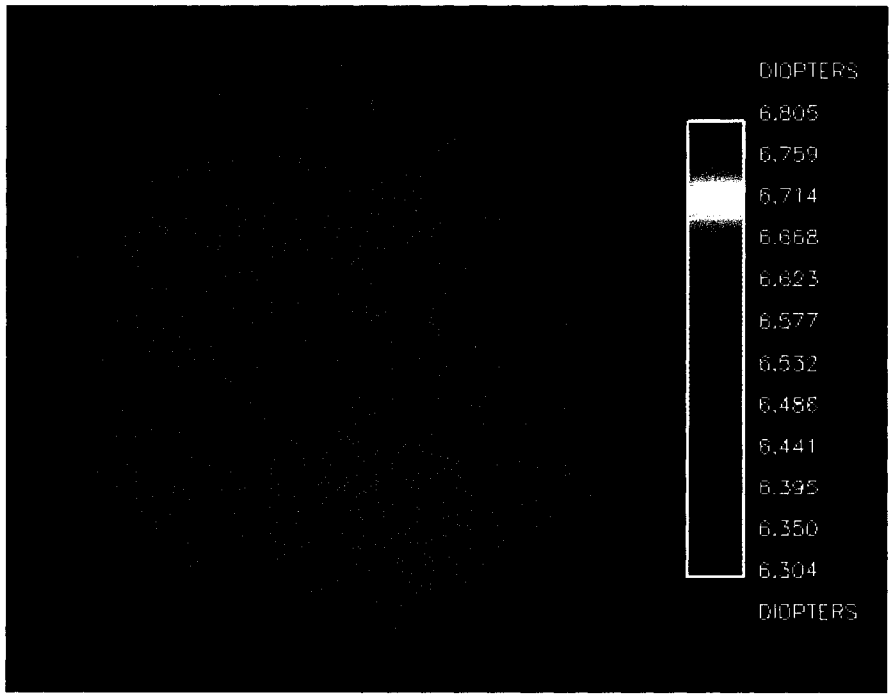

FIGURE 6.8 – Power map for modeled wavefront (W_T^M) for calibration lens.

The average power for this map is 6.569 D. The difference between the two average powers (measured minus modeled) is -0.044 D. The two maps can be subtracted directly, given a map of the deviation of the measured power from the modeled power. This is perhaps a better map to use to judge the quality of the output, in that any constant bias in the reported power is removed on a pixel-by-pixel basis.

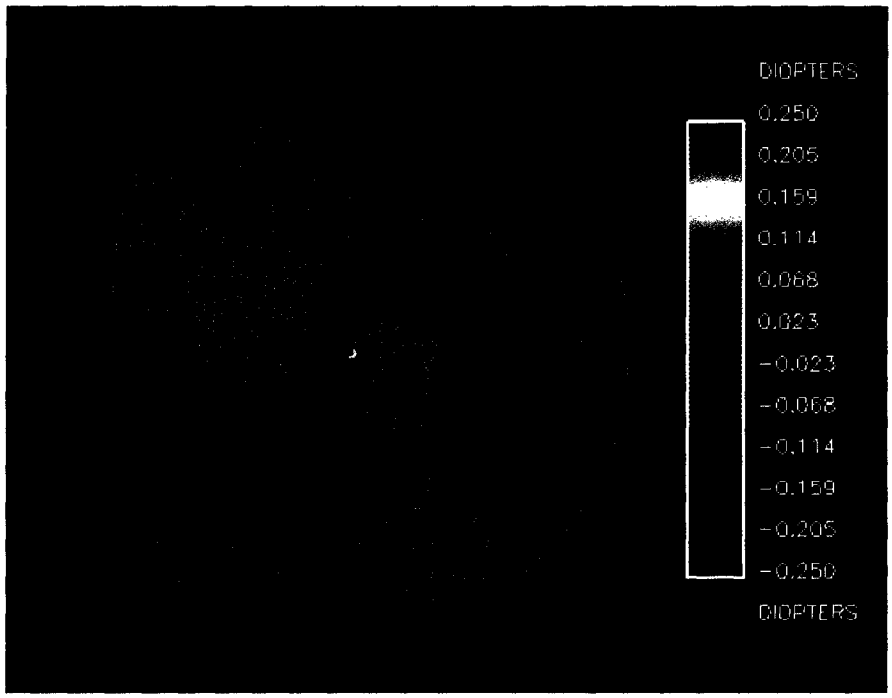

FIGURE 6.9 – Difference between measured and modeled power maps.

The average power for this map is -0.044 D, which matches the difference in average powers between the measured and modeled maps.

Before moving on to contact lenses, a point to reemphasize is that these maps are made from the Zernike fits to the wavefronts and not the wavefronts themselves. Just as the Zernike wavefronts allow for a better view of the shape of the wavefront, using the Zernike surface in the radial power calculations enables small changes in power to be seen. The determination of the radial derivative is not made with noisy data, which wreaks havoc with derivatives and would render the power maps useless. Furthermore, computing radial axial power over smooth data permits the use of the smallest grouping

of pixels possible (3-by-3) for the polynomial fit. This minimizes the extent of the instability in the central portion of the map.

For the -10 D contact lens, the power maps produced may not be what is expected, given that this is still a spherical lens. Figure 6.10 shows the power map associated with the measured wavefront. Once again, the central 2% is removed from the map.

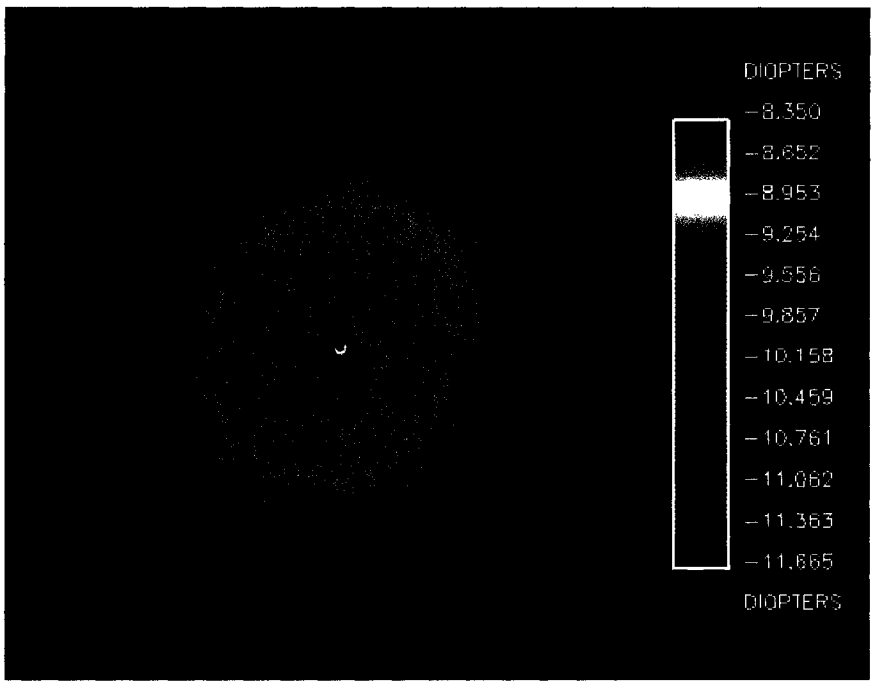

FIGURE 6.10 – Power map for the measured wavefront ($\tilde{W}_T$) for a -10 D contact lens.

The explanation for the map is that, unlike the plano-convex calibration lens, this lens has a significant amount of spherical aberration. The average power of this map is -10.503 D, owing to the fact that the spherical aberration is radially increasing the curvature of the wavefront. The difference map between measured and modeled powers

is perhaps more useful for this lens than for the calibration lens in that the effects of spherical aberration are eliminated. The map in Fig. 6.11 has been increased in resolution; pixels lying outside the range of the colorbar appear black.

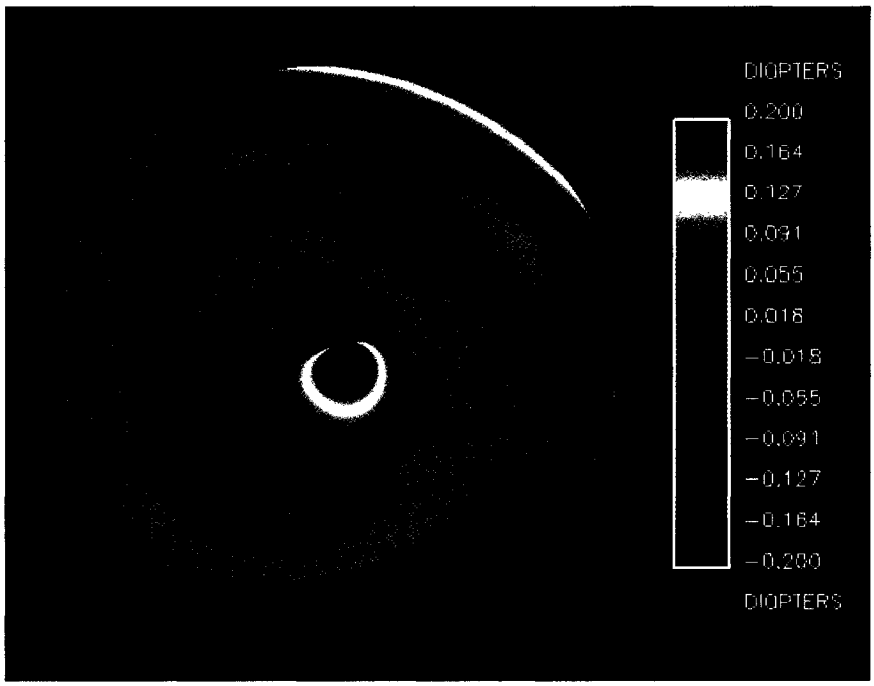

FIGURE 6.11 – Difference power map for a -10 D contact lens.

The average power of the full-resolution difference map is 0.024 D. This fact is supported by the dominance of green in the above map. Note that increase in resolution only eliminated pixels near the center, a result of the aforementioned instability near the center.

6.3.3 Output from Toric Lenses

Following the order in which the classes of contact lenses were initially presented, the next class is toric lenses. With an intuitive feel for radial axial power, one might expect the power map for a toric lens to look like Fig. 6.12.

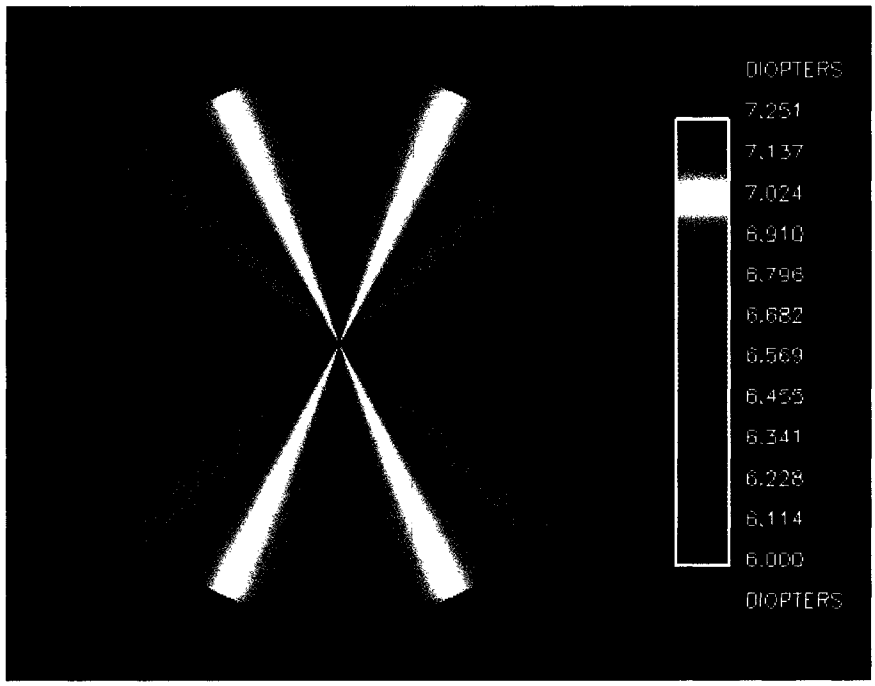

FIGURE 6.12 – Power map for a synthetic toric wavefront.

The map above was produced by using the general sag equation with different radii in each principal meridian. However, this is not what actual toric contact lenses produce. Once again, spherical aberration adds a significant conic to the wavefront. The maps produced by toric contact lenses look more like the map in Fig. 6.13, where conic constants have been added to the synthetic wavefront used in Fig. 6.12.

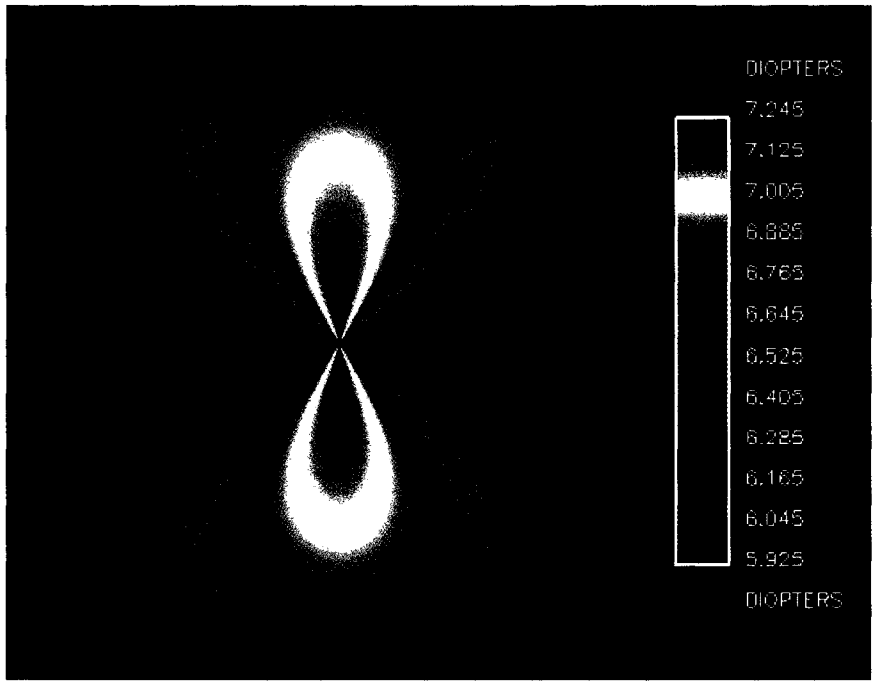

FIGURE 6.13 – Power map for a synthetic toric wavefront with different conic constants in each principal meridian.

The toric lens analyzed in Chpt. 5 produces the power map seen in Fig. 6.14. Here, the central 5% has been eliminated to better show the toric nature of the wavefront.

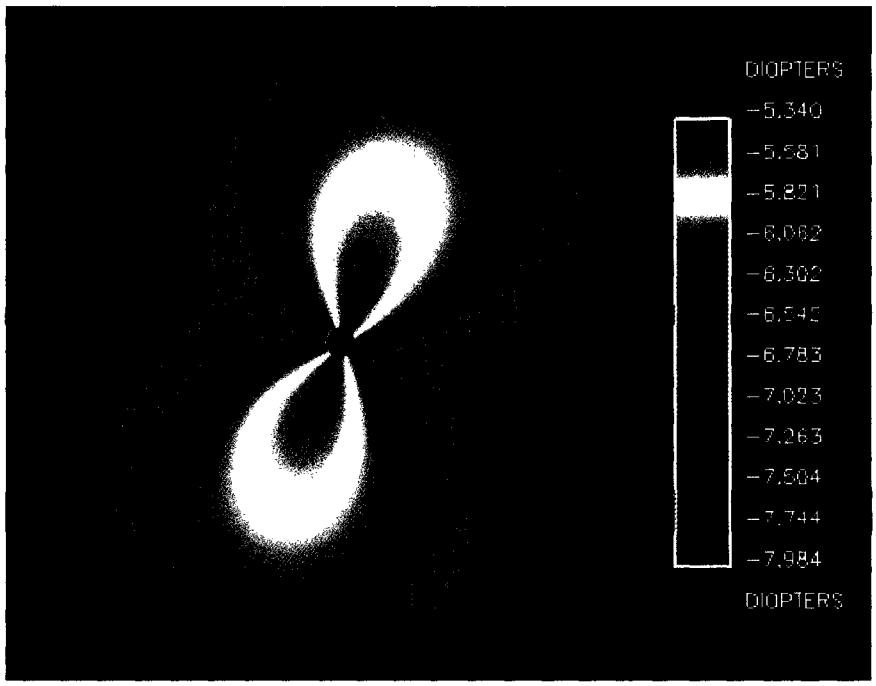

FIGURE 6.14 – Power map for the measured wavefront from a toric contact lens.

Note that the orientation of the map agrees with the interferogram of the lens (see Fig. 5.4). The power map for the modeled wavefront at the same resolution is shown in Fig. 6.15.

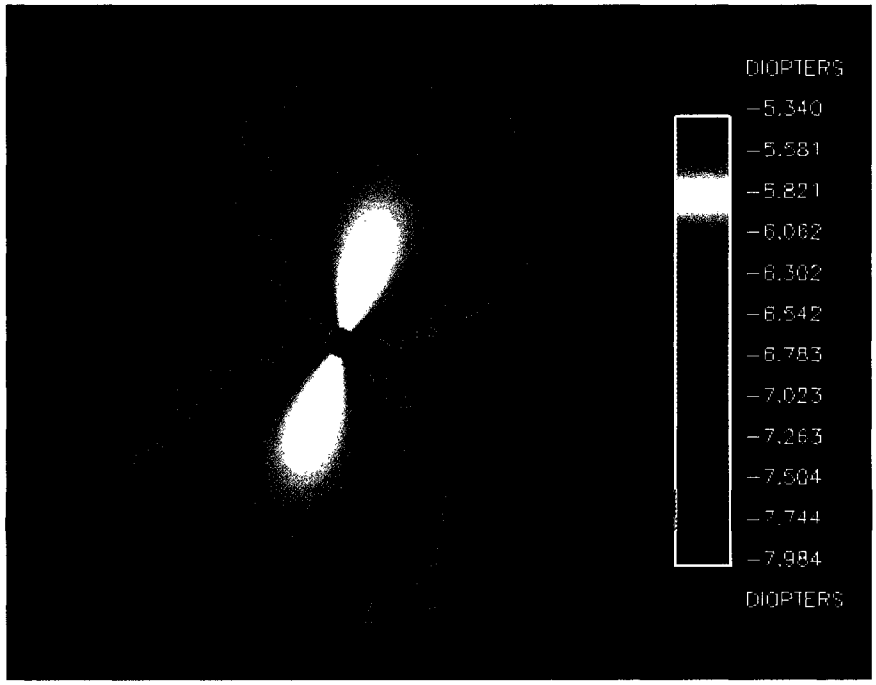

FIGURE 6.15 – Power map for the modeled wavefront.

The noticeable difference between the two power maps is in agreement with powers derived from the Zernike coefficients reported in Chpt. 5. For the measured wavefront, the prescription from the Zernikes is -5.373 / -1.233 x 177.8°. The modeled wavefront's prescription is -5.720 / -1.190 x 180°. From a qualitative point of view, these prescriptions are in agreement with the preceding power maps.

6.3.4 Output from Bifocal Lenses

Unlike torics, bifocal lenses do produce what one would think they should produce: a map with concentric rings dominated by the two colors corresponding to the near and distance powers. The power map for the bifocal lens measured in Chpt. 5 is in Fig. 6.16.

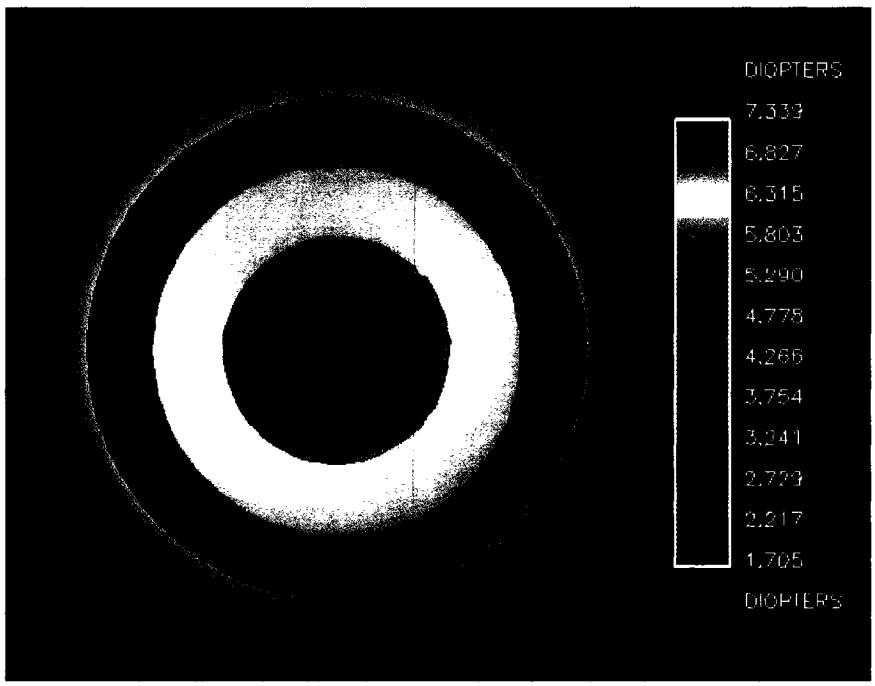

FIGURE 6.16 – Power map for the measured wavefront from a bifocal contact lens.

The central 2% of the map has been removed again, allowing for greater resolution in the colorbar. For bifocals, the power map for each zone is made individually, and then the individual maps are combined. The black rings bordering each zone are missing pixels due to the algorithm not producing a power for pixels at the data boundaries. These pixels also correspond to the unknown blend between zones or the junctions between the different modal-zonal fits. The darker color for the fourth ring compared to the second ring is most likely caused by an increased amount of spherical aberration in the outer ring.

As an afterthought, what do the power maps look like for the noisy, raw wavefronts? Fig. 6.17 shows the power map for the raw measured wavefront (see Fig. 5.9) for the analyzed bifocal.

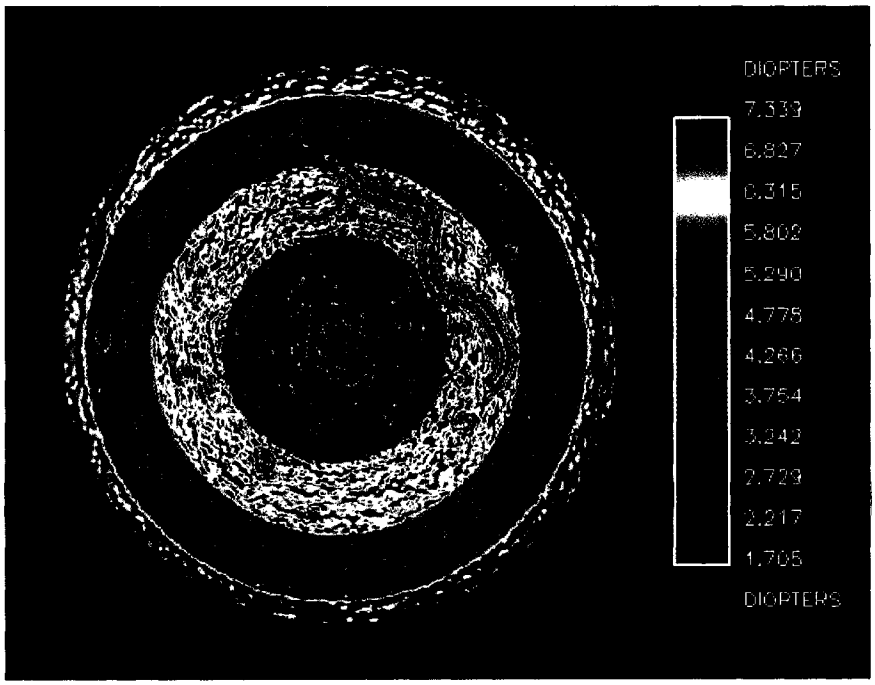

FIGURE 6.17 – Power map for the raw wavefront from a bifocal contact lens.

The fact that the output looks anything like the map shown in Fig. 6.16 is a welcome surprise. The success of this map should be credited to the method used to compute the radial derivative. This map has a number of interesting features to point out. First, the number of missing pixels is not so high as to obscure the power of each zone. Missing pixels are concentrated near the center and around areas where debris in the measurement path was located, but not at the junctions between zones. The most noticeable piece of debris is the long snake-like piece in the upper-right quadrant of the map. A close look at Fig. 5.8 shows the debris in the lower-left quadrant (remember that there is a 180°

rotation between the conjugate planes of the interferogram and measured wavefront). The pixels between zones are predominately green, indicating that the measured power in the boundaries is between the near and distant powers of the zones. This output is a strong indicator that the wavefront is continuous in slope and curvature across the zone boundaries.

6.3.5 Output from Multifocal Lenses

The power maps for the two measured multifocal lenses are surprisingly different given the similarity between the two measured wavefronts. Figure 6.18 contains the power map for the wavefront in Fig. 5.16. Once again, the central 2% of the map has been removed.

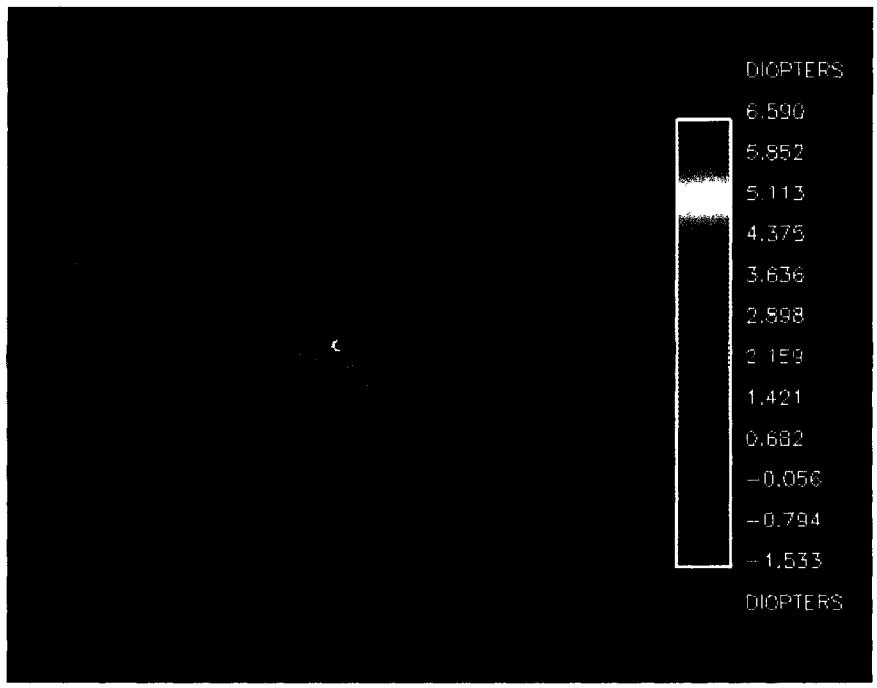

FIGURE 6.18 – Power map for a multifocal contact lens from the wavefront shown in Fig. 5.16.

The unexpected aspect of this power map is the oscillation in power seen in the periphery of the lens. There is no apparent indication of this in the wavefront shown in Fig. 5.16.

The other multifocal lens, shown in Fig. 5.17, produces the map seen in Fig. 6.19.

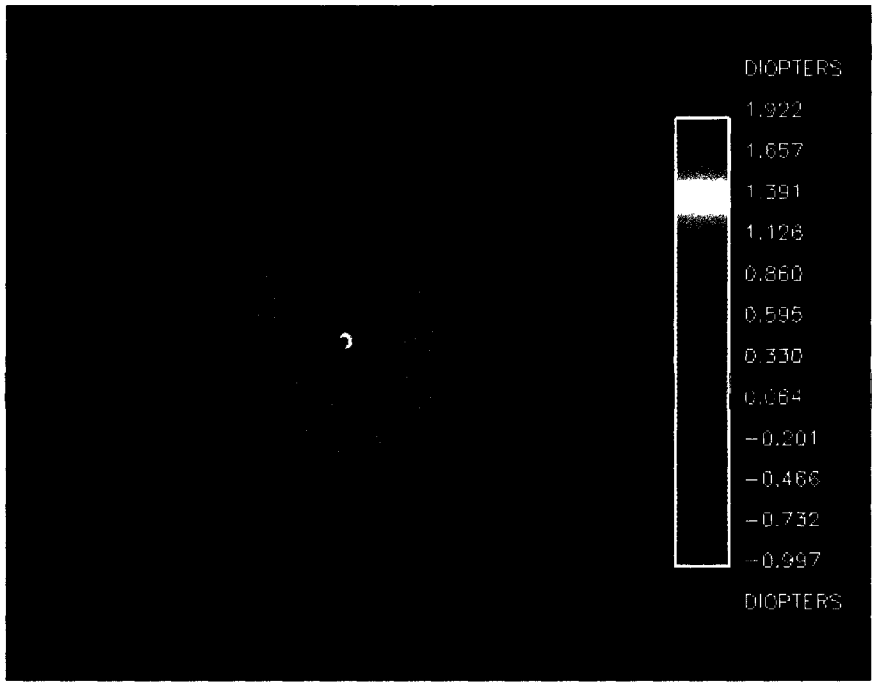

FIGURE 6.19 – Power map for a multifocal contact lens from the wavefront shown in Fig. 5.17.

For this multifocal lens, of a different design, the central power spans over a much larger area. Also, the oscillations in power seen in the prior lens are not seen in this lens. More needs to be known about the designs for these lenses before further conclusions can be reached.

7 TRADEOFF BETWEEN DYNAMIC RANGE AND SENSITIVITY

The last section of Chpt. 1 introduced the pros and cons of immersion testing. Basically, testing immersed optics should provide an increase in dynamic range and a decrease in sensitivity. Theoretically, the amount of the increase or decrease is dictated by the solution factor (SF), which is the ratio of the difference in indices between the test optic and its surrounding medium.

The goal here is to lay the foundation for a quantitative understanding of the tradeoff between dynamic range and sensitivity. How should the dynamic range and sensitivity be defined? Is there a direct, one-to-one correlation between the gain in dynamic range and loss in sensitivity? How does the Nyquist limit factor in with immersion testing? What are the practical concerns with such a testing scheme? These are the questions that need exploring.

7.1 Dynamic Range Ratio (DRR)

The idea that dynamic range and sensitivity are linked is intuitively obvious. For example, consider the task of measuring the distance between two points. If the two points are close together, say 100 nm apart, then the ability to measure the distance to something like 1 nm seems reasonable. But if the two points are far apart, say 100 km, making the measurement to same resolution of 1 nm now seems quite impossible. This

same situation holds in interferometry. The more wavefront sag, or OPD, that the interferometer is capable of measuring, the harder it is for the interferometer to provide a high degree of sensitivity.

The comparison between the dynamic range and sensitivity can be quantified by taking the ratio between the dynamic range and sensitivity, forming a dimensionless quantity that is defined here as the dynamic range ratio (DRR). The DRR is much like the signal-to-noise ratio (SNR) found throughout science and engineering. The common definition for SNR is the mean value for a parameter or signal divided by the standard deviation formed from measuring the parameter or signal several times (Frieden, 1991). With the DRR, the ratio is between the maximum possible departure for a wavefront divided by the minimum resolvable feature of the wavefront. The next step is defining these quantities.

Determining the maximum departure leads back to the discussions of Chpt. 2, where it was explained that the pixel frequency should be greater than twice the maximum fringe frequency, a direct result of satisfying the Nyquist condition. In the limiting case of twice the maximum fringe frequency equaling the pixel frequency, Eq. 2.19 and Eq. 2.21 (pertaining to spherical wavefronts) can be equated, giving:

$$2f_{\text{Max. @ Detector}} = f_{\text{Pixel}},$$
$$\frac{2r}{m\lambda R} = \frac{1}{\text{PS}}. \qquad \text{Equation 7.1}$$

In the above equation, r is the radius of the test aperture, m is the magnification, λ is the wavelength of the test, R is the radius of curvature for the wavefront, and PS is the pixel spacing of the detector. Since the parameters of m, λ and PS are independent of the test part, the above equation can be rearranged to give an R/r ratio for the interferometer. For CLOVER, this value is

$$\frac{R}{r} = \frac{2\text{PS}}{m\lambda} = \frac{2 \cdot 0.014}{2.044 \cdot 0.5435 \cdot 10^{-3}} = 25.2. \qquad \text{Equation 7.2}$$

This ratio says that this interferometer, over a test aperture with radius r, can measure wavefronts with a radius of curvature (R) greater than 25.2 times the radius of the test aperture. This ratio gives the upper bound on dynamic range, or the lower bound for the testable radius of curvature for a wavefront. Note that this can be used in conjunction with the parabolic approximation for OPD, giving the maximum testable OPD for a given test aperture radius:

$$\text{OPD} = \frac{r^2}{2R}, \qquad \text{Equation 7.3}$$
$$50.4\,\text{OPD}_{\text{MAX}} = r.$$

This relationship can be used to find the largest possible test aperture given a specific OPD, or the largest OPD that can be tested over a specific aperture. Remember that this discussion is assuming spherical wavefronts, but the general concepts can be applied to aspheric wavefronts as well.

The second half of the DRR is the minimum resolvable change in wavefront. This tells us how well a specific feature of the wavefront can be measured. There are several

different definitions that could be used here. To make use of data already collected, and in following with the overall measurement scheme employed, the parameter chosen is the radius of curvature as derived from the Zernike polynomial fit to the wavefront. The standard deviation of the radius is then converted into a standard deviation for OPD using the parabolic approximation. By using the Zernike fit, the derived sensitivity is for the wavefront as a whole; the sensitivity depends equally on all regions of the wavefront.

To study the effects of immersion on the DRR, the data collected for the calibration lens, both in air and immersed in saline, can be used. The data presented was collected over ten trials with a test aperture radius (r) of 2.5 mm. For the measurements made with the test optic immersed, the reported value for the radius of curvature has been scaled using the solution factor (2.8972) so that a direct comparison can be made. Table 7.1 lists the pertinent data from the repeatability study.

Testing Condition	R (mm)	σ (mm)
Lens in Air	154.264	0.0980
Lens in Cuvette	153.109	0.2236

TABLE 7.1 – Relevant data from the repeatability study on CLOVER using the calibration lens. Data was collected over ten trials.

Right away, the data shows the expected result that sensitivity decreases with immersion. However, the maximum dynamic range is greater for the immersed optic. To determine the impact on the DRR, first the standard deviations for R are converted into deviations for OPD. This is done by differentiating the parabolic approximation, giving:

$$\delta \mathrm{OPD} = \left| \frac{r^2}{2R^2} \right| \delta R. \qquad \text{Equation 7.4}$$

The other necessary formula is the second part of Eq. 7.3, relating the maximum OPD to the test aperture. For immersion testing, this equation becomes

$$\frac{50.4\ \mathrm{OPD}_{\mathrm{MAX}}}{\mathrm{SF}} = r. \qquad \text{Equation 7.5}$$

As SF grows, Eq. 7.5 says that the maximum testable OPD also grows for a constant r. Thus, the dynamic range for the measurement has been increased. This is really just the necessary scaling to compensate for the test optic's reduction in power via immersion. Fundamentally, nothing has changed with the interferometer when the claim is made that the dynamic range has been increased. The change is confined to the test optic. Finally, Eq. 7.6 states the DRR using the above notation.

$$\mathrm{DRR} = \frac{\mathrm{OPD}_{\mathrm{MAX}}}{\delta \mathrm{OPD}}. \qquad \text{Equation 7.6}$$

Applying the above analysis to the data in Table 7.1 gives the results shown in Table 7.2.

Testing Condition	$\mathrm{OPD}_{\mathrm{MAX}}$ (λ)	δOPD (λ)	DRR
Lens in Air	91.266	0.02368	3854
Lens in Cuvette	264.416	0.05484	4822

TABLE 7.2 – Derived DRR statistics for calibration lens.
The wavelength for the interferometer is 543.5 nm.

The DRR increased by 25% for the immersion test. This was foreshadowed by the given standard deviations on radius of curvature. The ratio of the two standard deviations is 2.28, which is less than the solution factor (2.8972) by about 25%. For this experiment,

the hypothesized one-to-one increase in dynamic range and decrease in sensitivity underestimates the actual system performance by 25%.

7.2 Testing Over a Range of Solution Factors

The goal of the next experiment is to see what affect changing the solution factor has on the output from a test optic. Wanting to branch out in terms of the types of optics tested, the next experiment is done on a cylindrical lens. Cylinder lenses are notoriously difficult to test. This stems from the difficulty in producing a high quality cylindrical reference beam. Most shop interferometers have the capability of producing only different spherical reference beams given common reference optics. Testing in an absolute, or non-null, configuration eliminates the problem of matching the test and reference beams. In addition, the immersion technique, with its ability to provide a specific increase in the allowable wavefront sag, is well suited for testing cylindrical lenses. The selected cylindrical lens is an f/2 lens with a diameter of 12.5 mm. This leads to nominal value for the wavefront's radius of curvature of 25 mm. Going back to the notion of the R/r ratio (25.2 for CLOVER), with a wavefront radius of about 25 mm, the maximum test aperture is about 1 mm when the lens is tested in air. When immersed, the wavefront's radius increases by the solution factor, and therefore so does the maximum possible test aperture. For this experiment, the solution factor is the variable between trials. Every other parameter is held constant, including the test aperture. The solution factor is determined by adjusting the measured Abbe refractometer values to the interferometer's wavelength.

The natural starting point for immersion testing is water. Water has the lowest index of all common liquids, and depending on glass type, can provide a solution factor between 2 and 6. For the lens in question, immersion provides a solution factor of 2.8079. The selected analysis aperture is 2.8 mm in diameter, which corresponds to half the maximum test aperture for the f/2 lens. This is done to ensure fringes in the aperture have high modulation. The testing of fringes out to the Nyquist frequency is taken up in a later section.

The full lens interferogram is shown in Fig. 7.1. The diameter of the lens is 12.5 mm and the field of view for the interferogram is just over 14 mm on a side. Immersion in water does not provide enough of a reduction in the power of the lens to keep the entire transmitted wavefront small enough to pass through the interferometer's optics. The dark regions inside the lens boundary in Fig. 7.1 are regions that have been vignetted by either the second beamsplitter or the imaging lens. The interferogram is not at full resolution, so the fringes that appear aliased are due to the sampling of the display or printer. However, the loss of modulation near the vignetted regions is real; the fringe frequency is greater than the Nyquist frequency.

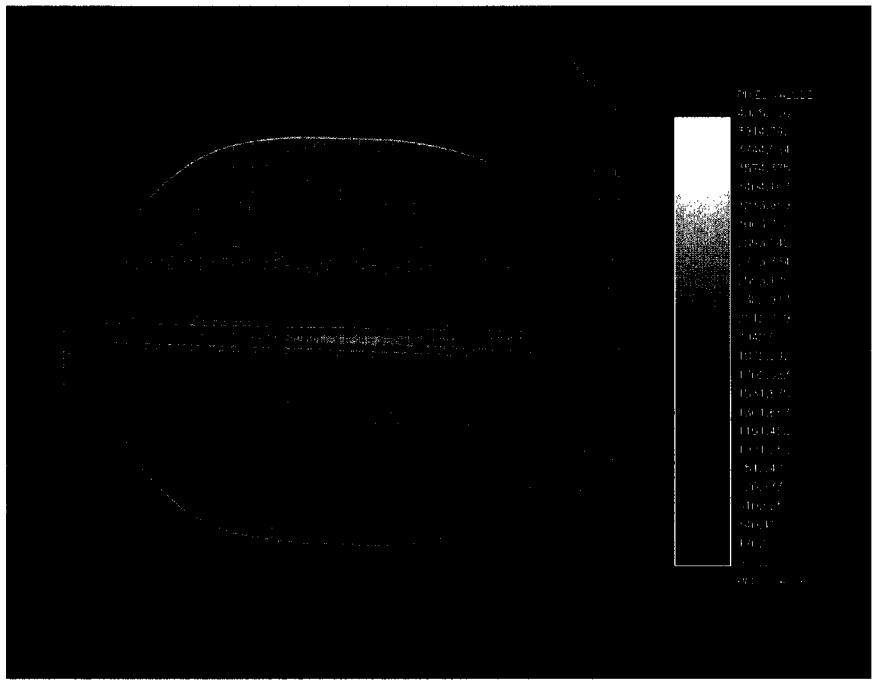

FIGURE 7.1 – Interferogram for f/2 cylindrical lens immersed in water. The solution factor is 2.8079.

Over the chosen analysis aperture, vignetting and low modulation are not an issue. With solution factor as the variable, the concern is how do the outputs, such as peak-to-valley (PV) and wavefront radius (R), change with solution factor? Figure 7.2 shows the interferogram over the chosen analysis aperture and Fig. 7.3 shows the Zernike fit to the measured wavefront ($\tilde{W}_T$).

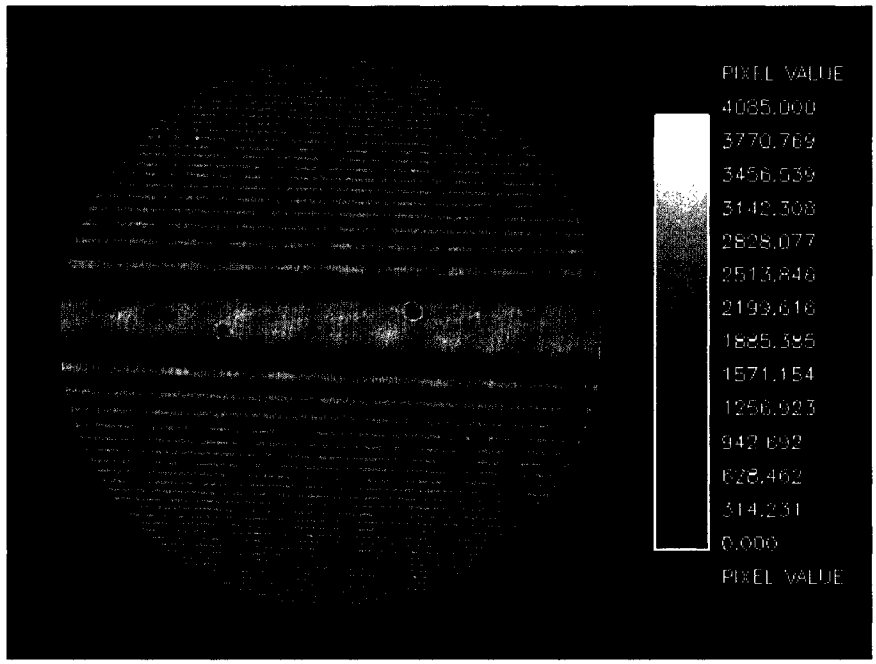

FIGURE 7.2 – Interferogram over a 2.8 mm test aperture (SF = 2.8079).

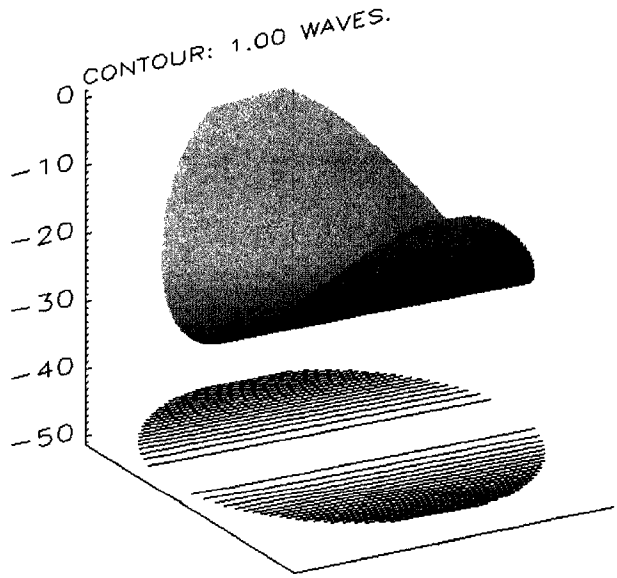

FIGURE 7.3 – Zernike fit to measured wavefront ($\tilde{W}_T$)
for f/2 cylindrical lens (SF = 2.8079).

An interesting surface is the measured wavefront minus the best-fit cylinder. This is accomplished by removing the first two Zernike terms associated with astigmatism in addition to the terms for tilt and focus. The resulting surface is in Fig. 7.4.

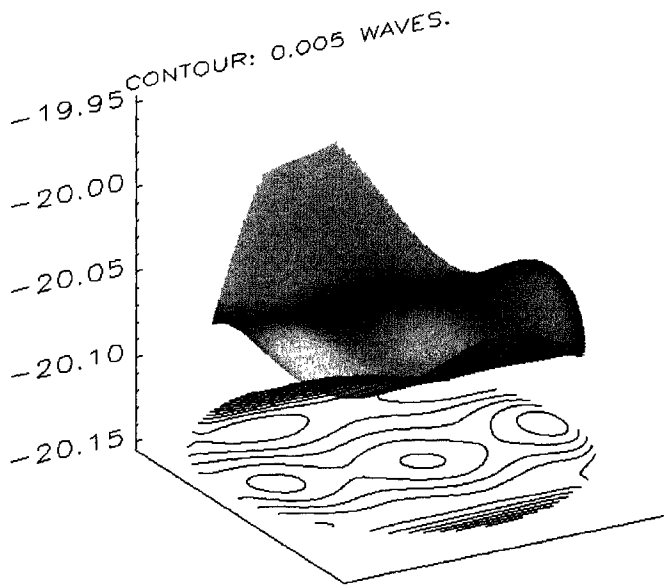

FIGURE 7.4 –Measured wavefront minus best-fit cylinder (SF = 2.8079).

The oscillation in the direction of the cylindrical power is to be expected. This is the remaining spherical aberration. What is unusual is the presence of humps along the plano-meridian. This is an unusual feature, one that has not been seen with any other test optic. The likely answer is that this is an error in the lens, perhaps due to the manufacturing process.

To proceed with the experiment on testing over a range of solution factors, the lens is now immersed in index-matching fluid with an index of 1.4018 at the interferometer's

wavelength, giving a solution factor of 4.4728. The lens is evaluated over the same 2.8 mm test aperture. Figure 7.5 shows the interferogram over the test aperture; note that fewer fringes are present here than in Fig. 7.2.

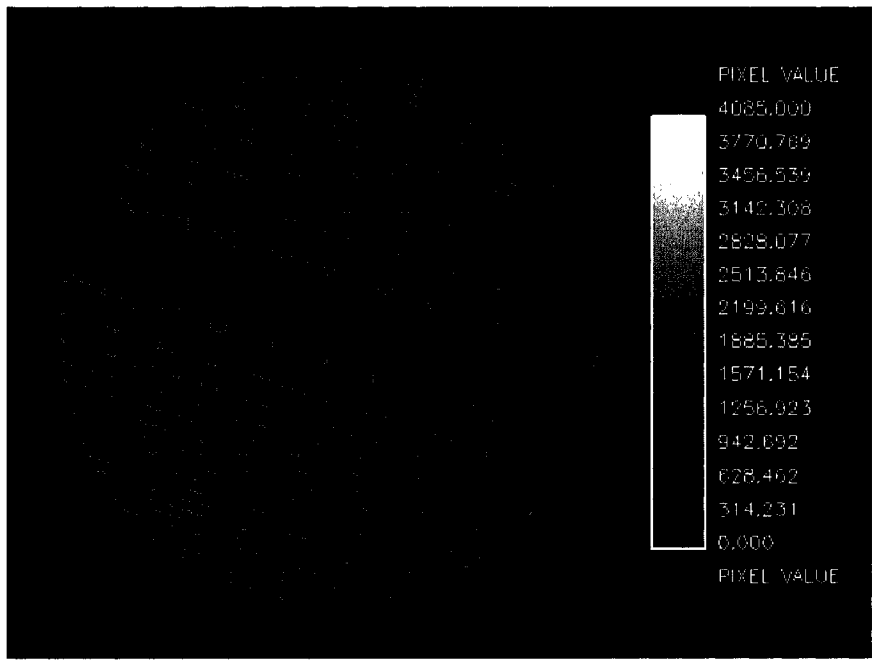

FIGURE 7.5 – Interferogram over a 2.8 mm test aperture (SF = 4.4728).

As expected, the bumps in the measured wavefront minus the best-fit cylinder have been reduced in amplitude. With contours at $\lambda/1000$, the three bumps are still distinguishable, although the spacing does not seem to be as regular.

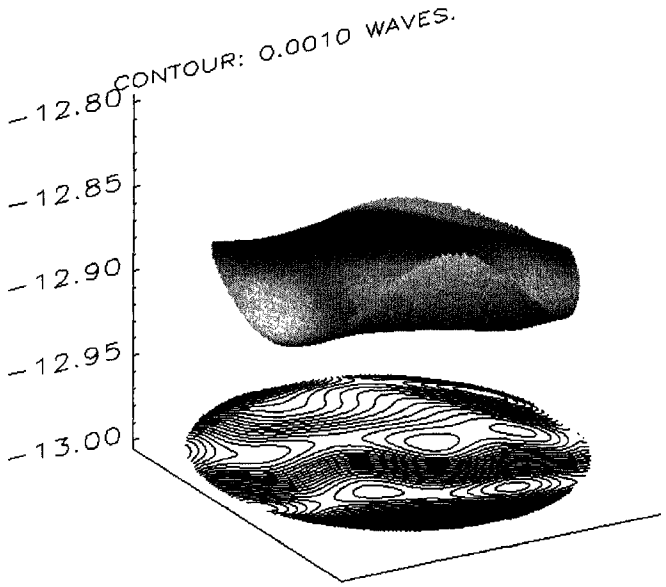

FIGURE 7.6 –Measured wavefront minus best-fit cylinder (SF = 4.4728).

The third fluid has an index at the interferometer's wavelength of 1.4614. This gives a solution factor of 9.2246, or a difference in index between the fluid and lens of only 0.0561. This is enough of an index match to collect the full beam from the test optic, as can be seen in the full lens interferogram shown in Fig. 7.7.

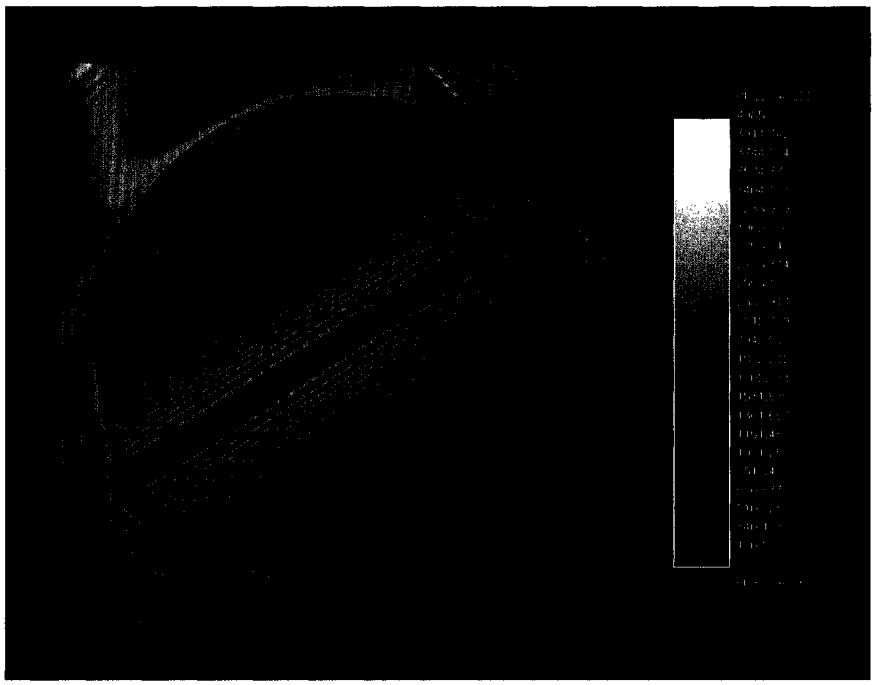

FIGURE 7.7 – Full lens interferogram for f/2 cylindrical lens (SF = 9.2246).

With so little power, the surface formed by subtracting the best-fit cylinder from the measured wavefront no longer resembles the surface seen in Fig 7.4. The three bumps seen in the prior surfaces are gone; the bumps that are present are no longer orientated with the plano-meridian.

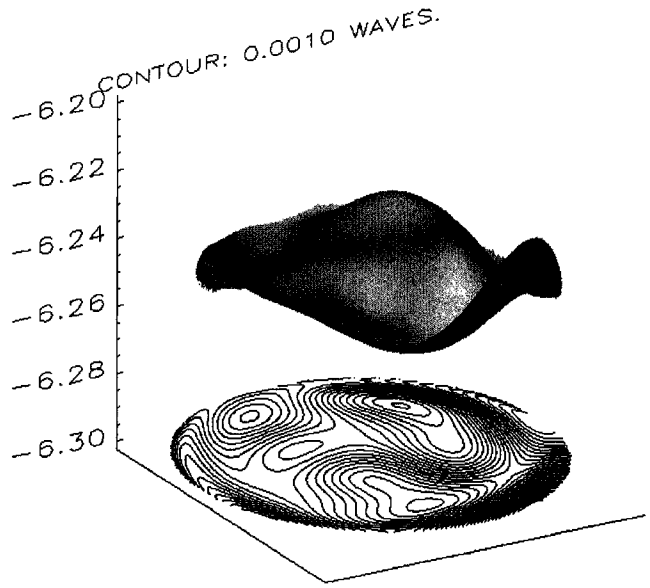

FIGURE 7.8 –Measured wavefront minus best-fit cylinder (SF = 9.2246).

Clearly the index-matching fluid is removing enough power to significantly alter the transmitted wavefront and the resulting best-fit cylinder. Increasing the solution factor has decreased the sensitivity to a point where the resolution needed to see the bumps has been lost.

Now that data has been collected with three different solution factors, comparisons can be made in the derived outputs. Table 7.3 shows the pertinent outputs for the three trials. The output for the wavefront's radius of curvature is derived from the ophthalmic prescription for the wavefront, as the analysis code is geared towards producing output measured in diopters. The prescriptions are reported in negative cylinder form and then converted to spherical and cylindrical powers (Schwiegerling, 2000). Finally, the powers are converted into air-equivalent (SF = 1) radii. Assuming a perfect lens and using

Gaussian formulas gives a radius of 25.043 mm for the wavefront at the interferometer's wavelength. The reported tolerance on focal length is ±3%.

Solution Factor	PV (λ)	Spherical Radius (mm)	Cylindrical Radius (mm)
2.8079	22.835	-12821	27.246
4.4728	15.042	-200000	25.894
9.2246	7.321	25000	24.959

TABLE 7.3 – Results for an f/2 cylinder over a range of solution factors. The spherical radius is shown only as a means of verifying the validity of the conversion between ophthalmic power and radius.

One interesting interpretation of the above results is to see how the ratio of given solution factors compares to the PV ratio for any two trials. These comparisons are shown in Table 7.4.

Solution Factor Pair	SF Ratio	PV Ratio
2.8079 / 4.4728	1.593	1.518
4.4728 / 9.2246	2.062	2.055
2.8079 / 9.2246	3.285	3.119

TABLE 7.4 – Results for an f/2 cylinder over a range of solution factors.

Overall, the agreement between the SF ratio and the PV ratio for the three trials is about 4%. The second pair of indices, representing the two trials with the lowest measured sag (lowest PV), has the best agreement between the two ratios. This could be due to the smaller absolute difference in the amount of wavefront sag between the two trials.

Another interesting trend in the data is the decrease in the cylindrical radius with an increase in solution factor. The reported radius is the best-fit sphere in the meridian of the measured cylindrical power. To first-order, this radius changes linearly with the solution factor. When third-order aberrations are considered, the cubic dependence of spherical aberration on power ruins the linear relationship between the solution factor and best-fit sphere (Welford, 1986). Of course, the other factor is that the linear relationship between power and solution factor assumes a thin lens. More experimenting and modeling is needed to determine to what extent these effects are in play.

7.3 Testing to the Nyquist Limit

The final experiment is to see how close to the Nyquist limit the test lens can be accurately tested. The lens is immersed in water to provide more pixels across the testable radius. Going back to Eq. 7.2, the relationship between wavefront radius and the radius of the test aperture under the current testing conditions is

$$\frac{R}{r} = 25.2. \qquad \text{Equation 7.7}$$

Including the solution factor for the lens immersed in water and assuming the ideal value for R of 25.043 mm gives a maximum test aperture of:

$$\frac{R \cdot \mathrm{SF}}{r} = 25.2,$$
$$r = \frac{25.043 \cdot 2.8079}{25.2} = 2.790 \text{ mm}. \qquad \text{Equation 7.8}$$

This is how the test aperture of 2.8 mm in diameter used in the last experiment was derived. Now the goal is to test out towards 100% of the maximum test aperture. Table 7.5 shows the results of testing from 50% to 95% of the Nyquist radius of 2.790 mm.

Nyquist Radius (%)	PV (λ)	Spherical Radius (mm)	Cylindrical Radius (mm)
50	25.465	-31250	24.686
60	37.249	-25000	24.228
70	51.975	-200000	24.119
80	68.590	-333333	24.030
90	88.239	-166667	23.838
95	101.889	2155	20.675

TABLE 7.5 – Results for an f/2 cylinder over an increasing test aperture.

First, the data at 95% is clearly in error, as verified by the erroneously small spherical radius. This could be due to a number of factors, including the loss of data due to poor modulation, errors in the phase unwrapping, or the MTF associated with the detector. The other data points are self-consistent. The decrease in radius, or an increase in power, is probably due to the increased spherical aberration included in the wavefront as the radius is increased. This puts this experiment at odds with the last experiment, where an increase in the solution factor, giving a decrease in the sag of the wavefront measured, also produced a decrease in the cylindrical radius. Again, more experimentation is needed, especially testing over a range of solution factors, which seems to provide the most unexpected results.

7.4 Discussion on Experiments Performed

The question now is what to make of the various experiments and their results. Certainly more needs to be done to provide proof of the trends seen, but the limited data collected offers several insights. First, the testing of the calibration lens in air and immersed in saline solution validates the notion that the solution factor can be used as a linear quantity for lenses with relatively small amounts of power. In Chpt. 3 the statement was made that the thin lens approximation was good to under a 1% error for lenses less than 10 D in power. The calibration lens, at 6.57 D, showed a difference of 0.75% between the power measured in-air and in the cuvette. The standard deviation was proportionally less compared to the maximum possible OPD when the lens was immersed, giving rise to the higher DRR.

Perhaps the high power of the f/2 cylinder lens (40 D) is the source of the trend exhibited over the range of solution factors. At the lower solution factors, the lens is still powerful enough that the assumption of the solution factor providing a linear change in power is not valid. Preliminary modeling of the lens over a range of solution factors shows a slight increase in the wavefront radius (R) as the solution factor is increased, which would be consistent with the idea of spherical aberration contributing to the difference in R for different solution factors or different test aperture sizes. This particular experiment needs more attention.

For the third experiment, the trend is a decrease in R with an increase in the test aperture's diameter. This is consistent with the notion of spherical aberration being the culprit of the difference in the measured power. Since the lens is positive, positive spherical aberration is added with a fourth-order dependence on the size of the test aperture. The increase in positive spherical aberration therefore gives a shorter best-fit sphere radius for the wavefront.

Combined, the experiments reveal some of the capabilities and limitations of the instrument and the technique of immersion. The first experiment shows the repeatability in the fit to the wavefront's curvature is 0.02368 λ, or λ/42, when tested in air. The repeatability decreases when the lens is immersed, as it should since the wavefront's curvature is reduced with immersion. The second and third experiments show that a solution factor of at least 9 can be used and the test optic can be measured out to 90% of the Nyquist limit. Combined, these numbers give a new R/r ratio of

$$\frac{R}{r} = \frac{25.2}{9 \cdot 0.9} = 3.11. \qquad \text{Equation 7.9}$$

This is a factor of eight improvement over the prior ratio, which assumes testing out to the full Nyquist limit. Nevertheless, the gain of immersion testing is significant. Another way to think about the R/r ratio is to consider R a focal length and r as half the diameter of the wavefront. In this case the R/r ratio equals twice the f-number. The benefit of this is that the necessary solution factor can be determined given the f-number. For example, the cylindrical lens tested is f/2. Twice this number is only f/4. In air, this lens cannot be

tested out to its full aperture; the *R/r* ratio is 25.2. The necessary solution factor is 25.2/4, or 6.3. This is why in the experiment over solution factors only the third index-matching fluid (SF = 9.2246) provided enough of an index-match to capture the entire wavefront. This illustrates the usefulness of the *R/r* ratio in determining the testability of a given optic. There are, however, two points of caution. One is that the test optic's diameter and interferometer's magnification must be considered to be sure that the entire diameter can be imaged. The other main caution is that the simplicity of comparing the *R/r* ratio to the *f*-number assumes spherical optics. The testing of aspheric optics requires the use of comparing waves/radius between the test optic's wavefront and the interferometer's detector.

If the lens can be tested in air, are there still benefits to immersing the optic? Probably not, for there are some important assumptions and concerns with immersion testing. First, the optic has to be capable of withstanding immersion, which could be an issue for some plastics. Second, a suitable cell or cuvette is necessary. This will become part of the overall test optic, and must be of high quality. The ideal cell is one that just surrounds the test optic, for quality index-matching fluids are quite expensive. In addition, passing through less fluid is better for homogeneity and optical path considerations. Third, the index of both the test optic and surrounding fluid must be known. An Abbe refractometer works well with liquids and plano-surfaces, but is not a good candidate for convex or concave surfaces. Finally, the assumption that the solution factor will provide a linear change in power must either be accepted or dealt with. An

exact solution can be obtained for a lens if one surface, the index, and thickness are all known. This may be too many assumptions or factors to measure to make immersion worthwhile.

Perhaps the biggest conclusion, aside from the need for more experimentation and modeling, is that immersion testing is a viable method for increasing the capabilities of transmitted wavefront testing. With contact lenses, there is no choice; the lenses must be tested immersed in saline. For other optics, the ability to immerse may be the difference between getting results and not getting results. The difficulties of immersion testing may be a small price to pay for meaningful data that can be obtained no other way.

8 TRANSMITTED WAVEFRONT TESTING OF OTHER COMPLEX OPTICS

In the previous chapters a variety of optics have been tested: immersed spherical, toric, bifocal, and multifocal contact lenses as well as in-air and immersed spherical and cylindrical glass lenses. Presented here are the results from testing two other complex types of optics: liquid crystal diffractive optics and microlenses made in solgel, a polymer with some similarities to the hydrogel materials used to manufacture contact lenses (Lee, 2003). Both of these complex optics are under development by researchers at the University of Arizona. The testing of these lenses was done primarily to see if they could be tested using interferometry and what preliminary results could be obtained. Given the exploratory nature of these tests, the wavefronts shown were not calibrated using the full calibration process including reverse raytracing. Any data analysis done with these lenses was done only in Intelliwave.

8.1 Diffractive Lenses

Research is ongoing at the University of Arizona in developing the technology of forming diffractive lenses via liquid crystals. This is a multi-faceted project; research includes studying the materials used, the systems engineering of the lenses and associated electronics, and the optical performance of the lenses. Optical performance is evaluated in a number of ways, including diffraction efficiency calculations and image resolution

measurements. The CLOVER interferometer was suggested as a means of measuring the quality of the wavefront produced by such lenses.

Initial testing involved a liquid crystal lens with a nominal focal length of 1000 mm. The lens is formed by applying different voltages to annular zones of the liquid crystal, thereby forming Fresnel zones. Figure 8.1 shows the lens in the interferometer with the reference arm blocked, which gives a bright field image of the test optic. One image is with the lens off (no voltage applied to crystal) and the other is with the lens on. The black strips seen at the top, bottom, and sides of the images are electrodes connected to the different annular zones.

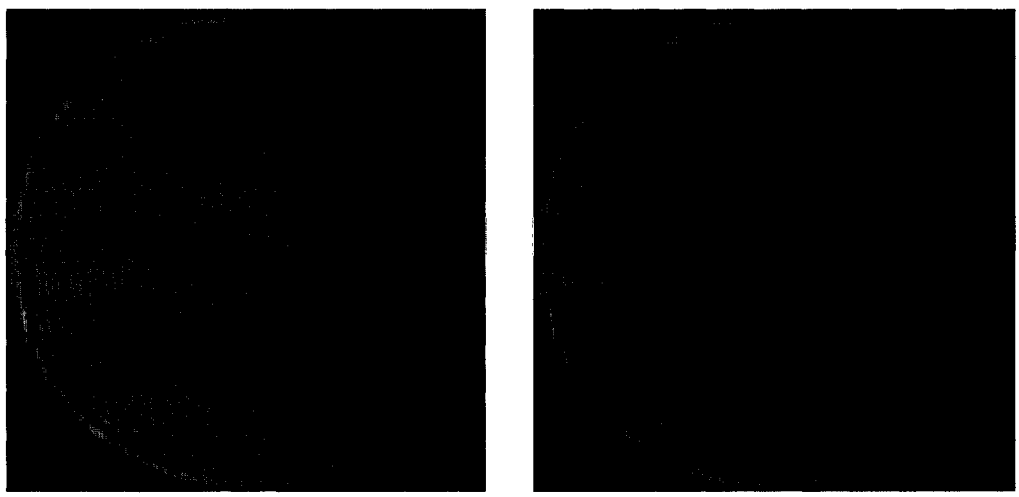

(a) (b)

FIGURE 8.1 – Bright field images of a diffractive lens formed via liquid crystal. The lens is off in (a) and on in (b).

Figure 8.1 (a) shows that until the lens is turned on, the presence of the lens or the zones is nearly impossible to tell. With the reference beam included, the resulting interferograms are those shown in Fig. 8.2.

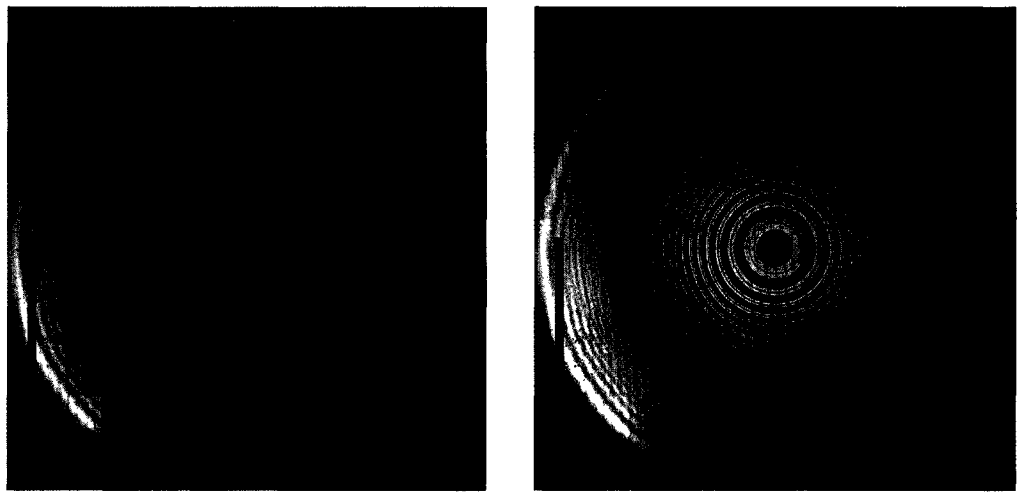

(a) (b)

FIGURE 8.2 – Interferograms for diffractive lens with (a) lens off and (b) lens on.

A couple of important features with this lens can only be seen in a close-up view of the interferogram, which is shown in Fig. 8.3.

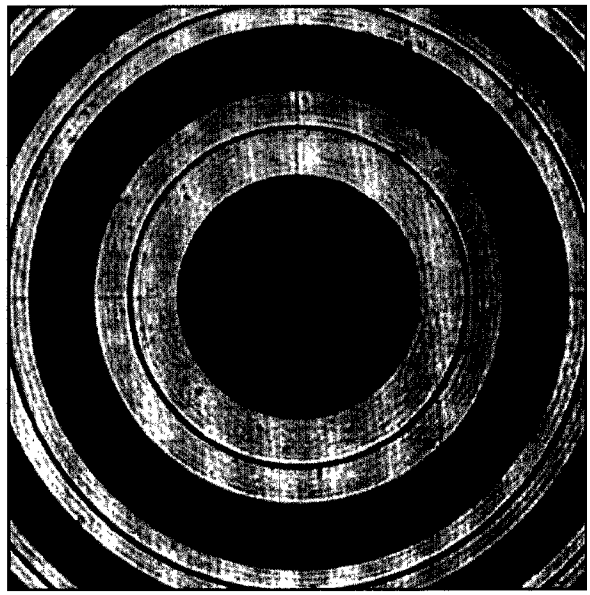

FIGURE 8.3 – Close-up of the interferogram in Fig. 8.2 (b).

First, the fact that each fourth zone has the same grayscale intensity says that this lens is a four-step binary optic, in that each wavelength of sag is broken into four different phases (Fischer, 2000). The second feature of this lens is that there are gaps, or regions of zero modulation, between each phase zone. This feature confused the sophisticated unwrapping algorithms in Intelliwave, but a simple algorithm where bad pixels are ignored was able to unwrap the phase. However, the presence of these gaps leads to other unwanted artifacts in the performance of the lens, including poor diffraction efficiency.

A second lens, one without gaps between the phase steps, was built and tested. Figure 8.4 shows the full interferogram and a close-up at the center, revealing the absence of

gaps. This new lens has a nominal focal length of 500 mm and employs a different electrode structure, as can be seen in Fig. 8.4.

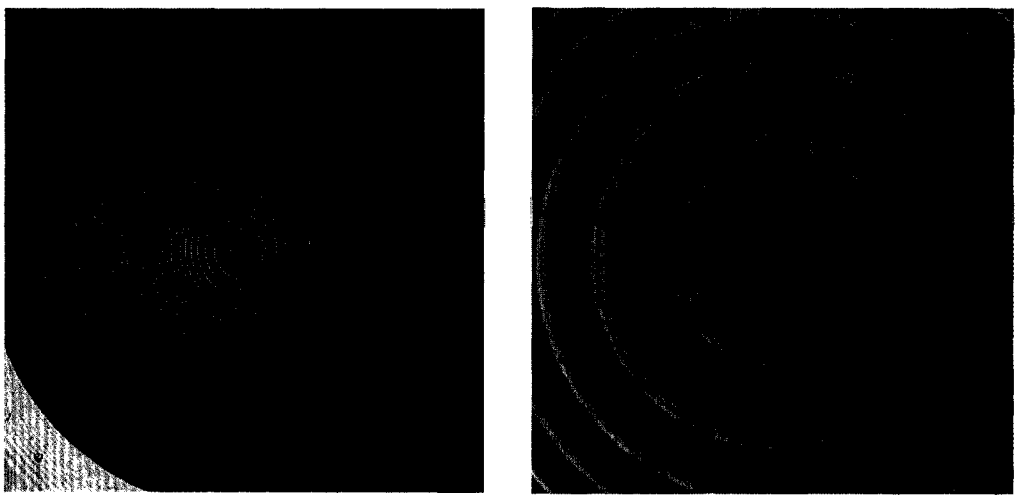

(a) (b)

FIGURE 8.4 – Interferogram (a) and close-up (b) for a new diffractive lens without gaps.

The reported imagery and overall performance of this lens was better than that for the lens with gaps. The unwrapped wavefront and the wavefront with tilt and focus removed are shown in Fig. 8.5.

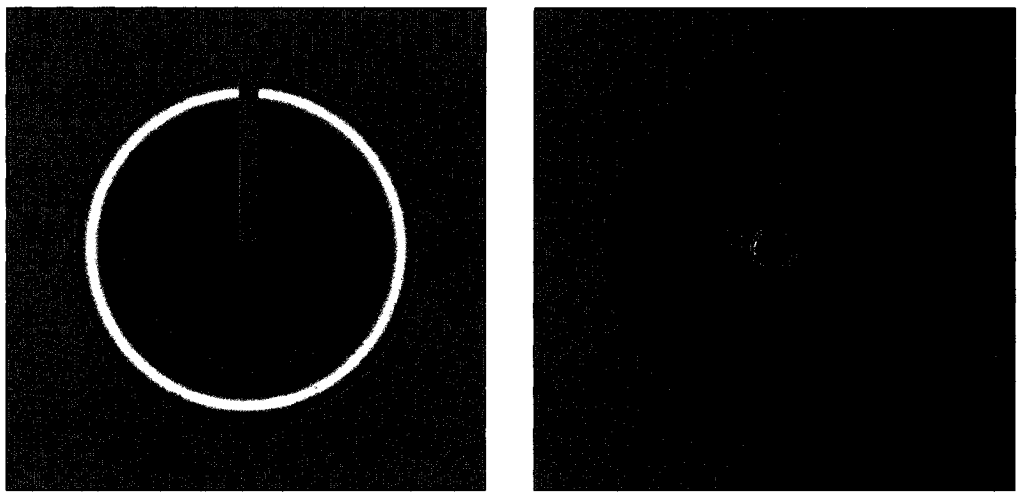

(a) (b)

FIGURE 8.5 – Unwrapped wavefront (a) and wavefront minus tilt and focus (b) for the diffractive lens.

The OPD over 10 mm leads to a focal length of 508.6 mm for the lens. At the design wavelength, the OPD leads to a focal length of 502.6 mm for a difference of only 0.5% from the design focal length of 500 mm.

As mentioned earlier, image resolution is an important metric for these lenses. Figure 8.6 shows two images using a lens assembly that contains the diffractive lens and a refractive element. The image on the left is with the diffractive lens off. On the right is the image with the lens on.

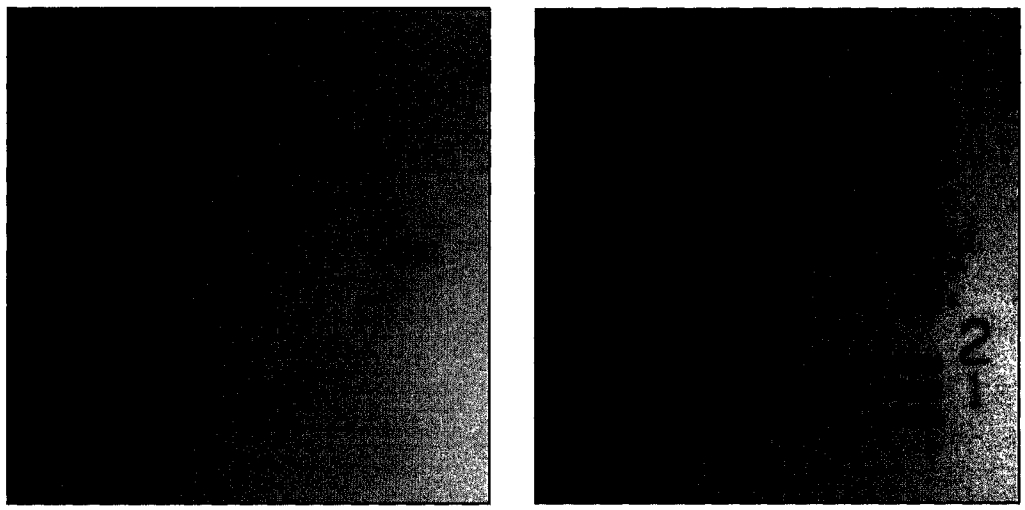

(a) (b)

FIGURE 8.6 – Images from compound diffractive-refractive imaging system: (a) diffractive lens off and (b) diffractive lens on.

Perhaps the most interesting output for this lens is the MTF plot produced in Intelliwave and shown in Fig. 8.7. In theory, the MTF plot is made by considering the wavefront minus tilt and focus as the pupil function for the test optic and computing the necessary autocorrelation (Goodman, 1996).

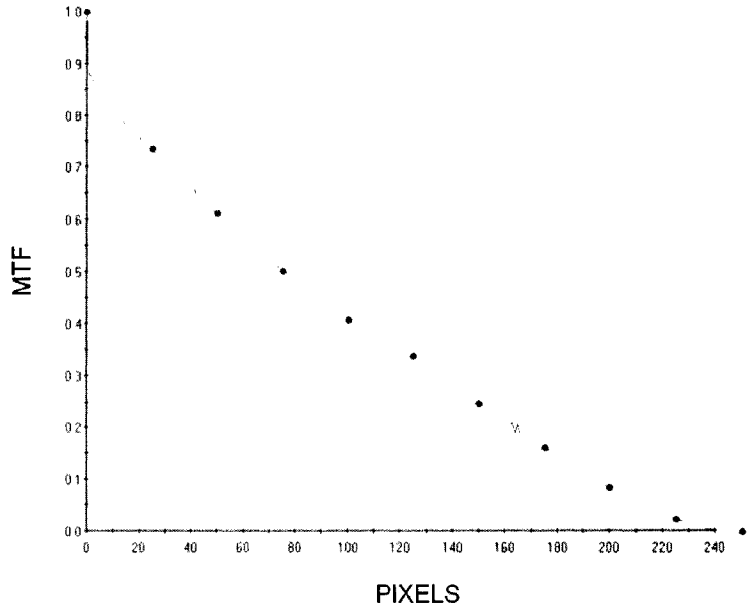

FIGURE 8.7 – MTF plot for the diffractive lens.

The important aspect of the MTF plot is the spike at zero spatial frequency. This is an artifact of the lens being a diffractive optic (Buralli, 1992). Being a diffractive optic, the point-spread function (PSF) for a given order has a central peak, or core, from the order under examination and a much broader, lower intensity base due to the other orders, which appear greatly out-of-focus. The idea of the PSF having two components leads to the MTF having two components as well, with the out-of-focus orders contributing only on-axis. This gives rise to the spike seen in the MTF on-axis. Buralli and Morris show that the MTF curve in fact approaches the diffraction efficiency for the given order. For the plot above, the diffraction efficiency appears to be 0.88. This does not agree with the measured diffraction efficiency of 0.69 using conventional techniques. One possible explanation for the diffraction efficiency computed with the interferometer being higher

is that the out-of-focus orders are vignetted by the second beamsplitter and imaging lens. Consequently, less out-of-focus light is present at the detector than expected, thereby increasing the diffraction efficiency. More needs to be known about Intelliwave's algorithm for computing MTF and the errors associated with the conventional technique for measuring diffraction efficiency to say which method is in error. However, the main conclusion is that this output shows that an interferometer can be used to measure diffraction efficiency. The versatility of interferometry is amazing.

8.2 Solgel Lenses

The development of miniature optics, optics whose diameters are on the order of a millimeter, is especially challenging to the developmental fields of fabrication and testing. There are a number of ways to manufacture such optics. The studied lenses are manufactured using photolithography techniques combined with materials that can be selectivity polymerized, such as solgel. The basic technique is to pattern the desired lens on a mask, using grayscale values to control sag (Lee, 2003). The solgel material is then exposed to the UV-illuminated mask, causing the exposed solgel to polymerize. Finally, the material is developed and baked, producing the desired lens.

Once the challenge of fabricating the lens is overcome, the next challenge is testing the lens. Not only are the lenses small, but the fabrication process allows for aspheric lenses to be made with the same ease as spherical lenses. This is a situation that seems perfect for CLOVER and the possibility of immersion.

The first lenses examined were trial lenses that were not expected to be of high quality. The lenses have a low enough power that testing could be done in air. Figure 8.8 shows the interferogram and unwrapped wavefront map for one of the trial lenses. The poor quality of the lens can be seen as irregularities in the interferogram and the unwrapped wavefront.

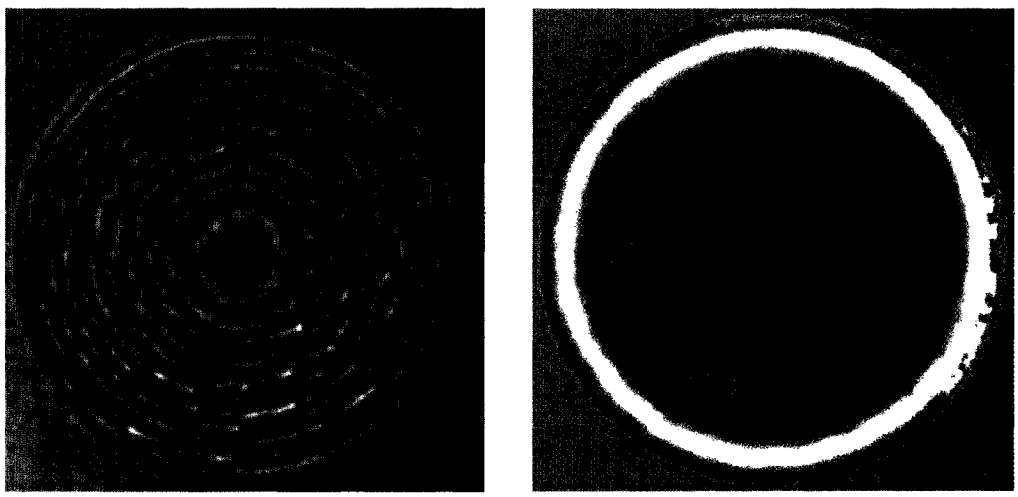

(a) (b)

FIGURE 8.8 – Initial solgel lenses examined over a diameter of 0.85 mm: (a) interferogram and (b) unwrapped wavefront.

The second set of lenses examined are of better quality then the trial lenses. However, these lenses have a higher power and therefore need to be tested while immersed in index-matching fluid. Therefore the index of the solgel and the surrounding fluid need to be known. For the solgel, data extrapolated from the IR to the interferometer's wavelength gives an index of 1.5175. This is in agreement with data taken on an Abbe refractometer. The index of the surrounding fluid is 1.4614 at the interferometer's

wavelength. The tolerance on these values is about 0.0002, and these values lead to a solution factor of 9.2245. Figure 8.9 shows the interferogram across the solgel sample, which contains three lenses. The sample appears dirty; this is actually residual material not properly cleaned from the lens. This is not due to the index-matching fluid, as can be noted by the clear nature of the lower-left corner of the interferogram.

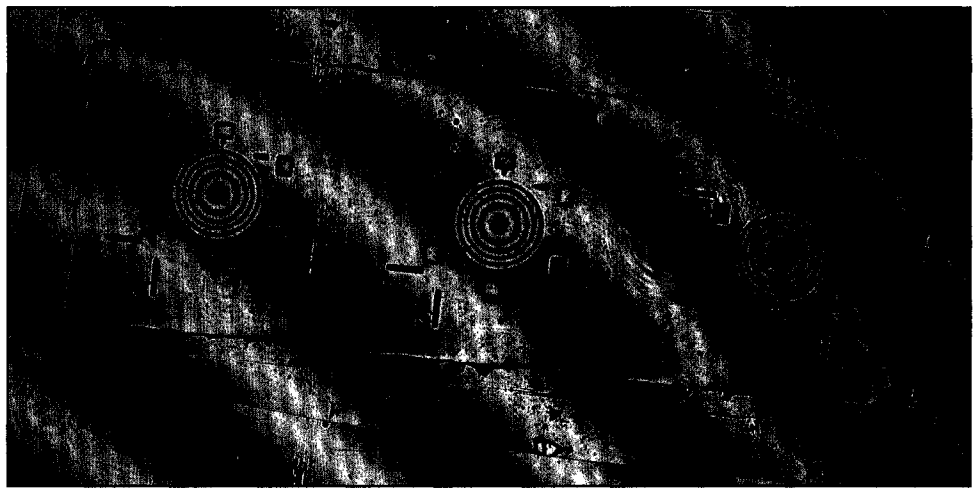

FIGURE 8.9 – Solgel sample with three high quality lenses.
From left-to-right are lenses R, C, and L.

The lenses were designed to a diameter of 1.3 mm, and that is what they measure. Clearly data can be taken over the full diameter; the lenses are showing only about 4.5 λ of power. However, the WYKO profilometer is only able to take data over the central 0.5 mm before the slope of the lens becomes too steep for testing. Thus, the interferometry data presented below is only over the central 0.5 mm for each lens. Figure 8.10 shows the unwrapped wavefront for the lenses. Note that each lens has a slightly different PV, and therefore a different colorbar resolution.

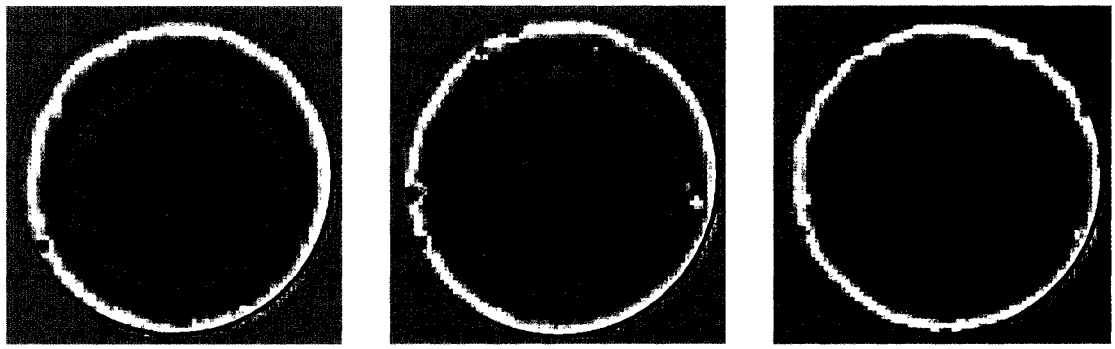

(a) (b) (c)

FIGURE 8.10 – Unwrapped wavefronts for solgel lenses: (a) lens R, (b) lens C, and (c) lens L. The PV numbers are 0.9870, 0.9439, and 0.8978 λ.

Since these lenses are plano-convex, the curvature of the wavefront can be used to compute the radius of curvature (R of C) for the convex surface, which is a derivable output from the WYKO data. This allows for a direct comparison between the two techniques. Table 8.1 lists the output from the two tests. The WYKO data was collected and analyzed by Jeremy Rogers.

Lens	R of C – CLOVER (mm)	R of C – WYKO (mm)	Difference (mm)
R	-3.794	-4.40	-0.606
C	-3.861	-4.47	-0.609
L	-3.881	-4.51	-0.629

TABLE 8.1 – Comparison in reported radius of curvature between CLOVER and WYKO profilometer for solgel lenses.

Clearly there is a systematic error between the two measurements. The constant difference and the agreement between the increase in radius of curvature and decrease in sag or PV are too strong for random errors. Could the culprit of the bias be the use of index-matching fluid to knock down the power of the lenses? To prove if this is the

error, the needed error in index to give the approximately 16% error in radius must be determined. The relationship between the radius of curvature for the wavefront (R_W) and the radius for the convex surface of the lens (R_L) is

$$\frac{R_W}{\mathrm{SF}} = \frac{R_L}{(n_L - 1)}. \qquad \text{Equation 8.1}$$

SF is the solution factor and n_L the index of the lens. This equation comes from the notion that the in-air radius for the wavefront is the reciprocal of the power of the lens. This assumes that the test plane is coincident with the rear principal plane of the lens. Substituting in the definition for SF simplifies the above equation:

$$\frac{R_W}{\frac{(n_L - 1)}{(n_L - n_S)}} = \frac{R_L}{(n_L - 1)},$$

$$\therefore (n_L - n_S) R_W = R_L, \qquad \text{Equation 8.2}$$

where n_S is the index of the matching fluid. Renaming the difference in indices Δn and computing the differential gives the familiar result:

$$\frac{\delta \Delta n}{\Delta n} + \frac{\delta R_W}{R_W} = \frac{\delta R_L}{R_L}. \qquad \text{Equation 8.3}$$

Attributing all of the error in R_L to Δn says that to change R_L by 16%, the difference in index must be off by 16%. The reported indices are n_L of 1.5175 and n_S of 1.4614, for a difference of 0.0561. An error of 16% would mean that the difference is in error by 0.009. Yet each index value is accurate to about 0.0002, which is well beyond an order of magnitude smaller than the necessary error. Consequently, the error is probably not due to inaccurate values for the two indices. The other CLOVER-related error would be

an error in magnification, or not being in focus on the lens. This seems unlikely given the in-focus appearance of the interferograms and agreement between the measured and designed lens diameters. In discussing these results with Jeremy Rogers, the validity of the WYKO data was questioned and doubted. Apparently, due to the relatively steep curvatures for these lenses, the reported radius of curvature can fluctuate with changes in the objective lens used or the field of view examined. The 16% difference between the two instruments could be due to the instability of the reported WYKO data. More experiments need to be done, both with the WYKO and with CLOVER, to determine and eliminate the measured variability. In spite of the different output from the two instruments, the results obtained clearly show that immersion testing is a valuable tool in evaluating these lenses.

9 CONCLUDING REMARKS

Over the last eight chapters, the need for, development of, and results from transmitted wavefront testing of complex optics have been presented. The need comes from a desire to increase and improve the testing options available for contact lenses. The field of testing, one of three fields in the development of any optic, has been explored and enhanced by showing that an absolute, or non-null, transmitted wavefront test can be performed by using a modified Mach-Zehnder interferometer. The design of the interferometer is rooted in three principles. First, the light from the test optic must be collected by the imaging optics. Second, the resulting interference must be resolved by the detector, meaning that at least two pixels must cover each fringe. The third principle is that the wavefront must be calibrated to account for the induced aberrations of the imaging optics. With an interferometer operating in a non-null configuration, the reference and test wavefronts pickup different levels of aberrations when imaged. This difference is accounted for in the calibration process based on reverse raytracing. By using a model of the interferometer, a reverse raytrace yields an estimate for the test wavefront at the test plane. The results from testing spherical, toric, and bifocal contact lenses show that the developed instrumentation and analysis algorithms are capable of meeting the needs of the sponsor. Since the transmitted wavefront is interfered with a planar reference wavefront, the absolute power of the test lens can be determined. The ability to test against a planar reference wavefront is made possible by the necessary

immersion of the contact lenses in saline solution, thereby increasing the dynamic range of the interferometer. This permits a wide range of prescriptions to be tested without the use of null optics or other means of removing the bulk power of the lens. The same raytracing code used in the calibration process can provide modeled wavefronts as well. This enables measured-to-modeled comparisons which quantify the answer to the paramount questions in transmitted wavefront testing: does the test optic perform as modeled?

Successful testing of soft contact lenses requires that the lenses be immersed in saline solution to prevent the lens material from drying out and thus changing its optical properties. The partial index match between the lens material and surrounding saline solution theoretically increases the dynamic range of the interferometer and, at the same time, reduces the sensitivity of the interferometer. The dynamic range and sensitivity can be linked through the dynamic range ratio (DRR). This single number provides a degree of difficulty metric for the instrument or test. Preliminary data shows that the DRR increases slightly for immersion in saline solution.

The developed instrumentation and software are robust enough to test a wide variety of test optics. CLOVER is not limited to contact lenses. A variety of other lenses have been tested and analyzed, including cylindrical lenses, liquid crystal diffractive optics, and progressive spectacle lenses. In each case, data derived from the transmitted wavefront, such as power, radius of curvature, or diffraction efficiency, has provided a

useful comparison to other tests or theoretical values. In some cases, the provided data was simply not obtainable by other tests.

9.1 Conclusions from Accomplished Tasks

Listing everything that has been learned in the course of completing the work encompassed by this dissertation is impossible. On the other hand, there have been a number of lessons learned that are worthy of at least a brief mention. Some of these conclusions have been mentioned elsewhere, other conclusions have been reached only once the totality of the work performed was realized.

The incorporation of raytracing code is vital to the success of advanced metrology. Only by having an accurate model of the instrumentation and the ability to trace rays through the model can sources of error and the necessary procedures to remove those errors be understood. Raytracing code is critical to CLOVER in that both measured and modeled wavefronts make use of the code. The tighter the integration between the codes used to collect data and raytrace, the better and faster the overall analysis package will be. Fortunately, Intelliwave is a robust application capable of talking directly with IDL. The IDL raytracing code developed in conjunction with others in the research group has been an indispensable asset to the project.

The ability to quantify the difference in measured and modeled wavefronts provides a number that can be used to answer the paramount question of transmitted wavefront

testing: does the optic perform as designed? The wavefront difference surface can be analyzed in a variety of ways (e.g. PV, RMS, power) to provide a quantifiable metric for pass/fail testing in a production environment.

Immersion testing has shown itself to be a valuable tool. Immersion in an index-matching fluid provides an easily adjustable increase in dynamic range, for all that needs to be adjusted is the index of the surrounding fluid. Combined with the technique of comparing measured and modeled wavefronts, the results from an immersion test are just as valuable as if the test were done in air. For some optics, such as contact lenses, immersion is the only possible method for getting meaningful data.

The trend towards bigger, faster, and deeper (bit-depth wise) detectors is making possible the ability to test smaller and faster optics. In addition, the results from immersion testing can only be improved with deeper detectors. As this trend continues, experiments that were only theoretically possible in the past will be feasible, furthering the capabilities of all three fields of optical development. Increased computing power is also improving the possibilities of instrumentation. All of the least-squares algorithms used throughout the analysis package for CLOVER would not be practical without today's computing power and availability.

Testing in a non-null configuration demands that some sort of calibration process be performed to remove the induced aberrations of imaging the test and reference

wavefronts. The induced aberrations are wavefront-dependent; no level of designing the perfect imaging lens will change this. The choice of calibration is debatable, but not the need for calibration.

The transmitted wavefront provides a wealth of information. All sorts of outputs, including Zernike coefficients, ophthalmic prescriptions, two-dimensional radial axial power maps, and diffraction efficiencies have been derived from this single quantity.

All of the information necessary to form an accurate prescription for a contact lens, whether the lens is a sphere, toric, or bifocal, is provided by the full lens interferograms and transmitted wavefront. The interferograms over the entire lens determine the orientation of the lens with respect to the detector, critical for toric lenses. The transmitted wavefront, by itself, reveals the annular zones for bifocal lenses. While auxiliary hardware could be used to provide the zone locations, this is not necessary; the transmitted wavefront is all that is necessary.

Simplicity is a valuable feature in any metrology system. Making the system: hardware, acquisition software, analysis software, and end-user controls, as simple as possible increases the likelihood of success. Perhaps this is just a restating of Occam's Razor or the inverse of Murphy's Law, but it is a point worth mentioning.

Power is a complicated parameter. Never mind the various distances that get inverted into powers in the ophthalmic community, just the difference between power derived from Gaussian parameters and power derived from wavefronts is important. The Gaussian power is really a way of combining all of the lens' physical parameters: curvature, thickness, and index, into a single number. The power measured from a wavefront, assuming the wavefront is of a consequential size, is of course subject to aberrations. The inclusion of aberrations is the fundamental difference between the two measures of power. This is analogous to the difference between paraxial focus and best focus, or focus at the minimum circle.

9.2 Future Work

This dissertation has taken an extensive look at several issues associated with transmitted wavefront testing via interferometry, with an emphasis on testing contact lenses immersed in saline solution. The core, fundamental issues have been examined in great detail. However, there are identified issues that have not been resolved. Some of these issues have been dealt with to some extent in the dissertation. All of these issues would serve as excellent starting points for future work in the field.

9.2.1 Immersion Testing

Clearly the experiments performed in Chpt. 7 leave a number of possibilities for future work. Perhaps the most pressing work is with testing over a range of solution factors to

see if the observed relationship between solution factor and power is real. This is also an excellent opportunity to compare measured and modeled outputs, something that was not done extensively with regards to the cylinder testing. Another interesting aspect to immersion testing would be in determining the maximum possible solution factor. There are a couple of possible upper bounds for the solution factor. One is the ability to unwrap wavefronts whose sag is similar to the noise level of the interferometer. Going by the standard deviations used to compute the DRR values in Chpt. 7, an index-match leaving less than $\lambda/40$ in wavefront sag will be impossible to accurately test. Another issue is the homogeneity of the index-matching fluid. The remaining wavefront sag should be significantly greater than the phase errors introduced by index inhomogeneity.

9.2.2 Reflection Testing

The technique of immersing an optic, thereby decreasing its power and making the resulting wavefront testable, is a powerful tool. This is a necessity for contact lenses, given the nature of their makeup, and ultimately allows for the determination of the transmitted wavefront's absolute power. The question is if this technique will work for a reflection test.

In short, the answer is the no. To understand why the technique does not work with reflection testing, a brief understanding of why it does work with testing in transmission is in order. In transmission testing, the slope of the wavefront, as was explained in Chpt. 2, determines the testability of a fringe pattern. Wavefront slope is a direct result of

bending rays. The more the rays are bent, the higher the slope, and the lower the likelihood that the local fringe pattern will be testable. Index matching a refracting surface reduces the bending; a direct application of Snell's Law. With reflecting surfaces, the angle of reflection equals the angle of incidence; no change in bending occurs with immersion.

An interesting note along the lines of opposite effects is that the ability to resolve a small bump or hole is decreased with immersion in transmission but increased with immersion in reflection. In transmission, the OPD due to the defect is proportional to the difference in index between the test optic and surrounding medium. With a reflection test, the induced OPD is twice the optical length of the defect, which is proportional to the index of the surrounding medium.

The common technique for getting more dynamic range out of a reflection test is to go to a longer wavelength, either by using a different source or artificially creating the longer wavelength by using two wavelengths in close proximity (Creath, "Holographic and ...", 1992). A couple of issues with longer wavelengths are the increase in detector noise for longer (IR) wavelength detectors and the need to achromatize all of the optics if two different wavelengths are used (Greivenkamp, 2003). The increase in dynamic range comes at the price of sensitivity, just as with immersion. So then the question is whether or not there are other ways to provide the convenient, tunable increase in dynamic range available with immersion testing that would work with testing in reflection.

9.2.3 Reverse Raytracing

Reverse raytracing was shown to be a vital part of the overall testing of optics in a non-null configuration. Wavefront calibration is one of the three principles of non-null testing. Also discussed was the apparent conflict between the calibration processes of reverse raytracing and subtracting a baseline measurement. Under the current mathematical description of imaging and interfering wavefronts, both processes cannot be used at the same time. Yet the two processes speak to different sources of error. Reverse raytracing removes the induced aberrations in imaged wavefronts, but assumes a perfect reference wavefront. A baseline measurement reveals the difference between the nominal test and reference wavefronts, but does not provide enough information to uniquely determine either wavefront. The ideal situation would be one where the baseline measurement could be used to unambiguously determine the reference wavefront used to start the reverse raytrace.

One method for incorporating both the baseline measurement and reverse raytracing has been developed: reverse optimization (Gappinger, "Non-null...", 2003; Gappinger, "Iterative reverse...", 2003; Gappinger, 2002). The problem, or at least an undesired feature, with reverse optimization is the complexity of the iterative process. Precise perturbations to the system are required, the model for the system is quite complex, and no fewer than three different merit functions must be optimized in a specific sequence. A simpler way to incorporate the information contained in the baseline measurement is desired. The success of this work thus far can be attributed to keeping the calibration

process as simple as possible. Simplicity should not be overlooked as a key component of any calibration process.

APPENDIX A: SAMPLE MODEL

The following IDL code is a sample model of the interferometer used in conjunction with the algorithms for reverse raytracing and analysis. The test part for this model is the calibration lens analyzed in Chpt. 4. Each surface is listed twice; first the reference arm and then the test arm. Dummy values, such as 0 for curvature and 1 for index, are used in the reference arm to keep the number of surfaces and distance between surfaces consistent. Any surface only listed once is identical in both arms.

```
TITLE New Clover System

AUTHOR Greg Williby

DATE 7 02 2003

UNITS mm

WAVELENGTH 0.5435e-3

DETECTORSURFACE 12

TESTSURFACE 6

;CONFIGURATIONS
; 0 = REFERENCE
; 1 = TEST

;EACH SURFACE IS LISTED TWICE - REFERENCE CONFIGURATION FIRST,
THEN TEST.

;ORDER OF DATA : CURVATURE THICKNESS INDEX DIAMETER
(CurvThickIndDiam)
```

```
;DATA THAT IS SUPPLIED BY THE GUI (e.g. Index, Magnification (thickness))
;SHOULD BE SET AS FOLLOWS:

;       All Distances = -1
;       Index of Saline = -1

;NOTE : DISTANCE BETWEEN 3RD WINDOW AND THE BOTTOM OF THE TOP
;WINDOW OF CUVETTE IS 7.05 mm.

;*****************************************************
;****************** Bottom Window of Dovetail Cuvette
SURFACE 0
        SPHERE
        0 4.99 1

        SPHERE
        0 4.99 1.45820
;*****************************************************
;****************** Saline
SURFACE 1
        SPHERE
        0 5.62 1

        SPHERE
        0 5.62 -1
;*****************************************************
;****************** Third window of Dovetail Cuvette
SURFACE 2
        SPHERE
        0 6.51 1

        SPHERE
        0 6.51 1.51594
;*****************************************************
;****************** Saline (TESTSURF)
SURFACE 3
        SPHERE
        0 0.01 1

        SPHERE
        0 0.01 -1
;*****************************************************
;******************** Cal_Lens_2 (Plano/Convex)
```

```
SURFACE 4
        SPHERE
        0.0 2.7504 1

        SPHERE
        0.0 2.7504 1.5128

SURFACE 5
        SPHERE
        0.0 0.001 1

        SPHERE
        -0.012815135840 0.001 -1

SURFACE 6
        SPHERE
        0.0 4.2886 1            ;4.2886 = (7.05-(0.001+2.7504+0.01))

        SPHERE
        0.0 4.2886 -1
;*****************************************************
;******************** Top window of Dovetail Cuvette
SURFACE 7
        SPHERE
        0 4.99 1

        SPHERE
        0 4.99 1.45820
;*****************************************************
;********************** Propagate to Imaging Lens
SURFACE 8
        SPHERE
        0 -1 1
;*****************************************************
;*****Imaging lens: NEWPORT PAC087 (Crown first!)
SURFACE 9
        SPHERE
        0.008241169587 8 1.518855 ;BK7

SURFACE 10
        SPHERE
        -0.01093553502 4 1.677988 ;SF5

SURFACE 11
```

```
        SPHERE
        -0.00368240034 -1 1
;**************************************************
;****************************************** Detector
SURFACE 12
        SPHERE
        0 0 1
;**************************************************

END
```

REFERENCES

Alonso, J., Gomez-Pedrero, J. A., and Bernabeu, E., "Local dioptric power matrix in a progressive addition lens", Ophthal. Physiol. Opt. **17**, 522-29 (1997).

Artzner, G., "Microlens arrays for Shack-Hartmann wavefront sensors", Opt. Eng. **31**, 1311-22 (1992).

Brumfield, R. B., "Measuring the Refractive Index of Hydrogel Material", Master's Report, University of Arizona, 2003.

Born, M. and Wolf, E., *Principles of Optics, Sixth (Corrected) Edition*, Cambridge University Press, Cambridge, UK, 1980.

Brophy, C. P., "Effect of intensity correlation on the computed phase of phase-shifting interferometry", J. Opt. Soc. Am. A **7**, 537-41 (1990).

Buralli, D. A., "Effects of diffraction efficiency on the modulation transfer function of diffractive lenses", Appl. Opt. **31**, 4389-96 (1992).

Burge, J. H., "Applications of computer-generated holograms for interferometric measurement of large aspheric optics", Proc SPIE **2576**, 258-69 (1995).

Canabal, H., Quiroga, J. A., and Bernabeu, E., "Improved phase-shifting method for automatic processing of moiré deflectograms", Appl. Opt. **37**, 6227-33 (1998).

Castellini, C., Francini, F., and Tiribilli, B., "Hartmann test modification for measuring ophthalmic progressive lenses", Appl. Opt. **33**, 4120-24 (1994).

CooperVision, History, www.coopervision.co.uk/uk/consumer/about/history.asp, Accessed October 10, 2003.

Creath, K., "Comparison of Phase-Measurement Algorithms", Proc SPIE **680**, 19-27 (1986).

Creath, K., and Wyant, J. C., "Holographic and Speckle Tests", in *Optical Shop Testing, Second Edition,* D. Malacara, ed., John Wiley & Sons, New York, 1992.

Creath, K., and Wyant, J. C., "Moiré and Fringe Projection Techniques", in *Optical Shop Testing, Second Edition,* D. Malacara, ed., John Wiley & Sons, New York, 1992.

REFERENCES - *Continued*

El-Nasher, N. and Larke, J. R., "Interference Measurement of Soft Contact Lenses", J. Br. Contact Lens Assoc. **3**, 64-70 (1980).

Engineering Synthesis Design, Inc., *Intelliwave, Revision 3.0*, Engineering Synthesis Design, Tucson, AZ, 2002.

Fischer, R. E., and Tadic-Galeb, B., *Optical System Design*, McGraw-Hill, New York, 2000.

Focus Software, Inc., *Zemax Optical Design Program User's Guide, Version 9.0*, Focus Software, Tucson, AZ, 2000.

Ford, M. W., and Stone, J., "Practical optics and computer design of contact lenses", in *Contact Lenses, Fourth Edition*, A. J. Phillips and L. Speedwell, eds., Butterworth-Heinemann, Oxford, UK, 1997.

Fowler, C. W., and Sullivan, C. M., "A comparison of three methods for the measurement of progressive addition lenses", Ophthal. Physiol. Opt. **9**, 81-85 (1989).

Frieden, R. B., *Probability, Statistical Optics, and Data Testing, A Problem Solving Approach, Second Edition*, Springer-Verlag, New York, 1991.

Gappinger, R. O., "Non-Null Interferometer for Measurement of Transmitted Aspheric Wavefronts", Ph. D. Dissertation, University of Arizona, 2002.

Gappinger, R. O., Greivenkamp, J. E., "Non-null interferometer for measurement of aspheric transmitted wavefronts", Proc SPIE **5180** (2003).

Gappinger, R. O., Greivenkamp, J. E., and Borman, C., "High modulation camera for use with a non-null interferometer", (to be submitted), 2003.

Gappinger, R. O., and Greivenkamp, J. G., "Iterative reverse optimization procedure for calibration of a non-null aspheric interferometer", (to be submitted), 2003.

Gaskill, J. D., *Linear Systems, Fourier Transforms, and Optics*, John Wiley & Sons, New York, 1978.

Geary, J. M., *Introduction to Optical Testing*, SPIE Optical Engineering Press, Bellingham, WA, 1993.

REFERENCES - *Continued*

Ghiglia, D. C., and Pritt, M. D., *Two-Dimensional Phase Unwrapping*, John Wiley & Sons, New York, 1998.

Ghozeil, I., "Hartmann and Other Screen Tests", in *Optical Shop Testing, Second Edition,* D. Malacara, ed., John Wiley & Sons, New York, 1992.

Goodman, J. W., *Introduction to Fourier Optics*, *Second Edition*, McGraw-Hill, New York, 1996.

Greivenkamp, J. E., "Sub-Nyquist Interferometry", Appl. Opt. **26**, 5245-58 (1987).

Greivenkamp, J. E., and Bruning, J. H., "Phase Shifting Interferometers", in *Optical Shop Testing, Second Edition,* D. Malacara, ed., John Wiley & Sons, New York, 1992.

Greivenkamp, J. E. Private communication. November 24, 2003.

Groening, S., et. al., "Wave-front reconstruction with a Shack-Hartmann sensor with an iterative spline fitting method", Appl. Opt. **39**, 561-67 (2000).

Hecht, E., *Optics, Second Edition*, Addison-Wesley, Reading, MA, 1987.

Huang, C., "Propagation errors in precision Fizeau interferometry", Appl. Opt. **32**, 7016-21 (1993).

Joenathan, C., "Phase-measuring interferometry: new methods and error analysis", Appl. Opt. **33**, 4147-55 (1994).

Johnson & Johnson Vision Care, Inc. (JJVCI), Inside-Out Mark, www.acuvue.com/products/inside_out.html, Accessed October 23, 2003.

Jozwicki, R., "Influence of aberrations of Fizeau interferometer elements on measurement errors", Appl. Opt. **30**, 3126-32 (1991).

Kafri, O., and Glatt, I., "Moiré deflectometry: a ray deflection approach to optical testing", Opt. Eng. **24**, 944-60 (1985).

Karow, H. H., *Fabrication Methods for Precision Optics*, John Wiley & Sons, New York, 1993.

REFERENCES - *Continued*

Kasana, R. S., and Rosenbruch, K. J., "The Use of a Plane Parallel Glass Plate for Determining the Lens' Parameters", Opt. Comm. **46**, 69-73 (1983).

Keren, E., et. al., "Quantitative Criteria for Determining the Quality of Ophthalmic Lenses", Proc SPIE **1752**, 264-273 (1992).

Klein, S. A., and Mandell, R. B., "Shape and Refractive Powers in Corneal Topography", Invest. Ophthalmol. Vis. Sci., **36**, 2096-109 (1995).

Klein, S. A., and Mandell, R. B., "Axial and Instantaneous Power Conversion in Corneal Topography", Invest. Ophthalmol. Vis. Sci., **36**, 2155-59 (1995).

Kreske, K., et. al., "Testing Soft Contact Lenses with a Moiré Deflectometer", Proc SPIE **1972**, 425-432 (1992).

Kreske, K., Keren, E., and Kafri, O., "Moiré deflectometry – applications to lens analysis", Proc SPIE **1038**, 92-99 (1988).

Larsen, H. O., inventor; Mia Lens Production A/S, assignee, "Preparation of hydrogel for soft contact lens with water displaceable boric acid ester", U. S. Patent 4,495,313, January 22, 1985.

Larsen, H. O., and Kindt-Larsen, T., inventors; Vistakon, Inc., assignee, "Method of forming shaped hydrogel articles", U. S. Patent 4,680,336, July 14, 1987.

Lee, J., "The Development of a Miniature Imaging System: Design, Fabrication and Metrology", Ph. D. Dissertation, University of Arizona, 2003.

Leithold, L., *The Calculus with Analytic Geometry, Sixth Edition*, HarperCollins Publishers, New York, 1990.

Loran, D. F. C., "The verification of hydrogel contact lenses", in *Contact Lenses, Fourth Edition*, A. J. Phillips and L. Speedwell, eds., Butterworth-Heinemann, Oxford, UK, 1997.

Lowman, A. E., and Greivenkamp, J. G., "Interferometer induced wavefront errors when testing in a non-null configuration", Proc SPIE **2004**, 173-81 (1993).

Lowman, A. E., and Greivenkamp, J. G., "Interferometer Errors Due to the Presence of Fringes", Appl. Opt. **35**, 6826-28 (1996).

REFERENCES - *Continued*

Mahajan, V. N., "Line of Sight of an Aberrated Optical System", J. Opt. Soc. Am. A **2**, 833-46 (1985).

Mahajan, V. N., "Zernike Annular Polynomials and Optical Aberrations of Systems with Annular Pupils', Suppl. to Opt. & Photo. News **5** in Appl. Opt. **33**, 8125-27 (1994).

Mahajan, V. N., "Zernike annular polynomials for imaging systems with annular pupils", J. Opt. Soc. Am. **71**, 75-85 (1981).

Malacara, D., "Twymann-Green Interferometer", in *Optical Shop Testing, Second Edition,* D. Malacara, ed., John Wiley & Sons, New York, 1992.

Malacara, D., and DeVore, S. L., "Interferogram Evaluation and Wavefront Fitting", in *Optical Shop Testing, Second Edition,* D. Malacara, ed., John Wiley & Sons, New York, 1992.

Mandell, R. B., *Contact Lens Practice, Hard and Flexible Lenses, Second Edition,* Charles C. Thomas, pub., Springfield, IL, 1974.

Mantravadi, M. V., "Newton, Fizeau, and Haidinger Interferometers", in *Optical Shop Testing, Second Edition,* D. Malacara, ed., John Wiley & Sons, New York, 1992.

Mantravadi, M. V., "Lateral Shearing Interferometers", in *Optical Shop Testing, Second Edition,* D. Malacara, ed., John Wiley & Sons, New York, 1992.

Miller, J. L., and Friedman, E., *Photonics Rules of Thumb*, McGraw-Hill, New York, 1996.

Mohr, W., "Interferometry and Progressive Lenses", Wissenschaftliche Vereinigung fur Augenoptik und Optometrie Germany (Optometrie) **2**, 31-35 (1989).

Murphy, P. E., Brown, T. G., and Moore, D. T., "Interference imaging for aspheric surface testing", Appl. Opt. **39**, 2122-29 (2000).

Pimentel, G. C., ed., *Chemistry - An Experimental Science,* W. H. Freeman and Co., San Francisco, 1963.

Platt, B. C., and Shack, R., "History and Principles of Shack-Hartmann Wavefront Sensing", Jo. Refractive Surgery, **17**, S573-577 (2001).

REFERENCES - *Continued*

Polderdijk, F., "Camera Electronics for the mK x nK CCD Image Sensor Family", DALSA Application Note FTF3020, www.dalsa.com (2002).

Proctor, E. J. D., "Contact lens manufacturing", in *Contact Lenses, Fourth Edition*, A. J. Phillips and L. Speedwell, eds., Butterworth-Heinemann, Oxford, UK, 1997.

Quiroga, J. A., Crespo, D., and Bernabeu, E., "Fourier transform method for automatic processing of moiré deflectograms", Opt. Eng. **38**, 974-82 (1999).

Robb, P., and Pawlowski, B., "Computer ray tracing speeds", Appl. Opt. **29**, 1933-39 (1990).

Roberts, C., "The Accuracy of 'Power' Maps to Display Curvature Data in Corneal Topography Systems", Invest. Ophthalmol. Vis. Sci., **35**, 3525-32 (1994).

Roberts, C., "Characterization of the Inherent Error in a Spherically-Biased Corneal Topography System in Mapping a Radially Aspheric Surface", J. Refract. Corneal Surg., **10** 103-11, (1994).

Saleh, B. E. A., and Teich, M. C., *Fundamentals of Photonics*, John Wiley & Sons, New York, 1991.

Schmit, J. and Creath, K., "Extended averaging technique for derivation of error-compensating algorithms in phase-shifting interferometry", Appl. Opt. **34**, 3610-19 (1995).

Schwider, J., et. al., "Digital wave-front measuring interferometry: some systematic error sources", Appl. Opt. **22**, 3421-32 (1983).

Schwiegerling, J., Greivenkamp, J. G., and Miller, J. M., "Representation of videokeratoscopic height data with Zernike polynomials", J. Opt. Soc. Am. A **12**, 2105-13 (1995).

Schwiegerling, J., *Visual Optics*, class notes for OPTI 435/535X, Visual Optics, Optical Sciences Center, University of Arizona, Spring 2000.

Shack, R. V., and Platt, B. C., "Production and Use of a Lenticular Hartmann Screen" (abstract only), J. Opt. Soc. Am. **61**, 656 (1971).

REFERENCES - *Continued*

Shannon, R. R., *The Art and Science of Optical Design*, Cambridge University Press, Cambridge, UK, 1997.

Shorey, A. B., Jacobs, S. D., Kordonski, W. I., and Gans, R. F., "Experiments and observations regarding the mechanism of glass removal in magnetorheological finishing", Appl. Opt. **40**, 24-33 (2001).

Sinclair, D. C., "Benchmarking computers for optical design", Sinclair Optics Design Notes **2**, No. 1 (1991).

Smith, D. G., Goodwin, E., and Greivenkamp, J. G., "Important considerations when using the Shack-Hartmann method for testing highly aspheric optics", Proc SPIE **5180**, (2003).

Smith, G., and Atchison, D., *The Eye and Visual Optical Instruments*, Cambridge University Press, Cambridge, UK, 1997.

Smith, W. J., *Modern Optical Engineering, Third Edition*, McGraw-Hill, New York, 2000.

Southwell, W. H., "Wave-front estimation from wave-slope measurements", J. Opt. Soc. Am. **70**, 998-1006 (1980).

Spiegel, M. R., and Liu, J., *Mathematical Handbook of Formulas and Tables, Second Edition*, McGraw-Hill, New York, 1999.

Spiers, T., and Hull, C. C., "Optical Fourier filtering for whole lens assessment of progressive power lenses", Ophthal. Physiol. Opt. **20**, 281-89 (2000).

Statton, C. M., Bauer, M. D., and Meyer-Arendt, J. R., "Evaluation of Ophthalmic Spectacle Lenses using the Hartmann Test", Am. Jo. Opt. & Phy. Op. **58**, 766-71 (1981).

Steel, W. H., *Interferometry*, Cambridge University Press, Cambridge, UK, 1967.

Steel, W. H., and Noack, D. B., "Measuring the radius of curvature of soft corneal lenses", Appl. Opt. **16**, 778-79 (1977).

REFERENCES - *Continued*

Stover, J. C., "Scatterometers", in *Handbook of Optics, Volume II, Devices, Measurements and Properties, Second Edition*, M. Bass, ed., McGraw-Hill, New York, 1995.

Strand, J., and Taxt, T., "Performance evaluation of two-dimensional phase unwrapping algorithms", Appl. Opt. **38**, 4333-44 (1999).

Sullivan, C. M., and Fowler, C. W., "Reading addition analysis of progressive addition lenses", Ophthal. Physiol. Opt. **11**, 147-55 (1991).

Tighe, B. J., "Contact lens materials", in *Contact Lenses, Fourth Edition*, A. J. Phillips and L. Speedwell, eds., Butterworth-Heinemann, Oxford, UK, 1997.

Twyman, F., *Prism and Lens Making, Second Edition,* Adam Hilger, Bristol, UK, 1998.

Welford, W. T., *Aberrations of Optical Systems*, Adam Hilger, Bristol, UK, 1986.

Welford, W. T., "Star Tests", in *Optical Shop Testing, Second Edition,* D. Malacara, ed., John Wiley & Sons, New York, 1992.

West, S. C., et. al., "Optical metrology for two large highly aspheric telescope mirrors", Appl. Opt. **31**, 7191-97 (1992).

White, T. C., chairman, Z80 Committee for Ophthalmic Lenses, *American National Standard for Ophthalmics - Contact Lenses – Standard Terminology, Tolerances, Measurements, and Physicochemical Properties,* ANSI Z80.20-1998, Optical Laboratories Association, Merrifield, VA, 1998.

Wyant, J. C., and Creath, K., "Basic Wavefront Aberration Theory for Optical Metrology", in *Applied Optics and Optical Engineering,* R. R. Shannon and J. C. Wyant, eds., Vol XI, Academic Press, Boston, 1992.

Wyant, J. C., and Smith, F. D., "Interferometer for measuring power distribution of ophthalmic lenses", Appl. Opt. **14**, 1607-1612 (1975).